UNIVERSITY OF SOUTHAMPTON

Aeroelastic analysis of a yacht rig

by Mark Hobbs

Thesis submitted in canditure for
the degree of Doctor of Philosophy

Faculty of Engineering and Applied Science
School of Engineering Science

September 2000

UNIVERSITY OF SOUTHAMPTON

ABSTRACT

FACULTY OF APPLIED SCIENCE AND ENGINEERING

SCHOOL OF ENGINEERING SCIENCES

Doctor of Philosophy

AEROELASTIC ANALYSIS OF A YACHT RIG

by Mark Andrew Hobbs

An aeroelastic solution for a mast sail system has been achieved and has been shown to predict realistic behaviour of the system. A nonlinear finite element analysis computer program has been developed, incorporating membrane and solid elements. This has been coupled with a potential flow panel code, PALISUPAN, developed in the University of Southampton, to acheive the aeroelastic solution using a velocity stepping procedure.

A mast sail rig has been analysed in an upwind configuration. The results of the analysis demonstrate the influence of the coupled nature of the mast and sail on the calculated sail forces and deformed shape. Mast compression predicted by the aeroelastic solution of the mast sail system was compared to compression calculated by distributing the sail forces on a nonlinear model of the mast. Results indicate that previous loading assumptions for finite element analysis of a mast significantly underestimate mast compression due to sail loading.

Contents

List of Tables

List of Figures

Nomenclature

Sail definition terms

Foot	The base of the sail
Luff	The forward edge of the sail (attached to the mast)
Leach	The aft edge of the sail
Clew	The corner of the foot and leach
Tack	The corner of the foot and luff
Head	The corner of the luff and leach

Subscripts and superscripts

The notation of Bathe [4] is employed in the non-linear finite element formulation. Left superscripts and subscripts for a derivative refer to the state of the variable and the configuration that the derivative is taken with respect to, so for example, ${}^{t}_{0}u_{i,j}$ is the derivative of u_i at time t with respect to x_j referred to the configuration at time 0.

Roman

E	Young's modulus
A_e	Element area
$\mathbf{B}$	Strain displacement matrix
$\mathbf{B}_L$	Linear component of strain displacement matrix
$\mathbf{B}_{NL}$	Non-linear component of strain displacement matrix
B_c	Half the chainplate beam of a yacht
$\mathbf{C}$	Constitutive matrix
C_p	Pressure coefficient
D	Flexural rigidity
$\mathbf{F}$	Model internal load vector
$\mathbf{F}^{(m)}$	Internal load vector for element m
$\mathbf{H}$	Vector of interpolation functions h_i
I	Second moment of inertia
$\mathbf{J}$	Jacobian matrix
$\mathbf{K}$	Stiffness matrix
$\mathbf{K}_L$	Linear component of stiffness matrix
$\mathbf{K}_{NL}$	Non-linear component of stiffness matrix
$\mathbf{K}_e$	Element stiffness matrix
$\mathbf{K}_e^G$	Element stiffness matrix in global coordinate system
$\mathbf{K}_e^L$	Element stiffness matrix in local coordinate system

L	Cantilever length
N_{le}	Number of points defining PALISUPAN input section leading edge
N_{sur}	Number of points defining PALISUPAN input section sail surface
N_p	Number of points defining PALISUPAN input section
N_t	Number of chordwise panels in PALISUPAN model
N_s	Number of spanwise panels in PALISUPAN model
RM_{30}	Heeling moment of a yacht at 30^0 heel angle
$P(x_1, x_2)$	Pressure distribution on membrane surface
$\mathbf{R}$	External load vector
$\Re$	Vector of finite element loading
$\mathbf{S}$	2nd Piola-Kirchoff stress matrix
$\hat{\mathbf{S}}$	2nd Piola-Kirchoff stress vector
$\mathbf{U}$	Vector of node displacements
V_{infty}	Free stream velocity
X_i^n	Element node n global coordinate
${}_0^t\mathbf{X}$	Deformation gradient

b	Span
c	Chord
c_c	Convergence check criteria
c_l	Convergence limit
d	Membrane thickness
${}_0e_{ij}$	Linear increment in strain referred to the configuration at time $t = 0$
f_i^B	Body loads in direction x_i
f_i^S	Surface loads in direction x_i
h_i	Interpolation function
k	Load coefficient
l_c	Section chord length
q_∞	Stagnation pressure
$\mathbf{q}$	Element pressure load vector
q_e	Difference in pressure between upper and lower element surfaces
n	Load step number
r, s, t	Element natural coordinates
t	Element thickness
t_m	Thickness multiplier used to calculate PALISUPAN input section thickness
t_s	PALISUPAN input section thickness
t_x	Membrane tension in the x_1 direction
t_y	Membrane tension in the x_2 direction

$\mathbf{t}_{2d}$ Two dimensional transformation matrix

$\mathbf{t}$ Three dimensional transformation matrix

u_i Displacement in global coordinate system

u_i^c Displacement of center of pressure loaded membrane

$\mathbf{u}$ Vector of finite element node displacements

v_i Displacement in local coordinate system

w Distributed load magnitude

w_i Numerical integration point weighting

x_i Global cartesian coordinates

$\mathbf{x}$ Matrix of element node coordintes

y_i Element local coordinate system cartesian coordinates

$\mathbf{y_i}$ Vectors defining the element local coordinate system

$\mathbf{y}^i$ Coordinates of node i in the element local coordinate system

k_{ij} Stiffness matrix component

Greek

Π_1	Aeroelastic number
α	Angle of incident flow
β_1, β_2	Relaxation factors
${}_0\eta_{ij}$	Non-linear increment in strain referred to configuration at time $t = 0$
$\partial\mathbf{h}$	Matrix of derivatives of interpolation functions
ϵ	Strain vector
${}_0\epsilon$	Increment in strain referred to configuration at time $t = 0$
ρ	Density
ϕ	Velocity potential
τ	Cauchy stress vector
σ_{ij}	Stress components
ν	Poissons ratio
ξ	Maximum camber

1 Introduction

A rig of a yacht acts as an engine, producing a driving force from airflow over the sails, and transmitting the forces to the hull. In a conventional rig (as opposed to a rig using a wing mast where the mast generates significant portions of the overall driving and side forces), the sails are supported by the mast and rigging, and produce the majority of the driving and side forces.

Modern racing yachts commonly use composite materials in rig construction, and this frees designers from the constraint of extruded aluminium sections to enable strength to be built in the required areas, to allow rig weight to be reduced without compromising the safety of the rig. Any reduction of weight in a yacht gives an increased stability, as reducing the weight of a rig enables more ballast to be carried for a given displacement. Reducing rig weight will also reduce the pitching moment of a yacht, and the smaller rig section sizes will also reduce the aerodynamic drag of the rig. Winning margins in yacht racing can be very small, as shown in the 1999-2000 Americas Cup, where over five races Team New Zealand had an average winning margin of 100 seconds during races of two and a half hours. This represents an elapsed time margin of just 1%, and this series was considered an easy victory for Team New Zealand. Any small performance gains that can be obtained from better understanding of the loading in a rig can make a significant difference to the results in a yacht race.

The limiting factor in mast structural design is avoiding buckling of the mast under the compressive loading generated from the sails and rigging. In the past, calculations of rig loading and the structural requirements of the of the rig have relied on empirical formulae such as Skenes method, as described in Boote [9], to calculate a design mast compression. These are based on a static consideration of the global forces on a yacht using large safety factors.

Finite element analysis of a yacht rig is now regularly used as a design tool for analysis of rig configurations. Yacht masts are subjected to a variety of point and distributed loads, including:

- Loading from the mainsail
- Loading from the boom
- Halyard loads
- Forestay loads
- Rigging pretension
- Inertia loading due to yacht motion

Applying the correct loads to a finite element model is a fundamental requirement for accurate results to be obtained. Point loads on a mast such as rigging and halyard loads can be estimated with a good degree of confidence, but the distribution of the loading from the mainsail has previously been generated from the total sail forces, and applied in a user defined manner along the mast. Constant [3] and parabolic [12] distributions have been considered, but these may not accurately represent the distributed loading from the sail luff. The coupled nature of the mast sail system will also affect the compression developed in the mast, particularly the compression induced from tension in the leech of the sail, and this is not taken into account by the finite element analysis of the mast uncoupled from the mainsail.

Model testing is used extensively for yacht design, and towing tank testing is a well established tool to attempt a hull optimisation. Wind tunnel tests can be used to give a comparison of the overall forces generated by different rig configurations, and to optimise the sail flown shapes. Wind tunnel testing

of model rigs is carried out at a similar Reynolds numbers to the full scale rig, to allow similar flow regimes in the model and full scale cases. Structural similitude for membranes under loading from fluid flow is obtained by matching the aeroelastic number Π_1, first suggested by Jackson and Christie [27]. This was altered by the introduction of a cube root by Smith and Shyy [56] in accordance with a theoretical analysis of large deflections of membranes by Seide [53] to the definition shown in equation 1, which is used in this text.

$$\Pi_1 = \left(\frac{Ed}{q_\infty b}\right)^{1/3} \tag{1}$$

To obtain a structural similitude of the model and full scale cases for a typical model scale of 1:10 assuming that the Reynolds number is similar for the two cases, the Young's modulus of the model sail would have to be 1% of that of the real life case. Dacron sail material has a Youngs modulus of about 25 GPa, so a model with scaled material properties would require a Young's modulus of about 250 MPa. An example of a material with a Youngs modulus of this order is polythene, and since even model sails are created from a number of panels in order to give them a flown shape, it would be extremely difficult to create a model sail from this material. A computer model will allow investigation of a yacht rig with realistic structural and fluid aspects.

Analysis of a yacht rig is complicated by the fact that structural and fluid aspects of the rig are linked, in that rig deformations under the fluid loading will result in a change of the flow over the sails, leading to a change in the loading on the rig, and a change in the rig deformations. Sail forces obtained from a fluid flow analysis of an as designed sail shape are calculated without considering the effect of sail deformations on the generated forces. Aeroelastic analysis of a sail [27] [56], which takes into account the coupled nature of the structural and aerodynamic solutions, can give some insight

into the flown shape of a sail and forces it generates. These forces can be used to give a more accurate estimation of the loading for a finite element model of the mast and rigging.

The mast, rigging and sails also act as a coupled system, as deformation of the mast will affect the shape of the sails it supports. The response of the mast sail system is known to have a significant effect on the sail shape and the forces it generates in real life. This is used in some sailing craft to produce a self adjusting rig, where a gust of wind results in bending of the top of the mast, opening the leech of the sail, reducing the forces generated by the sails and thus preventing the craft becoming overpowered [8]. Previous attempts to analyse a yacht rig have uncoupled the mast and sail which fails to model this important interaction of the mast and sail.

The aim of this thesis is to develop an aeroelastic solution for a mast sail system, which will model the interaction of the mast and sail and also inherently apply the correct distribution of loading from the sail to the mast. This will allow a more realistic analysis of yacht rigs, which could improve performance prediction and give a better understanding of mast loading and the response of a yacht rig.

Detailed analysis of a rig using this method would be of interest to high level racing yacht design, such as for the Volvo Ocean race or the Americas Cup, and the results from the analysis of a rig could be used to improve the loading models used for general yacht designs.

2 Literature review

2.1 Mast design methods

Traditional mast design methods calculate the compressive load in a mast due to the external loading applied to it, and this compression is used to calculate section areas sufficient to prevent the mast buckling. Skenes method uses the righting moment of the yacht at a 30^o heel, RM_{30} and the half beam at the chainplates, B_c to calculate a compressive loading in the mast, equation 2.

$$\text{Mast compression} = \frac{RM_{30}}{B_c} \tag{2}$$

The application of Skenes method is discussed by Boote [9]. Safety factors are used to take account of the loading due to stays, sheeting and halyards. Classification society rules use formulae based on this approach for calculation of required mast sections. Larsson [34] uses the Nordic Boat Standard rules to calculate the section requirements for a 40 foot yacht mast, and the spars and standard rigging scantling calculations of the Bureau Veritas rules for yacht design are summarised by Boote [9]. Mitchell [39] studied data obtained during sailing trials of the 130 foot yacht New Zealand, and used these to suggest refinements to Skene's equation for the mast compression, with separate calculation for the loading imposed by the halyards and rigging. These are based on the loading figures for one yacht, and application of these formulae to other yacht rig arrangements was not considered.

2.2 Finite element analysis of masts

A finite element analysis of a yacht mast and rigging allows a more detailed picture of the stresses developed in the mast to be obtained. In order to carry out a finite element analysis, the loading on the mast have to be specified.

The point loads from rigging and halyards are well defined in their point of application, and data from sailing trials or design calculations can provide the magnitude of these loads. Loading from the mainsail luff will apply a distributed load along the mast, and this is not evaluated as easily as the point loads. The total mainsail luff loading on the mast can be calculated by using the righting moment of the boat or from lift and drag coefficients of the sail. This total load can then be distributed along the mast, and constant, linear, parabolic and other distributions have been employed. Enlund *et al* [12] use the righting moment of the boat to derive the total sail loading on the mast, and apply this using an elliptical distribution. Hoffmeister [22] also uses the righting moment of the boat to calculate the mainsail forces, and these are applied as a distributed loading along the mast in proportion to the sail area. Cant [10] calculated the total mainsail forces from a potential flow analysis of the sails, and then applied this loading as a linear distributed load in conjunction with point loading from the halyards and rigging obtained from experimental measurement on the yacht being modelled. Sail coefficients from the IOR measurement rule were used by Selness [54] to derive the sail loading for a rig, although no details of how this was distributed onto the finite element model are provided. Keuning and Van der Werff [48] compared a linear and constant load distribution along the mast for masthead and fractional rigs. Differences of up to 40% in bending moment at the deck for both rigs, around 70% variation in bending moment for the top section of the fractional rig and a 10-30% difference in stay tensions occurred for the two loading distributions. This highlights the importance of having the correct loading applied to the mast in order to obtain an accurate finite element solution.

Selness [54] and Cant [10] carry out a linear analysis of the mast and

rigging, using loading data from a potential flow analysis of the as designed sail shape. Both Keuning and Van der Werff [48] and Hoffmeister [22] divide the mast loading into a number of load steps, and use a linear finite element analysis on each step, with the stiffness of the structure recalculated after each load step. This takes into account the change in stiffness of the rig due to rig deformations.

Mitchell [38] notes that the conditions applied to the mainsail luff loading are fairly arbitrary, and to find a more realistic distribution of the loading requires a model of the sail to be combined with the mast model. The sail is modelled using a membrane strip of high stress running from the mast head to the end of the boom (along the sail leech) to represent the sail, based on the reinforcing and structural design used by sailmakers. The mast is modeled by beam elements, and a modified Newton-Raphson solution to a direct stiffness finite element method which allows large displacements is employed, an equivalent method to the stepwise linear finite element calculations carried out by Keuning and Van der Werff [48] and Hoffmeister [22]. Sail loads are applied as discrete forces to the mast in the direction of the sail cloth at the mast, such that the net moment is equal to the righting moment of the yacht. This method is an improvement over simply applying the sail loads as distributed forces along the mast, but in order to model the coupled nature of the mast and sail and to apply the correct loading to the mast, it is necessary to develop a finite element model of the sail and mast together.

2.3 Membrane analysis

The analysis of membranes under the infiuence of fluid flow is complicated by the coupling between structural and aerodynamic responses. Under the action of an incident flow, the membrane will become pressure loaded which

will result in a deflection of the membrane resulting in a change in the airflow over the surface. This prevents a closed form solution of the flow over a flexible membrane. Membranes are also unable to support compressive stresses, which can introduce more difficulties in a three dimensional case. The problem can be simplified by assuming that the membrane is inextensible with a constant tension, or looking at a two dimensional case, and several solutions to a fluid flow loaded membrane have been presented using these approximations.

2.4 Inextensible membranes

Initial analyses of membranes under the action of incident flow looked at the case of inextensible membranes. Two dimensional cases with membranes under a constant tension were analysed by Thwaites [61] and Neilsen [42]. For the structure to be in equilibrium, the curvature of the membrane must be such that the tension in the membrane balances the pressure loading on it. A two dimensional sail equation is developed, using linearised airfoil theory and static equilibrium of the sail under pressure force and tension (constant over the sail). The resulting equation has no theoretical solution, but Thwaites develops an iterative numerical solution, dividing the membrane into elements. Neilsen [42] studies the same problem using fourier analysis, with a fourier series to describe the membrane shape. Analysis with a leading edge singularity is undertaken approximately, truncating the solution to the first 18 and 30 coefficients of the fourier series.

Greenhaulgh [17] measures experimental shapes of rectangular inextensible membranes with a variety of excess lengths, and compares experimental and calculated airfoil shapes, lift coefficients and membrane tensions. Pressure distribution is calculated using a vortex lattice method, with each ele-

ment of the membrane having a line vortex at 1/4 chord and a control point at 3/4 chord. Membrane tension is assumed to be constant, and the tension and local curvature of each element balance the pressure difference. Results from the calculations were found to be in good agreement with experimentation for lift, shape and membrane tension.

Newman [43] presents a review of the work performed on flexible inelastic membranes. Geometry and local tension of the membrane are related to the pressure difference across the membrane, and pressure distributions are calculated using potential flow. It was noted that the effect in change in tension and shear across the membrane thickness are third order, and so are neglected. Since membranes are unable to support compressive stresses, it is noted here that the smaller principle stress is significant, as the membrane will approach a wrinkled state as this reached zero.

Jackson [26] calculates the shape of a two dimensional sail in inviscid flow, extending the analysis to two interacting sails. The membrane is divided into segments, and a vortex lattice method is used to calculate the pressure distribution for a given membrane shape. To ensure that the surface streamline leaves the trailing edge smoothly, and additional point is used beyond the trailing edge. The structural method relates curvature and tension in the element to the pressure difference. Solution of the membrane problem requires two levels of iteration. A shape of the membrane is assumed, then the pressure distribution calculated. The membrane tension is guessed, and the shape calculated for this tension. After a deflected shape is found, the chord length of the membrane is calculated. If this is too long, the tension is increased and the shape is calculated again. When the shape has converged, the pressure distribution is recalculated and the procedure continued until the change in tension is below a convergence criteria. The convergence cri-

teria for the entire problem and the structural calculation are calculated to give the same level of accuracy. Jackson and Fiddes [28] extended this work to account for viscous flow past two dimensional flexible sail sections. The structural model used is the same as the previous paper, and a Navier Stokes solution with a flexible boundary layer was employed for the fluid model. A cosine distribution of the panel edges and collocation points is used, and the flow field takes into account a boundary layer on each side of the membrane and a separation bubble at the leading edge. Constant strength doublets are used to represent the vortex sheet, and integral methods are used to represent the boundary layer flow. Results show good agreement with experimentation, but the difficulty in obtaining experimental results with rigid spars that do not affect the airflow are highlighted. The inclusion of viscid effects were found to make a difference of only one percent in the membrane tensions.

2.4.1 Elastic membranes

Ormiston [47] studied an initially flat rectangular membrane with fixed leading edge and ribs. The trailing edge of the membrane is held by a cable under tension. Membrane tension is taken to be constant in the chordwise and spanwise directions, t_x and t_y. The membrane deflection equation, equation 3, relates curvature and tension to the pressure difference across the membrane, and is an extension from the two dimensional cases mentioned previously. Due to the elastic nature of the membrane, this equation is now non-linear with respect to deflections, as the partial derivatives of the deflections, $\partial^2 z/\partial(x)_i^2$ are multiplied by the membrane tensions, t_x, t_y, which are functions of the membrane deflections .

$$t_x \left(\frac{\partial^2 x_3}{\partial {x_1}^2} \right) + t_y \left(\frac{\partial^2 x_3}{\partial {x_2}^2} \right) = -P(x, y) \tag{3}$$

Non-linear chordwise and spanwise strains are calculated from the deflections, and this is used to calculate the membrane tensions. Equations for the sailwing surface are developed to include the deflections of a pretensioned elastic trailing edge wire, leading to a non-linear system approximating the structural response of the sailwing. The aero-elastic problem is uncoupled, and the wing loading is approximated by the first term in a fourier series expansion of a uniform loading. Tensions are found by solving the non-linear equilibrium equation by iteration. The resulting membrane slackness due to the elongation of the membrane and the trailing edge wire deflection is used to calculate the shape of the membrane. Use of the structural results allows calculation of the lift of the sailwing using thin airfoil and Prandtl lifting line theory. Values of deflection and tensions for arbitrary values of the lift coefficient can then be calculated, and the sailwing aerodynamics can be related to the structural properties of the membrane. The non-linearity of the sailwing lift curve is found to be due to the elastic effects of the membrane.

A computer orientated continuum approach to the sailwing problem is described by Holla *et al* [24]. They note that for a full structural analysis of the membrane, it is necessary to take into account the spar flexibility and variation of tension across the membrane. For this case, the tip ribs are assumed rigid, and a state of pure membrane stress exists with uniform chordwise and spanwise tensions. It is noted that these approximations are restrictive, but allow the solution of the problem with much less computation than a full finite element analysis. Average strains are calculated from the change in length in the chord and spanwise directions, and assuming linear elasticity, the instantaneous membrane tensions can be calculated. The aerodynamic problem is solved using a doublet lattice method. The deflected membrane

shape must satisfy both the aerodynamic and structural equations. To solve the problem, the deflected shape is assumed to be defined by a double fourier series, which results in equations for the constants of the series in terms of the instantaneous tensions in the membrane. An iterative solution method is used to calculate the equilibrium deflections of the membrane, as detailed below:

- Choose value for instantaneous tension
- Solve for fourier series coefficients
- Compute change in instantaneous tensions
- Check for convergence, otherwise start with updated instantaneous tensions.

Double skinned membranes are analyzed by Murai and Muruyama [41]. The three dimensional sailwing with trailing edge wire is idealized as a two dimensional case with the wire represented by a spring on the trailing edge of the membrane. The structural equation is given by a balance of the tension and curvature with the pressure difference for the top and bottom membranes separately. Pressure loading is obtained using a panel method over the membrane, and solution of the problem is obtained by iterating between the structural and aerodynamic problems. Iteration is also used to solve the non-linear structural equations and results are presented for a circular leading edge spar.

Smith and Shyy analyze two dimensional membrane wings under unsteady laminar flow [55]. The membrane is subject to pressure force and shear force, and is linearly elastic with prestress. The membrane is divided into elements with the structural equation solved using finite difference and

the aerodynamic problem solved using a pressure based numerical procedure. An iterative solution method is used to account for the coupling between the aerodynamic and structural aspects of the problem, using a body fitted langrangian formulation for the grid. The elastic and aerodynamic problems are solved cyclically until convergence. A steady state solution is obtained, and this is used as the starting configuration for an oscillating flow. In a second paper [56], the model is extended to account for turbulent flow, using Reynolds Averaged Navier Stokes equations with k-w eddy viscosity models for the aerodynamic problem, and the same structural model as before.

The assumptions of constant tension in membranes that have been used in obtaining numerical solutions to membrane problems have given good results for rectangular membranes in these studies. However, these restrictions are unrealistic for the triangular shapes encountered in yacht sails as the problem lacks the symmetry of the rectangular problems. In order to analyse these membrane shapes, it will be necessary to carry out a finite element analysis of the membranes. Due to the non linear relationship between the membrane displacements and the pressure they support, a non linear finite element analysis will be necessary to model the sails. This will also allow analysis of the rig as a whole, as the non linear nature of this system has been noted by, for example, Keuning and Van der Werff [48] and Hoffmeister [22].

Newman [44] presents a review of work on elastic membranes up to 1987, including much of the details from an earlier paper on inextensible membranes [43]. Additional cases of three dimensional sails including vortex and doublet lattice methods for solution of the aerodynamic problem and inelastic and isotropic finite element analysis of the structural problem are discussed.

2.5 Non linear finite element analysis

Analysis of structures undergoing large displacements during deformation require the use of a non linear formulation for the finite element governing equations. This results in a series of non-linear equations for the finite element problem. These are solved using incremental formulations, and a description of the incremental loading methods are given in Ross [51].

Mallett *et al* [36] develop finite element matrices that take into account large deformations of the model. Governing equations are developed using virtual work, and these are shown to be identical to those derived from variations in the models potential energy. A truncated Taylor series expansion around a known equilibrium position is used to obtain a linear incremental formulation to allow solution of the non-linear governing equations. For cases with non linear strain displacement relationships, a non linear incremental formulation, which uses the first two terms of a Taylor series expansion is developed. Finite element matrices for a truss element are developed using the direct, potential energy and linear incremental formulations. The linear finite element stiffness matrix is replaced by a summation of three matrices:

- Linear finite element stiffness matrix
- Stiffness matrix which is a linear function of displacement, which couples membrane and flexure action
- Stiffness matrix which is a quadratic function of displacement, which affects flexure action only.

Further development of this work is presented by Rajasekran and Murray[50]. Working from the strain energy for a linear elastic material and noting that the strain can be split into components linearly and quadratically dependent

on displacement, the potential energy of the model can be found. From this, the stiffness matrix for an element is developed in the same form as in [36]. It is noted that the forms of the stiffness matrices are important to enable them to repeat in both the equilibrium and incremental equations, which was not shown in Mallett's work. These formulations are shown by Wood and Schrefler [67] to be identical to the methods developed by Zienkiewicz [68] taking into account difference in notation and arrangement of the stiffness matrices.

Bathe *et al* [7] develop non linear finite element formulations from continuum mechanics. The loading path is divided into a number of steps, and equilibrium is obtained at each step before continuing. Two formulations are presented, the Total Langrangian and Updated Langrangian, which refer the current displacement derivatives to the initial and current state of the body respectively. These different formulations give the same numerical results, and choice of scheme is dependent only on the relative numerical efficiency for the problem being considered. Virtual work is used to formulate the governing equations, and the non-linear term in the equation is linearised using a Taylor series expansion, truncated to the first term. Due to this linearisation, the internal and external forces will not be in equilibrium at the end of the load step. It may be necessary to iterate within the load step to reduce the out of balance force in order to ensure that a stable solution is obtained for the full loading path.

2.6 Membrane finite element analysis

Timoshenko and Woinowsky-Kreiger [63] concluded that if the ratio of thickness to other dimensions for a membrane is less than 0.1, the bending stresses are small in comparison to other stresses and can be neglected, as noted in

Newman [44]. Yacht sails will typically have a ratio of thickness to chord of less than 1.0×10^{-3}, and this restriction can be incorporated into a finite element model by using elements that are planar and assuming a state of locally plane stress in each element.

Oden and Sato [46] employ elements with displacement coefficients that are independent of deformation, and calculated using the geometry of the undeformed elements, which corresponds to the Total Langrangian method described by Bathe [7]. A stiffness relationship is determined by equating external virtual work done by nodal forces to internal work, expressed in terms of an elastic potential function, W. The elastic potential function is itself a function of the membrane strains, and it's exact form depends on the membrane material. Examples are given for isotropic, perfectly elastic materials, where W is a function of the strain invarients. In the case of small strains, the relationship for a neo-Hookean membrane is obtained, and the familiar linear stiffness matrix is obtained. The element stiffness matrices are calculated in the element local coordinate system, and then transformed into the global coordinate system for assembly into the global stiffness matrix, using the connectivity of the elements. Boundary conditions are applied by prescribing forces or displacements on the nodes, and a system of non-linear equations in the node displacements is obtained.

To solve resulting the non-linear equations, a Newton-Raphson method is used. The non-linear stiffness term is expanded using a Taylor series and truncated to the first two terms - the linear stiffness relation and a correction due to increments in the node displacements. These equations are solved for displacement increments due to an increment in the nodal forces. Corrected values for the nodal forces are then calculated using the full non linear relationship. These are then used to calculate a correction

to the nodal displacements using an updated stiffness matrix. The solution is initialized with an assumed displacement field, and this is corrected until convergence of the displacements. At some stages in the solution, compressive stresses can develop in the membrane, which leads to the stiffness matrix becoming no longer positive definite and a failure of the iterative solution. When this occurred, the solution process was restarted with a new prescribed displacement field. Solution were obtained for the deformation of an initially square membrane under a prescribed in plane edge displacement, and for the inflation of a flat membrane.

2.7 Stein Hedgepath wrinkle model

Membranes do not support compressive stresses, and as compressive stresses develop in a membrane, wrinkling will occur. This behaviour is avoided by Oden and Sato [46] by altering the initial displacement field to find a starting point where no compressive stresses develop during the analysis. In reality, wrinkling due to development of compressive stresses often occurs in membrane structures, and it is possible to model this behaviour within the finite element solution using an algorithm developed by Millar and Hedgepath [37], which is a numerical implementation of a continuum theory developed by Stein and Hedgepath [58]. The development of a compressive principle stress will result in a state of uniaxial tension occurring at that location within the membrane, and this will result in the membrane wrinkling. When wrinkles occur, the contraction in the direction normal to the wrinkles exceeds what is predicted by the materials Poisson's ratio. This is incorporated into the wrinkle model by increasing the effective value of the Poisson's ratio in the wrinkled region. The algorithm to implement this compares the principle values of local strain, and determined if the element is in either the slack,

wrinkled or taut state, and a different constitutive matrix is given for each of the states. To ensure that a steady state is reached, it is necessary to iterate within each load step, changing the constitutive matrices of each element according to the last calculated value of local principle strains until the element state converges.

2.8 Fluid flow analysis of sails

As noted in [28], viscid effects change membrane tensions by only about 1% in a two dimensional analysis. Thus for the aeroelastic analysis of sails, the potential flow method of calculating fluid flow is sufficient to determine the pressure distribution on the sail providing that the sail configuration is such that the flow is not widely separated. The case of a yacht sailing upwind has flow that does not contain a large amount of separation, and is suited to analysis using potential flow methods. Potential flow methods have the advantage of short run times in comparison with viscous codes. Caponetto and Bonjour [11] obtained a flown shape of a mainsail and jib, using an aeroelastic solution which incorporating a potential flow vortex lattice code to calculate the pressure loading on the sails, and then carried out a Navier-Stokes analysis on the flown shape. Analysis of a yacht rig in an upwind configuration using a potential flow panel code, PALISUPAN [64] will take around two minutes on a single processor workstation, compared to a run time of about five hours on a 64 processor workstation for a viscous Navier Stokes analysis of a similar problem [11]. For an aeroelastic solution, which may require over two hundred separate aerodynamic calculations during the solution, this time penalty becomes prohibitive.

Vortex lattice codes have been used in previous aeroelastic analyses of sails by Jackson [27] and Smith [57]. The vortex lattice method is suited

to sail analysis as it effectively models thin structures. PALISUPAN is a potential flow source/doublet code that was developed at Southampton to study the effect of propeller rudder interactions [64], and has been successfully used to analyse upwind sail configurations [10] [45], and shown to give good agreement with experimental global force values and pressure distributions [49]. Due to the nature of the code, it is necessary to introduce an artificially large thickness to the sails, but this does not detract from the accuracy of the pressure calculations [49]. The source doublet method will allow the analysis of the sails and mast together, which is not possible with a vortex lattice code.

2.9 Aeroelastic analysis

Bathe [5] notes the importance of selecting the correct mathematical model for fluid structural interaction, and uses a finite element method for solution of both the aerodynamic and structural elements of the problem. He also notes that solution of the finite element equations by direct methods can become computationally expensive, as computing time and hardware requirements increase with the number of nodes, N, in proportion to N^2 and $N^{3/2}$ respectively.

Han and Olsen use an iterative coupled fluid structural model to study wind loaded pneumatic structures [18]. The aerodynamic problem is solved using a boundary element analysis, and this provides pressure loading for the finite element analysis. A Langrangian formulation is used for the structural problem with an incremental decomposition of the stresses and strains. The non linear stiffness term is linearised using a Taylor expansion, and a warped four noded quadrilateral shell element is used for the analysis. The deformation dependence of the pressure loading is accounted for in the el-

ement stiffness matrix calculations, and results in a non symmetric matrix. Iteration is used to solve the structural problem, with the linear stiffness relationship used to calculate increments to the displacement due to the load increments calculated using the non-linear equations from the previous displacement increments. A line search scheme is used to assist convergence of the node displacements. The starting point is an assumed or given profile of the structure, then the aerodynamic problem is solved to give the pressure loading for calculation of the new profile until convergence.

Jackson and Christie [27] use the membrane assumptions of Oden and Sato [46] applied to a finite element formulation to solve the structural problem for a three dimensional sail. The sail is divided into triangular elements which are used for both the fluid and structural solutions. A vortex lattice method is used to calculate the pressure loading on the sail, using triangular elements with control points at the element centroids. A wake sheet is extended in the direction of flow at the trailing edge of the sail. It is noted that a force free wake sheet would be required for accurate calculations for two sail interaction. Since both the elastic and pressure forces are non-linear with respect to the nodal displacements, it is necessary to employ an iterative solution to the structural problem, using a Newton-Raphson method. As in Han and Olsen [18], a linearised stiffness relationship is used to calculate approximate node displacements for an increment in force calculated from the full non-linear equations using the previous displacements. The wrinkling of the membrane is modeled by changing the constitutive relationship to an axial stress state in wrinkled regions. The aeroelastic solution is obtained by solving the aerodynamic problem, applying these pressures to the membrane and iterating until the structural equilibrium is found, then recalculating the pressures using the deformed shape, and continuing until the solution

converges.

Atkinson [2] went some way towards the analysis of a mast sail system, using curved membrane elements developed by Zienkiewicz [68]. An 'as designed' sail shape is used to calculate pressure loads using an unsteady lifting surface marine propeller method developed by Szantyr [59]. The mast is considered as a rigid boundary for calculation of stress in the sail with a non-linear finite element analysis. Stress resultants from the sail luff are then applied to an approximation to a non-linear beam analysis of the mast where the loading is applied in a number of increments, and a linear solution obtained using an updated stiffness matrix for each increment. The resulting mast bend is calculated and applied to the sail to gain a new shape which is analyzed to calculate the effect of the response on the sail driving coefficient, although no further coupling of the fluid and structural problems was undertaken. This approach was developed in a further paper by Atkinson and Szantyr [3]. The aerodynamic problem is solved using a vortex lattice method, with line vortices around the quadrilateral elements and a control point at the center of the element. This loading is applied to a membrane model of the sail as in [2], and the luff forces applied to a large deformation finite element analysis of a rig comprising beam elements for the mast and tension only rod elements for the rigging under pretension. The method is used for the solution of a two sail jib/main combination. Initial attempts modeled the jib stress resultants as a single force at the point of attachment to the mast, but this was extended to include a forestay made of discrete elements loaded by the stress resultants from the jib luff to model the forestay sag. As previously, the distorted geometry was run through the CFD calculations to determine the change in sail driving force, but no coupling between the structural and fluid problems was investigated.

Smith and Shyy [57] have produced the most complete analysis of a sail. The elastic membrane problem is solved using load stepping by incrementally increasing the freestream velocity. The non-linear structural problem is solved using the finite element formulation of Bathe [4] [7], with the strain displacement relationship altered to that used by Oden and Sato [46] for the membrane case, and use is made of the Stein-Hedgepath algorithm for wrinkled membranes [37]. A modified Newton-Raphson approach is used to iteratively solve the structural problem for each pressure distribution, and the fluid and structural problems are solved cyclically until convergence at each load step. A vortex lattice method is used for the calculation of the pressure distribution over the sail, according to the methods of James [30], using the same quadrilateral elements used for the structural calculations. Results are presented for a membrane under uniform pressure, a rectangular membrane wing with free trailing edge and an initially flat triangular membrane representing a mainsail. In all cases, prestrain is used to allow solution of the first load step (as otherwise the matrices are singular), but this is removed for following load steps.

Fukasawa has studied the dynamic response of a two dimensional membrane in water [14] and a three dimensional sail in air [15]. The strain displacement matrix is split into linear and non-linear parts. An incremental formulation is used, splitting the loading into a number of equilibrium states. the incremental stress strain relationship is assumed to be fully elastic, and higher order terms are neglected in calculation of the stiffness matrix. The final stiffness matrix contains the linear stiffness matrix, initial displacement stiffness matrix and initial stress stiffness matrix, and corresponds closely with the Total Langrangian formulation described by Bathe [7].

The two dimensional membrane in water is modeled for static equilibrium

using hydrostatic pressure. The pressure force is calculated using the previous load step displacements. As the load steps used are small, the deformation dependence of the loading is adequately described by this approximation. A dynamic case is then calculated using strip theory and Bernouilli's equation to obtain loads at each time step, with the static case used as a starting point. The three dimensional sail is modeled using triangular elements for both aerodynamic and structural analysis, as a triangle determines only one plane and is the natural shape to use for dividing up a triangular sail. The pressure loading is calculated using a vortex lattice method with a control point at the element centroid. The combined aerodynamic and structural case is solved using increments in the freestream velocity from zero to the required value. At each step the pressure distribution is calculated to provide the nodal loads for the finite element analysis, and updated shape is used for the next velocity step. A dynamic analysis of the sail under pitching and yawing is then carried out using Newmark-β time integration.

2.10 Experimental analysis of yacht rigs

There has been a large amount of testing done on various yacht rigs, but almost all of this work is commercially sensitive, and so is rarely published.

Ladesic [31] carried out studies of rigid cylindrical surfaces in the form of a single sail and a model with hull and a variety of main and headsail combinations. The wind tunnel was empirically adjusted to develop a scale velocity profile appropriate to yacht sails using a vertical distribution of flow impedance upstream from the model. Experimental results are compared to a vortex lattice model, and found to be in good agreement up to the point of stall.

Locke et al [35] develop a method of measuring the distribution of lift and

drag along the span of a sail. Lift and drag are inferred by measurements of velocity components and pressures in the sail wake, as this measurement method does not interfere with the flow over the sails. This allows details of the structure of the flow around the sails to be shown, and provides a better model for calibration of numerical methods. A strong vortex is found originating at the foot of the sail, due to the gap between the boom and deck, but no vortex was found originating from the head of the sail.

The requirements for simlitude for testing model sails in wind tunnels is discussed by Flay [13]. He notes the difficulty in assessing the dependence on forces due to Reynolds number as increasing wind speed in the tunnel results in deformation of the sail. It is also difficult to obtain similar aeroelastic numbers (defined by Jackson and Christie [27]), as a model sail would have to be made out of extremely elastic materials. He notes that this affects only the deformed shape of the sail, which can be altered by the crew using the sail controls. The effect of velocity profile and induced turbulence is discussed, in particular pointing out the difference between yachts and stationary buildings.

2.11 Summary

Aeroelastic solutions have been obtained for membrane structures which represent yacht sails, and this allows the coupled nature of the fluid and structural aspects of the sail to be modelled. The forces generated by a mainsail have been applied as distributed loads to finite element analysis of masts, but the distributions of the loading have been chosen arbitrarily. Considering the mast and sail as distinct bodies in this manner neglects the interaction of the rig elements. An aeroelastic model of a mast and mainsail body will apply the forces generated by the sail onto the mast in the correct manner, and

also model the interaction of the mast and sail deformations.

Potential flow allows the solution of the fluid aspect of the mast sail model in a timescale appropriate for the aeroelastic analysis of a rig. Vortex lattice potential flow codes have been used successfully in both fluid and aeroelastic analysis of sails. A non linear finite element program is required for the analysis of the structural aspect of sail deformation, due to the large deformations that can occur in the rig and the non linear nature of the membrane strain energy - displacement relationship. A Total Langrangian formulation developed by Bathe [7], including the membrane assumptions of Oden and Sato [46] and the membrane wrinkle algorithm of Millar and Hedegepath [37] has been employed by Smith and Shyy in the aeroelastic analysis of sails [57].

The aeroelastic analysis of a mast sail system will use a similar formulation to that employed by Smith and Shyy [57]. A Total Langrangian finite element formulation [7] will be developed, including membrane assumptions [46] and wrinkle model [37] for the sail elements and suitable elements for the mast analysis. A potential flow panel code, PALISUPAN will be used to model the mast and sail to calculate the pressure loads on the system. Programs to generate the required PALISUPAN model geometry from the finite element model and calculate the finite element model loads from the panel code pressures will be required to carry out the aeroelastic analysis.

3 Aeroelastic solution method

3.1 Analysis model assumptions

A yacht rig operates in a constantly changing environment. Wind speed and direction varies continuously, and the yacht on which the rig is supported will be in constant motion under the influence of the environment and the input of the crew sailing her, and is itself a flexible structure. In order to simplify the problem to a level which is soluble with modern techniques, it is necessary to apply restrictions to the real life case. The rig is simplified in this analysis, and a system of a single sail on a mast is considered. The methods used are capable of dealing with multiple sails and rigging elements, but this would result in a complex system with a large increase in computational time and the increased number of variables would make conclusions difficult to draw. The rig is assumed to be in a steady state and no heel is applied, which is close to the real life situation of a yacht sailing on flat water in a low, steady wind. The case of a yacht sailing close hauled into the wind is considered, as it is possible to obtain a reasonable prediction of fluid flow around the rig using potential flow analysis for this sailing heading. Although viscous effects, such as separation in the region of the mast can be appreciable, the extra computational time required for a viscous analysis would result in a prohibitively large solution time for the aeroelastic analysis.

3.2 Solution structure

The aeroelastic solution method which is used is illustrated in figure 1. The coupled nature of the fluid and structural aspects of the system requires an iterative solution to the aeroelastic problem. The rig is analysed using a fluid flow model to calculate the pressure distribution over it. This is used to gen-

erate the loading for the structural analysis of the rig. The deformed rig can then be analysed using the fluid flow model to obtain an updated pressure distribution. This cycle is continued until the solution has reached convergence. This solution structure has been employed in aeroelastic analysis of sails by Jackson and Christie [27] and Smith and Shyy [57], and in analysis of wind loaded pneumatic membrane structures by Han and Olsen [18].

Aeroelastic analysis of a sail carried out by Smith and Shyy [57] required over 200 loops of the fluid structural solution cycle to produce a solution. In order to allow solution within a reasonable time scale, taken to be 24 hours on a UNIX workstation for this thesis, the solution time for the fluid and structural aspects of the solution must be kept to a minimum. Use of a commercial finite element code will result in large time overheads to start up the program, and an in house program will also result in a faster solution as it will only contain the elements and solution techniques required for the aeroelastic analysis. The analysis of a sail using a commercial finite element code, ANSYS, was attempted by the author [21], and was unable to easily produce a solution for a membrane sail structure. To obtain a solution to the structural aspect of the problem in a reasonable time scale and to ensure that the desired structural models were implemented, it was decided to develop a nonlinear finite element analysis program, incorporating membrane sail elements and mast elements. Membrane elements were formulated in the manner of Smith and Shyy [57] which applies the membrane assumptions of Oden and Sato [46] to the finite element formulation and includes the membrane wrinkle algorithm of Millar and Hedgepath [37].

A potential flow analysis will be employed for the fluid analysis which allows solution of the fluid aspect of the problem in an appropriate timescale. Use of a viscous CFD program, such as an Euler code, would require at least

several hours to solve on a UNIX workstation at each loop and result in a prohibitively high solution time. Aeroelastic analysis of sails by Jackson and Christie [27] and Smith and Shyy [57] employed vortex lattice potential flow codes to calculate the fluid flow over the sails. These are well suited to analysis of sails, as they can be used to model thin structures, but are not suited to the analysis of a mast sail system due to the thickness of the mast. A potential flow panel code allows the solution of the mast and sail in a single model with an artificial thickness introduced to the sail. The timescale of the project precluded the development of a potential flow code for the analysis, and a panel code developed within the University of Southampton, PALISUPAN [64] will be used to model the fluid aspect of the problem. This has been shown to give good agreement with experimental pressure measurements on a mast mainsail model [49] when using an artificial thickness applied to the sail in the PALISUPAN model, and has been used to analyse yacht sails in an upwind configuration in several previous studies, including Prior [49], Cant [10] and Noury [45]. As the code was developed within the department, a command line version without any graphical interface was available, and this was used to reduce the time overhead required when starting the program.

Previous aeroelastic analysis of a yacht sail have employed an aeroelastic element, with the same discretisation being employed for the finite element and potential flow analysis. Jackson and Christie [27] employed triangular elements, and Smith and Shyy [57] used quadrilateral elements. The use of quadrilateral elements restricts the finite element analysis to initially plane membranes in order to be able to apply membrane restrictions to the sail elements, and also means that the sail must be truncated in the finite element mesh as the tip of the mainsail cannot be meshed with quadrilaterals. An

aeroelastic element is not suitable for the analysis of a rig, as it will not allow modeling of both the mast and sail in the aerodynamic and structural analysis. Distinct grids will be used for the finite element and potential flow analysis to enable the mast sail model to be analysed by the fluid and structural models. These distinct grids can be used to satisfy the different grid requirements for increased accuracy of the two aspects of the aeroelastic problem.

The potential flow program used in the aeroelastic analysis, PALISUPAN, generates a potential flow panel distribution for a body defined by a series of sections. To generate the PALISUPAN input file, a series of sections defining the rig in its deformed configuration is obtained from the finite element model of the rig, and these are used to generate the sections defining the body to be analysed by PALISUPAN. Pressures obtained from PALISUPAN are then used to calculate the pressure loading on the sail elements. Accuracy of the numerical solutions could be increased by using adaptive meshing for the finite element and potential flow analysis, which is possible due to the use of distinct grids. This is beyond the scope of this project due to the timescale which would be required, and a fixed finite element mesh and potential flow panel density is used through the solution path of the aeroelastic analysis.

3.3 Validation data

A search of literature did not find any validation data for yacht rigs in the public domain that would have been useful for validating the aeroelastic analysis. An attempt was made to gain some validation data by taking photographs of a yacht rig during wind tunnel tests that were carried out during a project at the University of Southampton [33]. Camber lines were placed on the sails to attempt to gain section profiles at three positions up

the rig. However these photographs proved to be of too small a scale and too poor quality for any quantitative data to be obtained from them. An example of the photographs is given in figure 2.

The assumptions necessary to allow solution of the aeroelastic problem, and the limitation of the analysis to a single sail and mast system prevents the use of real scale data for the validation of the program. Wind tunnel tests of rigs at a scale large enough to produce useful validation data for this problem are very expensive, and outside of the scope of this project. Almost all data from both scale model and full scale trials are obtained during the course of yacht development for events such as the Volvo Ocean Race and Americas Cup, and this data is commercially sensitive and therefore not in the public domain. There is also the problem of obtaining similitude of both the structural and aerodynamic aspect of yacht rigs for model testing, as discussed in the previous chapter.

In order to have confidence in the methods used in the analysis procedure, each stage of the structural analysis was validated against theoretical solutions. Mast elements were validated against a large deflection beam problem whose solution is presented by Holden [23]. This was also used as a validation case for the two dimensional nonlinear analysis programs. The nonlinear membrane formulation was validated against a solution for the large deformations of uniformly loaded membranes presented by Seide [53]. PALISUPAN has been shown to give good agreement with experimental pressure distributions by Prior [49], although the global force coefficients predicted do not have good agreement with experimental results due to the inviscid nature of the potential flow assumptions.

3.4 Development path

3.4.1 Linear Finite element development

In order to develop a finite element program that satisfies the requirements discussed previously, a series of programs were written to enable validation throughout the development of the finite element analysis, which enables confidence in the programs to be developed. A variety of elements which could be used to model the mast and sail structures were investigated initially in linear then in nonlinear programs to determine the most suitable elements for the structural aspect of the aeroelastic analysis. The use of a direct stiffness method results in a symmetric, banded stiffness matrix, so reduced matrix storage routines and an efficient matrix solution method were used to take advantage of this.

Initial development of the finite element program involved linear finite element analysis in two dimensions using triangle and quadrilateral elements. This allowed the program structure and data structures to be developed, and allowed debugging of the isoparametric formulation, reduced matrix storage and solution methods and numerical integration routines. The linear program was extended to three dimensions for investigation of solid elements for modeling the mast. A brief investigation of beam elements in a linear finite element program was carried out. Beam elements would reduce the problem size as fewer nodes would be required to model the masts compared to solid elements but introducing rotational degrees of freedom for only the mast nodes would require re-development of the stiffness matrix assembly and solution routines. The nonlinear formulation for beam elements [6] would also require separate development to the formulation which will be used for the sail elements. Using solid elements increases the number of nodes required

to model the rig, but they use only translational degrees of freedom, and thus do not require a distinct finite element formulation. The solid elements also define the mast cross section explicitly, making the PALISUPAN body section definition easier.

3.4.2 Nonlinear finite element development

A Total Langrangian method, presented by Bathe [7] is used as this allows the application of the deformation dependent pressure loading and application of the membrane restrictions for the membrane finite element analysis. Initial development took place in two dimensions to simplify the problem and enable confidence in the solution method to be developed. Eight node quadrilateral elements were used in the initial nonlinear program, as these had been found to give good agreement with theoretical deflections of a cantilever beam by Bathe [7]. Development continued to three node triangles, and then to a membrane formulation using element local coordinates which enable the membrane restrictions (which are similar to assuming a state of plane stress in the membrane) to be applied. Pressure loading on the membrane elements was implemented, and the membrane formulation was validated against the constant pressure case presented by Seide [53]. The solid elements were incorporated into a three dimensional nonlinear finite element formulation which was developed from the two dimensional case, and were validated for against the large deflection analysis of a distributed loaded cantilever beam by Holden [23].

3.4.3 Aeroelastic development

To enable solution of the aeroelastic problem, programs were developed to generate PALISUPAN input sections from the deformed finite element model,

and to calculate the finite element loading from the PALISUPAN results.

Rectangular membranes were analysed using the aeroelastic program. An initial model was restrained around all edges of the membrane, and produced a stable solution using an iterative solution procedure without using velocity stepping. Velocity stepping was introduced to the aeroelastic solution method for the analysis of a free trailing edge rectangular membrane. The wrinkle model was introduced to the finite element analysis and the updated finite element formulation employed to analyse the free trailing edge case and an initially flat triangular membrane, as analysed by Smith and Shyy [57]. The aeroelastic solution method was then extended to include the analysis of a mast, which required alteration of the PALISUPAN model generation routines and the finite element program. Dynamic relaxation was introduced to enable stable solutions of the aeroelastic analysis of the mast sail system.

The rig model was analysed with a restrained and unrestrained mast to show the effect of including the mast deformations on the sail analysis results. An initially curved membrane sail model was then analysed with both a restrained and free mast to prove the ability of the solution method to deal with 'as designed' sail profiles. Sail loads obtained from the aeroelastic analysis were applied as a distributed loading on a nonlinear finite element model of the mast alone, and the mast compression predicted were compared to those obtained from the aeroelastic analysis.

4 Linear finite element analysis

The theory of linear finite element analysis is well established, and a complete description of the formulation of the finite element method can be found in many texts, including Bathe [4] or Zienkiewicz [68]. A summary of the derivation is presented in appendix A. The body to be analysed is discretised into a number of elements, which are connected at a discreet number of node points on the boundaries. Displacements of these nodes are taken as the system unknowns, and the principle of virtual work is used to equate the internal work done in the model to the external work done by the applied loads. A set of simultaneous equations is obtained which can be solved to give the nodal displacements.

4.1 Program structure

The structure of the linear finite element programs is shown in figure 4. Model data is read in from a data file chosen during the program execution. Element stiffness matrices are evaluated and assembled into a model stiffness matrix. Boundary conditions and loading are applied to the model as defined in the data file, and the resulting finite element equations are solved to obtain node displacements. Element stress solutions are obtained from the calculated node displacements, and the results are output into a file.

During the development of the linear finite element analysis, a fixed array size was used to store the stiffness matrix and loading vector. The full stiffness matrix was stored, and solution of the finite element equations was carried out using Gaussian elimination of the full stiffness matrix. This requires the number of degrees of freedom to be set in the program before compilation. Although this is inconvenient when analysing a range of models, it simplifies

debugging of the program as the full stiffness matrix is easily output. Dynamically allocated stiffness matrix and force vector arrays were developed after validation of the two dimensional finite element analysis which allows models of arbitrary size to be analysed and reduced the solution time.

4.2 Data structure

The data structure used to store the finite element model is represented in figure 5. The top level structure contains model data including the number of components (nodes, elements, point loads and boundary conditions) and material properties. Pointers to arrays containing the component data which define the model are included in the top level of the structure. The component data is stored in arrays that are dynamically allocated in the input function according to the number of each component in the model. Component data structures contained in the model are listed below.

- Node data : contains node identification number and node coordinates.
- Element data : contains element identification number and pointers to each of the element nodes.
- Boundary condition data : contains the identification number of the node the constraint is applied to and a flag indicating which degree of freedom is restrained.
- Point load data : contains the identification number of the node the load is applied to, the load magnitude and a flag indicating the direction of the load.

4.3 Boundary conditions

The method used for application of the boundary conditions allows any displacement to be specified on a degree of freedom. The transformation used is shown in equation 4, where displacement u_2 is given an applied displacement, Z.

$$\begin{bmatrix} k_{11} & k_{12} & k_{13} & k_{14} \\ k_{21} & k_{22} & k_{23} & k_{24} \\ k_{31} & k_{32} & k_{33} & k_{34} \\ k_{41} & k_{42} & k_{43} & k_{44} \end{bmatrix} \begin{Bmatrix} u_1 \\ Z \\ u_3 \\ u_4 \end{Bmatrix} = \begin{Bmatrix} R_1 \\ R_2 \\ R_3 \\ R_4 \end{Bmatrix} \equiv \tag{4}$$

$$\begin{bmatrix} k_{11} & 0 & k_{13} & k_{14} \\ 0 & 1 & 0 & 0 \\ k_{31} & 0 & k_{33} & k_{34} \\ k_{41} & 0 & k_{43} & k_{44} \end{bmatrix} \begin{Bmatrix} u_1 \\ Z \\ u_3 \\ u_4 \end{Bmatrix} = \begin{Bmatrix} R_1 - k_{12}Z \\ Z \\ R_3 - k_{32}Z \\ R_4 - k_{42}Z \end{Bmatrix}$$

In the aeroelastic analysis, only boundary conditions with a zero applied displacement are required. This restriction reduces the storage requirements for the boundary conditions and simplifies their application to the finite element equations, and so is applied to all the finite element programs.

4.4 Loading

Loading is applied to the model as point loads on element nodes for the linear finite element analysis. Distributed loading is lumped to the element nodes during the model generation by evaluation of equation 5, where F^i is the equivalent load on node i due to a distributed load of intensity q over the element.

$$F^i = \int_{A^e} h_i q dA \tag{5}$$

4.5 Solution of banded stiffness matrix

Use of the banded nature of the stiffness matrix is made to reduce the storage requirements for the stiffness matrix. As the matrix is also symmetric, it is necessary to only store the upper half of the non zero band of the stiffness matrix (including the main diagonal terms). In order to allow solution of the finite element equations to calculate the node displacements using only the stored matrix elements, the bottom half of the stiffness matrix terms are eliminated for each column by addition of multiples of the corresponding row. As the matrix is banded, this only has to be carried out over the semibandwidth of the matrix, unlike in a full Gaussian elimination where the full column is eliminated with the exception of the main diagonal terms. The values of the elements below the main diagonal (which are not stored in this scheme) can be found from the symmetric elements above the main diagonal. After this elimination, back substitution can be used to calculate the node displacements from the remaining elements in the top half of the non zero band of the stiffness matrix. Solution of the finite element equations using this method reduces the calculations required for solution by a factor of about 30 for the rig models considered in the aeroelastic analysis when compared to a Gaussian elimination of the full matrix (thus will depend on the bandwidth of the stiffness matrix).

4.6 Isoparametric formulation

The iso-parametric element uses a element based natural coordinate system, shown for a linear triangle in figure 6. Calculation of the element stiffness matrix is carried out in the model coordinate system using the isoparametric formulation described in appendix A. Boundary conditions and point loads

are applied to the model in the global coordinate system, and the equations solved to obtain the node displacements. Element stresses are calculated from the node displacements in the global coordinate system.

4.6.1 Evaluation of the strain displacement matrix

In order to calculate the Jacobian matrix entries and the derivatives of the interpolation functions with respect to the global coordinates, a matrix containing the derivatives of the interpolation functions with respect to the natural coordinates, $\partial\mathbf{h}$ is calculated, equation 6.

$$\partial\mathbf{h} = \begin{bmatrix} h_{1,r} & h_{2,r} & \cdots & h_{N,r} \\ h_{1,s} & h_{2,s} & \cdots & h_{N,s} \end{bmatrix} \tag{6}$$

The Jacobian matrix can be calculated by multiplying the $\delta\mathbf{h}$ matrix by a matrix containing the element node coordinates, equation 7.

$$\mathbf{J} = \begin{bmatrix} x_{1,r} & x_{2,r} \\ x_{1,s} & x_{2,s} \end{bmatrix} = \delta\mathbf{h} \begin{bmatrix} x_1^1 & x_1^2 & \cdots & x_1^N \\ x_1^1 & x_1^2 & \cdots & x_1^N \end{bmatrix}^T \tag{7}$$

The $\delta\mathbf{h}$ matrix is then multiplied by the inverse of the Jacobian to obtain the derivatives of the displacement functions with respect to the global coordinate system. These are assembled into the strain displacement matrix, $\mathbf{B}$ as shown in equation 9.

$$h_{i,j} = \frac{\partial h_i}{\partial x_j} \tag{8}$$

$$\mathbf{B} = \begin{bmatrix} h_{1,1} & 0 & h_{2,1} & 0 & \cdots & h_{N,1} & 0 \\ 0 & h_{1,2} & 0 & h_{2,2} & \cdots & 0 & h_{N,2} \\ h_{1,2} & h_{1,1} & h_{2,2} & h_{2,1} & \cdots & h_{N,2} & h_{N,1} \end{bmatrix} \tag{9}$$

4.6.2 Constitutive relationship

The constitutive matrix used for the two dimensional finite element programs is the plane stress matrix for an isotropic solid, defined in equation 10.

$$\mathbf{C} = \frac{E}{1-\nu^2}\begin{bmatrix} 1 & \nu & 0 \\ \nu & 1 & 0 \\ 0 & 0 & \left(\frac{1-\nu}{2}\right) \end{bmatrix} \tag{10}$$

4.6.3 Calculation of stiffness matrix

The element stiffness matrix for a two dimensional element is calculated according to equation 11.

$$\mathbf{K_e} = \int_{A_e} \mathbf{B}^T\mathbf{C}\mathbf{B}t dA \tag{11}$$

Evaluation of the stiffness matrix is carried out using numerical integration where required. Gaussian quadrature is employed for numerical integration, and details of the schemes used for all the finite element analyses are given in appendix B.

4.7 Three node triangular element

Interpolation functions for the three node triangle in terms of the element natural coordinate system are given in equation 12.

$$\begin{bmatrix} h_1 \\ h_2 \\ h_3 \end{bmatrix} = \begin{bmatrix} 1-r-s \\ r \\ s \end{bmatrix} \tag{12}$$

Due to the linear interpolation of the displacements in the element, the element strain displacement matrix is constant, and it is not necessary to employ numerical integration in the calculation of the element characteristics. The

stiffness matrix can be calculated according to equation 13, where the area of the triangle is obtained from the determinant of the Jacobian matrix.

$$\mathbf{K} = \mathbf{B}^T\mathbf{C}\mathbf{B}t(0.5 \times \det \mathbf{J}) \tag{13}$$

The model shown in figure 7 was analysed using the isoparametric finite element program. Displacements and stresses obtained were compared to results calculated from finite element theory in Grandin [16] and were found to be identical.

4.8 Four node quadrilateral element

The four noded quadrilateral element assumes a linear variation of displacement, and is shown with the element natural coordinate system in figure 8. Interpolation functions for the element are given in equation 14.

$$\begin{bmatrix} h_0 \\ h_1 \\ h_2 \\ h_3 \end{bmatrix} = \begin{bmatrix} \frac{1}{4}(1+r)(1+s) \\ \frac{1}{4}(1-r)(1+s) \\ \frac{1}{4}(1-r)(1-s) \\ \frac{1}{4}(1+r)(1-s) \end{bmatrix} \tag{14}$$

Evaluation of the stiffness matrix for the four node quadrilateral elements is carried out using 2x2 Gaussian quadrature. The stress in the element is not constant, but can be evaluated at any point in the element by calculating the strain displacement matrix at that point as it is only a function of r,s, and is not a function of rs (as in the eight noded quadrilateral element). This can be multiplied by the element node displacements to give the strain vector at the point, which is multiplied by the constitutive matrix to evaluate the stress vector, equation 15.

$$\tau = \mathbf{CBU} \tag{15}$$

4.8.1 Validation

To validate the stress calculation method, the model shown in figure 9 was analysed, and corner stresses were calculated and compared to those obtained by Bathe [4]. The model has sides of 4m, thickness 0.1m, $E = 1.2 \times 10^6$, $\mu = 0.3$, $P = 100N$. The calculated stresses are given in table 2, and are identical to those obtained by Bathe.

4.9 Eight node quadrilateral element

The eight noded quadrilateral element assumes quadratic variation in displacement along the element sides, and is shown in figure 10. Interpolation functions for the element are given in equation 16.

$$\begin{bmatrix} h_1 \\ h_2 \\ h_3 \\ h_4 \\ h_5 \\ h_6 \\ h_7 \\ h_8 \end{bmatrix} = \begin{bmatrix} \frac{1}{4}(1-r)(1-s)(-r-s-1) \\ \frac{1}{4}(1+r)(1-s)(r-s-1) \\ \frac{1}{4}(1+r)(1+s)(r+s-1) \\ \frac{1}{4}(1-r)(1+s)(-r+s-1) \\ \frac{1}{2}(1-r^2)(1-s) \\ \frac{1}{2}(1+r)(1-s^2) \\ \frac{1}{2}(1-r^2)(1+s) \\ \frac{1}{2}(1-r)(1-s^2) \end{bmatrix} \tag{16}$$

Evaluation of the stiffness matrix is carried out using 2x2 Gaussian quadrature.

4.9.1 Stress calculation

The stresses calculated in the element is often more accurate at the integration points [4]. To obtain accurate stress values at other location in the

element, it is advisable to interpolate the stress obtained at the integration points to other locations in the element. The eight node element has a linear variation of stress over the element as shown in equation 17, where a, b, c, d are constants for each stress component in each element.

$$\sigma(r_i, s_j) = a + br_i + cs_j + dr_i s_j \tag{17}$$

The linear coefficients are obtained by Gaussian elimination of the matrices presented in equation 18, where r^k, s^k are coordinates of the integration points, and σ_{ij}^k are the stress components at these points. This results in a set of coefficients for each of the stress components which can be used in equation 18 to calculate the stress components at any point in the element.

$$\begin{bmatrix} 1 & s^1 & r^1 & s^1r^1 \\ 1 & s^2 & r^2 & s^2r^2 \\ 1 & s^3 & r^3 & s^3r^3 \\ 1 & s^4 & r^4 & s^4r^4 \end{bmatrix} \begin{bmatrix} a_x & a_y & a_{xy} \\ b_x & b_y & b_{xy} \\ c_x & c_y & c_{xy} \\ d_x & d_y & d_{xy} \end{bmatrix} = \begin{bmatrix} \sigma_x^1 & \sigma_y^1 & \tau_{xy}^1 \\ \sigma_x^2 & \sigma_y^2 & \tau_{xy}^2 \\ \sigma_x^3 & \sigma_y^3 & \tau_{xy}^3 \\ \sigma_x^4 & \sigma_y^4 & \tau_{xy}^4 \end{bmatrix} \tag{18}$$

4.10 Analysis of a tip loaded cantilever beam

Timonshenko [62] presents an analytical solution to the tip loaded cantilever shown in figure 11. The deflections predicted by theory for the centreline of the beam are given by equation 19 and the stress distribution within the element by equation 20, where R is the tip load applied to the cantilever.

$$v_{y=0} = \frac{Rx^3}{6EI} - \frac{Rxl^2}{2EI} + \frac{Rl^3}{3EI} \tag{19}$$

$$\sigma_{11} = \frac{-Rxy}{I}$$

$$\sigma_{22} = 0$$

$$\sigma_{12} = \frac{-R}{2I}(d^2 - y^2) \tag{20}$$

A 1 metre cantilever with a breadth and depth of 0.1 metres, material properties $E = 1.20 \times 10^6$ and $\nu = 0.2$, and a load of 100 N applied at the tip was chosen as a validation case for the linear finite element programs. Tip deflection for this cantilever predicted from equation 19 is 0.333 metres. The tip deflections obtained using the finite element analyses detailed below are given in table 3

4.10.1 ANSYS analysis

The end loaded cantilever were analyzed using a commercial finite element program, ANSYS, using four and eight noded quadrilateral elements. The models are shown in figures 12 and 13. Nodal displacements for the two cases were obtained to allow verification of the quadrilateral elements, and stress values at the corner nodes were obtained for the eight node model to allow comparison with the finite element program.

The four noded element model did not produce stress distributions as predicted by the theoretical solution, due to the coarse mesh used and the low order of the element. Tip deflection predicted is 0.230 metres, an error of 30%.

The eight noded quadrilateral model predicted a tip deflection of 0.334m, less than 0.5% error compared to the theoretical solution. As the eight node element has a quadratic variation in displacement assumed across the element, the stress in the element will have a linear variation across the element. The σ_{11} values obtained were exactly as predicted by the theoretical solution, and are plotted against theory in figure 14. As the theoretical σ_{11} varies linearly along the cantilever, it can be represented by the eight node elements. The shear stresses are predicted to be distributed parabolically

across the cantilever depth. The finite element analysis predicts a linear variation in shear stress through the cantilever depth due to the restrictions of the element formulation. As a result of this, the shear stresses predicted by the finite element analysis are in equilibrium with the applied forces, but the distribution is not as predicted by theory.

4.10.2 Three noded triangle element analysis

A symmetrical triangular finite element mesh was used to analyse the cantilever problem. An example of the mesh used is given in figure 15. A number of meshes with increasing numbers of elements were used to analyse the problem, and tip deflections obtained are listed in table 4, and the tip displacement in the x_2 direction is plotted against the number of elements in figure 16. The tip deflection calculated by the triangular finite elements gave an error of about 30% compared to theory for the densest mesh considered. The three node elements assume a linear variation in displacement, and so can not model the deformed shape of the cantilever accurately. The dense finite element mesh used also has high element aspect ratios, which may reduce the accuracy of the solution.

4.10.3 Four node quadrilateral elements

The cantilever was analysed using the quadrilateral finite element program with two meshes, containing 10 and 40 elements. The ten element model is identical to the one used for the ANSYS analysis, figure 12. The deflections of the centreline of the beam obtained with each mesh are plotted with the theoretical predictions in figure 17. Deflections for the 10 element model are exactly the same as those obtained from the ten four node element model ANSYS analysis. Increasing the number of elements to 40 resulted in the

tip deflection calculation of 0.300 metres, an error of 9% compared to the theoretical prediction.

4.10.4 Eight node quadrilateral elements

A model consisting of ten eight node elements was used to analyse the cantilever using the isoparametric finite element program. Deflections calculated were the same as those obtained from the ANSYS analysis using eight node elements, with a tip deflection of 0.334 metres. Stress at the element corners was initially calculated directly at the corner points. This was found to produce poor results compared to the theoretical model, with errors of up to 10% for the direct stresses in the x direction. The stresses were then calculated by using linear interpolation from the integration points according to the method described in section 4.12.1. The stress components obtained using this method were exactly the same as those obtained from the ANSYS analysis using eight node elements.

4.11 Three dimensional solid elements

In order to model the mast of a yacht using three dimensional brick elements, it is desirable to have a quadratic interpolation functions for the plane representing the mast cross section. This will enable the cross section of a circular or oval mast to be modeled using a single element. An isoparametric formulation is employed for the three dimensional analysis.

An eight node solid element was initially developed, as this is easier to debug. A 16 and 20 node element were also investigated. The 20 node model is shown in figure 18. The 8 and 16 node elements are obtained from this by using only the first 8 and 16 nodes respectively. The program structure is the same as used by the two dimensional finite element analysis programs.

Boundary conditions and point loads are applied to the model in the same manner as the two dimensional analysis, and full stiffness matrix storage is employed to simplify debugging.

4.11.1 Constitutive matrix

The constitutive matrix for a three dimensional isotropic solid is used for the solid elements, equation 21

$$\mathbf{C} = \frac{E(1-\nu)}{(1+\nu)(1-2\nu)} \begin{bmatrix} 1 & \frac{\nu}{1-\nu} & \frac{\nu}{1-\nu} & 0 & 0 & 0 \\ \frac{\nu}{1-\nu} & 1 & \frac{\nu}{1-\nu} & 0 & 0 & 0 \\ \frac{\nu}{1-\nu} & \frac{\nu}{1-\nu} & 1 & 0 & 0 & 0 \\ 0 & 0 & 0 & \frac{1-\nu}{2(1-\nu)} & 0 & 0 \\ 0 & 0 & 0 & 0 & \frac{1-\nu}{2(1-\nu)} & 0 \\ 0 & 0 & 0 & 0 & 0 & \frac{1-\nu}{2(1-\nu)} \end{bmatrix} \tag{21}$$

4.11.2 Calculation of the stiffness matrix

The element stiffness matrix is calculated according to equation 22. As the three dimensional program uses an isoparametric formulation, the integration occurs over the natural coordinate volume. Numerical integration is employed to evaluate the stiffness matrix.

$$\mathbf{K_e} = \int_{-1}^{+1} \int_{-1}^{+1} \int_{-1}^{+1} |\mathbf{J}|\, \mathbf{B}^T \mathbf{C} \mathbf{B} t \; dr \; ds \; dt \tag{22}$$

4.11.3 Interpolation functions

The interpolation functions for a 8 to 20 node element are given in Bathe [4], and the formulation is repeated here.

$$\mathbf{H}_s = \begin{bmatrix} h_1 & h_2 & \cdots & h_{20} \end{bmatrix}$$

$$\mathbf{H}_s^T = \begin{bmatrix} g_1 - (g_9 + g_{12} + g_{17})/2 \\ g_2 - (g_9 + g_{10} + g_{18})/2 \\ g_3 - (g_{10} + g_{11} + g_{19})/2 \\ g_4 - (g_{11} + g_{12} + g_{20})/2 \\ g_5 - (g_{13} + g_{16} + g_{17})/2 \\ g_6 - (g_{13} + g_{14} + g_{18})/2 \\ g_7 - (g_{14} + g_{15} + g_{19})/2 \\ g_8 - (g_{15} + g_{16} + g_{20})/2 \\ h_i = g_i \text{ for } i = 9, \cdots, 20 \end{bmatrix} \tag{23}$$

Where $g_i = 0$ if node i is not included, otherwise it is calculated according to equation 24.

$$g_i = G(r, r_i)G(s, s_i)G(t, t_i) \tag{24}$$

$$G(\beta, \beta_i) = \frac{1}{2}(1 + \beta_i\beta) \quad \text{for} \quad \beta_i = \pm 1$$
$$G(\beta, \beta_i) = (1 - \beta^2) \quad \text{for} \quad \beta_i = 0$$
$$\text{Where } \beta = r, s, t$$

The derivatives of the interpolation functions are calculated using the chain rule of differentiation to calculate derivatives of g_i. Equation 25 gives an example of this for derivatives of g_i with respect to r. The derivatives of the interpolation functions can then be calculated according to equation 23 from the derivatives of g_i. The derivatives of the interpolation functions with respect to the element natural coordinates are stored in the $\partial\mathbf{h}$ matrix as shown in equation 26.

$$\frac{\partial g_i}{\partial r} = \frac{\partial G(r, r_i)}{\partial r} G(s, s_i)G(t, t_i) \tag{25}$$

$$\partial\mathbf{h} = \begin{bmatrix} h_{1,r} & h_{2,r} & \cdots & h_{N,r} \\ h_{1,s} & h_{2,s} & \cdots & h_{N,s} \\ h_{1,t} & h_{2,t} & \cdots & h_{N,t} \end{bmatrix} \tag{26}$$

4.11.4 Calculation of the strain displacement matrix

The Jacobian matrix is calculated from the $\partial\mathbf{h}$ matrix and a matrix containing the node positions in global coordinates, $\mathbf{U}$, equation 28.

$$\mathbf{X} = \begin{bmatrix} x_1^1 & x_1^2 & \cdots & x_1^N \\ x_2^1 & x_2^2 & \cdots & x_2^N \\ x_3^1 & x_3^2 & \cdots & x_3^N \end{bmatrix}^T \tag{27}$$

$$\mathbf{J} = \partial\mathbf{h}\mathbf{X} \tag{28}$$

The differentials of the interpolation functions with respect to the global coordinates, $h_{i,j}$ are calculated by multiplying the $\partial\mathbf{h}$ matrix by the inverse of the Jacobian matrix. These are then assembled into the strain displacement matrix as shown by equation 29.

$$\mathbf{B} = \begin{bmatrix} h_{1,1} & 0 & 0 & h_{2,1} & \cdots & 0 \\ 0 & h_{1,2} & 0 & 0 & \cdots & 0 \\ 0 & 0 & h_{1,3} & 0 & \cdots & h_{N,3} \\ h_{1,2} & h_{2,1} & 0 & h_{2,2} & \cdots & 0 \\ 0 & h_{1,3} & h_{1,2} & 0 & \cdots & h_{N,2} \\ h_{1,3} & 0 & h_{1,1} & h_{2,3} & \cdots & h_{N,1} \end{bmatrix} \tag{29}$$

4.11.5 Stress calculation

The calculation of element stresses occurs in the same manner as for the two dimensional isoparametric elements. The strain displacement matrix is

used to calculate the element strain vector, defined in equation 30, from the element node displacements. This is multiplied by the constitutive matrix to give the element stress vector, defined in equation 31.

$$\epsilon = (\epsilon_{11},\ \epsilon_{22},\ \epsilon_{33},\ \epsilon_{12},\ \epsilon_{23},\ \epsilon_{13})^T \tag{30}$$

$$\tau = (\tau_{11},\ \tau_{22},\ \tau_{33},\ \tau_{12},\ \tau_{23},\ \tau_{13})^T \tag{31}$$

4.11.6 Single element validation

In order to check the interpolation function calculations, a single element cube with one face fully restrained under the action of a point load on the opposite face was analysed using the 8, 16 and 20 node elements, and the results compared to an analysis of the same model by ANSYS. Two cubes were analysed, with each cube having an opposite face restrained in order to check all the interpolation functions. The numerical integration scheme used for the 8 node element was 2x2x2 Gaussian integration, the 16 and 20 node element was analysed using both 3x3x3 and 14 point Gaussian integration. Details of the integration schemes are given in appendix B.

In all cases, the displacements obtained from the finite element programs matched the ANSYS displacements to the accuracy of the ANSYS output (6 significant figures). The 14 and 27 point integration schemes gave the same displacements for the single element validation.

4.11.7 Cantilever analysis

A 1 metre cantilever with breadth and depth of 0.1 metres with material properties of $E = 1.2 \times 10^5$, $\mu = 0.3$ under a tip point load of 0.3N was analysed using the solid element finite element programs. A theoretical solution using Timoshenko beam theory gives a predicted tip deflection of 0.1 metres.

The finite element mesh consists of a single element defining the cantilever cross section, with a range of number of elements used in the models analysed. The 16 node elements were arranged such that the linear interpolation ran along the cantilever length with the quadratic interpolation through the cantilever cross section, as would be used to define the mast.

Eight node element models with from 1 to 30 elements were analysed, with the finite element program employing 2x2x2 Gaussian quadrature for the stiffness matrix calculations. Tip deflections are listed in table 5 for each model. The cantilever was then analysed using the 16 node elements, with models containing between 1 and 30 elements. Results were obtained for programs using both 14 point and 3x3x3 Gaussian quadrature, and tip deflections are listed in table 5. Twenty node element models were then analysed using between 1 and 10 elements, using the two integration schemes from the 16 node elements. Tip deflections for the and twenty node elements are listed in table 5. The results are plotted in figure 19 for 8, 16 and 20 node elements.

Increasing the order of integration in both the 20 and 16 node elements resulted in less than 0.5% difference in tip deflection, and this suggests that the increase in computational time (calculation of the stiffness matrix using 14 point integration takes only just over 50% of the time required for 27 point integration) is not justified by the increase in solution accuracy for the linear finite element analysis. The twenty node elements gave the most accurate solution, with a 10 element model within 1.5% of the theoretical solution. This is expected, as the 20 node element has a quadratic variation in displacement along the beam which will enable the finite element model to more accurately represent the deformed shape of the cantilever with a small number of elements. The 16 node element gave more accurate solution than

the 8 node case, with a 10 element model having a calculated tip deflection within 29% of the theoretical prediction, compared to 35% error for the 8 node case. Increasing the number of elements to 30 resulted in a far more accurate solution for both the 16 and 8 node elements, with the error in tip deflection of 4.5% and 16.5% respectively.

The sixteen node element gives a more accurate solution than the 8 node element for the same mesh density as it can model the stress distribution through the beam more accurately, due to the quadratic variation in assumed displacement through the beam. The twenty node element gives the most accurate solution, as it has a quadratic variation in displacement along the beam, so can model the beam deflections more accurately.

4.12 Summary

Linear finite element programs have been developed and validated for two dimensional plane stress elements and three dimensional solid elements, in order to gain experience with finite element analysis and the elements to be used in the nonlinear analysis.

5 Non-linear finite element theory

The solution of the non-linear finite element problem employs an incremental formulation, applying the loading in a series of steps, and the equilibrium of the body is calculated at each load step. Time is used to describe the loading state of the body, following the notation of Bathe [7] [4]. This does not imply a time dependent analysis, and it is merely a convenient means to describe the loading of the body.

For the solution of the problem, a solution for a typical equilibrium position, $t + \Delta t$ is found, assuming that the solution for variables for all steps 0 to t have been calculated. This is repeated until the complete solution path has been solved. Using a Langrangian formulation, the principle of virtual work is used to formulate equation 32.

$$\int_{t+\Delta t V} {}^{t+\Delta t}\tau_{ij}\ \delta_{t+\Delta t}\ e_{ij}\ d^{t+\Delta t}V = {}^{t+\Delta t}\Re \tag{32}$$

$${}^{t+\Delta t}\Re = \int_{t+\Delta t V} {}^{t+\Delta t}f_i^B\ \delta u_i\ d^{t+\Delta t}V + \int_{t+\Delta t S_f} {}^{t+\Delta t}f_i^S\ \delta u_i^S\ d^{t+\Delta t}V \tag{33}$$

In equation 32, the left hand side is the internal virtual, and the right hand side external virtual work. It should be noted that the configuration of the body at time $t + \delta t$ is unknown, and in equation 32 integration occurs over the new configuration, with all stresses and strain are referred to this configuration. This has to be taken into account when deciding on the stress and strain measures to use for the analysis.

5.1 Stress and strain measures

Cauchy stresses are not suitable for the analysis, as they are dependent on the coordinate system they are measured in. It is not possible to obtain the Cauchy stresses at time $t + \Delta t$ by simply adding a stress increment due to the straining of the material to the Cauchy stresses at time t. The 2nd Piola-Kirchoff stresses S_{ij}, defined by equation 34 are invariant under rigid body rotation and translation, and so are suitable for use in the formulation of non-linear FE analysis.

$$ {}^{t}_{0}S_{ij} = \frac{{}^{0}\rho}{{}^{t}\rho} \, {}^{0}_{t}x_{i,m} \, {}^{0}_{t}x_{j,n} \, {}^{t}\tau_{mn} \tag{34} $$

The stresses have no direct physical meaning, so have to be converted into Cauchy stresses when investigating the results of the analysis. Conversion of the 2nd Piola-Kirchoff stresses is carried out using the inverse of equation 34, as shown in equation 35.

$$ {}^{t}\tau_{mn} = \frac{{}^{t}\rho}{{}^{0}\rho} \, {}^{t}_{0}x_{m,i} \, {}^{t}_{0}x_{n,j} \, {}^{t}_{0}S_{ij} \tag{35} $$

Strain energy can be calculated from the product of the 2nd Piola-Kirchoff stresses and the Green-Lagrange strain tensor, defined in 36, which is also invarient under rigid body rotation and translation, as these stress and strain measures are work conjugate.

$$ {}^{t}_{0}\epsilon_{ij} = \frac{1}{2} \left({}^{t}_{0}u_{i,j} + {}^{t}_{0}u_{j,i} + {}^{t}_{0}u_{k,i} \, {}^{t}_{0}u_{k,j} \right) \tag{36} $$

5.2 Total Langrangian formulation

The Total Langrangian formulation of the finite element problem has all static and kinematic variables referred to the initial configuration at time 0. An alternative formulation, the Updated Langrangian refers all variables to

the last calculated configuration at time t. The two schemes produce formulations that are identical if the appropriate transformations on the terms are carried out, and the choice of scheme is dependent on it's relative numerical efficiency for the problem being solved. Use of a Total Langrangian formulation allows the application of the membrane restrictions to elements that warp out of plane during the deformation, and so is more suited to the analysis of yacht sails.

5.3 Continuum mechanics formulation

The virtual work equation 32 using the stress and strain measures described above transforms to equation 37, where $\Re$ is defined as in equation 33.

$$\int_{{}_0V} {}_0^{t+\Delta t}S_{ij}\ \delta\ {}_0^{t+\Delta t}\epsilon_{ij}\ d^0V = {}^{t+\Delta t}\Re \tag{37}$$

5.3.1 Incremental decomposition

The stresses and strains can be incrementally decomposed as they are all (including the increments) referred to the original configuration. The stresses are decomposed as shown in equation 38.

$${}^{t+\Delta t0}S_{ij} = {}_0^tS_{ij} + {}_0S_{ij} \tag{38}$$

Strains are decomposed according to equation 39, with the incremental Green Lagrange strains defined in equation 43. Note that the underlined components of ${}_0e_{ij}$ are initial displacement effects (from the displacements of the nodes at time t).

$${}_0^{t+\Delta t}\epsilon_{ij} = {}_0^t\epsilon_{ij} + {}_0\epsilon_{ij} \tag{39}$$

$${}_0\epsilon_{ij} = {}^{t+\Delta t0}\epsilon_{ij} - {}_0^t\epsilon_{ij} \tag{40}$$

$$ {}_0\epsilon_{ij} = \frac{1}{2}\left({}^{t+\Delta t}_{0}u_{i,j} - {}^{t}_{0}u_{i,j} + {}^{t+\Delta t}_{0}u_{j,i} - {}^{t}_{0}u_{i,j} + {}^{t+\Delta t}_{0}u_{k,i}\,{}^{t+\Delta t}_{0}u_{k,j} - {}^{t}_{0}u_{k,i}\,{}^{t}_{0}u_{k,j}\right) \tag{41} $$

$$ {}_0\epsilon_{ij} = \frac{1}{2}\left({}_0u_{i,j} + {}^{t}_{0}u_{j,i} + {}^{t}_{0}u_{k,i}\,{}_0u_{k,j} + {}_0u_{k,j}\,{}^{t}_{0}u_{k,j} + {}_0u_{k,i}\,{}_0u_{k,j}\right) \tag{42} $$

$$ {}_0\epsilon_{ij} = {}_0e_{ij} + {}_0\eta_{ij} \tag{43} $$

$$ {}_0e_{ij} = \frac{1}{2}\left({}_0u_{i,j} + {}^{t}_{0}u_{j,i} + \underbrace{{}^{t}_{0}u_{k,i}\,{}_0u_{k,j} + {}_0u_{k,j}\,{}^{t}_{0}u_{k,j}}_{\text{initial displacement effects}} \right) \tag{44} $$

$$ {}_0\eta_{ij} = \frac{1}{2}\,{}_0u_{k,i}\,{}_0u_{k,j} \tag{45} $$

The variation in strain is taken about the configuration at time $t + \Delta t$, and hence $\delta\,{}^{t}_{0}\epsilon_{ij} = 0$. This means that the variation in strain in equation 37, $\delta\,{}^{t+\Delta t}_{0}\epsilon_{ij} = \delta({}^{t}_{0}\epsilon_{ij} + {}_0\epsilon_{ij}) = \delta\,{}_0\epsilon_{ij}$. Using this and the incremental decompositions in equation 39, we have:

$$ \int_{{}_0V} \left({}^{t}_{0}S_{ij} + {}_0S_{ij} \right) \delta\,{}_0\epsilon_{ij}\,{}^{0}dV = {}^{t+\Delta t}\Re \tag{46} $$

$$ \int_{{}_0V} {}_0S_{ij}\delta\,{}_0\epsilon_{ij}\,{}^{0}dV + \int_{{}_0V} {}^{t}_{0}S_{ij}\delta\,{}_0\eta_{ij}\,{}^{0}dV = {}^{t+\Delta t}\Re - {}^{t}_{0}S_{ij}\delta\,{}_0e_{ij}\,{}^{0}dV \tag{47} $$

5.3.2 Linearisation

The left hand side of equation 47 is non-linear with respect to displacement increments, u_i, so cannot be solved directly. The non-linear effects are due to the first term, and this is linearised using a Taylor series expansion, equation 48.

$$ \int_{{}_0V} {}_0S_{ij}\delta\,{}_0\epsilon_{ij}d^0V = \tag{48} $$
$$ \int_{{}_0V} \left(\left.\frac{\delta^t_0 S_{ij}}{\delta^t_0 \epsilon_{rs}}\right|_t ({}_0e_{rs} + {}_0\eta_{rs}) + \text{higher order terms} \right) \delta\,({}_0e_{ij} + {}_0\eta_{ij})\,d^0V $$

Neglecting higher order terms, including ${}_0\eta_{ij}$, equation 47 becomes equation 49, which is linear in the incremental displacements as $\delta\,{}_0e_{ij}$ is independent of u_i, and forms the basis for iso-parametric finite element analysis.

$$\int_{{}_0V} {}_0C_{ijrs}\ {}_0e_{rs}\ \delta\,{}_0e_{ij}\ d\,{}^0V + \int_{{}_0V} {}^t_0S_{ij}\ \delta\,{}_0\eta_{ij}\ d\,{}^0V$$
$$= {}^{t+\Delta t}\Re - \int_{{}_0V} {}^t_0S_{ij}\ \delta\,{}_0e_{ij}\ d\,{}^0V \qquad (49)$$

5.3.3 Solution of the approximation to the virtual work equation

The linearised virtual work equation 49 can be used to calculate an increment in displacements from t to $t+\Delta t$ which leads to an approximation to the displacements, strains and stresses at time $t+\Delta t$. The solution is not exact, due to the approximations in formulating equation 49.

With the approximate solution calculated, the difference between external virtual work and the internal virtual work evaluated with the variables for time $t+\Delta t$ can be found. This is an 'out of balance' virtual work after the solution as a result of the linearisations performed 50, where the approximate values are denoted using the superscript (1).

$$\text{Error} = {}^{t+\Delta t}\Re - \int_{{}_0V} {}^{t+\Delta t}_0S^{(1)}_{ij}\ \delta\,{}^{t+\Delta t}_0\epsilon^{(1)}_{ij}\ d\,{}^0V \qquad (50)$$

To reduce the error due to linearisation, iterations can be performed for each load step until the out of balance virtual work is within a convergence measure. This involves solving equation 51 repeatedly for $k = 1, 2, 3\ldots$, where the case for $k = 1$ is the relationship given in 49.

$$\int_{{}_0V} {}_0C^{(k-1)}_{ijrs}\ \Delta\,{}_0e^k_{rs}\ \delta\,{}_0e_{ij}d\,{}^0V \ + \ \int_{{}_0V} {}^{t+\Delta t}_0S^{(k-1)}_{ij}\ \delta\Delta\,{}_0\eta^k_{ij}\ d\,{}^0V$$
$$= {}^{t+\Delta t}\Re \ - \ \int_{{}_0V} {}^{t+\Delta t}_0S^{(k-1)}_{ij}\ \delta\,{}^{t+\Delta t}_0e^{(k-1)}_{ij}\ d\,{}^0V \qquad (51)$$

5.4 Matrix equations of continuum elements

Derivation of the finite element matrices for the non-linear analysis occurs in the same manner as for linear analysis. Element coordinates and displacements are expressed in terms of the nodal values using interpolation functions, with the same interpolation functions used for both the displacements and coordinates (iso-parametric formulation). By invoking the linearised principle of virtual displacements for each nodal point in turn, the governing finite element equations are obtained. The equilibrium equations of the model is assembled from individual elements using the direct stiffness method. For the Total Langrangian method, the governing equation is given by equation 52.

$$\left({}^{t}_{0}\mathbf{K}_{L} + {}^{t}_{0}\mathbf{K}_{NL} \right) \mathbf{u} = {}^{t+\Delta t}\mathbf{R} - {}^{t}\mathbf{F} \tag{52}$$

The matrices in equation 52 are evaluated according to equations 53 to 56.

$$\int_{{}^{0}V} {}_{0}C_{ijrs}\ {}_{0}e_{rs}\ \delta\, {}_{0}e_{ij}\ d\,{}^{0}V \rightarrow\ {}^{t}_{0}\mathbf{K}_{L}\,\mathbf{u} = \left(\int_{{}^{0}V} {}^{t}_{0}\mathbf{B}^{T}_{L}\ {}_{0}\mathbf{C}\ {}^{t}_{0}\mathbf{B}_{L}\ d\,{}^{0}V \right) \mathbf{u} \tag{53}$$

$$\int_{{}^{0}V} {}^{t}_{0}S_{ij}\ \delta\, {}_{0}\eta_{ij}\ d\,{}^{0}V \rightarrow\ {}^{t}_{0}\mathbf{K}_{NL}\,\mathbf{u} = \left(\int_{{}^{0}V} {}^{t}_{0}\mathbf{B}^{T}_{NL}\ {}^{t}_{0}\mathbf{S}\ {}^{t}_{0}\mathbf{B}_{NL}\ d\,{}^{0}V \right) \mathbf{u} \tag{54}$$

$$\int_{{}^{0}V} {}^{t}_{0}S_{ij}\ \delta\, {}_{0}e_{ij}\ d\,{}^{0}V \rightarrow\ {}^{t}_{0}\mathbf{F} = \int_{{}^{0}V} {}^{t}_{0}\mathbf{B}^{T}_{L}\ {}^{t}_{0}\hat{\mathbf{S}} d\,{}^{0}V \tag{55}$$

$${}^{t+\Delta t}\mathbf{R} = \int_{{}^{0}S_{f}} \mathbf{H}^{sT}\ {}^{t+\Delta t}_{0}\mathbf{f}^{S}\ d\,{}^{0}S + \int_{{}^{0}V} \mathbf{H}^{T}\ {}^{t+\Delta t}_{0}\mathbf{f}^{B}\ d\,{}^{0}V \tag{56}$$

The matrices used in these evaluations are given in the finite element program descriptions for two and three dimensional elements and membrane elements in terms of the displacement interpolation functions and node displacements at time t. Since the Total Langrangian formulation is employed, all differentials are referred to the body state at time $t = 0$.

5.4.1 Loading

Loading of the finite element models is achieved by lumping the distributed forces on the model to the element nodes, in the manner described in equation 56. As a total Langrangian formulation is employed, these loads will be constant through the deformation of the body. As the loads are lumped at the nodes in the model generation, the evaluation of equation 56 does not need to be carried out during the solution of the problem, and the point loads can simply be added to the model external load vector as defined in the model definition. The exception to this is pressure loading on the membrane elements, as this will change during the aeroelastic analysis as the fluid flow around the sail alters. The pressure loading of the membrane elements is described in more detail in the membrane element formulation in section 6.4.7.

6 Non-linear finite element analysis

The non-linear formulation described in section 5 is employed to develop a non-linear finite element analysis program. Membrane finite elements incorporating the membrane assumptions of Oden and Sato [46] are developed, and solid elements are developed in the non-linear formulation.

6.1 Two dimensional non-linear finite element analysis

Isoparametric formulation was employed throughout the non-linear finite element series of programs. In order to simplify the programming and solution of the initial non-linear finite element analysis, no iteration is used within the load steps. As the non-linear equations of equilibrium are linearised to allow solution, the displacement increments calculated are approximations (as discussed in section 5.3.3). These approximations can be reduced to insignificant levels by increasing the number of load step, as demonstrated in section 6.2.1. The 2D elements have a constant thickness, and the volume integrals used to calculate the stiffness matrices and internal loading contributions, equation 49, become integrals over the area of the element multiplied by the element thickness. As with the linear finite element development, full stiffness matrix storage was used in the development of the non-linear finite element programs. The reduced matrix storage was introduced to the membrane and solid finite element programs after validation of the programs.

6.1.1 Program structure

The structure of the two dimensional finite element analysis is shown in figure 20. Model data is read in from a user defined file. The number of each of the model components is read in and used to allocate the required memory

for storage of the model data. Material properties and the model components are then input from the file. Node displacements ${}^{t}_{0}\mathbf{u}$ are initialised to zero. The program then runs through a loop for the user defined number of load steps. Element stiffness matrices are calculated for each element in turn using the methods described below. The element stiffness matrix entries are then added to the model stiffness matrix before calculation of the next element contribution. External loading is added into the model force vector, then internal loading is calculated, with each element contribution assembled into the global force vector before calculation of the next element contribution. Boundary conditions are applied in the same manner as for the linear finite element case, and the resulting finite element equations are solved by Gaussian elimination to calculate a vector of nodal displacement increments. These are used to update the node displacement values, ${}^{t}_{0}\mathbf{u}$. At the end of the load path, element Cauchy stresses are calculated and output with the node displacements.

6.1.2 Data structures

The data structure used for the two dimensional non-linear analysis has the same structure as the one used for the linear finite element analysis, shown in figure 5. The top level of the data structure is the model structure which contains pointers to the arrays of node, element, boundary condition and point load data which are dynamically allocated during the program execution. Contents of the data structures are:

- Model data structure : numbers of each of the components of the model (nodes, elements, boundary conditions, point loads), material properties, element thickness and number of load steps.
- Node data structure : node identification number, initial position and

displacements at time t, ${}^{t}_{0}u$.

- Element data structure : element identification number and pointers to the nodes which define the element.
- Point load data structure : The identification number of the node that the load is applied to, flag indicating the direction of the load and load magnitude.
- Boundary condition data structure : node identification number and flag indicating the degree of freedom restrained.

The use of pointers to the element nodes in the element data structure allows easy access to the data required for element stiffness matrix calculations, and also defines the element connectivity through the node identification number.

6.1.3 Evaluation of the strain displacement matrices

In order to calculate the strain displacement matrices used in the non-linear finite element analysis, the differentials of the interpolation functions, ${}_{0}h_{i,j}$ and the l_{ij} components, defined in equation 57, must be evaluated.

$$l_{ij} = \sum_{k=1}^{N} {}_{0}h_{k,j}\, {}^{t}u_{i}^{k} \tag{57}$$

The evaluation of $h_{i,j}$ proceeds as for the linear isoparametric formulation described earlier, and these are stored in a matrix, $\partial\mathbf{h}$, defined in equation 58. The element Jacobian matrix is calculated using the element node local coordinates at $t = 0$.

$$\partial h_{ij} = h_{j,i} \quad \text{where} \quad i = 1 \cdots N;\ j = 1, 2 \tag{58}$$

Values for the l_{ij} entries are calculated by multiplying the $\partial\mathbf{h}$ matrix by a the ${}^{\mathbf{t}}\mathbf{u}$ matrix as shown in equation 59, and stored in a matrix $\mathbf{L}$. The matrix

${}^t\mathbf{u}$ contains the element node displacements at the end of the previous load step.

$$\mathbf{L} = \begin{bmatrix} l_{11} & l_{12} \\ l_{21} & l_{22} \end{bmatrix} = [\partial \mathbf{h}] \left[{}^t\mathbf{u} \right] = \begin{bmatrix} h_{1,1} & h_{2,1} & \cdots & h_{N,1} \\ h_{1,2} & h_{2,2} & \cdots & h_{N,2} \end{bmatrix} \begin{bmatrix} {}^tu_1^1 & {}^tu_1^2 \\ {}^tu_2^1 & {}^tu_2^2 \\ \vdots & \vdots \\ {}^tu_N^1 & {}^tu_N^2 \end{bmatrix} \tag{59}$$

Strain displacement matrices, ${}^t_0\mathbf{B}_L$, ${}^t_0\mathbf{B}_{NL}$ can be assembled from the entries in the $\partial \mathbf{h}$ and $\mathbf{L}$ matrices according to equations 60, 61, 62 and 63.

$${}^t_0\mathbf{B}_L = {}^t_0\mathbf{B}_{L0} + {}^t_0\mathbf{B}_{L1} \tag{60}$$

$${}^t_0\mathbf{B}_{L0} = \begin{bmatrix} {}_0h_{1,1} & 0 & {}_0h_{2,1} & 0 & \cdots & {}_0h_{N,1} & 0 \\ 0 & {}_0h_{1,2} & 0 & {}_0h_{2,2} & \cdots & 0 & {}_0h_{N,2} \\ {}_0h_{1,2} & {}_0h_{1,1} & {}_0h_{2,2} & {}_0h_{2,1} & \cdots & {}_0h_{N,2} & {}_0h_{N,1} \end{bmatrix} \tag{61}$$

$${}^t_0\mathbf{B}_{L1} = \begin{bmatrix} l_{11}\,{}_0h_{1,1} & l_{21}\,{}_0h_{1,1} & \cdots \\ l_{12}\,{}_0h_{1,2} & l_{22}\,{}_0h_{1,2} & \cdots \\ (l_{11}\,{}_0h_{1,2} + l_{12}\,{}_0h_{1,1}) & (l_{21}\,{}_0h_{1,2} + l_{22}\,{}_0h_{1,1}) & \cdots \\ l_{11}\,{}_0h_{N,1} & l_{21}\,{}_0h_{N,1} \\ l_{12}\,{}_0h_{N,2} & l_{22}\,{}_0h_{N,2} \\ (l_{11}\,{}_0h_{N,2} + l_{12}\,{}_0h_{N,1}) & (l_{21}\,{}_0h_{N,2} + l_{22}\,{}_0h_{N,1}) \end{bmatrix} \tag{62}$$

$${}^t_0\mathbf{B}_{NL} = \begin{bmatrix} h_{1,1} & 0 & h_{2,1} & 0 & \cdots & h_{N,1} & 0 \\ h_{1,2} & 0 & h_{2,2} & 0 & \cdots & h_{n,2} & 0 \\ 0 & h_{1,1} & 0 & h_{2,1} & \cdots & 0 & h_{N,1} \\ 0 & h_{1,2} & 0 & h_{2,2} & \cdots & 0 & h_{N,2} \end{bmatrix} \tag{63}$$

6.1.4 Stress calculation

The 2nd Piola-Kirchoff stress vector, ${}^{t}_{0}\hat{\mathbf{S}}$ is calculated from the element Green-Lagrange strains. To calculate the strains in the element, displacement derivatives are evaluated using the shape function derivative matrix and the nodal displacements, as shown in equation 64.

$$ {}^{t}_{0}u_{i,j} = \frac{\partial u_i}{\partial\, {}_{0}x_j} = \sum_{k=1}^{N} \frac{\partial N_k}{\partial x_j}\, {}^{t}_{0}u^{k}_{i} \qquad (i,j = 1,2) \tag{64} $$

The components of the Green-Lagrange strain tensor, ${}^{t}\varepsilon_{ij}$ can be calculated according to equation 65, and the Green-Lagrange strain vector $\hat{\varepsilon}$ is assembled from these.

$$ {}^{t}\varepsilon_{ij} = \frac{1}{2}\left({}^{t}_{0}u_{i,j} + {}^{t}_{0}u_{j,i} + {}^{t}_{0}u_{k,i}\, {}^{t}_{0}u_{k,j} \right) \tag{65} $$

$$ \hat{\varepsilon} = \begin{Bmatrix} \varepsilon_{11} \\ \varepsilon_{22} \\ 2\varepsilon_{12} \end{Bmatrix} $$

The 2nd Piola-Kirchoff stress vector can then be calculated directly from the Green-Lagrange strain using the two dimensional plane stress constitutive matrix, ${}_{0}\mathbf{C}$, as shown in equation 66.

$$ {}^{t}_{0}\hat{\mathbf{S}} = {}_{0}\mathbf{C}\hat{\varepsilon} \tag{66} $$

6.1.5 Calculation of stiffness matrix

The element stress matrix, ${}^{t}_{0}\mathbf{S}$ is assembled from the 2nd Piola-Kirchoff stress components according to equation 67.

$$ {}^{t}_{0}\mathbf{S} = \begin{bmatrix} {}^{t}_{0}S_{11} & {}^{t}_{0}S_{12} & 0 & 0 \\ {}^{t}_{0}S_{21} & {}^{t}_{0}S_{22} & 0 & 0 \\ 0 & 0 & {}^{t}_{0}S_{11} & {}^{t}_{0}S_{12} \\ 0 & 0 & {}^{t}_{0}S_{21} & {}^{t}_{0}S_{22} \end{bmatrix} \tag{67} $$

Linear and non-linear contributions to the element stiffness matrix, ${}^{t}_{0}\mathbf{K}_{L}$ and ${}^{t}_{0}\mathbf{K}_{NL}$ can then be calculated according to equations 68 and 69.

$$ {}^{t}_{0}\mathbf{K}_{L} = \int_{{}^{0}A} {}^{t}_{0}\mathbf{B}_{L}^{T} \; {}_{0}\mathbf{C} \, {}^{t}_{0}\mathbf{B}_{L} \; t \; d \, {}^{0}A \tag{68} $$

$$ {}^{t}_{0}\mathbf{K}_{NL} = \int_{{}^{0}A} {}^{t}_{0}\mathbf{B}_{NL}^{T} \; {}^{t}_{0}\mathbf{S} \, {}^{t}_{0}\mathbf{B}_{NL} \; t \; d \, {}^{0}A \tag{69} $$

As the strain displacement and stress matrices are functions of the natural coordinates of the elements, the integrations to calculate the stiffness matrices are evaluated over the natural coordinate area of the element, in the same manner as for the linear finite element isoparametric elements (see equations 170 and 171). Element linear and non-linear stiffness matrices are added to give the element stiffness matrix, and these are assembled into the model stiffness matrix using the element connectivity.

6.1.6 Loading calculations

A model loading vector, ${}^{t+\Delta t}\Re$ is calculated from the external loads, ${}^{t+\Delta t}\mathbf{R}$ and internal loads ${}^{t}_{0}\mathbf{F}$, as shown in equation 70.

$$ {}^{t+\Delta t}\Re = {}^{t+\Delta t}\mathbf{R} - {}^{t}_{0}\mathbf{F} \tag{70} $$

Internal loads contributions for each element, ${}^{t}_{0}\mathbf{F}^{(m)}$, are calculated according to equation 71.

$$ {}^{t}_{0}\mathbf{F}^{(m)} = \int_{{}^{0}A}^{(m)} {}^{t}_{0}\mathbf{B}_{L}^{T} \; {}^{t}_{0}\hat{\mathbf{S}} t d \, {}^{0}A^{(m)} \tag{71} $$

In order to calculate ${}^{t}_{0}\mathbf{F}^{(m)}$, the strain displacement matrix and stress vector are calculated as described for the stiffness matrix calculations. Contributions to the internal loading vector from each element are assembled into the model internal loading vector using the element connectivity.

External loading applied to the model is in the form of point loads. Due to the Total Langrangian formulation, distributed loading can be lumped to the nodes in the model definition, as since they are referred to the body configuration at time $t = 0$, they do not alter as the body deforms, equation 56. The external load vector, ${}^{t+\Delta t}\mathbf{R}$ is generated by applying the point loads to the body global degree of freedom defined by the finite element model. Magnitude of the load is calculated according to equation 72, where P is the magnitude of the force, n is the load step number and the subscripts $t + \Delta t$ and T refer to the current and final load steps.

$$P_{t+\Delta t} = \frac{n_{t+\Delta t}}{n_T} P_T \tag{72}$$

6.1.7 Calculation of displacement increments

The governing finite element equations for load step $t + \Delta t$, equation 73, are solved to obtain nodal displacement increments, u_k^j.

$${}^{t}_{0}\mathbf{K}\mathbf{u} = {}^{t+\Delta t}\Re \tag{73}$$

Solution of the finite element equations is achieved using the same methods as for the linear finite element analysis. Gaussian elimination is used for programs using fixed array sizes and full stiffness matrix storage, and decomposition and back substitution for programs using dynamic arrays and reduced matrix storage. Node displacement increments are added to the displacements at the start of the load step to give the model solution for this time step.

6.1.8 Validation model

The programs were validated using an analytical solution for the large scale deflections of a cantilever beam under uniform distributed load, obtained by

Holden [23]. A non dimensional load coefficient, k, is defined in equation 74, where w is the magnitude of the distributed load, L the length of the beam and D the flexural rigidity of the cantilever ($D = EI$).

$$k = \frac{wL^3}{D} \tag{74}$$

The deflection coefficient, (δ/L), of the cantilever tip is given by the solid line in figure 21 for load coefficients from 0 to 10, and the dotted line in this figure shows the results of experimental observations of this problem. This case was used by Bathe [7] as a validation case for the non-linear finite element formulation using eight noded quadrilateral elements and he noted that *'excellent agreement has been obtained with an analytical solution reported by Holden [23]'* for both the total and updated langrangian formulations.

Values for the analytic solution from Holden [23] have been obtained from the graph presented in the paper, which is shown in figure 21. A cantilever of length 1.0 metres, breadth and height 0.1 metres and Youngs modulus of 1.2×10^6 was analysed. This corresponds to a distributed loading magnitude of $w = 10\ N/m^2$ for a load factor, k of 1.

6.2 Eight noded quadrilateral element

A non-linear finite element program, FENLA1 was written employing the eight noded quadrilateral element, shown in figure 10, and the formulation described above. Integrations over the element area to determine the stiffness matrix and internal loading were initially evaluated using four by four Gaussian quadrature.

A simple single element model, shown in figure 22 was analysed with FENLA1. Stress in the non-linear program elements was initially evaluated using the strain displacement matrix, ${}^t_0\mathbf{B}_L$ to evaluate the element strains.

Results for a case with one load step (linear analysis) were compared to a solution obtained from the linear eight noded finite element program, and the displacements obtained were identical. A tip loaded cantilever model was then analysed with the non-linear program, using a range of load steps. The case with one load step corresponds to a linear analysis, and the displacements calculated were identical to those calculated using the linear finite element program. Increasing the number of load steps resulted in an unstable solution. The stress calculation method used was incorrect, as only the linear component of the strain is calculated from $\varepsilon = {}^{t}_{0}\mathbf{B}_{L}\,{}^{t}_{0}u^{k}_{i}$, and hence the stress calculated from this is not the total stress required for the stiffness matrix and internal load evaluation. For the cases with only one load step, the element stresses do not make any contribution to the stiffness matrix or load calculations, and so the calculation of the displacements was not affected. When a non-linear analysis was carried out the incorrect stress calculations resulted in the wrong equilibrium equations being formulated, and hence the solution was incorrect. The stress calculation method was changed to that described in section 6.1.4, calculating the Green-Lagrange strain components from the ${}^{t}_{0}u_{i,j}$ values.

6.2.1 Point loaded cantilever

The tip loaded cantilever was analysed using a range of load steps, to ascertain if the solution would converge with increasing number of load steps. Tip deflections obtained are given in table 6, and plotted against number of load steps in figure 23. The case with one load step gives the same displacements as the linear finite element analysis, -0.334 m. As the number of load steps are increased, the displacement of the cantilever tip converges to a value of -0.299043 m to six significant figures. About 50 load steps are required

to obtain a value within 1% of this, and 100 load steps gives a deflection within 0.002% of the converged value. As there is no iteration within the load steps, the approximations used to formulate the equilibrium equations results in poor solutions and a large variation in displacements for the cases with small numbers of load steps. As an example, 5 load steps gives a tip displacement of -0.288559 m (4% error) and 6 load steps gives a tip displacement of -0.255825 m (14% error). Increasing number of load steps results in an increase in CPU time for solution, as the stiffness matrix has to be re calculated at each stage. Using a modified Newton Raphson method to solve the loading path, where iterations within a load step are calculated using the stiffness matrix at time t to iterate until the internal and external virtual work are within a convergence limit, may reduce the total solution time, as the stiffness matrix would be calculated fewer times. Further investigation of this was carried out during the development of the membrane finite element programs.

6.2.2 Distributed loaded cantilever analysis

An evenly distributed loading along the edge of a quadrilateral element can be lumped at the nodes as shown in figure 24. These values are obtained by evaluating equation 75 for each of the three nodes along the edge. As the loading is applied to the top of the elements, evaluations occur by integrating between $-1 \leq r \geq 1$ at $s = 1$.

$$r_n = Pl \int_{-1}^{+1} |h_n|_{s=1} \, dr \tag{75}$$

Cantilevers with load coefficients, k, of 1 and 10 were analysed using a range of number of load steps using 10 elements to determine the number of load steps required to obtain a converged solution. Tip deflections for these runs

are given in table 7 and the deflections for up to 50 load steps are plotted against the number of load steps in figure 25. A series of models with load coefficients of 1 to 10 were analysed using 5, 10, 25 and 50 load steps, and the tip deflections are given in table 8. Tip deflections for the 50 load step case are plotted against load coefficient with the analytical solution from Holden [23] in figure 26. Finally the effect of order of integration was examined by altering the program to use 9 and 25 point Gaussian quadrature in the evaluation of the stiffness matrix and internal loading. Changing the order of integration had no effect on the tip deflections calculated by FENLA1.

The sensitivity study showed that an analysis using 50 load steps gave a deflection within 0.01% of the converged solution. Analysis of a distributed loaded cantilever gave results that were within 3% of the theoretical solution obtained by Holden [23]. The values from the analytical solution were obtained from the graph of results, figure 21, and the error is within the accuracy that can be obtained from this method. Changing the order of integration within the program had no effect on the results obtained for the distributed cantilever, and nine point integration is sufficiently accurate for the eight noded element in the non-linear formulation. Using fewer load steps gave good agreement for lower load coefficients, but the solutions for higher load coefficients did not give good agreement, as can be seen by the results for the analysis with 5 load steps. In these cases, the increased error in solution is due to the linearisation error from the finite element formulation becoming significant due to the large size of the load steps.

6.3 Membrane elements

The formulation of membrane elements was first considered by Oden and Sato [46]. To apply the membrane restriction in the non-linear finite element

analysis, the Green-Lagrange strain tensor is altered to take account of the nature of membrane behaviour. Assuming that the membrane has a small thickness compared to it's other dimensions, the strain can be assumed uniform over the thickness (Timoshenko [63]). Hence $\gamma_{\alpha 3} = 0$, there is no shear through the element thickness and γ_{33} is a measure of change in thickness of the membrane. This is equivalent to applying a state of plane stress to the element. The membrane restriction is incorporated into the finite element analysis of membranes by alteration of the strain displacement matrices as shown by Smith and Shyy [57]. Element characteristics are calculated in a local coordinate system which is defined such that the element in it's initial configuration lies in the local y_1 y_2 plane, and the strain components in the local y_3 direction are assumed to be zero. The element must be planar at the start of the analysis so that the local y_3 direction corresponds to the normal to the elements surface over the entire element. As the Total Langrangian formulation used in the non-linear analysis refers back to the undeformed configuration of the element, the element can warp out of plane during the analysis without compromising the membrane restrictions. Use of a three node triangular element will allow initially curved structures to be analysed, as this element will always define a plane (although there will be some discretisation error as the model will be an approximation of the curved surface). This element also has a constant strain, and so does not require numerical integration to calculate the stiffness matrix.

6.3.1 Program structure

The program structure for the membrane analysis program is depicted in figure 27, and is similar to the structure employed in the previous FENLA programs. After the model data is read from the data file, the node local

coordinates and global to local transformation matrix is calculated for each element in turn and stored in the element data structure. Calculation of the stiffness matrix contribution from each element occurs in the element local coordinate system, and this matrix is transformed to the global coordinate system before assembly into the model stiffness matrix. Point loads are defined in the global coordinate system, and can be added directly to the global force vector. Internal stresses in the elements are calculated in the element local system using the node displacement components in the local coordinate system. The element internal loading contribution which is evaluated from the strain displacement and stress matrices in the local coordinate system is transformed to the global coordinate system before assembly into the global force vector. Boundary condition application and solution is carried out as for the previous FENLA series. After solution, the global displacements stored in the node data structure are updated, and then the node displacements for each element's nodes are calculated in the element coordinate system, and stored in the element data structure.

6.3.2 Data structure

A revised data structure is employed, with the element data additionally storing:

- A matrix of the element node initial local coordinates.
- The local to global transformation matrix, $\mathbf{t}_{3D}$.
- A matrix of the element node displacements in the local coordinate system, $[{}^{t}_{0}\mathbf{u}]^{L}$.

As the Total Langrangian formulation was employed, the node local coordinate and the global to local transformation matrix only need to be calculated

at the start of the analysis, and are not updated as the body deforms, as all calculations are referred to the initial body configuration. These are calculated before the load step loop is commenced, and stored in the element data structure.

6.3.3 Local coordinate calculations

Calculation of the unit vectors defining the element local coordinate system in terms of the global coordinate system are described here for a three node triangle element, but the method is suitable for any element which is initially in a plane.

The element based local cartesian coordinate system is shown in figure 77. Two vectors are created, from node a to b, $\vec{ab}$, and from node a to c, $\vec{ac}$. The local $\mathbf{y_1}$ vector is set as a unit vector in the direction of $\vec{ab}$. The local $\mathbf{y_3}$ vector is perpendicular to the plane of the element, and is calculated by taking a unit vector in the direction of the cross product of $\vec{ab}$ and $\vec{ac}$. Finally the local $\mathbf{y_2}$ vector is found by taking the cross product of the local $\mathbf{y_1}$ and $\mathbf{y_3}$ vectors.

A local to global transformation matrix can be assembled from the components of the vectors defining the local coordinate system, equation 76, which is stored in the element data structure and used in the transformation of the element stiffness and internal load contributions. The global coordinate system components of the local coordinate unit vectors are represented as $[x_1, x_2, x_3]^i$ for the vector $\mathbf{y_i}$.

$$t_i = [x_1, x_2, x_3]^i \tag{76}$$

To calculate the node local coordinates, the transformation matrix, $\mathbf{t}$ is inverted and this global to local transformation matrix is used to transform the

node coordinates to a coordinate system parallel to the element local system. Finally the node local coordinate system is translated such that the origin is at node a by subtracting the calculated local coordinates of this node from the element node local coordinates. The resulting node local coordinates are stored in the element data structure. As the element is in the local y_1, y_2 plane, the nodes local y_3 coordinate is zero, and hence is not stored.

6.3.4 Strain displacement matrices

Calculation of the components of the strain displacement matrices proceeds as described for FENLA1, but takes place in the element local coordinate system. Jacobian matrix entries and l_{ij} components are calculated using the node coordinates and displacements referred to the element local coordinate system. The $\partial\mathbf{h}$ components are evaluated using the Jacobian matrix, and hence the ${}_0h_{i,j}$ are calculated with respect to the element local coordinate system. Strain displacement matrices, ${}^t_0\mathbf{B}_L$ and ${}^t_0\mathbf{B}_{NL}$ are assembled from the $\partial\mathbf{h}$ and $\mathbf{L}$ entries according to in equations 77 to 80.

$$ {}^t_0\mathbf{B}_L = {}^t_0\mathbf{B}_{L0} + {}^t_0\mathbf{B}_{L1} \tag{77} $$

$$ {}^t_0\mathbf{B}_{L0} = \begin{bmatrix} {}_0h_{1,1} & 0 & 0 & \cdots & {}_0h_{N,1} & 0 & 0 \\ 0 & {}_0h_{1,2} & 0 & \cdots & 0 & {}_0h_{N,2} & 0 \\ {}_0h_{1,2} & {}_0h_{1,1} & 0 & \cdots & {}_0h_{N,2} & {}_0h_{N,1} & 0 \end{bmatrix} \tag{78} $$

$$
{}^{t}_{0}\mathbf{B}_{L1} = \begin{bmatrix}
l_{11}\,{}_{0}h_{1,1} & l_{21}\,{}_{0}h_{1,1} & l_{31}\,{}_{0}h_{1,1} & \cdots \\
l_{12}\,{}_{0}h_{1,2} & l_{22}\,{}_{0}h_{1,2} & l_{32}\,{}_{0}h_{1,2} & \cdots \\
(l_{11}\,{}_{0}h_{1,2} + l_{12}\,{}_{0}h_{1,1}) & (l_{21}\,{}_{0}h_{1,2} + l_{22}\,{}_{0}h_{1,1}) & (l_{31}\,{}_{0}h_{1,2} + l_{32}\,{}_{0}h_{1,1}) & \cdots \\
l_{11}\,{}_{0}h_{N,1} & l_{21}\,{}_{0}h_{N,1} & l_{31}\,{}_{0}h_{N,1} & \\
l_{12}\,{}_{0}h_{N,2} & l_{22}\,{}_{0}h_{N,2} & l_{32}\,{}_{0}h_{N,2} & \\
(l_{11}\,{}_{0}h_{N,2} + l_{12}\,{}_{0}h_{N,1}) & (l_{21}\,{}_{0}h_{N,2} + l_{22}\,{}_{0}h_{N,1}) & (l_{31}\,{}_{0}h_{N,2} + l_{32}\,{}_{0}h_{N,1}) &
\end{bmatrix} \tag{79}
$$

$$
{}^{t}_{0}\mathbf{B}_{NL} = \begin{bmatrix}
h_{1,1} & 0 & 0 & \cdots & h_{N,1} & 0 & 0 \\
h_{1,2} & 0 & 0 & \cdots & h_{N,2} & 0 & 0 \\
0 & h_{1,1} & 0 & \cdots & 0 & h_{N,1} & 0 \\
0 & h_{1,2} & 0 & \cdots & 0 & h_{N,2} & 0 \\
0 & 0 & h_{1,1} & \cdots & 0 & 0 & h_{N,1} \\
0 & 0 & h_{1,2} & \cdots & 0 & 0 & h_{N,2}
\end{bmatrix} \tag{80}
$$

6.3.5 Calculation of element stress

Element strains are calculated using the node displacements in the local coordinate system to evaluate the displacement derivatives used to define the Green-Lagrange strains, equation 81. This differs from the two dimensional case in that the derivatives of the x_3 component of displacement are now required for the strain calculation.

$$
{}^{t}_{0}u_{i,j} = \frac{\partial\, {}^{t}u_i}{\partial_0 x_j} = \sum_{k=1}^{N} \frac{\partial h_k}{\partial_0 x_j}\, {}^{t}_{0}u_i^k \qquad (i = 1,2,3;\ j = 1,2) \tag{81}
$$

The components of the Green-Lagrange strain tensor, ${}^{t}\varepsilon_{ij}$ are calculated according to equation 82, and the Green-Lagrange strain vector $\hat{\varepsilon}$ is assembled from these.

$$
{}^{t}\varepsilon_{ij} = \frac{1}{2}\left({}^{t}_{0}u_{i,j} + {}^{t}_{0}u_{j,i} + {}^{t}_{0}u_{k,i}\, {}^{t}_{0}u_{k,j} \right) \tag{82}
$$

$$\hat{\varepsilon} = \begin{Bmatrix} \varepsilon_{11} \\ \varepsilon_{22} \\ 2\varepsilon_{12} \end{Bmatrix}$$

The 2nd Piola-Kirchoff stress vector can then be calculated directly from the Green-Lagrange strain using the two dimensional plane stress constitutive matrix, ${}_0\mathbf{C}$, as for previous FENLA programs, equation 66. At the start of the loading path, the elements have zero node displacements and zero stress. In order to prevent the stiffness matrix becoming singular, an initial stress is applied to the elements for the first load step by setting the stress vector to a value defined in the model data file. This is removed for subsequent load steps, and the stress vector is evaluated from the Green-Lagrange strain vector and constitutive matrix.

The stress matrix, ${}^t_0\mathbf{S}$ is assembled from the stress vector components as shown in equation 83.

$${}^t_0\mathbf{S} = \begin{bmatrix} {}^t_0S_{11} & {}^t_0S_{12} & 0 & 0 & 0 & 0 \\ {}^t_0S_{21} & {}^t_0S_{22} & 0 & 0 & 0 & 0 \\ 0 & 0 & {}^t_0S_{11} & {}^t_0S_{12} & 0 & 0 \\ 0 & 0 & {}^t_0S_{21} & {}^t_0S_{22} & 0 & 0 \\ 0 & 0 & 0 & 0 & {}^t_0S_{11} & {}^t_0S_{12} \\ 0 & 0 & 0 & 0 & {}^t_0S_{21} & {}^t_0S_{22} \end{bmatrix} \tag{83}$$

6.3.6 Calculation of stiffness matrix

Calculation of the element linear and non-linear stiffness matrices is carried out in the same way as in the previous FENLA programs, equations 68 and 69. Linear and non-linear components of the stiffness matrix can be summed to obtain the element stiffness matrix in the element local coordi-

nates, as in equation 84.

$$ {}^{t}_{0}\mathbf{K} = {}^{t}_{0}\mathbf{K}_{L} + {}^{t}_{0}\mathbf{K}_{NL} \tag{84} $$

6.3.7 Calculation of loading

External point loads are applied to the model ${}^{t+\Delta t}\mathbf{R}$ vector as in the previous FENLA programs. Point load contributions are placed directly into the model $\Re$ loading vector to reduce the memory requirements. The membrane elements can be loaded by a pressure acting on the membrane surface. This is assumed to be constant over the element, and a positive pressure acts in the direction of the local y_3 vector. Pressure contribution to the element external load vector in the element local coordinate system, ${}^{t+\Delta t}\mathbf{R}^{e}$ can be calculated according to equation 85, where q_e difference in pressure on the element upper and lower surfaces.

$$ {}^{t+\Delta t}\mathbf{R}^{e} = \int_{A^e} \mathbf{H}^{T}\, {}^{t+\Delta t}\mathbf{q}\, dA \tag{85} $$

$$ \mathbf{H} = \begin{bmatrix} h_1 & 0 & 0 & h_2 & 0 & 0 & \cdots & h_N & 0 & 0 \\ 0 & h_1 & 0 & 0 & h_2 & 0 & \cdots & 0 & h_N & 0 \\ 0 & 0 & h_1 & 0 & 0 & h_2 & \cdots & 0 & 0 & h_N \end{bmatrix} $$

$$ \mathbf{q} = \begin{bmatrix} 0 \\ 0 \\ q_e \end{bmatrix} $$

The element internal loading contribution, ${}^{t}_{0}\mathbf{F}^{e}$, is calculated from the element stress vector and strain displacement matrix as for previous formulations, equation 71. Element pressure and internal loading vectors are

combined to give an element loading vector, $\Re^e$, equation 86.

$$ {}^{t+\Delta t}\Re^e = {}^{t+\Delta t}\mathbf{R}^e - {}^{t}_{0}\mathbf{F}^e \tag{86} $$

The element load vector is calculated in the element local coordinate system, and is transformed to the model coordinate system before assembly into the model loading vector.

6.3.8 Transformation of element matrices

As the element stiffness matrices and load vectors are calculated in the element local coordinate system, they must be transformed to the global coordinate system before assembly into the global stiffness matrix and loading vector. The element local to global transformation matrix, $\mathbf{t}$, is stored in the element data structure, and is used to effect this transformation. Transformation of the three noded triangular element stiffness matrix is carried out according to equation 88, and transformation of the load vector is achieved as shown in equation 89.

$$ \mathbf{T} = \begin{bmatrix} \mathbf{t} & \mathbf{0} & \mathbf{0} \\ \mathbf{0} & \mathbf{t} & \mathbf{0} \\ \mathbf{0} & \mathbf{0} & \mathbf{t} \end{bmatrix} \tag{87} $$

$$ \mathbf{0} = \begin{bmatrix} 0 & 0 & 0 \\ 0 & 0 & 0 \\ 0 & 0 & 0 \end{bmatrix} $$

$$ {}^{t}_{0}\mathbf{K} = \mathbf{T}^T \, {}^{t}_{0}\mathbf{K}^e \mathbf{T} \tag{88} $$

$$ {}^{t+\Delta t}_{0}\Re = \mathbf{T} \, {}^{t+\Delta t}_{0}\Re^e \tag{89} $$

The full transformation matrix, $\mathbf{T}$ is assembled from the element local to global transformation matrix, $\mathbf{t}$, and the transformation carried out in separate functions for the stiffness matrix and force vector. Assembly of the transformed matrix and vector occurs using the element connectivity in the same manner as for the previous finite element analyses.

6.3.9 Calculation of element node local displacements

After solution of the finite element equations, the calculated global displacement increments are added to the node global displacements stored in the node data structure. The element local to global transformation matrix is inverted to obtain the global to local transformation matrix, and the element node displacements in the element local coordinate system are calculated for each of the element nodes in turn, and then stored in the element data structure for use in the calculation of the strain displacement matrices and stress evaluation in the following load step.

6.3.10 Iterative solution

The iterative solution method involves the use of a modified Newton-Raphson method for solution of the finite element equations. This involves solving equation 90 until the displacement increments are within some tolerance. The nonlinear finite element programs developed use an iterative solution on the final load step, as suggested by Smith and Shyy [57] for the aeroelastic analysis of a membrane.

$$\left({}_0^t\mathbf{K}_L + {}_0^t\mathbf{K}_{NL}\right)\Delta u^{(i)} = {}^{t+\Delta t}\mathbf{R} - {}_0^{t+\Delta t}\mathbf{F}^{(i-1)} \quad i = 1, 2, 3\cdots \tag{90}$$

$${}_0^{t+\Delta t}\mathbf{F}^{(i-1)} = \int_{V_0} {}_0^{t+\Delta t}\mathbf{B}_L^{(i)T}\ {}_0^{t+\Delta t}\mathbf{S}^{(i)}\ {}_0\, dV \tag{91}$$

$$^{t+\Delta t}u^{(i)} = ^{t+\Delta t}u^{(i-1)} + \Delta u^{(i)}$$

During the iterative solution, a copy of the stiffness matrix is made and passed to the solution function for the solution of the finite element equations. This allows continuation of the iterative process without having to recalculate the stiffness matrix for each iteration. Internal and pressure loading are calculated for each element and assembled into the model $^{t+\Delta t}_{0}\mathbf{F}^{(i-1)}$ and $^{t+\Delta t}\mathbf{R}$ vectors, and external point loads are applied to the model $^{t+\Delta t}\mathbf{R}$ vector. The solution of equation 90 allows the calculation of node displacement increments, which are checked for convergence as the displacements are updated.

Convergence is tested in the membrane analysis programs by checking each increment in displacement against the displacement at the start of the iteration before updating it. The percentage change in displacement is calculated and the maximum change is compared with the convergence limit stored in the model data structure, which is defined in the model data file. When the convergence limit is passed for all unrestrained degrees of freedom, the iterative loop is stopped. If the convergence limit is not achieved within the maximum number of iterations stored in the model data structure, a warning is printed and the iterative loop exited. The change in displacement is only calculated for degrees of freedom with non zero displacements, to avoid division by zero when considering restrained degrees of freedom.

6.4 Three noded triangle element membrane analysis

A membrane finite element analysis program using three noded triangle elements, FENLA3, was developed, using the non-linear formulation described

previously. A local element coordinate system was employed to calculation the element characteristics to enable the membrane assumptions to be applied to the element.

6.4.1 Evaluation of integrals

As the three noded triangle has a linear variation of displacement and hence constant strain through the element, the terms within integrals evaluated for the element stiffness matrix, internal force vector and pressure loading are constant, and the integrations can be evaluated without numerical integration by multiplying the value of the terms by the element area and thickness. The element area, A is equal to half the determinant of the element Jacobian, $|\mathbf{J}|$, and this is calculated during the evaluation of the $\partial\mathbf{h}$ components. Linear and non-linear element stiffness matrices can be evaluated according to equations 92 and 93.

$$ {}^{t}_{0}\mathbf{K}_L = {}^{t}_{0}\mathbf{B}_L^T \; {}_0\mathbf{C} \; {}^{t}_{0}\mathbf{B}_L \; A_e t \tag{92} $$

$$ {}^{t}_{0}\mathbf{K}_L = {}^{t}_{0}\mathbf{B}_{NL}^T \; {}^{t}_{0}\mathbf{S} \; {}^{t}_{0}\mathbf{B}_{NL} \; A_e t \tag{93} $$

The element internal force vector and pressure load vector are evaluated according to equations 94 and 95.

$$ {}^{t}_{0}\mathbf{F} = {}^{t}_{0}\mathbf{B}_L^T \; {}^{t}_{0}\hat{\mathbf{S}} t A_e \tag{94} $$

$$ {}^{t+\Delta t}\mathbf{R} = \mathbf{H}^T \; {}^{t+\Delta t}\mathbf{q} A_e \tag{95} $$

6.4.2 Distributed loaded cantilever

A model of the distributed loaded cantilever used to validate FENLA1 and 2, was generated for analysis by FENLA3. The cantilever was modelled in

the global x_1, x_2 plane, and all the model nodes were restrained in the global x_3 direction, reducing the analysis to the equivalent of a 2D plane stress analysis, allowing comparison with the analytical solution of Holden and the previous non-linear analysis. All the models used a symmetrical mesh, and no iteration was used in the solution.

The distributed loaded cantilever series was modelled initially using 40 elements, as shown in figure 15. A convergence test was carried out on the beam with the highest load coefficient, and the results of this are given in table 9. For this model about 20 load steps are required to get a solution within 0.5% of the converged solution. The cantilever was analysed for a range of load coefficients, and resulted in deflection coefficients of about 50% of the values obtained from theory and the higher order elements.

The assumption used for the three node triangle elements is a linear variation of displacement across the element. Due to this, they cannot model the deformed shape of the distributed loaded cantilever exactly, as this is at least a parabolic curve. Higher order elements, such as the eight noded quadrilateral and six noded triangle are able to do this, and so would be expected to give a more accurate solution for a small number of elements. In an attempt to improve the 3 noded triangular element solution, the cantilever series was analysed using models with 80 then 320 elements. Convergence data for these models is given in table 9. Due to the long time taken to solve the 320 element beam case, only 30 load steps were used for the calculation of the tip displacements for the series of load coefficients, compared to 50 load steps for the other two models. The results of the cantilever analysis for the 3 noded triangle models are plotted against the theoretical solution in figure 29. The accuracy of the results improves with the mesh is refined, as would be expected. However, the 320 element model takes approximately

20 times as much CPU time to solve as the 10 element 8 node quadrilateral element, mainly due to the larger number of nodes, and hence much greater computation required to solve the finite element equations using Gaussian elimination on the full stiffness matrix.

6.4.3 Point loaded membrane

An initially flat, square membrane under the action of a central point load was investigated to determine if a converging solution could be obtained. No analytical solution was found for this problem, but it provided a simple to generate problem for checking the membrane formulation and convergence. A 1 m by 1 m membrane was modelled in the global x_1, x_2 plane with a load of -100 N applied in the global x_3 direction at the membrane center. Due to the symmetry of the problem, it is possible to model one quarter of the membrane with suitable boundary conditions along the free edges, and hence the model was 0.25 m square. Material properties of the membrane were $E = 120000$, $\nu = 0.2$, with a membrane thickness of 1mm. No iteration was used within the load stepping procedure.

The displacement of the central point of a 16 element model, shown in figure 30, with varying number of load steps is plotted against the number of load steps in figure 31, and converged to within 1% after 20 load steps. A series of models with increasing number of elements was analysed, and the central deflection of the membrane is plotted against the number of elements in figure 32 for 100 load steps. This shows the central deflection converging to a steady value as the finite element mesh density increases. Initial stress values of 100 and 1000 N/m^2 were applied to a 16 element model using 20 load steps, and the calculated central deflection was found to be identical. The initial stress magnitude has no effect on the solution providing that suf-

ficient load steps to obtain a converged solution are used. These results give confidence in the analysis method, but since there is no theoretical validation data for this problem, the analysis cannot be validated using this problem.

6.5 Four node triangular elements

The 20 node solid element has a quadrilateral variation of displacement in all three axes of the element. In order to have the option of using this element to model the mast with three noded linear elements used to model the sail in the rig analysis, a membrane transition element with quadratic variation in displacement along one side and linear along the remaining two sides is requires. The four node triangle, shown in figure 33 fulfills these requirements. Interpolation functions for the element are given in equation 96.

$$\begin{bmatrix} h_1 \\ h_2 \\ h_3 \\ h_4 \end{bmatrix} = \begin{bmatrix} 1 - r + 2rs - 3s + 2s^2 \\ r \\ 2rs - s + 2s^2 \\ 4s - 4rs - 4s^2 \end{bmatrix} \tag{96}$$

A finite element program using this element, FENLA3-4, was developed from FENLA3, using 3 point integration for evaluation of area integrals.

6.6 Four node quadrilateral element

A membrane finite element program using the four noded quadrilateral elements described in section 4.11, FENLA4, was written. The numerical integration scheme employed was 2x2 Gaussian quadrature.

6.7 Analysis of an initially flat membrane under constant pressure

6.7.1 Analytical solution

Seide [53] presents an analytical solution to the large deflections of an initially flat membrane under constant pressure. Solutions for central deflections for a variety of aspect ratio membranes are presented, and the central deflection for a square membrane with Poisson's ratio of 0.3 is defined in equation 97, where η is a constant which depends on the aspect ratio of the membrane. For a square membrane, $\eta = 0.2866$.

$$\frac{w_c}{h} = \eta \left[\frac{q_\infty}{E} \left(\frac{b}{d} \right)^4 \right]^{1/3} \tag{97}$$

This result indicates that the central deflection of the membrane non dimensionalised with respect to the membrane span, w_c/b is inversely proportional to the aeroelastic number, Π_1 presented by Smith and Shyy [57], defined in equation 1.

6.7.2 Analysis using the finite element programs

An initially flat, square membrane of size 1 m and thickness 1 mm with material constants of $E = 1.2 \times 10^5$, $\mu = 0.3$ under a constant pressure loading of $15 N/m^2$ was analysed by the membrane finite element analysis programs. Aeroelastic number of the membrane is $\Pi_1 = 2.0$, and the central deflection predicted by Seide is 0.1433 meters. Due to the symmetrical nature of the problem, one quarter of the membrane was modelled using appropriate boundary conditions along the free sides to reduce the problem size. Convergence limit was set at 0.01%, and 10 load steps were used, with a maximum number of iterations set at 100. In practice, all the cases analysed converged

within 6 iterations.

Both FENLA3 and FENLA4 were used to analyse the membrane. Two mesh arrangements were investigated for the triangular elements, the symmetrical mesh shown in figure 34, and an asymmetric arrangements, shown in figure 35. A regular mesh of quadrilateral element was used by FENLA4, figure 36 . In all cases, the membrane was analysed using a series of mesh densities, from 2 elements per side up to around 15 elements per side. The mesh density was limited by the memory available for the program, which limits the size of the stiffness matrix that can be stored and hence limits the number of nodes the model can contain. Maximum model size was increased in later versions of the programs by the use of dynamic arrays and storage of only the top half of the non zero band of the stiffness matrix.

Mid point deflections for the three mesh arrangements are plotted against the number of elements in figure 37. As the number of elements is increased, the solution tends towards the value obtained by Seide. For the most dense meshes considered, the error in central deflection with respect to the analytical solution was less than 0.5%.

A series of membranes with Π_1 varying between 1 and 20 were analysed using each of the three meshes for models with around 150 elements. The variation in the aeroelastic number was obtained by changing the membrane Youngs modulus. Central deflections and the error compared to Siede for the analyses are given in table 10, and the central deflections are plotted against $(\Pi_1)^{-1}$ in figure 38. Excellent agreement was obtained for all the mesh arrangements for the range of aeroelastic numbers considered. The error increased as the aeroelastic number was reduced, but even then deflections were calculated to within 1% of the theoretical predictions. For a typical sail the aeroelastic number would be in the region of 15, and the accuracy of the

finite element analysis in this region is better than 0.5% for the case analysed here.

FENLA3 was altered to use dynamic arrays and storage of the top half of the non zero band of the stiffness matrix. The revised program was used to analyse the initially square membrane using a symmetrical mesh arrangement. The alterations to the program resulted in a solution time that was about 20 times faster than the previous version, and the maximum model size (limited by memory available on the UNIX workstation) was increased from 250 to over 3700 nodes. This enabled the membrane to be analysed with meshes of up to 7200 elements. Results for the coarse meshes were equal to the results obtained with the previous version of FENLA3, and the fine mesh results are given in table 11.

FENLA3-4 was used to analyse a membrane with $\Pi_1 = 2$ using the mesh arrangement shown in figure 39. A series of models with varying number of elements was analysed using 10 load steps and maximum number of iterations set to 50. Central deflections are given in table 12. The first six models were then analysed using 13 point integration, and the results of this are given in table 13. These results were within 0.01% of those obtained with 3 point integration, and indicate that the increase in computation required for the increased order of integration is not necessary, although a solution was obtained for the 2 element model within the maximum number of iterations for the 13 point integration. Four noded triangular elements gave an increase in accuracy compared to the three node element case for an equal number of elements, although the improvement becomes less significant as the number of elements is increased.

6.8 Three dimensional solid elements

A non-linear solid element program was developed using the solid elements described in section 4.15. Calculation of the element characteristics is carried out in the global coordinate system using an isoparametric formulation, and an iterative solution was employed on the final load step using the convergence criteria introduced for the membrane elements . A 20 node element was initially investigated, and although the element gave accurate solutions to the distributed loaded cantilever beam problem, the program was not stable for a range of load steps. A range of solution methods and convergence criteria were investigated, but these did not result in an improvement in the convergence of the element. A 16 node element with linear interpolation in one dimension was then implemented in the three dimensional non-linear program. This does not require the four node triangle element to allow joining of the mast and sail, hence simplifying the rig model, and will also allow a rig with an initially curved mast to be discretised. The 16 node element was found to give stable solutions for all loading cases examined.

6.8.1 Strain displacement matrices

The three dimensional Jacobian matrix is calculated in the same manner as for the linear three dimensional elements, section 4.15. Components of the $\delta\mathbf{h}$ matrix are evaluated with respect to the global coordinate system using the derivatives of interpolation functions with respect to the element natural coordinates and the Jacobian matrix, in the same manner as for the linear three dimensional elements. The $\mathbf{L}$ matrix is calculated as for the previous non-linear cases, and the strain displacement matrices can then be assembled

from these components according to equations 98 to 102.

$$ {}^{t}_{0}B_{L} = {}^{t}_{0}B_{L0} + {}^{t}_{0}B_{L1} \tag{98} $$

$$ {}^{t}_{0}\mathbf{B}_{L0} = \begin{bmatrix} h_{1,1} & 0 & 0 & h_{2,1} & \cdots & 0 \\ 0 & h_{1,2} & 0 & 0 & \cdots & 0 \\ 0 & 0 & h_{1,3} & 0 & \cdots & h_{N,3} \\ h_{1,2} & h_{2,1} & 0 & h_{2,2} & \cdots & 0 \\ 0 & h_{1,3} & h_{1,2} & 0 & \cdots & h_{N,2} \\ h_{1,3} & 0 & h_{1,1} & h_{2,3} & \cdots & h_{N,1} \end{bmatrix} \tag{99} $$

$$ {}^{t}_{0}\mathbf{B}_{L1} = \begin{bmatrix} l_{11}\,{}_{0}h_{1,1} & l_{21}\,{}_{0}h_{1,1} & l_{31}\,{}_{0}h_{1,1} \\ l_{12}\,{}_{0}h_{1,2} & l_{22}\,{}_{0}h_{1,2} & l_{32}\,{}_{0}h_{1,2} \\ l_{13}\,{}_{0}h_{1,3} & l_{23}\,{}_{0}h_{1,3} & l_{33}\,{}_{0}h_{1,3} \\ (l_{11}\,{}_{0}h_{1,2} + l_{12}\,{}_{0}h_{1,1}) & (l_{21}\,{}_{0}h_{1,2} + l_{22}\,{}_{0}h_{1,1}) & (l_{31}\,{}_{0}h_{1,2} + l_{32}\,{}_{0}h_{1,1}) \\ (l_{12}\,{}_{0}h_{1,3} + l_{13}\,{}_{0}h_{1,2}) & (l_{22}\,{}_{0}h_{1,3} + l_{23}\,{}_{0}h_{1,2}) & (l_{32}\,{}_{0}h_{1,3} + l_{33}\,{}_{0}h_{1,2}) \\ (l_{11}\,{}_{0}h_{1,3} + l_{13}\,{}_{0}h_{1,1}) & (l_{21}\,{}_{0}h_{1,3} + l_{23}\,{}_{0}h_{1,1}) & (l_{31}\,{}_{0}h_{1,3} + l_{33}\,{}_{0}h_{1,1}) \end{bmatrix} $$

$$ \begin{bmatrix} l_{11}\,{}_{0}h_{2,1} & \cdots & l_{31}\,{}_{0}h_{N,1} \\ l_{12}\,{}_{0}h_{2,2} & \cdots & l_{32}\,{}_{0}h_{N,2} \\ l_{13}\,{}_{0}h_{2,3} & \cdots & l_{33}\,{}_{0}h_{N,3} \\ (l_{11}\,{}_{0}h_{2,2} + l_{12}\,{}_{0}h_{2,1}) & \cdots & (l_{31}\,{}_{0}h_{N,2} + l_{32}\,{}_{0}h_{N,1}) \\ (l_{12}\,{}_{0}h_{2,3} + l_{13}\,{}_{0}h_{2,2}) & \cdots & (l_{32}\,{}_{0}h_{N,3} + l_{33}\,{}_{0}h_{N,2}) \\ (l_{11}\,{}_{0}h_{2,3} + l_{13}\,{}_{0}h_{2,1}) & \cdots & (l_{31}\,{}_{0}h_{N,3} + l_{33}\,{}_{0}h_{N,1}) \end{bmatrix} \tag{100} $$

$$ {}^{t}_{0}\mathbf{B}_{NL} = \begin{bmatrix} {}^{t}_{0}\tilde{\mathbf{B}}_{NL} & \tilde{\mathbf{0}} & \tilde{\mathbf{0}} \\ \tilde{\mathbf{0}} & {}^{t}_{0}\tilde{\mathbf{B}}_{NL} & \tilde{\mathbf{0}} \\ \tilde{\mathbf{0}} & \tilde{\mathbf{0}} & {}^{t}_{0}\tilde{\mathbf{B}}_{NL} \end{bmatrix} \tag{101} $$

$$ {}^{t}_{0}\tilde{\mathbf{B}}_{NL} = \begin{bmatrix} {}_{0}h_{1,1} & 0 & 0 & \cdots & {}_{0}h_{N,1} \\ {}_{0}h_{1,2} & 0 & 0 & \cdots & {}_{0}h_{N,2} \\ {}_{0}h_{1,3} & 0 & 0 & \cdots & {}_{0}h_{N,3} \end{bmatrix} \quad \tilde{\mathbf{0}} = \begin{bmatrix} 0 \\ 0 \\ 0 \end{bmatrix} \tag{102} $$

6.8.2 Calculation of element stress

Element node displacements in the global coordinate system are used to evaluate displacement derivatives used to define the Green-Lagrange strains, equation 103.

$$ {}^{t}_{0}u_{i,j} = \frac{\partial\, {}^{t}u_i}{\partial_0 x_j} = \sum_{k=1}^{N} \frac{\partial h_k}{\partial_0 x_j}\, {}^{t}_{0}u_i^k \qquad (i,j = 1,2,3;) \tag{103} $$

Components of the strain tensor are calculated from the displacement derivatives according to equation 104, and the strain vector is assembled from these, equation 105.

$$ {}^{t}\varepsilon_{ij} = \frac{1}{2}\left({}^{t}_{0}u_{i,j} + {}^{t}_{0}u_{j,i} + {}^{t}_{0}u_{k,i}\, {}^{t}_{0}u_{k,j} \right) \tag{104} $$

$$ \hat{\varepsilon} = \left\{ \begin{array}{cccccc} \varepsilon_{11} & \varepsilon_{22} & \varepsilon_{33} & \varepsilon_{12} & \varepsilon_{23} & \varepsilon_{13} \end{array} \right\} \tag{105} $$

The 2nd Piola-Kirchoff stress vector, ${}^{t}_{0}\hat{\mathbf{S}}$ defined in equation 106, can then be calculated from the Green-Lagrange strain vector using the three dimensional constitutive matrix, ${}^{0}\mathbf{C}$ in the same manner as in the two dimensional non-linear finite element analysis.

$$ {}^{t}_{0}\hat{\mathbf{S}} = \left[\begin{array}{cccccc} {}^{t}_{0}S_{11} & {}^{t}_{0}S_{22} & {}^{t}_{0}S_{33} & {}^{t}_{0}S_{12} & {}^{t}_{0}S_{23} & {}^{t}_{0}S_{13} \end{array} \right]^{T} \tag{106} $$

6.8.3 Calculation of Cauchy stress vector

The deformation gradient of an element is defined as shown in equation 107.

$$ {}^{t}_{0}X_{ij} = \frac{\partial\, {}^{t}x_i}{\partial\, {}^{0}x_j} \tag{107} $$

Calculation of the Cauchy stresses from the 2nd Piola-Kirchoff stresses can then be calculated according to equation 108. The ratio of the mass densities can be calculated from the determinant of the deformation gradient, equation 109.

$$ {}^{t}\tau = \frac{{}^{t}\rho}{{}^{t}\rho} \, {}^{t}_{0}\mathbf{X} \, {}^{t}_{0}\mathbf{S} \, {}^{t}_{0}\mathbf{X}^{T} \tag{108} $$

$$ \frac{{}^{t}\rho}{{}^{t}\rho} = \frac{1}{\det({}^{t}_{0}\mathbf{X})} \tag{109} $$

Components of the deformation gradient can be calculated as shown in equation 110.

$$ \frac{\partial \, {}^{t}x_i}{\partial \, {}^{0}x_j} = \sum_{k=1}^{N} {}_{0}h_{k,j} \, {}^{t}x_i^k \tag{110} $$

The element node deformed positions, ${}^{t}x_i^k$, are calculated from the node starting coordinate and displacements, and put in a matrix, ${}^{t}\mathbf{x}$. The deformation gradient is then calculated by multiplying the $\partial\mathbf{h}$ and ${}^{t}\mathbf{x}$ matrices, and this is used to calculate the Cauchy stress components from the 2nd Piola-Kirchoff stress components.

6.8.4 Calculation of the stress matrix

The stress matrix for the three dimensional elements can then be assembled from the stress components according to equation 111.

$$ {}^{t}_{0}\mathbf{S} = \begin{bmatrix} {}^{t}_{0}\tilde{\mathbf{S}} & \tilde{\mathbf{0}} & \tilde{\mathbf{0}} \\ \tilde{\mathbf{0}} & {}^{t}_{0}\tilde{\mathbf{S}} & \tilde{\mathbf{0}} \\ \tilde{\mathbf{0}} & \tilde{\mathbf{0}} & {}^{t}_{0}\tilde{\mathbf{S}} \end{bmatrix} \tag{111} $$

$$ \tilde{\mathbf{0}} = \begin{bmatrix} 0 & 0 & 0 \\ 0 & 0 & 0 \\ 0 & 0 & 0 \end{bmatrix} $$

$$ {}^{t}_{0}\tilde{\mathbf{S}} = \begin{bmatrix} {}^{t}_{0}S_{11} & {}^{t}_{0}S_{12} & {}^{t}_{0}S_{13} \\ {}^{t}_{0}S_{21} & {}^{t}_{0}S_{22} & {}^{t}_{0}S_{23} \\ {}^{t}_{0}S_{31} & {}^{t}_{0}S_{32} & {}^{t}_{0}S_{33} \end{bmatrix} $$

Linear and non-linear stiffness matrices for the element can then be calculated according to equations 56. Integration over the element volume is carried out using 13 point Gaussian quadrature, defined in appendix B. The element stiffness matrices are assembled into the model stiffness matrix after calculation.

6.8.5 Loading calculations

Internal loading contributions for the elements are calculated in the same manner as for the two dimensional non-linear case, with the integration taken over the element volume, and the loads are calculated in the model coordinate system. Element internal load contributions are added to the model loading vector for each element in turn. External loading is applied as point loads at the model nodes. The external loading includes distributed loads on the element which are lumped at the model nodes in the model definition. The magnitude of the external loads at each load step are calculated in the same manner as for the two dimensional case, equation 72.

6.9 Twenty node solid element

A three dimensional non-linear finite element analysis program, FENLA5 was generated using the twenty node element described in section 4.15. Thirteen point Gaussian quadrature was employed in calculation of the element stiffness matrices and internal loading vectors. In order to simplify debugging, the program uses full stiffness matrix storage and Gaussian elimination for

solution of the finite element equations, and an iterative solution was used for the final load step.

6.9.1 Cantilever analysis

A tip loaded cantilever with material properties $E = 1.2 \times 10^6$ and $\mu = 0.3$, with a length of 1.0 metre and depth and width of 0.1 metres was analysed using FENLA5. Ten elements were used in the finite element model with a convergence limit of 1.0×10^{-5}. Deflections obtained using one load step were equal to the results obtained from the three dimensional linear 20 node element analysis. A non-linear analysis using 20 load steps using an iterative solution on the final load step did not converge after 100 iterations. Displacements of the cantilever were within the convergence limit for the x_1 and x_3 (along the length and through the depth of the cantilever) directions after about 10 iterations, but the displacement increments in the x_2 direction were up to 200% of the displacements after 100 iterations. Magnitude of the displacements in this direction were of the order of 10^{-17} over the model, compared to displacements of up to 10^{-2} for other directions, and were oscillating about zero. This suggests that the changes in displacement are due to rounding errors in the program. As the displacements in the other directions had converged, these non converging displacements are not significant for the solution of the problem.

6.9.2 Convergence check

The convergence check was altered to only examine significant degrees of freedom for convergence. Convergence checking is carried out for each global axis in turn. The maximum displacement over this degree of freedom is obtained, and each nodal displacement increments in this degree of freedom

is only checked for convergence if the node displacement at the start of the iteration satisfies equation 112, where c_c is a convergence check parameter defined in the finite element data file.

$$ {}^{t}_{0}(u_j^n)^i > (u_j^{max})^i c_c \tag{112} $$

6.9.3 Non-linear analysis results

The tip loaded cantilever was analysed using $c_c = 10^{-7}$, and a convergence limit of 0.01% . The tip loading was $0.3N$, which corresponds to a deflection of 0.1m using linear beam theory. A series of models was used with between 1 and 10 elements for a varying number of load steps, and tip deflections are given in table 14. The number of load steps used had no effect on the converged solution, and tip defiection is plotted against number of elements in figure 40. The convergence of the results and the trend to a solution with increasing number of elements gave confidence in the convergence checking method used for a tip loaded analysis case.

6.10 Distributed loaded cantilever

FENLA5 was used to analyse the distributed loaded cantilever used for previous non-linear finite element program validation. Equivalent nodal loads for a face of the element under a uniformly distributed loading are shown in figure 41. This loading is calculated by evaluating equation 113 for each of the face nodes, where the integration occurs over the element face area.

$$ P_n = \int_{Af} h_n p_f dA \tag{113} $$

The cantilever was modelled using ten 20 node elements, initially with load coefficients of 1 and 2. Solutions were obtained for these load coefficients

which were within 5% of the theoretical predictions. The solution of the model with load factor 2 took over 50 iterations with 20 load steps, and 27 iterations with 30 load steps, and consequently the solution was taking up to an hour to converge.

Analysis of the displacement increments showed that the displacements in the global x_2 direction were taking about 5 times as many iterations to converge than those in the x_1 and x_2 directions, and were about 10^{-5} times smaller in magnitude. These displacements had negligible effect on the final solution, and to improve the solution times the convergence check criteria was changed. Displacement increments were only checked for convergence if the node displacement at the start of the iteration passed the check shown in equation 114, where $(u^{max})^i$ is the maximum displacement at the start of iteration i over all model degrees if freedom.

$$ {}^{t}_{0}(u^n_j)^i > (u^{max})^i c_c \tag{114} $$

6.10.1 Effect of convergence check parameter

A cantilever beam with distributed loading factor 2 was analysed for a range of convergence check and convergence limit parameters. Deflections of the tip of the cantilever and the mid point of the bottom of the end face are given in tables 15 and 16 for convergence limits of 0.01% and 0.05% with the convergence check ranging from 1.0×10^{-2} to 1.0×10^{-7}. Reducing the convergence check from 1.0×10^{-4} to 1.0×10^{-5} results in a change in tip deflection of 0.01%, within the accuracy sought by a convergence limit of 0.01%. As reducing the convergence check further would result in an increase in solution time, this was taken as a suitable value for the convergence check criteria.

A reduction in c_c results in a greater number of iterations to convergence,

and hence a higher solution time. It is important to set c_c at a value where only sufficient iterations for all significant displacements to be within the convergence limit are performed.

6.10.2 Order of integration and relaxation

A cantilever model with load factor of 10 was analysed using $c_l = 10^{-3}$ and $c_c = 10^{-4}$, varying the number of load steps. An average tip deflection of 0.6616 was obtained for 20 and 30 load steps, but using 10, 15 or 25 load steps resulted in a solution that diverged, with displacements tending towards infinity. The case with 10 or 15 load steps could be unstable due to insufficient number of load steps before the iterative solution began, but this would not be the case for the 25 load step analysis as a convergent solution was obtained using 20 load steps. Thirteen point integration, which has the same order of accuracy as 3x3x3 Gaussian quadrature is employed in the calculation of element characteristics. In order to confirm that this is sufficiently accurate for the element, the order of integration was increased to 4x4x4 Gaussian quadrature. There was no change in the deflections obtained or the stability of the solution for the distributed loaded cantilever with increased order of integration.

The failure of the model could be due to a growing instability in the iterative solution, which could be improved by using relaxation and FENLA5 was altered to incorporate a relaxation factor, β_1, defined in the model data file. Calculated node displacement increments at the end of each iteration are multiplied by the relaxation factor before being added to the node displacements, equation 115. Setting β_1 to 1.0 results in a solution without relaxation.

$$^{t+\Delta t}\mathbf{U}^{(i)} = {}^{t+\Delta t}\mathbf{U}^{(i-1)} + \beta_1 \Delta \mathbf{U}^{(i)} \tag{115}$$

Analysis of the distributed loaded cantilever with load coefficient of 10 using a relaxation factor of 0.5 or 0.75 did not give a convergent solution for 15 or 25 load steps.

6.10.3 Effect of number of load steps

The full series of cantilever loading cases was run with $c_l = c_c = 0.005$, using 19, 20 and 21 steps. The results are tabulated in table 17. Cantilevers with load factors over 4 gave divergent solutions when using either 19 or 21 load steps. Convergent solutions were obtained using 20 load steps for all the load coefficients, and the tip deflections are plotted against load coefficient in figure 42. The displacements are within 5% of the analytical results of Holden giving accuracy comparable to the two dimensional non-linear finite element analysis.

6.10.4 Effect of solution method

The current solution method only iterates to a converged solution on the final load step. Two different methods of solution were investigated to attempt to improve the stability of the 20 node element:

- Iterate at all load steps
- Iterate at all load steps except the first
- No iteration

Solutions were attempted for the three element cantilever model under a load factor of 10 using 20 load steps using the first two solution methods. In both cases the solution diverged after the third load step.

A non iterative solution was then used to analyse a 10 element model with a load factor of 10. The results for a range of load steps, from 10 to 175 are

given in table 18. The magnitude of the tip deflection oscillates with number of load steps, as shown in figure 43. This may be linked to the instability of the iterative solution at certain number of load steps. The displacement of the non iterative solution is more accurate when compared to the analytical solution for high numbers of load steps than the iterative solution, but the solution time is much longer.

The reason for the instability of the twenty node three dimensional elements for the distributed loaded cantilever case using an iterative solution has not been determined, although it seems to be related to the magnitude of the deflections at the start of the iterative solution. Stability could probably be improved by using the dynamic relaxation and alternative convergence criteria developed for the 16 node element, but lack of time prevented investigation of this.

6.11 Sixteen node element

A three dimensional non-linear finite element analysis program, FENLA5-1, was written using 16 node solid elements. An iterative solution was employed on the final load step. Convergence criteria used for this program was changed to the criteria which is used in the aeroelastic analysis of a rig. A displacement residual is calculated according to equation 116, where l is a characteristic length of the model, taken to be the length of the cantilever beam for the validation models.

$$\textbf{residual} = \sum^{\textbf{all dof}} \frac{\Delta u}{l} \tag{116}$$

The residual is calculated as the node displacements are updated at the end of each iteration, and compared against the convergence limit, c_l, input from the model data file, to determine if the solution has converged. Convergence

limit was set to 1.0×10^{-5} for the cantilever analysis, based on experience that had been gained during initial aeroelastic analysis.

6.11.1 Dynamic relaxation

A distributed loaded cantilever with load coefficient 10 was analysed using a ten element model using a range of load steps from 20 to 25. Some of the load steps gave a diverging solution. Further investigation of the displacement history during the iterative solution for the converging and diverging solutions showed that diverging solutions had a tip deflection larger than the converged solution after one iteration, compared to the solutions which converged that had a tip deflection of less than the converged solution. Diverging solution deflections then grew to infinity as the iterations continued.

Dynamic relaxation was introduced to the iterative solution. The value of the residual for iteration i is compared to the value from iteration $i-1$. If the residual has increased, β_1 is set to the value defined in the model data file, and if the residual is decreasing, it is set to 1.0. This solution method gave converging solutions for all the numbers of load steps considered. An analysis using 20 load steps gave a tip deflection of 0.606920 metres for the original solution method and 0.60915 metres using $\beta_1 = 0.5$. Therefore the use of dynamic relaxation does not significantly affect the results obtained when using 20 load steps

6.11.2 Distributed loaded cantilever

Results for the tip deflection of the distributed loaded cantilever for load factors from 1 to 10 using 20 load steps and $\beta_1 = 0.5$ for a 10 element model is given in table 19, and plotted against theory along with the 20 node element results in figure 44. The arrangement of the elements in the model

is with the linear variation in displacement along the length of the beam. This is as they would be used in the mast, with a quadratic variation over the cross section which allows a rounded mast cross section to be modelled. This arrangement gives less accurate results compared to the twenty node element as the linear variation along the cantilever length cannot model the deformed shape of the beam as well as the quadratic variation of the twenty node model. The sixteen node element has an error in tip deflection of 13% for a cantilever of load coefficient 10 compared to Holden.

The cantilever beam with load coefficient of 10 was analysed using a series of models with from 10 to 100 elements along the beam length, and 20 load steps. Tip deflections are listed in table 20, and plotted against the number of elements in figure 45, and the accuracy of the solution improves as the number of elements in increased, with a model using 30 elements giving an error of 5% compared to Holden.

6.12 Summary

A nonlinear finite element program has been developed, using an iterative solution on the final load step. Three node triangle elements were chosen to represent the sail, as the elements allow an initially curved surface to be discretised. As the elements are constant strain elements, no numerical integration is needed to calculate the element internal loading or stiffness matrix, resulting in a rapid formulation of the finite element equations. Three node triangle membrane elements have been implemented and the program has been validated against a theoretical solution for large deformations of an elastic membrane under constant pressure.

Twenty node solid elements were implemented in the nonlinear finite element analysis, and gave good agreement with a theoretical solution for large

deformation analysis of a cantilever beam. These elements require a transition element to ensure compatibility with the three node membrane elements, and a four node triangle membrane element was developed to satisfy these criteria. The twenty node solid elements produced unstable solutions for certain numbers of load steps. Relaxation methods, variations in solution methods and alteration of convergence check methods were employed to try and improve the stability, but this was not successful. A 16 node solid element was implemented in the nonlinear finite element program, as this does not require transition elements and also would allow the modeling of an initially curved mast. The 16 node element was validated against a theoretical large deformation analysis of a cantilever beam, and proved to be stable for all cases attempted. This element was chosen to model the mast in the rig analysis as it resulted in a simpler rig model and was more stable than the 20 node element.

7 Potential flow

Potential flow theory assumes inviscid incompressible flow, and expresses the flow field in terms of a scalar velocity-potential function, ϕ. The continuity equation for motion of the flow reduces to Laplace's equation, equation 117.

$$\nabla^2\phi = 0 \tag{117}$$

The potential functions for elementary solutions of Laplace's equation for sources, sinks and vortices can be added as Laplace's equation is linear. These solutions can be combined to describe the flow over an arbitrary body. A complete description of the potential flow method is found in many texts, such as White [66].

Development of a CFD program for the analysis of the rig was considered to be outside the scope of this project because of the time available. An potential flow panel code, PALISUPAN, which was developed at The University of Southampton by Turnock [64], was used to calculate the pressure loading for the aeroelastic analysis. PALISUPAN has been used in several previous studies to analyse yacht rigs in an upwind configuration, including investigations by Prior [49], Cant [10] and Noury [45].

7.1 PALISUPAN

Panel codes such as PALISUPAN [64] represent a body by panels placed on the surface of the body containing source and dipoles. Lamb [32] showed that a quantity satisfying Laplace's equation can be written as an integral over the bounding surface, S, of a source distribution per unit area, s and a normal dipole distribution per unit area m distributed over the bounding surface. If the disturbance velocity field due to the bounding surface or body

is defined as $\bar{v}$, this is related to the disturbance potential, ϕ by equation 118

$$\bar{v} = \nabla\phi \tag{118}$$

The disturbance potential can be expressed in terms of a surface integral as shown in equation 119, where S_B is the surface of the body, S_W is a trailing wake sheet, r the distance from the point for which the potential is being determined and $\partial/\partial n$ a partial derivative in the direction normal to the wake sheet.

$$\phi = \int_{S_B} \left[\frac{1}{r}\sigma + \frac{\partial}{\partial n}\left(\frac{1}{r}\right)\mu\right] dS + \int\int_{S_W} \frac{\partial}{\partial n}\left(\frac{1}{r}\right)\mu dS \tag{119}$$

The boundary conditions imposed on the disturbance potential are, from Hess [20]:

1. the velocity potential satisfies Laplace's equation everywhere outside of the body and wake,
2. disturbance potential due to the body is zero at infinity,
3. normal components of the velocity is zero on the body surface,
4. the Kutta-Joukowski condition of finite velocity at the body trailing edge is satisfied,
5. the trailing wake sheet is a stream surface with equal pressure either side.

The first two conditions are satisfied as functions of μ and σ, conditions (3) and (4) are used to determine μ and σ on the body, and the Kutta condition applies only at the leading edge. The distribution of the sources and doublets over the body have to be determined by some other method. A pertubation

potential method taken from the work of Morino and Kuo [40] was chosen for PALISUPAN.

The numerical procedure of Morino is based on representing the body surface by a series of N quadrilateral panels with each containing an unknown constant dipole strength. The wake sheet is represented by M panels placed on the stream surface from the trailing edge of the body, and the dipole strength per unit area of the wake, μ_W is related to the difference in potential between the upper and lower surface of the trailing edge, ϕ_u and ϕ_l, equation 120

$$\mu_W = \phi_u - \phi_l \tag{120}$$

The source strength per unit area of the body is prescribed by satisfying the condition for zero normal velocity at the panel centroid, equation 121

$$\sigma_s = \bar{U} \cdot \bar{n} \tag{121}$$

The numerical discretisation of equation 119 gives the potential at the centre of panel i as shown in equation 122, where for panel j, S_{ij} is the source influence coefficient of a unit strength panel, D_{ij} is the dipole influence coefficient and W_{ik} is the influence of the constant strength wake strip extending to infinity.

$$\phi_i = \frac{1}{2\Pi} \sum_{j=1}^{N} ((U_\infty \cdot n_j) S_{ij} - \phi_j D_{ij}) + \sum_{k=1}^{M} \Delta\phi_k W_{ik} \tag{122}$$

As there are N independant equations corresponding to the N body surface panels, equation 122 can be evaluated, and expressed in matrix form this becomes equation 123.

$$\mathbf{D}_{ij}\phi + \mathbf{W}_{ij}\Delta\phi = \mathbf{S}_{ij}(U_\infty) \cdot n) \tag{123}$$

As Morino's original trailing edge Kutta condition directly relates $\Delta\phi$ to the difference in trailing edge panel potential, equation 123 can be directly solved to give the vector of dipole potentials, ϕ. Numerical differentiation of the dipole potential along the body surface allows the surface velocity and hence pressure to be calculated.

As PALISUPAN is a panel code, it is necessary to introduce an artificial thickness in the sails to enable solution, unlike the vortex lattice codes that have been used in past aeroelastic analysis of sails. The sail has to have an artificial thickness to prevent the panels on one side of the sail influencing the flow on the other side. However, the panel code allows solution of the mast and sail as a single body. Prior [49] studied the effect of the thickness introduced to the sail, and concludes that a thickness to chord ratio of 2.5% gives the most accurate solutions when compared to experimental results. Both Prior [49] and Cant [10] found that the global force predictions obtained from PALISUPAN were not very accurate compared to experimental results. However, the error in global force components can be attributed to the viscous effects which occur in the experimental cases, and the difficulty in accurately replicating the experimental conditions. Prior [49] found good agreement between experimental measurements of pressure distribution on a mast/sail model and values predicted by PALISUPAN using an artificially thick sail for areas away from the leading edge area where separation can occur at the mast. As the aeroelastic analysis is concerned with the pressure values obtained by the CFD code, the results of Prior [49] give confidence in the ability of PALISUPAN to model the problem adequately. An example of the pressure distribution obtained from a PALISUPAN analysis of a yacht rig sailing upwind is given in figure 46. This shows the pressure distribution on the windward side of a mast mainsail model calculated during an aeroelastic

analysis of the model.

7.2 Model definition for PALISUPAN

PALISUPAN takes a definition of the bodies to be analysed and generates panels required for the analysis according to the number of panels in the chord and spanwise directions defined in a control file. The body is defined in the geometry input file as a series of sections, and for a closed body such as a rudder or the combined mast sail model, the definition of the section starts and finishes at the trailing edge. PALISUPAN evaluates cubic spline curves to fit the input data points and generate a mathematical description of the body which is used for the discretisation into panels. It is important to ensure that the body definition points will result in a smooth surface when this procedure is carried out, as a rapid change in slope between points can cause errors in the cubic spline definition.

7.3 PALISUPAN grid generation

During the aeroelastic analysis, the deflected node positions obtained from the finite element analysis will be used to generate the updated body definition for PALISUPAN analysis. A series of points defining cross sections through the rig will be extracted from the finite element model, and these will be used to generate the sections for the PALISUPAN input file. The rig will be oriented in the global coordinate system in the same manner for all the aeroelastic analysis cases, as shown in figure 47. This orientation results in the pressure side of the artificially thick sail having an x_2 coordinate that is lower than the suction side. All the PALISUPAN models are generated with the chord of the sections lying along the global x_1 axis. This means

that the input velocity vector is defined as shown in equation 124.

$$\mathbf{V} = (V\cos\alpha, V\sin\alpha, 0) \tag{124}$$

In all cases, the PALISUPAN analysis was carried out without a reflection plane.

For the case of a sail modeled without a mast, the sail section can be divided into three main parts, the leading edge, trailing edge and the sail surfaces. Previous experience with PALISUPAN analysis of sails (Turnock [65]) has shown that optimum results are obtained using a section where the leading edge is an ellipse covering 5% of the chord length, followed by a constant thickness main section, where the artificial thickness is in a direction normal to the sail surface and placed symmetrically about the surface, and a linear taper to the trailing edge over the final 5% of the chord length. To avoid errors that could occur in the cubic splines used by PALISUPAN to generate the mathematical model of the body where the section slope changes at the leading and trailing edges, three points are placed along the sail upper and lower surfaces either side of the leading and trailing edge definition points. These points are placed at a spacing of 1% of the local chord length before and after the 5% of the chord covered by the leading and trailing edge sections and ensure that the PALISUPAN splines form a smooth curve over the output section. Surface points are then evenly spaced over the remaining length of the section, from 5.3% to 94.7% of the chord length. The wake sheet should leave the trailing edge smoothly with the slope between the sail and wake sheet being continuous, then curve back to the free stream direction over a length roughly equal to the sail chord, with the semi infinite wake sheet then extending in the free stream direction. As the model will experience the highest velocity gradients around the leading edge of the sail, a panel distribution which clusters in the center of the section (around the

leading edge) is employed in the chordwise direction. It is important to define the PALISUPAN sections so that the sections are defined running up the mast (increasing x_3), with the section definitions containing points which are ordered from the trailing edge, along the surface of the sail with higher x_2 values (suction surface), around the leading edge and back along the surface of the sail with lower x_2 values (pressure surface) to the trailing edge. This ensures that the orientation of the panel normals are in the correct direction, as otherwise PALISUPAN could calculate the flow inside the body.

To model a rig consisting of a mast and sail, a constant artificial thickness is added over the sail as for the case discussed above. A linear taper is used from the trailing edge over 5% of the chord length, and three points are placed on the sail surface where the taper ends to force the PALISUPAN splines to model this area correctly. The mast cross section is joined to the sail section where the artificially thick sail intersects the mast. As there is an abrupt change of slope at this point, three points are placed on the sail surface and mast section either side of the join to ensure that the splines produce an accurate definition of this area. PALISUPAN provides a special panel distribution which is suitable for the rig model, where the section is split into three parts with the chordwise number of panels in the model split between the three sections with a different distribution possible for each of the three sections. For the analysis of the rig, a panel distribution was used where the panel density increases along the suction surface from the trailing edge to the mast, remains constant around the mast and then decreases from the mast to the trailing edge on the pressure surface of the sail. This ensures that there is an increased panel density in the area of highest velocity gradients.

The membrane, sail and rig models considered will form closed sections in

the chordwise direction, and the body will be open in the spanwise direction. This allows the possibility that the flow could wrap around inside of the body at the tip and foot of the model. It is possible to define separate bodies to close the model at the tip and foot, although this would introduce added complexity into the model definition, and increase the time taken for the CFD runs. Since the section is thin, the flow is unlikely to wrap around into the body, and as previous models of sails have not found this to be a significant problem, the section has been left open in the spanwise direction to simplify the input file generation program.

7.4 CFD grid generation program development

A computer program was developed to output sail section and wake data in a PALISUPAN input format from a network of points in 3D space which are read in from a file. These points represent the displaced node positions which will be obtained from the FENLA program in the aeroelastic analysis. The network of points is arranged into a series of sections of the body in the x_1, x_2 plane, at increasing x_3 values. Thickness of the section, t_s is calculated according to equation 125, where l_c is the local chord length and t_m is a constant usually set to 0.025 to give a thickness to chord ratio of 2.5%.

$$t_s = l_s t_m \tag{125}$$

The grid generation computer program was developed to process an arbitrary number of sections, with arbitrary numbers of points in each section. Program development was carried out as follows:

- Program to generate a PALISUPAN input body with a sail cross section from a 3D model of flat membrane.

- Program to generate a single 2D sail section from a set of input points that define a curve in the x_1, x_2 plane.
- Program to develop 3D model from points which represent a series of curved sections.

7.5 Flat membrane

Initial development of the PALISUPAN input file generation program considered the case of a plane membrane. The problem is simplified as the normal to the membrane is constant over the model, and thus the artificial thickness will be applied in a constant direction over the surface. As the membrane is defined in the x_1 x_3 plane, the thickness is applied in the x_2 direction.

7.5.1 Program structure

Program structure of the computer program to generate PALISUPAN input files from a grid of points, F-2-P, is shown in figure 48. The surface definition file contains the number of sections, followed by the definition of each section which contains the number of points in that section followed by the coordinates of each point. Input data is stored in a data structure containing dynamically allocated arrays of section data and point data to allow the processing of arbitrarily sized models. Input sections are defined with the chord along the x_1 direction. The number of points used to define the leading edge, N_{le} and each of the sail surfaces, N_{sur} is input during the program execution. This enables the calculation of the number of points which will define each section output to the PALISUPAN input file.

Coordinates of the points defining each PALISUPAN section are calculated for each section in turn, and stored in the output data structure. After

calculation of the body definition, the wake section definition points are calculated, and these are also stored in the model definition. The number of panels to be used in the PALISUPAN discretisation in the chordwise and spanwise, directions, N_t and N_s respectively, is input during the program execution, and the PALISUPAN model definition is output to a file in the required format.

7.5.2 Calculation of flat membrane model

The number of points used to define the PALISUPAN section, N_p is calculated according to equation 126.

$$N_p = N_{le} + 2N_{sur} + 14 \tag{126}$$

This is made up of the trailing edge point at the start and end of the section definition, the 12 points used in groups of three to ensure a smooth transition from trailing edge taper and leading edge ellipse to the sail surface, N_{le} points around the leading edge and N_{sur} points on each of the sail surfaces. Initial runs of the grid generation program used $N_{sur} = 10$ and $N_{le} = 7$, and 5 points were employed to define the wake. These values were found to produce fair sections in all the grid generations undertaken.

An array of coordinate points of size N_p is allocated for the output section definition, and points at the trailing edge location are placed into the first and last location to define the start and end of the section. Section length is calculated from the distance between the first and last points in the input section, and the section thickness calculated according to equation 125. Points are then defined at the required locations along the chord length, with the section thickness applied symmetrically about the mid chord line of the section defined by the input points.

The leading edge ellipse is created by an even distribution of the N_{le} points across the thickness of the section, covering 5% of the chord length, as illustrated in figure 49.

Wake definition is calculated using cubic Bezier curves. Control points for the Bezier curves are calculated from the local chord length and the angle of incident flow, input by the user during program execution, and the location of the control points is illustrated in figure 50. The wake definition points are then calculated at locations equally spaced along the Bezier curve.

A section of the PALISUPAN input data generated using the F-2-P program is shown in figure 51, for a case with $N_{le} = 7$ and $N_{sur} = 10$.

7.6 Curved section

To generate a curved sail section, the input points for the section is used to define a series of cubic spline curves that represent the input section line. The local chord, calculated as the distance between the first and last input section points is used to calculate the section thickness according to equation 125, and this is applied symmetrically about the input line in the direction of the curves principle normal. This stage in the program development was used to develop sail section generation and spline routines for a single section, to simplify debugging of these routines, before moving on to the full three dimensional case. No wake definition was investigated for this case, as only a single section was defined, which is unsuitable for PALISUPAN analysis.

7.6.1 Parametric spline curves

The input section line is defined as a parametric curve in g, running from 0 at the leading edge to 1 at the trailing edge. The parametric coordinate, g_i of point i along the line is approximated by taking the straight line length be-

tween the curve definition points as a distance along the curve, equation 127, where l_s is the sum of the straight line lengths.

$$g_i l_s = \left(\sum_{j=1}^{3} (x_j^i - x_j^{te})^2 \right)^{\frac{1}{2}} \tag{127}$$

Cubic spline equations [29] are used to calculate the curvatures, M_j^i at each point for each of the global coordinates $j = 1, 2, 3$. These can be used to calculate the coordinates of a point at parametric coordinate g, as shown in equation 128, where $g_i \leq g \geq g_{i+1}$, and h_i is the parametric length of curve i, which lies between points i and $i + 1$.

$$\begin{aligned} x_j = & \frac{M_j^i}{6h_i}(g_{i+1} - g)^3 + \frac{M_j^{i+1}}{6h_i}(g - g_i)^3 \\ & + \left(\frac{x_j^{i+1}}{h_i} - \frac{M_j^{i+1} h_i}{6} \right)(g - g_i) + \left(\frac{x_j^i}{h_i} - \frac{M_j^i h_i}{6} \right)(g_{i+1} - g) \end{aligned} \tag{128}$$

7.6.2 Principal normal calculations

The principle normal direction is defined in equation 129 from Taylor [60].

$$\mathbf{N} = \left[\frac{\partial_1^2 x}{\partial g^2}, \frac{\partial_2^2 x}{\partial g^2}, \frac{\partial_3^2 x}{\partial g^2} \right] \tag{129}$$

The curvature values at a point with parametric coordinate g are calculated by linear interpolation between the input points defining the curve that the point lies on, equation 130.

$$\left. \frac{\partial_j^2 x}{\partial s^2} \right|_g = \frac{M_j^i}{h_i}(g_{i+1} - g) + \frac{M_j^{i+1}}{h_i}(g - g_i) \tag{130}$$

The vector resulting from these calculations is normalized, then multiplied by the section thickness. The resulting vector can then be added and taken away from a point on the cubic spline curve to give the required points on the upper and lower surface of the section.

7.6.3 Leading edge calculations

The points defining the leading edge profile are calculated using the method described for the plane section in a local y_1, y_2 coordinate system. These coordinates are then rotated to the global system using a cosine matrix calculated from the locations of the leading edge point and the input point closest to 5% of the arc length. Finally the points are translated so that the central point in the leading edge ellipse coincides with the point defining the model leading edge.

7.6.4 Section point calculation

The three points at the boundary of the trailing edge taper and leading edge ellipse are placed at 1% of arc length separation from $g = 0.95$ and $g = 0.05$. Surface points are then equally spaced between $g = 0.052$ and $g = 0.948$ along the section, with pressure and suction surface points calculated using the principle normal. The order of the surface definition follows that described in the flat membrane case.

7.7 Three dimensional general membrane

A computer program which generates PALISUPAN input files from a series of input sections defining an arbitrary surface, F-2-P-II, was developed. The program uses the same structure as the F-2-P program, and the single section generation method described above is used for each section.

The definition of the principle normal used in the 2D section fails for a straight line (zero curvature), as a straight line does not have a single principle normal. In order to ensure that F-2-P-II could deal with arbitrary models, an alternative method for calculating surface normal is used at points

where the curvature is found to be zero. The wake definition used in the flat plate model is extended to a general three dimensional case. The program allows variation of:

- Input and output files
- Number of panels in the t and s direction for the PALISUPAN meshing
- Number of points used to define the output sections leading edge ellipse, surfaces and wake sheet
- Thickness multiplier

A file containing the model definition in the PALISUPAN original geometry input file format is output from the program.

7.7.1 Normal calculation

After calculation of the principle normal for any point, t, equation 129, the magnitude of the vector obtained is calculated. If this is zero, the input section is a straight line, and an alternative method of calculating the surface normal is used. Two vectors on the input surface are calculated, as shown in figure 52. The normalised cross product of these vectors is calculated and used as the surface normal at this point. The two in plane vectors are calculated using point i and point $i+1$ on the current section, and point i on the current section and point i on the next section. If the point i is the last point on the current section, the first vector is taken in the direction of point i to point $i-1$, and if the section being considered is the last input section, the second vector is taken from point i on the current section to point i on the previous section. The change in orientation of the normal calculated using the alternative points is taken into account when calculating the surface normal used for application of the artificial thickness.

7.7.2 Wake definition

During calculation of the output section, the slope of the curve at the trailing edge is calculated using equation 131.

$$\frac{\partial x_j^{le}}{\partial g} = \frac{h_{n-1} M_j^{n-1}}{6} + \frac{h_{n-1} M_j^n}{6} - \frac{x_j^{n-1}}{h_{n-1}} + \frac{x_j^n}{h_{n-1}} \tag{131}$$

Components of the slope, $\partial x_j / \partial g$ can be used to define a unit vector tangent to the input curve at the trailing edge, which is stored in the output section data structure. During calculation of the wake section, the incident flow is used to define a unit vector in the direction of the free stream flow. These two vectors are then used to define the Bezier control points, as shown in figure 53, for the Bezier curve defining the wake section. Wake definition points are then generated at equal spacing over the wake section curve. An example of a curved membrane PALISUPAN section generated by F-2-P-II is shown in figure 54

7.8 Generation of PALISUPAN rig model

The structure of the grid generation program used to generate the rig model for analysis by PALISUPAN is shown in figure 55. This generation program is employed within the aeroelastic analysis, and the parameters used to generate the output file are obtained from the analysis control file, and consist of:

- Number of point to define the sail surface, N_{sur},
- Number of points to define the mast surface, N_m,
- Number of panels to define the model in the PALISUPAN discretisation, in chordwise, N_t, and spanwise, N_s, directions,
- Number of panels used to define the mast in the PALISUPAN discretisation, N_{mast},

- Thickness multiplier, t_m.

Input sections include points defining the sail shape and the mast cross section. Cubic splines are generated which define the sail section as in the program F-2-P-II, and the mast cross section is also defined by a set of parametric cubic splines, with t running from 0 to 1 around the mast in a clockwise direction when viewed from the top of the rig. The mast splines form a closed section, with the first and last points of the curve taken as the joining point between the mast and sail (which also defines the end point of the sail curve). Figure 56 shows the orientation of the spline curves used to define the mast and sail.

7.8.1 Output section generation

The number of points used to define an output section is calculated according to equation 132, and the array of points defining the output section is allocated accordingly.

$$N_p = N_m + 2N_{sur} + 18 \tag{132}$$

The thickness of the sail section is calculated as for the previous program according to equation 125. The point defining the trailing edge is placed into the start and end point of the output section, and the order in which the points are placed into the output section are indicated in figure 57. Three points are placed at the end of the trailing edge taper at $g = 0.93, 0.94, 0.95$ on the pressure and suction surfaces of the sail, and three points are placed at $g = 0, 0.01, 0.02$ on the pressure and suction surfaces of the sail to define the start of the sail section. The parametric coordinates along the mast curve which defines the mast sail intersection at the start of the mast section, g_s (pressure surface of the sail) and the end of the mast section, g_e (suction

surface of the sail) are calculated using the method described below. Two points are placed at $g_e - 0.01$ and $g_e - 0.02$, then the number of points defining the mast are equally spaced along the mast parametric curve between $g_e - 0.02$ and $g_s + 0.02$. The mast definition is completed by placing two points at $g_s + 0.02$ and $g_s + 0.01$.

7.8.2 Calculation of the mast sail intersection

To obtain a smooth join of the mast and sail surfaces in the output section, the parametric coordinates of the end point of the mast curve used for the rig section is calculated by obtaining the parametric coordinates on the mast definition curve which are within 1% of the location where the x_2 coordinates of the mast curve are equal to the x_2 coordinates of the suction and pressure surfaces of the sail.

The x_2 coordinate of the start of the suction surface of the sail, x_2^s is used to find the coordinate of the assumed intersection point at the end of the mast curve. Starting at the end of the mast, each spline curve for the mast is checked until the correct interval, i is found, such that $x_2^i > x_2^s > x_2^{i+1}$. Starting at the parametric coordinate of point i, g_i, g is increased in steps of 0.01 until $x_2^g < x_2^s$. The end intersection point coordinate, g_e on the mast curve is then taken to be $g - 0.01$, so that $x_2^{g_e+0.01} < x_2^p < x_2^{g_e}$. The starting intersection point of the mast curve is calculated in a similar way, with g_s taken as the point such that $x_2^{g_s} < x_2^p < x_2^{g_s-0.01}$, where x_2^p is the x_2 coordinate of the start of the pressure surface of the sail.

7.9 Analysis of a rectangular membrane

The program F-2-P-II was used to generate a sail cross section from a grid of points representing a rectangular membrane with a chord of 1 metre and

a span of 5 metres. A flat membrane and a membrane with a curved cross section were used to generate models which were analysed by PALISUPAN to gain some experience in using the program and to verify that the model generation programs were working correctly. In addition to the panel density and distribution on the model, PALISUPAN allows alteration of the Kutta convergence criteria and block matrix convergence criteria (BMCC). Kutta convergence criteria sets the convergence limit of the maximum trailing edge pressure difference. Reducing this value will result in a more accurate prediction of pressure forces, but will increase the number of iterations required for a solution, and hence increase the solution time. The BMCC sets the limit to which the block iterative matrix solver is forced to converge, and is usually set to 0.0001 according to Turnock [64].

7.9.1 Calculation of lift and drag coefficients

Force components in the global coordinate system are output from PALISUPAN in non dimensional form, with the force non dimensionalised with respect to an area of $0.6667m^2$ as in equation 133. This area is fixed in the program, and takes no account of the geometry of the input body. The PALISUPAN forces must therefore be multiplied by (0.6667/5.0) to give the global forces non dimensionalised with respect to the area of the 5 metre by 1 metre membrane.

$$(C_f)_{pal} = \frac{F}{\frac{1}{2}\rho V^2 \times 0.6667} \tag{133}$$

Lift and drag coefficients can be calculated from global forces (non dimensionalised with respect to the membrane area) as shown in equations 134 and 135.

$$C_L = C_{fy}\cos\alpha - C_{fx}\sin\alpha \tag{134}$$

$$C_D = C_{fy} \sin \alpha + C_{fx} \cos \alpha \tag{135}$$

7.9.2 Three dimensional thin wing theory

Abbott and Von Doenhoff [1] provide a method of calculating lift and drag for a three dimensional thin wing, which is obtained using lifting line theory and is related to the two dimensional data for the wing section. The method is applicable to wings with aspect ratios of 2 and above. Lift curve slope per degree, a, for the wing can be calculated using equation 136. The factor f, depends on the aspect ratio of the wing and the ratio of the root and tip chords (wing taper), and is obtained from a chart [1]. For a wing of aspect ratio 5, with the tip and root chords of equal length, $f = 0.991$.

$$a = f \frac{a_e}{1 + (57.3 a_e / \pi A)} \tag{136}$$

The effective lift curve slope, a_e, is defined as in equation 137, where a_0 is the average two dimensional lift curve slope of the wing. Jones edge velocity factor, E is the ratio of the (span + chord) of the wing to the span of the wing.

$$a_e = \frac{a_0}{E} \tag{137}$$

Using these relationships, the theoretical lift curve slope for a rectangular flat section of aspect ratio 5 is 3.891 rad^{-1}.

Induced drag for a three dimensional wing with no twist can be calculated from equation 138. The term u is found from a chart presented in Abbott and Von Doenhoff [1], depending on the aspect ratio and taper of the wing.

$$C_{Di} = \frac{C_l^2}{\pi A u} \tag{138}$$

For a case with aspect ratio of 5, and zero taper $u = 0.983$, and from equation 138 $C_{Di} = 0.065 C_L^2$.

7.9.3 Theoretical calculations for a curved surface

A quadratic curve is used to define the curved membrane shape, with a maximum camber ξ located at the mid chord point, $x_1 = c/2$. The equation of the curved surface is given in equation 139.

$$x_2 = \frac{-4\xi}{c^2}x_1^2 + \frac{4\xi}{c}x_1 \tag{139}$$

The two dimensional section lift coefficient at angle of incidence α, calculated using thin wing theory, is given by equation 140.

$$C_L = 2\pi\left(\alpha_0 + \frac{2\xi\pi}{c}\right) \tag{140}$$

When corrected for three dimensional effects as described in the previous section, the lift curve slope of the surface is 3.892 rad^{-1}, and the zero lift angle of attack, α_0 is $-2\xi\pi/c$.

7.10 PALISUPAN analysis of rigid rectangular flat membrane

The flat rectangular membrane was analysed using two panel densities for a range of incidence from -10^o to 10^o. The panel densities used were:

- Coarse grid, $N_t = 10$, $N_s = 25$
- Fine grid, $N_t = 20$, $N_s = 50$.

PALISUPAN [64] allows the use of a variety of panel distributions in the chord and spanwise directions. A sinusoidally distribution of panels was used in the spanwise direction with the maximum density at the mid point of the section (around the leading edge of the membrane), and a constant distribution was used in the spanwise direction. Average panel aspect ratio

for the two grids was 1.0, although the panel aspect ratio will vary due to the clustering of the panels at the leading edge. The Kutta convergence criteria was set at 0.001 and the BMCC was set at 0.0001 for these PALISUPAN runs.

Results for the two grids are given in table 21, and the lift coefficient is plotted against incidence in figure 58. Lift curve slope, $\delta C_L/\delta\alpha$ obtained from the coarse and fine grids was 3.9371 and 3.9311, errors of 1.2% and 1.0% respectively compared to theory. The gradient of C_D against C_L^2 graph was 0.131 and 0.0433 for the coarse and fine grids, giving errors of 100% and 33% compared to lifting line theory. The inaccuracy of the drag predictions is due to the low number of panels used in the chordwise direction, even in the fine grid case.

7.10.1 Block matrix solver convergence limit

A flat plate of aspect ratio 5 was analysed using a fine grid, $N_t = 50$, $N_s = 50$, with a range of block matrix iterative solver convergence limits, from 0.1 to 1×10^{-6}, and the results are shown in table 22 . The effect of this on the calculated lift coefficient is shown in figure 59. The block matrix solver convergence limit has little effect on the solution obtained with global force values using a BMCC of 0.1 within 3% of the value obtained using a BMCC of 1.0×10^{-6}. Computation times increase as the value is reduced, and this is particularly noticeable below 1.0×10^{-4}. The number of iterations does not increase significantly (this is affected by the Kutta condition convergence limit), but each iteration takes more time. The global force and lift coefficients using a BMCC of 1.0×10^{-4} are predicted to within 0.5% of the values obtained with a BMCC of 1.0×10^{-6}, and to reduce the computational time required for further analysis 1.0×10^{-4} will be used in future for the PAL-

ISUPAN analysis, as this gives a sufficiently accurate level of solution for the influence matrix.

7.10.2 Effect of panel average aspect ratio

The effect of the panel average aspect ratio was then investigated for the case of a 5 degree incident flow. Average panel aspect ratios of 0.5 to 1.5 were considered, with number of panels up to about 1800 panels. The results for these cases are presented in tables 23 and 24. For a constant average panel aspect ratio, the error in lift coefficient compared to theory reduces as the number of panels is increased. However, the accuracy of the result is dependent on whether there is an odd or even number of panels in the chordwise direction. Figure 60 shows this for a series of models with average panel aspect ratio of 0.5, where an model with an even number of chordwise panels predicts a more accurate lift coefficient for a given number of panels. A model with an even number of panels will have a symmetric distribution of panels around the leading edge, which will result in a better definition of the model than in case with an odd number of chordwise panels. Using an odd number of panels can also result in a slight error in the spline generation routines used within PALISUPAN. However, as the number of panels increases the difference between the odd and even number of panels in the chordwise direction becomes less significant.

The lift coefficient against number of panels for the range of panel aspect ratio cases with even numbers of chordwise panels is shown in figure 61. Altering the panel average aspect ratio does not significantly affect the value of the lift coefficient calculated for fine meshes. For a 1000 panel model, the calculated lift coefficient differs by less than 0.1% for models with average panel aspect ratios of 0.5 and 1.5. For models with coarse meshes, the

extreme panel ratios (0.5 and 1.5) give slightly less accurate results.

7.11 PALISUPAN analysis of a curved membrane

A set of points representing a curved membrane, chord 1 metre, span 5 metres, with a camber of 5% of chord length was created, and a PALISUPAN input file was generated using the program F-2-P-II. The model was analysed using two grids:

- Coarse grid, $N_t = 10$, $N_s = 25$
- Fine grid, $N_t = 50$, $N_s = 50$.

PALISUPAN was used to analyse the models at angles of incidence from -10^o to 10^o, and the results are listed in tables 25 and 26. The lift coefficient is plotted against angle of attack in figure 62. Thin airfoil theory predicts a lift curve slope of 3.892rad^{-1} and zero lift angle of -5.7^o for the membrane. The lift curve slope obtained by the coarse grid is 3.97, and by the fine grid is 3.87, errors of 2.0% and 0.5%. Zero lift angle calculated from the PALISUPAN analysis was 2.0^o for the coarse grid and -4.8^o for the fine grid.

Both the coarse and fine grids gave good prediction of the lift curve slope, and the fine grid gave a good prediction of the zero lift angle.

7.11.1 Effect of panel density

The effect of panel density on the calculated lift coefficient was investigated for a plate with initial curvature of 5% and aspect ratio of 5 at $\alpha = 0^o$. In all cases, the block matrix convergence criteria was set to 1.0×10^{-4}, 10 points were used to define the leading edge and surfaces and 8 points were used to define the wake sheet.

Runs were carried out with N_t or N_s held constant at 20, 36 and 50, and varying the number of panels in the other direction from 20 to 52 in steps of 4 (this ensures that there is always an even number of panels in the chordwise direction, and removes the oscillation in results that odd/even N_t produces as discussed in section 7.9.2). A series of runs with $N_t = N_s$ for 20 to 56 panels in each direction was also carried out.

The lift coefficient is plotted against total number of panels for these runs in figure 63. The lift coefficient is only very weakly dependent on N_s, with a difference in lift coefficient of only 1.5% for total number of panels between 720 and 1800 with $N_s = 36$. Lift coefficient values are highly dependent on N_t, and for the case with $N_s = 36$, the lift coefficient changes by 60% for total number of panels between 720 and 1800. This effect can be seen more readily in figure 64, where the lift coefficient is plotted against N_t for N_s of 20, 36 and 50. The lift coefficient is tending towards a converged solution as the number of panels is increased.

Since the results seem almost independent of N_s, the case with $N_s = 20$ was investigated for N_t up to 100, and a series of models with $N_t = 60$ and varying N_s was investigated, to ensure that the weak dependence of C_L upon N_s occurs with higher N_t. These results are shown in figure 65, and confirm that there is little dependence of C_L upon N_s with high N_t. The lift coefficient seems to be converging for values of N_s over 100. A series of models with N_t of over 50 was run for $N_s = 36$, to observe whether a similar convergence occurs in this case at high N_t values. The lift coefficient results for N_s of 20 and 36 are plotted against N_t in figure 66, and a similar trend to the $N_s = 20$ case can be seen. A model was attempted with $N_s = 36$ and $N_t = 100$, but this was extremely slow to run the analysis was terminated after 30 hours.

7.12 PALISUPAN analysis of a deformed sail model

The deformed shape of one of the initial runs of the aeroelastic program on a sail model restrained along the leading edge was used to provide a deformed membrane definition for analysis using PALISUPAN to study the effect of variation of the PALISUPAN model and convergence parameters on the calculated forces on the sail. Kutta condition, BMCC limits, panel density and distribution were varied to enable the input model parameters to be set to give a good relative accuracy without the analysis being too time consuming. Figure 67 shows three sections of the PALISUPAN input model used in the sensitivity study at heights of 0.5, 1.0 and 1.5 metres up the mast.

During the development of the aeroelastic program, it was noticed that the wake definition method being used in F-2-P-II did not always result in the wake sheet returning to the direction of the incident flow, as the cubic splines used to define the wake were not forced into having the correct slope at the end of the wake definition. To ensure that this occurred, three points were placed at distances of 10%, 11% and 12% of the local chord from the previous final point in the wake definition in the direction of the incident flow.

The sail model used is triangular, with a 1 metre chord at the bottom of the sail, and a 2 metre span. To enable PALISUPAN to mesh the body, the triangle is truncated at a height of 1.75 metres to form a quadrilateral body.

7.13 Convergence criteria

7.13.1 Block matrix convergence criteria

A model with panel density of $N_t = 40$, $N_s = 20$ with an even distribution along the span and clustered distribution at the leading edge along the chord (as used for the previous model) was used to observe the effect of the convergence criteria (BMCC and Kutta condition).

A series of runs with BMCC ranging from 1.0×10^{-1} to 1.0×10^{-7} were carried out. Results are tabulated in table 27, and a graph of the lift coefficient values is given in figure 68. The drag coefficient for all cases was within 0.001% of the value obtained with BMCC of 1.0×10^{-1}, where $C_D = 0.1097$. Lift coefficient values showed no clear trend as BMCC was reduced, and there was a change of only 0.005% over the range of BMCC used. Solution time increased as BMCC was reduced, and it was decided to use a value of 1.0×10^{-4} in further investigations, as this gave an acceptable solution time of around 2 minutes on an UNIX workstation.

7.13.2 Kutta condition

Using a value for BMCC of 1.0×10^{-3}, the Kutta condition limit was varied from 1.0×10^{-1} to 1.0×10^{-6}. The case with Kutta limit of 1.0×10^{-6} was stopped when no solution had been obtained after 7 hours. Lift coefficient values varied by 2% over the range of Kutta condition limits examined. The results are tabulated in table 28, and a graph of the lift coefficient values is given in figure 69. The number of iterations to solution increased with decreasing Kutta limit, and this is shown graphically in figure 70. There was no significant change in the lift or drag coefficient results (less than 0.1%) when the Kutta condition was reduced below 1.0×10^{-2}, and this value was

chosen for future PALISUPAN runs to keep solution time to a minimum.

7.14 Panel density

The deformed triangle mode was run using a Kutta limit of 1.0×10^{-2} and BMCC of 1.0×10^{-4}. The effect of changing the panel density was analysed by keeping N_t or N_s constant and varying the number of elements in the other direction. In all cases, an even number of panels was chosen in the chordwise direction, as this was found to give more accurate results than odd numbers of panels as discussed in the analysis of the rectangular membrane. was used for all the cases.

7.14.1 Effect of changing N_s

Models were run with $N_t = 40$ and N_s varying from 10 to 45. The results are tabulated in table 29, and graphs of the lift and drag coefficient are plotted against N_s in figures 71 and 72. The lift coefficient values converge rapidly with N_s, and with 20 panels along the span the lift coefficient is within 0.5% of the value obtained with 45 panels. Drag coefficient does not converge as quickly, and the model with $N_s = 20$ has an error of 20% in C_D compared to the case with 45 spanwise panels. Increasing the number of spanwise panels to 30 gives a 0.25% difference in lift and 7% difference in drag compared to the case with 45 spanwise panels.

7.14.2 Effect of changing N_t

The number of spanwise panels was kept constant at $N_s = 20$, and number of chordwise panels was varied from 20 to 90. The results are tabulated in table 30, and the lift coefficient is plotted against the number of chordwise elements in figure 73. The convergence is not as rapid as for the case with

varying N_s, the case with $N_t = 30$ has an error of 10% compared with $N_t = 90$ whilst $N_t = 60$ has an error of 4%. Number of chordwise panels has a more significant effect on the accuracy of the lift and drag coefficient calculations than the number of spanwise panels.

7.14.3 Effect of panel aspect ratio

In order to determine the effect of the panel aspect ratio, a series of runs with fixed average panel aspect ratios (ratio of N_t to N_s)of 0.5 and 1.0 with increasing number of panels were carried out. Since a clustered distribution of panels is used in the chordwise direction, the panel aspect ratio referred to is an average panel aspect ratio over the model. Results are tabulated in tables 31 to 33, and the lift coefficient is plotted against number of panels in figure 74.

Both the series with APAR of 0.5 and 1.0 converge to a solution of $C_L = 1.06$ as the number of panels increases. An accuracy of 5% in C_L is obtained with approximately 1400 and 1000 panels for the cases with APAR of 0.5 and 1.0 respectively. Solution time increases dramatically with the number of panels used in the model, and to minimise the error for a given solution time, models with APAR of 1.0 give the best results.

Solution time for a PALISUPAN analysis depends on the Kutta convergence limit, the BMCC and the number of panels used to define the surface. Due to the iterative nature of the aeroelastic solution, 200 PALISUPAN analyses will be carried out during a typical aeroelastic solution, and it is important to limit the panel density in order to keep the solution time at a reasonable level. A solution time of three minutes was chosen which results in a run time of the aeroelastic analysis in the region of 12 hours on a UNIX workstation. Using the BMCC and Kutta limits set according to the results

of sections 7.12.1 and 7.12.2, a mesh of around 1000 panels gives a run time of three minutes, which is acceptable for the aeroelastic analysis to keep total solution time to around 12 hours. A panel distribution of $N_t = 64$, $N_s = 16$ was chosen to provide an average panel aspect ratio of 1.0, with around 1000 panels.

7.15 Panel distribution

Panel distribution for the chordwise direction is set to give a higher concentration of panels around the leading edge, as this is the area of highest pressure gradient. Two distributions were examined for the spanwise panels, an even distribution and one with sinusoidal distribution with higher panel density at the head of the sail. The resulting force output from the two cases are given in table 34, and altering the distribution of the spanwise panels made a 5% difference in the lift coefficient. As there is no theoretical case to compare this against, it is difficult to say which of the cases is more accurate. A constant spanwise distribution was used by Cant [10] in the analysis of a mainsail, and this distribution was chosen for the analysis of the sail geometries.

7.16 PALISUPAN in aeroelastic analysis

Grid generation programs to generate PALISUPAN input model definitions from grids of points have been developed and shown to give smooth PALISUPAN model definitions. The number of panels for the aeroelastic analysis of a rig will be set at $N_t = 64$, $N_s = 16$, to give a total number of panels of 1024, which will allow solution of the aerodynamic aspect of the aeroelastic solution in a suitable time. BMCC will be set at 1.0×10^{-4}, and the Kutta condition criteria will be set at 1.0×10^{-2}, as these values have shown to give

a low solution time whilst maintaining as accurate solution of the potential flow analysis for a given panel distribution.

8 Aeroelastic analysis

The generic structure of the aeroelastic solution method is shown in figure 75. The body to be analysed is defined by the finite element model of the body in its initial configuration. The points defining sail sections are extracted from the finite element model, and used as an input to the F-2-P-II program, which is used to generate a PALISUPAN model of the body, and then PALISUPAN is employed to calculate the pressure distribution over the body. The panel pressures calculated by PALISUPAN are used to calculate the loading on the finite element model, which is solved to obtain an updated configuration of the body. The updated configuration is then used to generate an updated PALISUPAN model, and this loop is continued to obtain a solution.

The solution strategy for the aerodynamic analysis will depend on the stability of the model being considered. A well restrained model, such as a rectangular membrane restrained along all sides gives a stable solution without employing velocity stepping, and looping between the potential flow and structural analysis gives a rapidly converging solution. As the models become less restrained, as in the free trailing edge rectangular membrane, the membrane is less stable under this aeroelastic solution method, and an alternative velocity stepping solution method used by Smith and Shyy [57] was implemented to ensure that membrane remains in a stable configuration throughout the solution path. The Stein-Hedgepath wrinkle model was implemented for the analysis of membranes by the aeroelastic method as described in section 8.5.1.

8.1 Development of the aeroelastic solution method

The first case to be analysed using an aeroelastic solution method was an initially flat rectangular membrane of aspect ratio 5 and chord of 1 metre fully restrained around the perimeter, as this model had been used in the PALISUPAN investigations described in the previous chapter. Analysis of this model allowed development of the solution method and program structure to be employed for the subsequent aeroelastic analysis of a mast sail structure. The membrane was analysed in a flow with free stream velocity of 5m/s with $\alpha = 10°$. The membrane was analysed with a Youngs modulus of 3.0125×10^6, giving an aeroelastic number of 3.4. The Poissons ratio was set at $\nu = 0.5$.

8.2 Calculation of finite element pressure loading

PALISUPAN can be set to output a file containing the pressure and centroid for each of the panels used in the analysis. The data from this file is used to calculate the pressure loading on the finite elements representing the body. A program to obtain the pressure loading for an arbitrary finite element mesh, P-2-F was developed using the structure shown in figure 76. The PALISUPAN panel output is ordered as a series of strips of panels, running from the trailing edge along the suction surface, then back along the pressure surface in the chordwise direction, at increasing x_3 values along the span. The number of panels in each chordwise strip can be obtained from the N_t parameter used to generate the PALISUPAN input model. As an even number of panels is employed in the discretisation of the PALISUPAN input model, the strip can be split into the suction and pressure surfaces of the strip with half the panels on each surface. The strips are assumed to be

at a constant x_3 value, and the pressure data is used to generate a set of cubic splines of the pressure for each of the suction and pressure surfaces with respect to the x_1 coordinate of the panel centroid.

In order to calculate the pressure loading on a finite element, the centroid of the finite element is calculated from the deformed node positions defining the element. The PALISUPAN panel strip with the closest x_3 value to the element centroid is used to calculate the pressure on the element. As the PALISUPAN model is truncated at the tip of a triangular sail model, the top most panel strip is used for the calculation of the pressures of all elements above this level in this case. The pressure coefficient for the suction and pressure surfaces, C_p^s and C_p^p are calculated from the appropriate spline curve at the x_1 location of the finite element centroid. Pressure loading for the element is then calculated according to equation 141, where A_e is the area of the finite element.

$$q_e = \frac{1}{2}\rho V_\infty^2 A_e (C_p^p - C_p^s) \tag{141}$$

8.2.1 FENLA3-3 analysis of a rectangular membrane

FENLA3-3 was used to analyse a rectangular membrane of aspect ratio 5 under a constant pressure loading, to ensure that the finite element analysis mesh is appropriate for the high aspect ratio membranes. The material properties used were $E = 1.2 \times 10^5 N/m^2$, $\nu = 0.5$. The membrane was 1 metre by 5 metres, under a load of $15 N/m^2$. This gives an aeroelastic number of $\Pi = 2$, and a theoretical prediction from Seide [53] of central deflection of 0.1729 metres. A symmetrical finite element mesh, of the same format as shown in figure 78, with 500 elements was used to analyse the membrane. The deflection predicted by FENLA3-3 was 0.1750, a 1.2% error compared to theory, and this gives confidence in the format of the finite element mesh

being employed for the aeroelastic analysis.

8.2.2 Aeroelastic solution structure

The aeroelastic program, MONSTA1 contains the P-2-F load calculation program, a non linear finite element analysis program based on the FENLA3-3 membrane program and the F-2-P-II model generation program. Communication between PALISUPAN and the aeroelastic program, MONSTA1 is carried out using data files, and the loops of the aeroelastic solution are controlled by a batch file. The data files used by the program are listed below:

- command file - contains data used for generation of the PALISUPAN model and load calculations from the PALISUPAN log file
- FE data file - contains the finite element model data
- FE displacement file - contains the displacements of the finite element model nodes
- PALISUPAN input file - PALISUPAN model data
- PALISUPAN log file - PALISUPAN output pressure data used to calculate the finite element model loading

For the first loop of the program, the pressure calculation and finite element analysis sections of MONSTA1 are skipped, and the initial PALISUPAN input file is generated using the finite element model and data contained in the control file by the P-2-F-II model generation program. A PALISUPAN analysis is then carried out on the initial membrane shape. The pressure data from this is used to apply loads to the finite element program. The finite element program uses a number of load steps defined within the finite element data file, iterating at the last load step to the defined convergence

tolerance. The deflected membrane shape is used to generate a new PALISUPAN model and the node displacements are output to a file. In subsequent loops of the program, the node displacements are read in from the file and define the node initial displacements at the start of the finite element load steps. The finite element program has a Total Langrangian formulation, and so all quantities are referred to the initial coordinates of the model at the start of the aeroelastic analysis, which remain in the finite element model data file. Iteration between the finite element and fluid models continues up to a pre-set number defined in the batch file used to run the analysis. The convergence checking method used in the finite element analysis section of MONSTA1 was the checking of individual degree of freedom percentage change in displacement against a defined convergence limit as described in section 6.4.10.

8.2.3 FENLA modifications

The finite element analysis program, FENLA, was modified for use in the iterative loop with PALISUPAN. The node displacements, ${}^{t}u_i^n$ are stored in a file at the end of the finite element analysis for each iterative loop before the MONSTA program exits. This allows the initial model definition to be maintained in the finite element data file, so allowing the Total Langrangian formulation to be employed throughout the loops of the aeroelastic analysis. Displacements of the nodes are zero at the start of the first loop, and so for this case the ${}^{t}u_i^n$ are not read in from the file and instead are initialised to zero. Initial stress is used for the first load step for the first loop only, as the finite elements will have initial stress due to the node displacements for subsequent loops. Element pressures are calculated from the PALISUPAN output data, and so it is no longer necessary to read in the element pressures

from the finite element model data file.

8.2.4 Output

The data visualisation program, AVS was used to check the solutions obtained from the aeroelastic analysis. A data file in the AVS format was output by MONSTA1 at the end of each iterative loop, containing the deformed shape of the model, along with the node displacements and element stresses.

8.2.5 Problems encountered during development

During the analysis of the rectangular membrane, a number of problems were identified with the MONSTA1 program. It was noticed that the wake sheets did not always finish with the end slope in the direction of the free stream. Three points were added to the wake curve definition, as described in section 7.11 to overcome this problem. During some of the solution attempts of the rectangular membrane, a saddle point appeared in the deformed shape of the sections used for the PALISUPAN model generation. This results in an error in the application of the artificial thickness, as the principle normal direction switches to the opposite direction over these points, resulting in a incorrect definition of the PALISUPAN input section of the form shown in figure 79. To ensue that the F-2-P-II program can deal with arbitrary shaped sections, the normal calculation for all points on the surface was altered to the one previously used for straight lines using the cross product of vectors on the sail surface, as described in section 7.6.1.

To enable the solution history to be examined during the aeroelastic analysis, a routine was inserted into the MONSTA1 program which outputs the PALISUPAN global forces and the deflection of a salient point of the model

(for the restrained membrane the mid point deflection was output) to a results file at the end of each of the MONSTA1 runs.

8.2.6 Results of MONSTA1 analysis of initially flat rectangular membrane

A rectangular membrane was analysed using a PALISUPAN grid of $N_t = N_s = 50$, with 10 points used to define both the surfaces and leading edge of the PALISUPAN input model sections. A symmetric triangular finite element grid of the form shown in figure 78 with 500 elements was used for the structural analysis, using 20 load steps and a convergence limit of 0.001, and 10 loops of the aeroelastic solution were used. A solution was obtained for the model with a rapid convergence. The deflection of the mid-point of the membrane obtained after each iterative loop is shown in figure 80. The deflection obtained after 3 loops is within 3% of the value obtained after 10 loops, and it can be seen that the analysis rapidly reaches convergence.

8.2.7 Effect of PALISUPAN model panel density

A series of membranes were analysed using PALISUPAN mesh densities from 600 to 2500 panels, using 500 finite elements for the structural model. The grid used all had equal numbers of panels in the chord and spanwise directions. The results are presented in table 35, and the central deflection is plotted against number of panels in figure 81.

The panel density has a small effect on the central deflection. Increasing the panel density from 600 to 2500 changes the central deflection by only 7%, and a grid with 1225 panels gives central deflections to within 3% of the value obtained using 2500 panels.

8.2.8 Effect of finite element mesh density

The PALISUPAN mesh using 1225 panels was used to examine the effect of the finite element mesh density. A number of meshes with 320 to 3920 elements were analysed. These were all of the same format as shown in figure 78. The results are given in table 36, the lift coefficient is plotted against the number of panels in figure 82, and the central deflections are plotted in figure 83. The oscillation of the central deflection graph is due to the fact that for models with an even number of elements along the short side, there is no node in the center of the membrane, and in these cases, the central deflection of the membrane was taken as the deflection of the nearest node.

The results of the aeroelastic analysis are only very weakly dependent on the number of finite elements used. The lift coefficient results vary by only 1.7% across the range of meshes used, and central deflections vary by only 1.2%. Neither of these quantities have any strong trend with the number of elements. If meshes with 500 elements or more are considered, the central deflections vary by only 0.6%.

8.3 Analysis of membrane with free trailing edge

As a step towards a triangular sail model, a membrane with a free trailing edge was analysed. A 2500 panel PALISUPAN grid and 500 element finite element model were used to model a membrane with $\Pi = 10$ as in the previous, fully restrained cases. The finite element analysis would not produce an iterated solution in the first iterative loop. The deflections seemed to have converged after the 20 load steps (to less than 1% change per load step for a central strip of nodes over any degree of freedom), but during the it-

eration within the finite element analysis the solution became unstable and eventually exploded. The number of load steps was increased to 40, but no improvement was found. To attempt to obtain a solution, the finite element analysis was altered to just use the 40 load steps without iteration on the final load step. This produced a solution for the first loop with a realistic deflected shape and deflections of up to 0.35 metres in the x_2 direction at the center of the trailing edge. However, during the second loop, the finite element solution was extremely distorted and the analysis was halted. The PALISUPAN results for the second loop resulted in primarily negative pressures on the elements. Since the elements had deformed to support a positive pressure, obtained from the first loop, this caused the model to become unstable. This indicates that the application of the full free stream velocity on the undeformed model is not a suitable solution method for the membrane with a free trailing edge.

The finite element analysis of the membrane will produce a model that is in equilibrium with the applied loading. However, for the free trailing edge membrane case the model deforms enough to significantly change the fluid flow over the membrane in the first iterative loop and hence the membrane is too far from the equilibrium position with the updated pressures to allow a stable solution to be obtained. As the finite element formulation is based on the use of load steps, it is logical to extend this to using a velocity stepping procedure for the aeroelastic analysis as used by Smith and Shyy [57].

8.4 MONSTA2 analysis of rectangular membrane with free trailing edge

The velocity increment solution strategy was implemented in the MONSTA2 aeroelastic program. Freestream velocity is increased in a number of velocity

steps, and the initial shape of the membrane is analysed using PALISUPAN for the first velocity increment. The resulting pressures are used to calculate a deformed membrane shape, which is then analysed by PALISUPAN using the incremented free stream velocity. This analysis provides the loading for the next finite element load step. In this manner, the calculated membrane shape will be close enough to equilibrium at the end of each velocity step to give a stable solution path. At the final velocity step, the aeroelastic solution loop is carried out until convergence of the node displacements is obtained.

The model used for the aeroelastic analysis of an initially flat membrane with free trailing edge is a rectangular membrane with aspect ratio of 2 and 1 metre chord. This was chosen as the case had been analysed by Smith and Shyy [57], which enables a comparison could be made with the mid point deflection obtained from a plot of the deformed shape of the membrane. Using this model also allows a higher number of elements along the chordwise direction of the model for a similar number of nodes (and hence solution time) as the membrane with aspect ratio of 5, without having higher aspect ratio elements. This will improve the section definition used to generate the PALISUPAN model. The membrane has an aeroelastic number, Π_1 of 15 with $\alpha = 15^o$ and $\mu = 0.5$. A free stream velocity of $5m/s^2$ was used, giving a Youngs modulus of 1.0167×10^8. The finite element mesh used a symmetrical distribution of triangular elements, shown in figure 84.

8.4.1 MONSTA2 convergence criteria

The convergence criteria for the model was altered to the criteria used by Smith and Shyy [57]. The displacement increments calculated by the FE method were non-dimensionalised with respect to the model span, and summed

over all degrees of freedom in the model to give a residual, R, equation 142.

$$R = \sum_{k=1}^{N} \sum_{i=1}^{3} \frac{\Delta u_i^k}{b} \tag{142}$$

The value of the residual is compared to the convergence value obtained from the finite element data file. If the residual is less than this value, the MONSTA2 program causes the batch file to stop the iteration between the PALISUPAN and MONSTA programs.

8.4.2 Analysis results

The aeroelastic analysis program was run with a convergence criteria of 0.0001, using 200 velocity steps. A PALISUPAN panel density of $N_t = 40$, $N_s = 20$ was chosen for the aeroelastic analysis, from the experience gained with the PALISUPAN sensitivity studies on a curved membrane to give a good compromise between computational time and accuracy. An initial stress value of 100 N/m^2 resulted in a failure after 4 velocity steps. The displacement history of the node at the center of the trailing edge suggested that this was due to the initial stress being too high, as the displacement of the node became negative after the second velocity step. High initial stress in the elements lead to a small displacement and hence small stress in the element for the first velocity step. This was confirmed by examining the AVS output file from the MONSTA program, which shows that the element stresses are less than 10 N/m^2 after the first velocity step. When the initial stress is removed on the second velocity step, the element stress is too small for the pressure loading applied, and the membrane becomes unstable. Initial stress was reduced to 10 N/m^2, and the solution failed after 11 steps. When the initial stress was reduced to 5 N/m^2, a successful solution was obtained, with only two iterations required to obtain convergence. The convergence

criteria was reduced to 1×10^{-10}, and the analysis continued. The residual remained between 5×10^{-6} and 5×10^{-5} for 550 iterations, at which point the analysis was stopped. It was noted that the PALISUPAN results were oscillating slightly, and the analysis was restarted using the same PALISUPAN result file for subsequent FEA analyses. The residual then reduced to 1.45^{-12} within 2 iterations, and remained at exactly the same value (to the output accuracy of 8 significant figures) for the next 10 iterations, at which point the analysis was finally stopped.

Results obtained from the aeroelastic analysis of the free trailing edge membrane gave a solution that converged and had the shape that would be expected from this problem. The central point of the trailing edge deflected by 0.0326 metres. This shows good agreement with the value obtained from the deformed plot of the membrane analysed by Smith and Shyy [57] of 0.033 metres.

8.5 Initially flat triangular membrane

The next stage in the development of an aeroelastic model of a yacht rig was analysis of an initially flat triangular membrane. The triangle has an aspect ratio of 4, $\Pi_1 = 17$, $\alpha = 20^o$ and $\nu = 0.5$. In this case a triangle of 2 metres height and a 1 metre base chord was chosen. The incident flow was chosen as $v_\infty = 5m/s^2$, which gives $E = 153.53 \times 10^6$ for $\Pi_1 = 17$. A grid generation program was written, which generates models defining the initial model geometry with the required finite element mesh density. General element layout is illustrated in figure 85, and the model has the same number of elements along the foot and the luff of the membrane, resulting in an element aspect ratio of up to 4. This aspect ratio is quite high, and future models were altered to avoid this. PALISUPAN models the sail without the

tip, as the quadrilateral elements used within it cannot mesh this area. The PALISUPAN model generation program was altered to only use a set number of finite element sections (obtained from the command file) to generate the PALISUPAN model, which truncates the triangle to form a quadrilateral body for the potential flow analysis. Usually this will be set to 2 less than the number of finite element sections defining the model, but this may vary according to the mesh density.

A model using 20 elements per side for the finite element mesh and a PALISUPAN grid of $N_t = 40$, $N_s = 20$ was used to analyse the membrane. Convergence was set to 0.0001, and 200 velocity steps were used. Attempts to obtain a solution of the initially flat triangular membrane resulted in failure of the model. A range of initial stresses was used, and with it set to $10N/m^2$, the solution failed after 3 steps. Decreasing initial stress to $5N/m^2$ resulted in failure after 4 steps, and $2.5N/m^2$ failed after 2 steps. In most cases, a large deflection occurred within the sail, and this then resulted in the model generation for PALISUPAN producing an diverging model for the next load step.

The failure of the sail model could be due to compressive stresses developing in the sail during the solution, which would lead to an ill conditioned stiffness matrix. Widespread compressive stresses will result in the stiffness matrix becoming singular [46] [57] and the solution will fail. The Stein-Hedgepath wrinkle model was incorporated in the finite element program to allow solution of models which could exhibit wrinkling behaviour.

8.5.1 Membrane element wrinkle model

The Stein-Hedgepath wrinkle model [37] is a numerical implementation of the Stein Hedgepath continuum theory [58]. The theory is based on the experi-

mental observations that when in a wrinkled state, a membrane will contract more in the direction normal to a wrinkle than predicted by the Poissons ratio effect. In order to incorporate these geometric features of wrinkling, the local effective Poissons ratio is increased in the wrinkled regions. This effective value of the Poissons ratio is determined by imposing a locally uniaxial stress state in the wrinkled region in the direction of the first principle stress, and this results in the effective Hookean material properties becoming dependent on the local state of strain.

The numerical algorithm assigns an element one of three constitutive matrices depending on whether the element is in a slack, wrinkled or taut state. The element state is calculated using the principle strains in the element as shown in equation 143, where $\epsilon_{1,2}$ are the ordered principle strains, and the relevant matrices for slack $\mathbf{C}_s$, wrinkled $\mathbf{C}_w$ and taut $\mathbf{C}_t$ elements are given in equations 144 to 146.

$$\mathbf{C} = \begin{cases} \mathbf{C}_s & \epsilon_1 \leq 0 \\ \mathbf{C}_w & \epsilon_1 \geq 0 \text{ and } \nu\epsilon_1 < -\epsilon_2 \\ \mathbf{C}_t & \text{otherwise} \end{cases} \tag{143}$$

$$\mathbf{C}_s = [0] \tag{144}$$

$$\mathbf{C}_w = \frac{E}{4}\begin{bmatrix} 2(1+P) & 0 & Q \\ 0 & 2(1-P) & Q \\ Q & Q & 1 \end{bmatrix} \tag{145}$$

$$P = \frac{\epsilon_{11} - \epsilon_{22}}{\epsilon_1 - \epsilon_2} \quad Q = \frac{2\epsilon_{12}}{\epsilon_1 - \epsilon_2}$$

$$\mathbf{C}_t = \frac{E}{1-\nu^2}\begin{bmatrix} 1 & \nu & 0 \\ \nu & 1 & 0 \\ 0 & 0 & (1-\nu)/2 \end{bmatrix} \tag{146}$$

8.5.2 Calculation of principle strain

The element strain state is two dimensional in the element plane, and a geometric transformation using Mohr's circle can be used to calculate the principle strains from the element strain components in the element local coordinate system according to equation 147.

$$\epsilon_{prin} = \frac{\epsilon_{11} + \epsilon_{22}}{2} \pm \left[\left(\frac{\epsilon_{11} - \epsilon_{22}}{2} \right)^2 + (\epsilon_{12})^2 \right]^{1/2} \tag{147}$$

8.5.3 Implementation of the Stein-Hedgepath wrinkle model

The Stein-Hedgepath wrinkle model was incorporated into the MONSTA2 aeroelastic analysis solution. Element strain state is calculated during the evaluation of the stiffness matrix. For the first velocity step, the element is taken as being in a taut state, $\mathbf{C} = \mathbf{C}_t$, and the element stress is set at the initial stress value. For subsequent velocity steps, the element strain state at the start of the step is used to calculate the element principle strains, and the constitutive matrix is chosen based on these strains according to algorithm developed by Millar and Hedgepath [37], described in section 8.5.1. Element stresses are then calculated and used in the evaluation of the stiffness matrices. The element state for each element is output to the node displacement file at the end of the velocity step, which allows these values to be input at the start of the next velocity step. The updated element state is compared to the element state at the start of the velocity step, and a flag in the element data structure is set to 1 if the element has changed state, and 0 if the element stress state has remained constant.

The wrinkle model normally requires iteration to obtain the correct stress state throughout the model, as a change in element state will result in the stiffness matrix for the model changing. Since the program uses a large

number of explicit steps to full velocity, no further loops within the finite element scheme were used for the initial implementation of the wrinkle model in the aeroelastic solution. This was found to give a stable solution for the rectangular membrane analysis, where the number of elements changing stress state is employed to provide an additional convergence check during the solution of the final velocity step. Further development of the aeroelastic solution method for the initially flat triangular sail required iteration within the velocity stepping procedure to provide a stable solution when using the wrinkle model.

8.6 Wrinkle model analysis of the rectangular membranes

The fixed and free trailing edge rectangular membranes were analysed for incident flow of $\alpha = 15^o$ and $\Pi_1 = 15$, using the wrinkle model described above. Deflections for the center of the membrane (fixed trailing edge) and central point of the trailing edge (free trailing edge) are given in table 37 for 100 and 200 velocity steps, and compared to the values obtained without the wrinkle model. The finite element analysis with no wrinkle model predicted higher deflections in both the free and fixed trailing edge cases. About half the elements in the free trailing edge case were in a wrinkled state, with the remaining elements taut. The fixed trailing edge case converged to $R < 0.0001$ within 4 iterations. The free trailing edge case had 4 elements changing from taut to wrinkled state during the iterative stage of the analysis, and due to this the residual was of the order 10^{-3} to 100 iterations, where the analysis was stopped. Deflections of the mid point of the trailing edge for these cases had converged to 0.001% (the accuracy of the deflection output in the batch file) within 5 iterations, and the solution had converged with the exception

of two small areas at mid chord towards the tips of the membrane, which were changing state from taut to wrinkled.

8.7 Wrinkle model analysis of initially flat triangular membranes

The finite element mesh used for the analysis of the triangular membrane was altered to reduce the aspect ratio of the finite elements. An example of the grid used is shown in figure 86. Initial attempts to analyse the triangular models resulted in failure.

The wrinkle model used in the MONSTA2 program calculated the element state according to the strain in the element after the previous velocity step. If elements are changing state, this could result in a model that is not in equilibrium at the end of the velocity step. Millar [37] notes that an iterative solution is required within each loading step for the model to reach an equilibrium state (both in terms of element states and global equilibrium) before advancing to the next load step. The MONSTA2 program did not implement this, as it was thought that the large number of velocity steps used would not result in many state changes at each velocity step. This was not the case for the triangular membrane, in particular for the first few velocity steps where most of the elements were changing shape, and this proved to be the reason for the failure of the triangular membranes when analysed using MONSTA2.

An iterative solution was implemented within MONSTA. The finite element calculations were repeated at each velocity step, using a constant loading obtained from the PALISUPAN analysis at the start of the velocity step. The number of elements changing state for each iteration was calculated, and the model reached a converged state when there were no elements

changing state. At this point the aeroelastic analysis moves on to the next velocity step. Since the pressure loading is obtained from the initial shape of the model at the start of the velocity step, the aerodynamic and structural loads may not be in equilibrium at the end of the velocity step, but discrepancies should be insignificant due to the large number of velocity steps. Re-calculation of the pressures at each finite element iteration during the velocity stepping would result in a prohibitive increase in solution time. The potential flow solution takes more computational time than the finite element analysis, around 180 seconds compared with 10-60 seconds for a model with similar numbers of finite element and PALISUPAN panels. The analysis using this solution method takes around 12 hours for a typical model, and re-calculation of pressures using PALISUPAN at each iteration would increase this to the region of 48 hours. The solution method used here gave stable converging solutions without a prohibitive increase in computational time.

A series of triangular models with increasing finite element mesh density were analysed using the revised aeroelastic solution method. The PALISUPAN grid used had a panel density of $N_t = 64$ and $N_s = 16$, which was found to give a good compromise between solution time and accuracy in the PALISUPAN sensitivity study on a deformed triangular membrane. The analysis used 100 velocity steps, with an finite element iterative residual limit of 1.0×10^{-5}. Results of the analysis are given in table 38, and lift coefficient of the body and deflection of the center of the sail are plotted against the number of finite elements in figures 87 and 88. The solution converges as the number of elements is increased.

8.8 Rig analysis

The 16 node solid elements were incorporated into the aeroelastic model in the program MONSTA3. The model data structure was altered to store arrays of three node triangular membrane elements and 16 node solid elements. A data structure for material properties was created, and the model material properties were stored in an array of these, with each element containing a pointer to the element material property entry appropriate to it as defined in the finite element data file. Stiffness matrix contributions were calculated for the membrane elements and then the solid elements and assembled into the model stiffness matrix as described in chapter 6. Internal loading contribution from each element was calculated according to the element type and assembled into the loading vector. The pressure loading on the mast was assumed to be zero for the rig analysis carried out here. Sail pressure loading was calculated using a modified version of the P-2-F program, where the PALISUPAN section panels defining the mast were not considered in the generation of the pressure spline curves for the sail element pressure loading calculations.

8.8.1 Program execution

The data files used by MONSTA3 are listed below. A description of the file structure for the data and control files are listed in appendix C.

- FE data file. This contains the finite element model definition at the start of the analysis.
- Control file. Contains parameters used in the creation of the PALISUPAN model and calculation of the element pressures.

- Displacement file. At the end of each MONSTA3 run, the node displacements, followed by the current element states are written to this file.

- Residual file. The current residual value is output to this file at the end of each MONSTA3 run, so that it can be input for the MONSTA3 run of the next iterative loop. This is to enable dynamic relaxation where required.

A velocity stepping procedure is used for the solution of the rig analysis, with a batch file used to run MONSTA3 and PALISUPAN through the solution path. MONSTA3 is run with two arguments, the velocity step and iteration number. For the start of the analysis, MONSTA3 is run with both the velocity step and iteration number set to 0. The finite element model data is input, and the program skips the pressure calculation and finite element analysis and generates a PALISUPAN input file for the first velocity step according to the settings in the control file. This model is analysed by PALISUPAN, and the results file containing the global force coefficients, panel centroids and pressures is used to calculating the element pressure loading. An iterative solution to the finite element analysis using a constant pressure loading is used to calculate a deformed shape with the element stress states converged (no elements change state). At this point the deformed shape is used to generate the PALISUPAN model for the next velocity step. This procedure continues until the final velocity step.

For the final velocity step, an iterative solution is carried out, looping between the finite element and PALISUPAN analysis. MONSTA3 solves the finite element analysis of the model, again iterating using a constant pressure loading until the element stress state has converged. The deformed shape is then analysed by PALISUPAN to obtain updated pressure loading.

During the iterative solution, the residual is calculated at each finite element iteration, and when this reduces below the convergence criteria the aeroelastic analysis is complete.

During the solution path, the PALISUPAN global force coefficients, deflections of salient points (mast tip and mid point of the trailing edge), number of elements changing state and residual magnitude are output to a results file after each iteration of the finite element program. The deformed model shape, node displacements, element stresses, stress state and whether the element stress state has changed can be output in the AVS visualisation program format at user defined intervals (usually at the end of each iteration at the final velocity step) is output to file to enable graphical representation of the solution.

The aeroelastic program has the capability of using dynamic relaxation to improve the stability of the solution. Two relaxation factors, β_1 and β_2 are defined in the finite element data file. After solution of the finite element equations and calculation of the model residual, node displacement increments are multiplied by β_1 if the residual has reduced from the last finite element analysis, and β_2 if the residual has increased. A solution with no relaxation can be obtained by setting $\beta_1 = \beta_2 = 1.0$.

8.8.2 Calculation of mast compression

Stress components are calculated at the integration points and converted to Cachy stress components following the methods of section 6.9.3. The Cachy σ_{33} components are then integrated over the element and divided by the element volume to give a compressive stress in the mast element.

8.8.3 Rig models

The rig analysed using the MONSTA3 program has a mast height of 2 metres, and a sail foot length of 1 metre. In order to represent a typical yacht rig configuration, the mast should be restrained at the base, and the sail restrained at the clew. The first series of models, rig1, were fully restrained along the foot of the sail as well as at the base of the mast. Increasing the restraint on the model in this manner results in a more stable solution, which is suitable for initial development of the solution methods for the rig analysis. The sail is meshed using the same arrangement as in the sail analyses described in section 8.7, and an example of the rig geometry is shown in the side view of a deformed rig model in figure 93. The mainsail on a yacht has a bolt rope sewn into the luff of the sail, and this is held inside a track on the mast. It is possible for the sail to slide up and down the mast track, but in the upwind sailing condition, the forces generated by the mainsail combined with the friction between the bolt rope and mast track mean that there is very little movement. To simplify the rig model and to allow the mast and sail to be modelled as a single entity, the sail is assumed to be attached to the mast at the luff in this analysis.

The Youngs modulus used for the sail of 153 MPa, chosen to give an appropriate aeroelastic number, is about 0.6% of the value of a realistic sail material modulus [52] of 25 GPa. To obtain realistic structural interaction between the sail and mast in the aeroelastic model, a Youngs modulus of 1.0 GPa was chosen for the mast material, which is 0.5% of the Youngs modulus of aluminium. The resulting mast will be stiffer than a real case, as the mast section is solid as opposed to a hollow section, but in a yacht rig the mast is supported by rigging which reduces the deflections of the rig, and this value was taken to be appropriate for the analysis conducted here. The mast

material Poissons ratio was set as $\mu = 0.3$. A further series of rig models analysed, rig3, have a free foot with the clew and mast base restrained using the same mesh arrangement as the rig1 models. The model mesh density is defined by the number of elements along the sail foot, so the rig1-10 model has 10 elements along the foot and 20 elements defining the mast.

In order to simplify the model, the mast is assumed to be restrained at the level of the foot of the sail. A typical rig will have the clew of the sail supported by a boom which is attached to the mast at the level where the mast is restrained in the rig model. Including the boom in the analysis of a rig would increase the number of nodes required for the solution, and hence increase the solution time and the complexity of the model. As the analysis is aimed towards an understanding of the compression loads induced in the mast due to the support of the sail the boom was not considered in the rig analysis. The rig configuration used here approaches that used on some modern Open 60 class monohulls, where the boom is deck stepped, and the sail luff runs almost to the base of the mast.

The attachment of the sail to the mast on a yacht is normally achieved by the use of a mast track, allowing the sail to slide up and down the mast. In practice there is little movement of the sail once the sail is hoisted, as the friction in the track and forces generated by the sail on the luff restrict any movement, particularly in the upwind sailing condition being analysed. The sail is assumed to be fixed to the mast in the aeroelastic analysis, which allows the use of a single finite element model to define the mast and sail.

8.9 Aeroelastic analysis of the rig1 models

A series of rig1 models with increasing finite element mesh density were analysed using MOSNTA3 and PALISUPAN. The PALISUPAN panel density

was fixed at $N_t = 64$, $N_s = 16$ with 14 panels used around the mast.

Rig models with between 8 and 44 mast elements (which correspond to between 60 and 2280 sail elements) were analysed using 100 velocity steps, and a residual convergence criteria of 1.0×10^{-5}, with a maximum number of iterations set to 50. In practice, the residual of the mode only reduced to below the convergence criteria when changing sail element states resulted in the finite element analysis carrying out more than four or five internal loops. Recalculating the element pressures using PALISUPAN resulted in a residual of the order of 1.0×10^{-3} over the iterative solution path for the range of models tested. Analysis of the displacement history of the model showed that the displacement increments were of the order of 0.1% either side of a mean position after about 10 iterations. It was decided to leave the residual set at 1.0×10^{-5} to ensure that sufficient number of iterations would occur to ensure a converged solution. The rig1 analyses were carried out using $\beta_1 = 1.0$ and $\beta_2 = 0.5$.

The lift coefficient and mast tip displacements obtained from the aeroelastic analysis of the rig1 models are given in table 39. Lift coefficient and magnitude of the mast tip displacement are plotted against the number of finite elements in figures 89 and 90. The aeroelastic solution of the rig1 model converges as the finite element mesh density is increased. Solution time for the aeroelastic analysis ranged from 9 to 26 hours on a UNIX workstation.

8.9.1 Effect of the relaxation factors

The rig1-10 model was analysed using a range of relaxation factors as listed below:

- $\beta_1 = 1.0$, $\beta_2 = 1.0$
- $\beta_1 = 0.75$, $\beta_2 = 0.5$

- $\beta_1 = 0.5$, $\beta_2 = 0.5$ and $\beta_2 = 0.25$.

After completing 50 iterative loops the PALISUPAN force coefficients, mast tip displacements and displacement of the mid point of the trailing edge and centre of the membrane varied by less than 0.1% for all the cases. PALISUPAN force coefficients and mast deflections are given in table 40. Reducing the relaxation factors resulted in a longer solution time, but this technique can be used to obtain a stable solution without compromising the accuracy of the solution providing that sufficient iterative loops are carried out at the final velocity step.

8.9.2 Analysis of rig3 models

Loose foot sail models, rig3-14, rig3-16 and rig3-18 were analysed, and the results are given in table 41. The magnitude of the mast tip deflection is plotted against number of sail elements in figure 91, and the solution can be seen to be converging with increasing finite element mesh density as in the rig1 case. The rig3-18 meshes required relaxation factors of $r_1 = 0.5$, $r_2 = 0.25$ in order to obtain a converging solution, and consequently the solution time increased to over 20 hours.

8.10 Comparison of free and restrained mast cases

A finite element mesh density of 14 elements along the boom was chosen for comparative analysis of the aeroelastic solution methods, as this gave reasonable accuracy with a solution time of around 14 hours. A rig3 model with fully restrained mast, designated rig3R was generated and analysed using the aeroelastic solution method. A view of the deformed rig shapes obtained by the analysis are shown in figures 94 and 95 for the restrained

and unrestrained mast cases. The sail sections obtained for the restrained mast case, shown in figure 92 show a realistic deformed sail shape, as obtained by Smith and Shyy [57]. The bending of the mast in the unrestrained case has resulted in a reduction in the leech tension in the sail, and the top sections have twisted off. In this case, the sail has inverted over the top sections of the mast, resulting in an unrealistic flown shape. This indicates the importance of taking into account the coupled nature of the mast sail system, as the deformations of the mast significantly affect the sail shape. Previous aeroelastic analysis of a sail by Smith and Shyy [57] looked at an initally flat sail restrained along the mast track and obtained realistic deformed shapes as predicted by the restrained mast case here. Extension of the analysis to include mast deformations results in an unrealistic deformed shape.

8.11 Analysis of curved sail

Sails are designed to assume a flown shape with curvature even in the absence of loading. A curved sail model was generated with quadratic curves defining the sail cross section in the x_1, x_2 plane, using the same method as for the generation of the curved rectangular plates for PALISUPAN analysis, equation 139 for each section. The section camber, $x_2^{\max}$ is calculated according to equation 148 where x_3^{sec} is the section x_3 coordinate, and s is the span of the sail (equal to the height of the mast).

$$x_2^{\max} = k\frac{x_3^{sec}}{s} \tag{148}$$

Two models with 14 elements along the boom, having restrained and free masts, rig3CR and rig 3C, were analysed with the same material properties and flow fields as the rig3 and rig3R models. The deformed shape of the rigs is

shown in figures 97 and 96 for the free and restrained mast cases respectively. In the free mast case, the bending of the mast results in the twisting off of the upper part of the sail, and this effect can be seen by comparison of the leech shapes in figures 99 and 98. This effect can also be seen in by comparing the photographs of a mast sail model in a wind tunnel in figures 2 and 3, obtained during testing [33]. In figure 3, the tension in the mainsheet has been reduced. This results in a lower leech tension in the sail, and the top section of the sail has twisted off more than in figure 2. In these cases the change in leech tension is introduced through control of the mainsheet rather than as a result of mast bend, but the effect on the sail trim is the same.

The twisting off of the sail reduces the aerodynamic force coefficients predicted by the analysis, as shown by the comparison of the force components in table 42. This is as expected by experience in real life, and again shows the importance of modeling the coupled nature of the mast sail system. In the converged state of the rig model, the majority of the sail elements were in a wrinkled state, with some taut elements in the central area of the sail. This is due to the high levels of tension predicted from the clew to the head of the sail, with a much smaller tension predicted along the chord of the sail, which ties in with the reinforcement patterns placed in real life sails.

8.11.1 Comparison of mast stress calculations

In previous finite element analyses of masts (for example Cant [10], Enlund [12] and Hoffmeister [22]) the sail loading has been obtained from either potential flow or force balance on the yacht and applied to the mast using various distributions. In order to gauge the effectiveness of this method in calculating the mast compression, a series of non linear finite element analysis were made of a point loaded mast consisting of 28 elements. The mast

loading was obtained from the PALISUPAN global force coefficients from the aeroelastic solution of the rig3C-14 model, which allows a comparison with the compression calculated by the aeroelastic solution of the rig, and was applied to the mast using the following distributions:

1. Constant distribution;
2. Linear distribution : maximum at bottom of the mast, zero at the top;
3. Sinusoidal distribution : maximum at centre of mast, zero at top and bottom.

The mast compressive stresses obtained from these analyses and from the aeroelastic analysis of rig3C-14 are given in table 43. The compressive stress along the mast is plotted for the three load distributions in figure 100, and for the aeroelastic solution of the rig3C-14 model in figure 101.

The linear distribution of sail loads on the mast predicts 20% less mast compression at the foot of the mast compared to the constant or parabolic distributions. The loading in this case is concentrated at the foot of the mast, and as a result the mast does not deflect as much as in the other distributions. All three assumed distributions predict a similar variation in stress along the mast height. The stress predicted by the analysis of the mast under the aeroelastic analysis forces is only 5% of the values obtained from the aeroelastic analysis. In the aeroelastic analysis case, the deflections of the mast tip result in tension in the sail leech. This tension will introduce a compressive stress in the mast in order to satisfy equilibrium at the head of the sail, and as this is not modelled in the point loaded analysis of the mast, the compression is underestimated by a significant amount. Tip deflections obtained from the point loaded case are also significantly different to the aeroelastic analysis results. This shows the importance of the interaction

of the mast and sail in the rig analysis, and these interactions cannot be modelled by separate analysis of the mast and sail.

The finite element analysis of a mast by Cant [10] loaded the mast with sail forces obtained from a PALISUPAN analysis of the rig, applied using a linear distribution on the mast, and point loads obtained from sailing trials data. Although the mast deflections obtained from the analysis were within 10% of data obtained from trials, the compressive mast stress obtained from the analysis was found to be only 45% of the measured value. The results of the stress comparisons suggest that this discrepancy is partially due to the loading assumptions used in the finite element analysis, as the effect of the leach tension on mast compression is not accounted for. Cant [10] included forestay, rigging and halyard loads on the mast which also induce compression. As these values were obtained from sailing trials they were easily quantified, and the discrepancy in the predicted and measured compression is smaller than the difference obtained in the comparison of mast compression for the rig3C-14 case, due to the compression induced by the point loads.

9 Conclusions

An aeroelastic solution method for a mast sail system has been developed. It has been shown to predict realistic behaviour of the system when an initially curved sail is analysed.

A potential flow model is used to calculate the pressure loading on a mast sail system, which allows solution of the aerodynamic problem in an acceptable time scale. A panel code was chosen for the analysis, which enables the mast and sail to be analysed as a single body. A computer program has been developed to generate the input model for the potential flow analysis from a deformed finite element model. The distribution of panels for the models analysed was investigated in order to determine a suitable panel distribution which gives a good compromise between solution accuracy and run time of the analysis.

The Total Langrangian formulation for non-linear finite element analysis was found to be suitable for the analysis of a mast sail system. Three node triangular membrane elements, incorporating a wrinkle model algorithm have been implemented in the non-linear analysis, and the elements have been validated against a theoretical solution of large displacements of a rectangular membrane under uniform pressure loading. The three node triangular elements are capable of modeling an arbitrary initial shape of the membrane, allowing analysis of initially curved sail models. A sixteen node solid finite element was implemented in the non-linear analysis program to model the mast. These elements can represent a mast with circular or elliptical sections, and have been validated against the theoretical solution of large deformations of a thin beam.

A computer program to calculate the sail membrane element pressure loading from the results of the potential flow analysis was been developed.

This was incorporated with the non-linear finite element analysis and the potential flow model generation program to form an aeroelastic analysis program using the potential flow code to obtain the aerodynamic loading of the mast sail system. A velocity stepping solution method incorporating an iterative solution for the wrinkle model algorithm in the non-linear finite element analysis was used to obtain a solution to the aeroelastic problem. Dynamic relaxation was introduced to the aeroelastic solution method which has been shown to increase the stability of the solution, and have insignificant effect on the predicted sail forces and deflections.

An aeroelastic solution of a mast sail system was obtained, and compared to a solution obtained with a restrained mast. An unrealistic solution was obtained for a free mast case using an initially flat membrane. Analysis of an initially curved membrane, which more closely models a real life sail, predicted the twisting of the upper sail sections due to bending of the mast, a phenomena observed in mast sail systems in real life. Aerodynamic forces predicted by the model with a free mast were less than for a restrained mast case, due to the twisting off of the upper sections of the sail. This indicates the necessity of modeling the mast and sail together in the consideration of an aeroelastic solution of a yacht rig. The aeroelastic analysis of an initially curved sail shape results in a significant difference in calculated force and sail deformations compared to the initially flat case, and this indicates the importance of using membrane finite elements which can model the initially curved surfaces of yacht sails.

Comparison of the mast compression obtained from the aeroelastic analysis of a mast sail system with a previous method which distributes the sail loads along the mast shows that the uncoupled mast sail analysis predicts compression in the mast 95% lower than the aeroelastic analysis. This is

due to the interaction of the mast and sail, and in particular the effect of the leech tension on the mast compression. Failure to model this in an uncoupled system results in mast compression being underestimated.

The aeroelastic solution method developed inherently models the interaction of the mast and sail, which has been shown to affect both the predicted sail forces generated, the flown sail shape and the predicted mast compression. The use of distinct discretisations for the finite element and potential flow analyses enables the solution of the mast sail system. No quantative validation data for the aeroelastic solution of a mast sail system is available, but validation of the individual aspects of the solution method give confidence in the comparisons of aeroelastic analysis, and the solution method has been shown to model physical phenomena found in real life studies.

9.1 Future work

Generation of suitable validation data for the aeroelastic analysis of a mast sail system was beyond the scope of this project, and obtaining appropriate data would enable the quantitative results of the aeroelastic analysis to be validated. The method could be extended to account for the pressure loading on the mast, which although small in area compared to the sail, is located around the region of the rig where the highest pressure peaks are found. The inclusion of this loading could effect the mast deformations, and hence the deformations of the rig

The structure of the program has been developed to enable improved aerodynamic models to be incorporated into the aeroelastic analysis. Modern reinforced sails consist of reinforcing fibres which are sandwiched between membrane films. These structures could be analysed with the finite element method developed here, using rod elements for the reinforcement fibres and

membrane elements to represent the membrane films.

References

[1] I.H. Abbott and A.E. von Doenhoff. *Theory of Wing Sections.* Dover Publications, Inc, 1959.

[2] P. Atkinson. On the structural response of a mast sail system. In *International conference on Computer Aided Design for Small Craft - Sail and Power*, volume 1, May 1988.

[3] P. Atkinson and J.A. Szantyr. An integrated approach to the analysis of mast-sail systems. *Transactions of RINA*, 133:73–84, 1991.

[4] K-J. Bathe. *Finite Element Procedures.* Prentice Hall, 1996. ISBN 0-13-349679-X.

[5] K-J Bathe. Simulation of structural and fluid flow response in engineering practice. *Computer modelling and simulation in Engineering*, 1(1):48–75, 1996.

[6] K-J Bathe and S Bolourchi. Large displacement analysis of three dimensional beam structures. *International Journal for Numerical Methods in Engineering*, 14:961–986, 1979.

[7] K-J Bathe, E. Rahm, and E. Wilson. Finite element definitions for large deformation analysis. *International Journal for Numerical Methods in Engineering*, 9:353–386, 1975.

[8] F. Bethwaite. *High Performance Sailing.* Waterline Books, 1993. ISBN 1-8531-0337-3.

[9] D. Boote. Mast and rigging design. In A. Shenoi A. Claughton, J. Wellicome, editor, *Sailing Yacht Design, Theory*, pages 191–214. Addison Wesley Longman Limited, 1998.

[10] C. Cant. Aerodynamic and structural analysis of a rotating and canting wingmast. BEng, University of Southampton, 1999.

[11] M. Caponnetto and B. Bonjour. Sailing yahct design using advanced numerical flow techniques. In *The Fourteenth Chesapeake Sailing Yacht Symposium*, pages 97–104, 1999.

[12] H. Enlund, A. Pramila, and P.-G. Johansson. Calculated and measured stress resultants in the mast and rigging of a Baltic 39 type yacht. OBTAINED from the Wolfson Unit, Southampton University.

[13] R.G.J. Flay and P.S. Jackson. Flow simulation for wind tunnel studies of sail aerodynamics. *Journal of Wind Engineering and Industrial Aerodynamics*, 41-44:2703–2714, 1992.

[14] T. Fukasawa. Hydroelastic responses of a membrane structure in waves. In W.G. Price, P. Temarel, and A.J. Keane, editors, *Dynamics of Marine Vehicles and Structures in Waves*, pages 147–155. Elsevier, 1991.

[15] T. Fukasawa and M. Katori. Numerical approach to aeroelastic responses of three dimensional flexible sails. In *The Eleventh Chesapeake Sailing Yacht Symposium*, pages 87–105, 1993.

[16] H. Grandin, Jr. *Fundamentals of the Finite Element Method.* Macmillan, 1986.

[17] S. Greenhaulgh, H.C. Curtiss, and B. Smith, Jr. Aerodynamic properties of a two dimensional inextensible flexible airfoil. *AIAA Journal*, 7(22):865–870, 1984.

[18] P.S. Han and M.D. Olsen. Interactive analysis of wind-loaded pnumatic membrane structures. *Computers and Structures*, 25(5):699–712, 1987.

[19] T.K. Hellen. Effective quadrature rules for quadratic solid isoparametric finite elements. *International Journal for Numerical Methods in Engineering*, 4:597–600, 1972.

[20] J. Hess. Panel methods in computational fluid dynamics. *Annual Review of Fluid Mechanics*, 22:255–274, 1990.

[21] M. Hobbs. Finite element analysis of a 60 foot open class trimeran rig. Msc, Southampton University, 1996.

[22] H. Hoffmeister. Stability and strength analysis on yacht rigs with crp spars. In *International Conference on the Modern Yacht.* RINA, 1998.

[23] J.T. Holden. On the finite deflections of thin beams. *International Journal of Solids and Structures*, 8:1051–1055, 1972.

[24] V.S. Holla, K.P. Rao, C.B.Asthana, and A. Arokkiaswamy. Aerodynamic characteristics of pretensioned elastic membrane rectangular sailwings. *Computer methods in Applied mechanics and Engineering*, 44:1–16, 1984.

[25] B.M. Irons. Quadrature rules for brick based finite elements. *International Journal for Numerical Methods in Engineering*, 3:293–294, 1971.

[26] P.S. Jackson. Two dimensional sails in inviscid flow. *Journal of Ship Research*, 28(1):11–17, 1984.

[27] P.S. Jackson and G.W. Christie. Numerical analysis of three dimensional elastic membrane wings. *AIAA Journal*, 25(5):676–682, 1987.

[28] P.S. Jackson and S.P. Fiddes. Two dimensional viscous flow past flexible sail sections close to ideal incidence. *Aeronautical journal*, pages 217–225, 1995.

[29] Yogesh Jaluria. *Computer Methods for Engineering.* Allyn and Bacon, Inc, 1988. ISBN 0-205-11414-8.

[30] R.M. James. On the remarkable accuracy of the vortex lattice method. *Computer methods in Applied mechanics and Engineering*, 1:59–79, 1972.

[31] J.G. Ladesic and R.K. Irey. An experimental investigation of yacht sail aerodynamics. *AIAA monographs*, 29:28–50, 1983.

[32] H. Lamb. *Hydrodynamics.* Cambridge University Press, 1932. Sixth edition.

[33] D. le Pelley, P. Mancebo, and R. Smith. A technical proposal for the design of an IACC yacht for the year 2000. Meng, University of Southampton, 1998.

[34] L.Larsson and R. Eliasson. *Fundamentals of Yacht Design.* Adlard Coles Nautical, 1995. ISBN 0-7136-3855-9.

[35] N.J. Locke, P.S. Jackson, and R.G.J. Flay. Lift and drag distributions of yacht sails using wake surveys. *Journal of Fluids Engineering*, 118:346–351, 1996.

[36] R.H. Mallett and P.V. Marcal. Finite element analysis of nonlinear structures. *Journal of the Structural Division of ASCE*, 9:2081–2105, 1968.

[37] R.K. Millar and J.M. Hedgepath. An algorithm for finite element analysis of partly wrinkled membranes. *AIAA Journal*, 20(12):1761–1763, 1982.

[38] C.J. Mitchell. Computer aided analysis of yacht rigs. In *Conference on Yachting Technology*. University of Western Australia, January 1986.

[39] C.J. Mitchell. Rigging loads on yacht New Zealand and rig design formulae. *RINA Transactions*, 1993.

[40] L. Morino and C-C. Kuo. Subsonic potential aerodynamics for complex configurations: A general theory. *AIAA Journal*, 12, 1974.

[41] H. Murai and S. Maruyama. Theoretical investigation of sailwing airfoils taking account of elasticities. *Journal of Aircraft*, 49(5):385–389, 1982.

[42] J.N. Neilson. Theory of flexible aerodynamic surfaces. *Journal of Applied mechanics*, 3:435–442, 1963.

[43] B.G. Newman. The aerodynamics of flexible membranes. In *Proceedings of the Eighth Canadian Congress of Applied Mechanics*, pages 63–78, June 1981.

[44] B.G. Newman. Aerodynamic theory for membranes and sails. *Progress in Aerospace Sciences*, 24:1–27, 1987.

[45] P. Noury. Numerical approach to the structural design procedure of an ocean racing trimeran. Msc, University of Southampton, 1995.

[46] J.T. Oden and T. Sato. Finite strains and displacements of elastic membranes by the finite element method. *International Journal of Solid Structures*, 3:471–488, 1967.

[47] R.A. Ormiston. Theoretical and experimental aerodynamics of the sailwing. *Journal of Aircraft*, 8(2):77–83, 1971.

[48] T.F. Van Der Werff P.J. Keuning. Rig load measurements and comparison with calculations. In *11th International Symposium on Yacht Architecture*, 1990.

[49] R.P. Prior. An investigation into how results from a panel code are affected by geometry modifications. MSc, University of Southampton, 1995.

[50] S. Rajasekaran and D. Murray. Incremental finite element matrices. *Journal of the Structural Division of ASCE*, 12:2423–2438, 1973.

[51] C.T.F. Ross. Non-linear structural mechanics. In *Finite Element Methods in Engineering Science*. Ellis Horwood, 1990.

[52] C.J. Satchwell. *Elements of Lifting Membrane Analysis*. PhD thesis, University of Southampton, 1982.

[53] P. Seide. Large deflections of rectangular membranes under uniform pressure. *International Journal of Non Linear Mechanics*, 12:397–406, 1977.

[54] J.N. Selness. The finite element method of structural analysis applied to mast rigs. In *The 10th AIAA Symposium of Sailing, The Ancient Interface X*, volume 26, 1990.

[55] R. Smith and W. Shyy. Computation of unsteady laminar flow over a flexible two dimensional membrane wing. *Physical Fluids*, 7(9):2175–2184, 1995.

[56] R. Smith and W. Shyy. Computation of aerodynamic coefficients for a flexible membrane airfoil in turbulent flow: A comparison with classical theory. *Physical Fluids*, 8(12):3346–3353, 1996.

[57] R. Smith and W.Shyy. Incremental potential flow based membrane wing element. *AIAA Journal*, 35:782–788, 1997.

[58] M. Stein and J.M. Hedgepath. Analysis of partly wrinkled membranes. Technical Report D-813, NASA, July 1961.

[59] J.A. Szantyr. A new method for the analysis of unsteady propellor cavitation and hull surface pressures. *Transactions of RINA*, 127:153–167, 1985.

[60] A.E. Taylor. *Advanced Calculus.* Ginn and Company, 1955.

[61] B. Thwaites. The aerodynamic theory of sails i. two dimensional sails. *Proceedings of the Royal Society of London*, A261, 1961.

[62] S.P. Timoshenko and J.N. Goodier. *Theory of Elasticity.* McGraw Hill, 1970. ISBN 0-07-085805-5.

[63] S.P. Timoshenko and S. Woinowsky-Kreiger. *Theory of Plates and Shells.* McGraw-Hill, 1959.

[64] S. Turnock. *Prediction of ship rudder-propeller interaction using parallel computations and wind tunnel measurements.* PhD thesis, University of Southampton, 1993.

[65] S. Turnock. Private communication, 1998.

[66] F. White. *Fluid Mechanics.* Waterline Books, 1986. ISBN 0-0706-6525-7.

[67] R.D. Wood and B. Schrefler. Geometrically nonlinear analysis - a correlation of finite element notations. *International Journal for Numerical Methods in Engineering*, 12:635–642, 1978.

[68] O.C. Zienkiewicz. *The Finite Element Method.* McGraw Hill, fourth edition, 1989. ISBN 0-07-084174-8.

Displacement	Grandin	FE program
$u_3\ (m)$	7.74×10^{-5}	7.74×10^{-5}
$v_3\ (m)$	1.58×10^{-4}	1.58×10^{-4}
$u_4\ (m)$	-1.62×10^{-5}	-1.62×10^{-5}
$v_4\ (m)$	1.35×10^{-4}	1.35×10^{-4}

result	Grandin		FE program	
	el 1	el 2	el 1	el 2
$\sigma_x\ (N/m^2)$	-65.0	264.0	-65.0	264.0
$\sigma_y\ (N/m^2)$	-32.0	65.0	-32.0	65.0
$\tau_{xy}\ (N/m^2)$	135.0	65.0	135.0	65.0

Table 1: Results of triangle element finite element validation

Node	σ_{xx}	σ_{yy}	σ_{xy}
Element 0			
4	-55.2	107.1	-113.6
1	-95.9	-28.8	-420.3
0	-972.1	-291.6	-467.8
3	-931.4	-155.8	-161.2
Element 1			
5	1123.2	319.7	1.7
2	1128.9	338.7	-426.9
1	-95.9	-28.8	-420.3
4	-101.6	-47.8	8.4
Element 2			
7	-79.8	-286.7	-237.5
4	47.6	137.9	-331.1
3	-219.9	57.6	-182.6
6	-347.3	-366.9	-88.9
Element 3			
8	298.3	-914.9	-370.8
5	624.0	169.9	-588.8
4	1.15	-16.96	-209.1
7	-324.3	-1101.8	8.9

Table 2: Nodal stress values for four noded quadrilateral test

Model	Tip deflection (m)
Theoretical	0.333
10 of 8 node quad	0.334
10 of 4 node quad	0.230
40 of 4 node quad	0.300

Table 3: Results of finite element analysis of tip loaded cantilever

Model	N_{elem}	δ_{tip} (metres)
beam-5	20	0.09496
beam-10	40	0.18825
beam-15	60	0.21769
beam-20	80	0.22380
beam-25	100	0.22395

Table 4: Tip deflections of tip loaded cantilever modelled with three node triangular finite elements

N_{elem}	Tip deflection (m)				
	8 node	16 node		20 node	
		14 point	27 point	14 point	27 point
1	0.00254	0.00255	0.00255	0.07344	0.07335
2	0.00929	0.00937	0.00937	0.08949	0.08942
3	0.01840	0.01878	0.01878	0.09419	0.09417
4	0.02802	0.02900	0.02900	0.09600	0.09605
5	0.03700	0.03882	0.03882	0.09702	0.09705
6	0.04481	0.04762	0.04762	0.09761	0.09765
7	0.05136	0.05518	0.05518	0.09801	0.09806
8	0.05676	0.06155	0.06155	0.09830	0.09835
9	0.06117	0.06686	0.06686	0.09851	0.09857
10	0.06478	0.07126	0.07126	0.09867	0.09873
20	0.07993	0.09053	0.09054		
30	0.08359	0.09542	0.09541		

Table 5: Tip deflections of tip loaded cantilever modelled by solid elements

N_{ls}	δ_{tip}/L
	(metres)
1	0.333958
2	0.173504
3	0.274570
4	0.226282
5	0.288559
6	0.255825
7	0.295533
8	0.271605
9	0.296375
10	0.280584
25	0.288221
50	0.298958
75	0.299024
100	0.299038
125	0.299043

Table 6: Non linear analysis of tip loaded cantilever using FENLA1

N_{ls}	δ_{tip}/L	
	$k=1$	$k=10$
1	0.12545	1.25450
2	0.07920	0.53552
3	0.11339	0.44097
4	0.10427	0.50023
5	0.11713	0.59473
7	0.12105	0.64322
10	0.12394	0.67345
15	0.12517	0.71807
20	0.12546	0.71352
25	0.12557	0.71707
30	0.12561	0.71658
40	0.12565	0.71697
50	0.12566	0.71707
500	0.12568	0.71717
750	0.12568	0.71717
1000	0.12568	0.71717

Table 7: Sensitivity study on distributed loaded cantilever using FENLA1

k	δ_{tip}/L				
	Analytical	$N_{ls}=5$	$N_{ls}=10$	$N_{ls}=25$	$N_{ls}=50$
1	0.124	0.117132	0.123937	0.125568	0.125664
2	0.234	0.234993	0.231570	0.244895	0.245526
3	0.336	0.331953	0.326908	0.350787	0.352293
4	0.424	0.390574	0.411714	0.440326	0.442575
5	0.490	0.438691	0.481489	0.514225	0.516443
6	0.552	0.496267	0.537868	0.574172	0.575867
7	0.600	0.561469	0.581387	0.622061	0.623400
8	0.640	0.598972	0.616179	0.660425	0.661500
9	0.676	0.637538	0.646644	0.691331	0.692100
10	0.704	0.594728	0.673451	0.716432	0.717070

Table 8: FENLA1 analysis of distributed loaded cantilever

N_{ls}	Tip deflection (m)		
	40 elem	80 elem	320 elem
5	-0.421055	-0.514481	-0.653853
10	-0.430197	-0.555558	-0.643351
15	-0.451524	-0.586130	-0.685377
20	-0.452870	-0.582416	-0.683080
25	-0.454233	-0.585455	-0.683680
30	-0.454233	-0.586147	-0.683933
35	-0.455012	-0.586481	-0.684250
40	-0.455145	-0.586654	-0.684392
45	-0.455222	-0.586752	-0.684470
50	-0.455269	-0.586811	-0.684516
100	-0.455364	-0.586927	-0.684600

Table 9: Results of convergence tests for distributed loaded cantilever, load coefficient 10, analysed using FENLA3-3 with increasing number of elements

Π_1	Central deflection						
	Analytical	F4	Error(%)	F3-3(1)	Error(%)	F3-3(2)	Error(%)
1	0.28660	0.28795	0.470	0.28784	0.432	0.28445	0.752
2	0.14330	0.14323	0.050	0.14315	0.104	0.14162	1.170
3	0.09553	0.09545	0.087	0.09539	0.146	0.09440	1.182
4	0.07165	0.07159	0.087	0.07154	0.149	0.07081	1.175
5	0.05732	0.05727	0.087	0.05723	0.149	0.05665	1.169
6	0.04777	0.04773	0.085	0.04770	0.148	0.04721	1.165
7	0.04094	0.04091	0.084	0.04088	0.147	0.04047	1.162
8	0.03582	0.03580	0.083	0.03577	0.146	0.03541	1.161
9	0.03184	0.03182	0.082	0.03180	0.146	0.03148	1.159
10	0.02866	0.02864	0.082	0.02862	0.145	0.02833	1.158
21.5	0.01330	0.01329	0.080	0.01328	0.144	0.01315	1.155

Table 10: Central deflection of pressure loaded square membrane predicted by FENLA3-3 and FENLA4 for varying Π_1. FENLA3-3 grids: (1) symmetrical, (2) asymmetrical.

N_{elem}	Characteristic element length (m)	δ_{centre} (m)
2	0.5000	0.167977
8	0.2500	0.153930
18	0.1667	0.149137
32	0.1250	0.146902
50	0.1000	0.145678
72	0.0833	0.144935
98	0.0714	0.144449
128	0.0625	0.144112
162	0.0556	0.143869
200	0.0100	0.143687
242	0.0455	0.142547
288	0.0417	0.143436
338	0.0385	0.143347
392	0.0357	0.143274
450	0.0333	0.143214
512	0.0313	0.143163
578	0.0294	0.143120
648	0.0278	0.143083
722	0.0263	0.143050
800	0.0250	0.143022
1250	0.0200	0.142924
1800	0.0167	0.142865
2450	0.0143	0.142827
3200	0.0125	0.142800
4050	0.0111	0.142781
5000	0.0100	0.142765
7200	0.0083	0.142743

Table 11: Dynamic array FENLA3-3 membrane analysis

N_{elem}	Characteristic element length (m)	N_{it}	δ_{centre} (m)
2	0.500	> 50	n/c
8	0.250	4	0.154329
18	0.167	4	0.149375
32	0.125	4	0.147064
50	0.100	4	0.145784
72	0.083	4	0.145007
98	0.071	4	0.144500
128	0.063	4	0.144149
182	0.056	4	0.143896
200	0.050	4	0.143707

Table 12: FENLA3-4 membrane analysis with varying number of elements using 3 point integration

N_{elem}	Characteristic element length (m)	N_{it}	δ_{centre} (m)
2	0.500	7	0.164099
8	0.250	4	0.154325
18	0.167	4	0.149381
32	0.125	4	0.147067
50	0.100	4	0.145787
72	0.083	4	0.145009

Table 13: FENLA3-4 membrane analysis using 13 point integration

N_{elem}	N_{node}	N_{ls}	N_{it}	δ_{tip} (m)
1	20	10	20	-0.0685571
		20	13	-0.0685571
		30	12	-0.0685571
2	32	10	31	-0.0876148
		20	13	-0.0876148
		30	11	-0.0876148
3	44	10	40	-0.0926471
		20	15	-0.0926471
		30	13	-0.0926471
4	56	10	44	-0.0945578
		20	16	-0.0945578
5	68	10	45	-0.0955442
		20	15	-0.0955442
6	80	10	47	-0.0961342
		20	16	-0.0961342
7	92	10	48	-0.0965261
		20	16	-0.0965261
8	104	10	48	-0.0968044
		20	16	-0.0968044
9	116	10	49	-0.0970121
		20	16	-0.0970121
10	128	10	49	-0.0971728
		20	16	-0.0971728
		30	13	-0.0971728

Table 14: FENLA5 analysis of tip loaded cantilever

20 Load steps, $c_l = 0.05$			
c_c	N_{it}	δ_{tip}	u^3_{127}
1×10^{-2}	1	0.225569	0.223289
5×10^{-2}	1	0.227315	0.225030
1×10^{-3}	4	0.227398	0.225115
1×10^{-4}	11	0.227289	0.225005
1×10^{-5}	18	0.227315	0.225033
1×10^{-6}	26	0.227315	0.225030
1×10^{-7}	33	0.227315	0.225030

Table 15: Tip loaded cantilever, 20 load steps, $c_l = 0.05$, all displacements in metres

20 Load steps, $c_l = 0.01$			
c_c	N_{it}	δ_{tip}	u^3_{127}
1×10^{-2}	1	0.225569	0.223289
1×10^{-3}	4	0.227398	0.223289
1×10^{-4}	11	0.227289	0.225005
1×10^{-5}	18	0.227317	0.225033
1×10^{-6}	26	0.227315	0.225030
1×10^{-7}	33	0.227315	0.225030

Table 16: Tip loaded cantilever, 20 load steps, $c_l = 0.01$, all displacements in metres

Load factor	$N_{ls} = 19$		$N_{ls} = 20$		$N_{ls} = 21$	
	N_{it}	δ_{tip} (m)	N_{it}	δ_{tip} (m)	N_{it}	δ_{tip} (m)
1	2	0.119391	2	0.119389	2	0.119386
2	3	0.227003	3	0.226904	3	0.226772
3	> 50	n/c	3	0.319420	> 50	n/c
4	2	0.397640	2	0.397640	2	0.397518
5	-	diverged	2	0.462728	-	diverged
6	-	diverged	2	0.516970	-	diverged
7	-	diverged	2	0.562290	-	diverged
8	-	diverged	2	0.600352	-	diverged
9	-	diverged	2	0.632533	-	diverged
10	-	diverged	2	0.659944	-	diverged

Table 17: FENLA5 analysis of distributed loaded cantilever with 19, 20 and 21 load steps

Load steps	δ_{tip} (m)
10	0.622565
15	0.663835
16	0.653134
17	0.663189
18	0.654961
19	0.663344
20	0.656148
21	0.663492
25	0.663827
30	0.658139
35	0.664261
40	0.658529
45	0.664364
50	0.658698
55	0.664422
100	0.664548
150	0.664548
151	0.664548
175	0.664558

Table 18: FENLA5 non iterative solution of distributed loaded cantilever, load factor=10, for varying number of load steps

k	δ_{tip} (m)
1	0.098548
2	0.190338
3	0.272029
4	0.343496
5	0.405961
6	0.459085
7	0.503725
8	0.543189
9	0.577297
10	0.60692

Table 19: Tip deflections for distributed loaded cantilever, analysed by FENLA5-16 using 10 elements.

N_{elem}	δ_{tip} (m)
10	0.608958
15	0.64477
20	0.657703
25	0.663505
30	0.666467
50	0.669998
100	0.670318

Table 20: Tip deflections for distributed loaded cantilever, $k = 10$ analysed by FENLA5 using 16 node elements.

α (degrees)	Force coefficients		C_L	C_D
	C_{Fx}	C_{Fy}		
Coarse grid, $N_t = 10$, $N_s = 25$				
0	0.00143	0.00000	0.00000	0.00143
5	-0.01339	0.35300	0.35282	0.01743
10	-0.05670	0.68777	0.68717	0.06360
Fine grid, $N_t = 20$, $N_s = 50$				
0	0.00334	0.00000	0.00000	0.00334
5	-0.02187	0.34814	0.34873	0.00856
10	-0.09576	0.67982	0.68612	0.02375

Table 21: PALISUPAN analysis of flat rectangular membrane, aspect ratio 5. Force coefficients are non dimensionalised with respect to the membrane area

BMCC	PALISUPAN o/p		Non dim. forces		N_{it}	C_L	C_D
	C_{Fx}	C_{Fy}	C_{Fx}	C_{Fy}			
1.0×10^{-1}	-0.6344	5.1048	-0.0846	0.6810	34	0.6853	0.0349
1.0×10^{-2}	-0.6504	5.1770	-0.0868	0.6906	31	0.6952	0.0345
1.0×10^{-3}	-0.6532	5.1903	-0.0871	0.6924	31	0.6970	0.0344
1.0×10^{-4}	-0.6546	5.1976	-0.0873	0.6934	32	0.6980	0.0344
1.0×10^{-5}	-0.6548	5.1991	-0.0874	0.6936	32	0.6982	0.0344
1.0×10^{-6}	-0.6549	5.1993	-0.0874	0.6936	32	0.6982	0.0344

Table 22: Results of PALISUPAN block matrix convergence limit investigation for flat membrane, aspect ratio 5

			PALISUPAN o/p		Non dim. forces			
N_t	N_s	N_{panel}	C_{Fx}	C_{Fy}	C_{Fx}	C_{Fy}	C_L	C_D
AR = 0.50								
5	25	125	SOLUTION DIVERGES					
6	30	180	-0.0439	-2.8456	-0.0059	-0.3796	0.3787	0.0272
7	35	245	0.1050	-2.9244	0.0140	-0.3901	0.3874	0.0480
8	40	320	-0.0666	-2.6665	-0.0089	-0.3557	0.3551	0.0221
9	45	405	0.0485	-2.7698	0.0065	-0.3695	0.3675	0.0387
10	50	500	-0.0992	-2.6281	-0.0132	-0.3506	0.3504	0.0174
11	55	605	-0.0016	-2.7260	-0.0002	-0.3636	0.3623	0.0315
12	60	720	-0.1248	-2.6130	-0.0167	-0.3486	0.3487	0.0138
13	65	845	-0.0425	-2.6979	-0.0057	-0.3599	0.3590	0.0257
14	70	980	-0.1432	-2.6169	-0.0191	-0.3491	0.3494	0.0114
15	75	1125	-0.0740	-2.6862	-0.0099	-0.3583	0.3578	0.0214
16	80	1280	-0.1547	-2.6125	-0.0206	-0.3485	0.3490	0.0098
17	85	1445	-0.0944	-2.6653	-0.0126	-0.3555	0.3553	0.0184
18	90	1620	-0.1612	-2.6088	-0.0215	-0.3480	0.3486	0.0089
19	95	1805	-0.1069	-2.6242	-0.0143	-0.3501	0.3500	0.0163
AR = 0.75								
9	30	270	0.0483	-2.7748	0.0064	-0.3702	0.3682	0.0387
12	40	480	-0.1253	-2.6240	-0.0167	-0.3500	0.3502	0.0139
15	50	750	-0.0737	-2.6793	-0.0098	-0.3574	0.3569	0.0214
18	60	1080	-0.1610	-2.6088	-0.0215	-0.3480	0.3486	0.0089
21	70	1470	-0.1179	-2.6442	-0.0157	-0.3527	0.3528	0.0151
24	80	1920	-0.1596	-2.5889	-0.0213	-0.3454	0.3459	0.0089

Table 23: Results of investigation into average panel aspect ratio I

			PALISUPAN o/p		Non dim. forces			
N_t	N_s	N_{panel}	C_{Fx}	C_{Fy}	C_{Fx}	C_{Fy}	C_L	C_D
AR = 1.00								
8	20	160	-0.0679	-2.7028	-0.0091	-0.3606	0.3600	0.0224
10	25	250	-0.1001	-2.6460	-0.0134	-0.3530	0.3528	0.0175
12	30	360	-0.1258	-2.6317	-0.0168	-0.3511	0.3512	0.0139
14	35	490	-0.1433	-2.6177	-0.0191	-0.3492	0.3495	0.0114
16	40	640	-0.1548	-2.6157	-0.0207	-0.3489	0.3494	0.0098
18	45	810	-0.1610	-2.6079	-0.0215	-0.3479	0.3484	0.0089
20	50	1000	-0.1638	-2.6099	-0.0219	-0.3482	0.3487	0.0086
22	55	1210	-0.1635	-2.6130	-0.0218	-0.3486	0.3491	0.0087
24	60	1440	-0.1610	-2.6103	-0.0215	-0.3482	0.3488	0.0090
26	65	1690	-0.1573	-2.6035	-0.0210	-0.3473	0.3478	0.0094
AR = 1.25								
10	20	200	-0.1010	-2.6646	-0.0135	-0.3555	0.3553	0.0176
12	24	288	-0.1263	-2.6377	-0.0168	-0.3519	0.3520	0.0139
14	28	392	-0.1440	-2.6287	-0.0192	-0.3507	0.3510	0.0114
16	32	512	-0.1550	-2.6167	-0.0207	-0.3491	0.3495	0.0098
18	36	648	-0.1615	-2.6149	-0.0215	-0.3488	0.3494	0.0089
20	40	800	-0.1643	-2.6164	-0.0219	-0.3490	0.3496	0.0086
22	44	968	-0.1636	-2.6130	-0.0218	-0.3486	0.3492	0.0086
24	48	1152	-0.1614	-2.6137	-0.0215	-0.3487	0.3492	0.0089
26	52	1352	-0.1582	-2.6149	-0.0211	-0.3488	0.3493	0.0094
27	54	1458	-0.1323	-2.6231	-0.0176	-0.3499	0.3501	0.0129
28	56	1568	-0.1542	-2.6111	-0.0206	-0.3483	0.3488	0.0099
29	58	1682	-0.1334	-2.6100	-0.0178	-0.3482	0.3484	0.0126
30	60	1800	-0.1497	-2.5989	-0.0200	-0.3467	0.3471	0.0103
AR = 1.50								
9	15	135	0.0470	-2.8229	0.0063	-0.3766	0.3746	0.0391
12	20	240	-0.1271	-2.6502	-0.0170	-0.3535	0.3537	0.0139
15	25	375	-0.0750	-2.7033	-0.0100	-0.3606	0.3601	0.0215
18	30	540	-0.1622	-2.6222	-0.0216	-0.3498	0.3504	0.0089
21	35	735	-0.1185	-2.6509	-0.0158	-0.3536	0.3537	0.0151
24	40	960	-0.1617	-2.6165	-0.0216	-0.3490	0.3496	0.0089
27	45	1215	-0.1327	-2.6266	-0.0177	-0.3504	0.3506	0.0129
30	50	1500	-0.1506	-2.6110	-0.0201	-0.3483	0.3487	0.0103
33	55	1815	-0.1343	-2.5991	-0.0179	-0.3467	0.3470	0.0124

Table 24: Results of investigation into average panel aspect ratio II

	PALISUPAN o/p		Non dim. forces			
α	C_{Fx}	C_{Fy}	C_{Fx}	C_{Fy}	N_{it}	C_L
-10	-0.3226	-2.8315	-0.0430	-0.3777	30	-0.3795
-5	0.0698	-0.1372	0.0093	-0.0183	25	-0.0174
0	0.1190	2.5369	0.0159	0.3384	24	0.3384
5	-0.1743	5.1289	-0.0233	0.6842	23	0.6836
10	-0.7995	7.5487	-0.1067	1.0070	35	1.0102

Table 25: Results of PALISUPAN analysis of a curved plate using a coarse mesh, $N_t = 10$, $N_s = 25$

	PALISUPAN o/p		Non dim. forces			
α	C_{Fx}	C_{Fy}	C_{Fx}	C_{Fy}	N_{it}	C_L
-10	-0.3346	-5.9122	-0.0446	-0.7887	66	-0.3795
-5	-0.0011	-3.5479	-0.0001	-0.4733	70	-0.0174
0	0.0855	-1.0378	0.0114	-0.1384	71	0.3384
5	-0.0781	1.5457	-0.0104	0.2062	71	0.6836
10	-0.4876	4.1284	-0.0650	0.5507	70	1.0102

Table 26: Results of PALISUPAN analysis of a curved plate using a coarse mesh, $N_t = 10$, $N_s = 25$

BMCC	Kutta	PALISUPAN o/p			Non dimensionalised		
		C_{Fx}	C_{Fy}	C_{Fz}	C_{Fx}	C_{Fy}	C_{Fz}
1.0×10^{-2}	0.01	-0.30431	1.31705	-0.01677	-0.20297	0.87847	-0.01119
5.0×10^{-3}	0.01	-0.30431	1.31706	-0.01677	-0.20297	0.87848	-0.01119
1.0×10^{-3}	0.01	-0.30431	1.31707	-0.01677	-0.20298	0.87848	-0.01119
5.0×10^{-4}	0.01	-0.30431	1.31707	-0.01677	-0.20298	0.87849	-0.01119
1.0×10^{-4}	0.01	-0.30431	1.31708	-0.01677	-0.20298	0.87849	-0.01119
5.0×10^{-5}	0.01	-0.30431	1.31707	-0.01677	-0.20297	0.87848	-0.01119
3.0×10^{-5}	0.01	-0.30430	1.31704	-0.01677	-0.20297	0.87847	-0.01119
1.0×10^{-5}	0.01	-0.30429	1.31701	-0.01677	-0.20296	0.87845	-0.01119
1.0×10^{-6}	0.01	-0.30429	1.31700	-0.01677	-0.20296	0.87844	-0.01119
1.0×10^{-7}	0.01	-0.30429	1.31699	-0.01677	-0.20296	0.87843	-0.01119

BMCC	C_L	C_D	N_{it}
1.0×10^{-2}	0.89492	0.10972	57
5.0×10^{-3}	0.89492	0.10972	57
1.0×10^{-3}	0.89493	0.10972	57
5.0×10^{-4}	0.89493	0.10972	57
1.0×10^{-4}	0.89493	0.10972	57
5.0×10^{-5}	0.89493	0.10972	57
3.0×10^{-5}	0.89491	0.10972	57
1.0×10^{-5}	0.89489	0.10972	57
1.0×10^{-6}	0.89488	0.10972	57
1.0×10^{-7}	0.89487	0.10972	57

Table 27: Results of investigation into BMCC condition variation for deformed triangular membrane

Kutta	PALISUPAN o/p			Non dimensionalised		
	C_{Fx}	C_{Fy}	C_{Fz}	C_{Fx}	C_{Fy}	C_{Fz}
1.0×10^{-1}	-0.31051	1.35596	-0.01693	-0.20711	0.90443	-0.01129
5.0×10^{-2}	-0.30639	1.32612	-0.01681	-0.20436	0.88452	-0.01121
1.0×10^{-2}	-0.30431	1.31707	-0.01677	-0.20298	0.87848	-0.01119
5.0×10^{-3}	-0.30426	1.31685	-0.01677	-0.20294	0.87834	-0.01119
1.0×10^{-3}	-0.30423	1.31674	-0.01677	-0.20292	0.87827	-0.01119
1.0×10^{-4}	-0.30422	1.31672	-0.01677	-0.20292	0.87825	-0.01119
1.0×10^{-5}	-0.30422	1.31672	-0.01677	-0.20291	0.87825	-0.01119

Kutta	C_L	C_D	N_{it}
1.0×10^{-1}	0.92072	0.11471	10
5.0×10^{-2}	0.90108	0.11049	21
1.0×10^{-2}	0.89493	0.10972	57
5.0×10^{-3}	0.89478	0.10971	73
1.0×10^{-3}	0.89470	0.10970	110
1.0×10^{-4}	0.89469	0.10970	164
1.0×10^{-5}	0.89469	0.10970	222

Table 28: Results of investigation into Kutta condition variation for deformed triangular membrane

	PALISUPAN o/p			Non dimensionalised		
N_s	C_{Fx}	C_{Fy}	C_{Fz}	C_{Fx}	C_{Fy}	C_{Fz}
10	-0.21256	1.27508	-0.01802	-0.14178	0.85048	-0.01202
15	-0.27518	1.31036	-0.01723	-0.18355	0.87401	-0.01149
20	-0.30431	1.31707	-0.01677	-0.20298	0.87848	-0.01119
25	-0.31844	1.31716	-0.01646	-0.21240	0.87855	-0.01098
30	-0.32586	1.31576	-0.01623	-0.21735	0.87761	-0.01083
35	-0.33007	1.31419	-0.01605	-0.22016	0.87656	-0.01071
40	-0.33236	1.31208	-0.01591	-0.22168	0.87516	-0.01061
45	-0.33392	1.31085	-0.01580	-0.22273	0.87434	-0.01054

N_s	C_L	C_D	N_{it}
10	0.84768	0.15765	31
15	0.88408	0.12645	53
20	0.89493	0.10972	57
25	0.89821	0.10089	57
30	0.89902	0.09592	56
35	0.89900	0.09292	54
40	0.89820	0.09101	81
45	0.89779	0.08975	130

Table 29: Results for deformed triangular membrane model with constant $N_t = 40$, varying N_s

	PALISUPAN o/p			Non dimensionalised		
N_t	C_{Fx}	C_{Fy}	C_{Fz}	C_{Fx}	C_{Fy}	C_{Fz}
20	-0.30414	1.17735	-0.01612	-0.20286	0.78529	-0.01075
30	-0.28782	1.20611	-0.01600	-0.19197	0.80447	-0.01067
40	-0.30431	1.31707	-0.01677	-0.20298	0.87848	-0.01119
50	-0.30670	1.41809	-0.01735	-0.20457	0.94586	-0.01157
60	-0.30119	1.48724	-0.01747	-0.20089	0.99199	-0.01165
70	-0.29620	1.52840	-0.01797	-0.19757	1.01944	-0.01199
80	-0.29122	1.55103	-0.01884	-0.19424	1.03453	-0.01257
90	-0.28555	1.56159	-0.01980	-0.19046	1.04158	-0.01321

N_s	C_L	C_D	N_{it}
20	0.80732	0.07796	80
30	0.82162	0.09475	71
40	0.89493	0.10972	57
50	0.95879	0.13127	34
60	1.00087	0.15050	30
70	1.02554	0.16302	45
80	1.03858	0.17130	49
90	1.04391	0.17726	51

Table 30: Results for deformed triangular membrane model with constant $N_s = 20$, varying N_t

			PALISUPAN o/p			Non dimensionalised		
N_t	N_s	N_{pan}	C_{Fx}	C_{Fy}	C_{Fz}	C_{Fx}	C_{Fy}	C_{Fz}
20	10	200	-0.25484	1.16003	-0.01722	-0.16998	0.77374	-0.01149
30	15	450	-0.27140	1.20475	-0.01643	-0.18102	0.80357	-0.01096
40	20	800	-0.30431	1.31708	-0.01677	-0.20298	0.87849	-0.01119
50	25	1250	-0.32582	1.42291	-0.01700	-0.21732	0.94908	-0.01134
60	30	1800	-0.33536	1.49845	-0.01679	-0.22368	0.99946	-0.01120
70	35	2450	-0.34462	1.54529	-0.01700	-0.22986	1.03071	-0.01134
74	37	2738	-0.34777	1.55856	-0.01722	-0.23196	1.03956	-0.01149

N_{pan}	C_L	C_D	N_{it}
200	0.78521	0.10491	81
450	0.81702	0.10473	70
800	0.89493	0.10972	57
1250	0.96617	0.12039	38
1800	1.01569	0.13164	32
2450	1.04717	0.13652	48
2738	1.05620	0.13758	50

Table 31: PALISUPAN results for deformed triangle with APAR of 0.25

N_t	N_s	N_{pan}	PALISUPAN o/p			Non dimensionalised		
			C_{Fx}	C_{Fy}	C_{Fz}	C_{Fx}	C_{Fy}	C_{Fz}
16	16	256	-0.30739	1.21199	-0.01688	-0.20503	0.80839	-0.01126
20	20	400	-0.30415	1.17737	-0.01612	-0.20287	0.78531	-0.01075
26	26	676	-0.29464	1.17533	-0.01549	-0.19652	0.78395	-0.01033
30	30	900	-0.29870	1.20242	-0.01550	-0.19924	0.80202	-0.01034
36	36	1296	-0.31803	1.26472	-0.01569	-0.21213	0.84357	-0.01047
40	40	1600	-0.33236	1.31207	-0.01591	-0.22168	0.87515	-0.01061
46	46	2116	-0.34662	1.37991	-0.01608	-0.23120	0.92040	-0.01073
50	50	2500	-0.35067	1.41939	-0.01613	-0.23390	0.94673	-0.01076
52	52	2704	-0.35192	1.43733	-0.01611	-0.23473	0.95870	-0.01074

N_{pan}	C_L	C_D	N_{it}
256	0.82977	0.08382	86
400	0.80733	0.07796	80
676	0.80388	0.08345	74
900	0.82179	0.08709	70
1296	0.86525	0.08918	61
1600	0.89819	0.09101	81
2116	0.94396	0.09754	105
2500	0.96963	0.10401	117
2704	0.98116	0.10732	122

Table 32: PALISUPAN results for deformed triangle with APAR of 0.50

N_t	N_s	N_{pan}	PALISUPAN o/p			Non dimensionalised		
			C_{Fx}	C_{Fy}	C_{Fz}	C_{Fx}	C_{Fy}	C_{Fz}
32	8	256	-0.18803	1.16836	-0.01775	-0.12541	0.77930	-0.01184
40	10	400	-0.21254	1.27498	-0.01801	-0.14176	0.85041	-0.01201
48	12	576	-0.23504	1.36279	-0.01819	-0.15677	0.90898	-0.01213
56	14	784	-0.25389	1.43530	-0.01809	-0.16934	0.95734	-0.01206
64	16	1024	-0.26755	1.48834	-0.01803	-0.17846	0.99272	-0.01203
72	18	1296	-0.28017	1.52540	-0.01833	-0.18687	1.01744	-0.01223
80	20	1600	-0.29122	1.55103	-0.01884	-0.19424	1.03454	-0.01257
88	22	1936	-0.30027	1.56894	-0.01942	-0.20028	1.04648	-0.01295
96	24	2304	-0.30792	1.58068	-0.02002	-0.20538	1.05431	-0.01335
104	26	2704	-0.31465	1.58818	-0.02061	-0.20987	1.05932	-0.01375

N_{pan}	C_L	C_D	N_{it}
256	0.77519	0.14869	61
400	0.84761	0.15765	31
576	0.90778	0.16357	23
784	0.95753	0.16830	33
1024	0.99389	0.17183	45
1296	1.02000	0.17238	48
1600	1.03858	0.17131	49
1936	1.05187	0.16972	49
2304	1.06097	0.16760	48
2704	1.06721	0.16509	47

Table 33: PALISUPAN results for deformed triangle with APAR of 1.0

Distribution	C_{Fx}	C_{Fy}	C_{Fz}
Even	-0.267553	1.488335	-0.018033
Clustered	-0.223288	1.495455	-0.018537

Table 34: PALISUPAN force output for deformed triangular membrane using different panel clustering in the spanwise direction

Grid	Panels	Central deflection (m)			C_L	C_D
		x	y	z		
25x25	625	-0.00047	0.05081	-1.2E-09	0.5658	0.0256
30x30	900	-0.00045	0.05167	-1.5E-09	0.5916	0.0254
35x35	1225	-0.00043	0.05252	-2.4E-09	0.6154	0.0281
40x40	1600	-0.00041	0.05324	-3.2E-09	0.6402	0.0320
45x45	2025	-0.00039	0.05382	7.45E-11	0.6611	0.0326
50x50	2500	-0.00038	0.05428	-1.6E-10	0.6763	0.0355

Table 35: Central deflections of initially flat membrane analysed by MONSTA1 with varying number of PALISUPAN panels

Run	Number of elements	Central deflection (m)			C_L	C_D
		x	y	z		
4	320	-0.00038	0.05321	-2.18E-9	0.6186	0.0284
5	500	-0.00043	0.05252	-2.35E-9	0.6154	0.0281
6	720	-0.00044	0.05282	-6.55E-10	0.6210	0.0283
7	980	-0.00045	0.05269	-1.18E-9	0.6232	0.0284
8	1280	-0.00045	0.05281	-2.47E-9	0.6241	0.0284
9	1620	-0.00045	0.05273	-1.92E-9	0.6252	0.0285
10	2000	-0.00045	0.05282	-2.18E-9	0.6267	0.0285
11	2420	-0.00046	0.05261	9.82E-10	0.6201	0.0282
12	2880	-0.00045	0.05285	-1.98E-9	0.6290	0.0286
13	3380	-0.00045	0.05264	1.14E-09	0.6211	0.0282
14	3920	-0.00045	0.05268	-2.94E-10	0.6214	0.0282

Table 36: Central deflections of initially flat membrane analysed by MONSTA1 with varying number of FEA elements

Analysis	Velocity steps	Deflection (m)	
		Fixed t.e.	Free t.e.
No wrinkle model	200	0.01699	0.03215
Wrinkle model	200	0.01389	0.02986
Wrinkle model	100	0.01389	0.02986

Table 37: Comparison of deflections for fixed and free trailing edge rectangular models, $A_r = 2$, $\alpha = 15^o$, $\Pi_1 = 15$

N_e boom	N_e model	Displacement of mid point of TE			C_L
		u_1	u_2	u_3	
8	248	-0.00325	0.04399	-0.00050	0.87729
10	390	-0.00336	0.04331	-0.00059	0.90871
12	564	-0.00337	0.04295	-0.00058	0.92403
15	865	-0.00350	0.04273	-0.00064	0.92937
20	1580	-0.00360	0.04246	-0.00071	0.93476

Table 38: Results of MONSTA3 analysis of initially flat triangular membrane

N_e boom	N_e sail	Mast tip deflection (m)			C_L
		u_1	u_2	u_3	
rig1-4	60	0.005392	0.00127	-0.000024	0.815075152
rig1-6	138	0.009537	0.002558	-0.000041	0.858976795
rig1-8	248	0.012997	0.003667	-0.000062	0.848767743
rig1-10	390	0.016179	0.004782	-0.00009	0.830132757
rig1-12	564	0.018698	0.00569	-0.000116	0.810866329
rig1-14	770	0.020829	0.006481	-0.000142	0.792650109
rig1-16	1008	0.022502	0.007116	-0.000164	0.775178714
rig1-18	1278	0.023883	0.007606	-0.000184	0.764614126
rig1-20	1580	0.024876	0.007958	-0.000198	0.752963096
rig1-22	1914	0.025611	0.008119	-0.000209	0.732082906
rig1-24	2280	0.02469	0.00856	-0.000224	0.736701827

Table 39: Results of aeroelastic analysis of rig1 model

β_1	β_2	C_{Fx}	C_{Fy}	C_{Fz}	u_{tip} (m)	v_{tip} (m)	w_{tip} (m)
1.00	1.00	-0.306560	1.212562	-0.029677	0.016181	0.004782	-0.00009
0.75	0.50	-0.306567	1.212301	-0.029675	0.016178	0.004781	-0.00009
0.50	0.50	-0.306604	1.212841	-0.029671	0.016179	0.004782	-0.00009
0.50	0.25	-0.306560	1.212562	-0.029677	0.016181	0.004782	-0.00009

Table 40: PALISUPAN force coefficients obtained from analysis of rig1-10 model using a range of relaxation factors

N_e boom	N_e sail	Mast tip deflection (m)			C_L
		u_1	u_2	u_3	
rig3-12	564	0.062645	0.011958	-0.001152	1.228202411
rig3-14	770	0.068384	0.01516	-0.001381	1.155455033
rig3-16	1008	0.073027	0.018496	-0.00159	1.147850387
rig3-18	1278	0.076431	0.020853	-0.001753	1.14433377
rig3-20	1580	0.079625	0.023423	-0.00192	1.143309138

Table 41: Results of aeroelastic analysis of rig3 model

Model	C_{Fx}	C_{Fy}	C_{Fz}
rig3C-14	-1.197660	2.531566	-0.028207
rig3CR-14	-0.297817	1.208530	-0.034654

Table 42: Aerodynamic force coefficients calculated by aeroelastic analysis of rig3C-14 and rigC3R-14 models

Element centroid x_3 (m)	Compression (N/m^2)			
	AEA	Constant	Linear	Sinusoidal
0.036	-7513.54	-226.16	-186.48	-231.95
0.107	-7442.75	-196.51	-161.97	-206.08
0.179	-7336.32	-174.10	-142.14	-185.80
0.250	-7180.40	-153.41	-124.61	-166.03
0.321	-6994.12	-135.06	-109.34	-147.71
0.393	-6781.64	-118.64	-95.93	-130.71
0.464	-6548.56	-104.03	-84.17	-115.14
0.536	-6294.33	-91.08	-73.81	-101.00
0.607	-6019.13	-79.63	-64.67	-88.26
0.679	-5725.27	-69.54	-56.57	-76.86
0.750	-5409.27	-60.68	-49.38	-66.72
0.821	-5075.82	-52.92	-42.96	-57.73
0.893	-4727.28	-46.13	-37.23	-49.78
0.964	-4351.34	-40.21	-32.08	-42.75
1.036	-3960.52	-35.05	-27.46	-36.53
1.107	-3555.63	-30.55	-23.30	-31.01
1.179	-3144.30	-26.63	-19.56	-26.11
1.250	-2728.33	-23.19	-16.19	-21.73
1.321	-2313.18	-20.15	-13.19	-17.81
1.393	-1902.08	-17.45	-10.51	-14.32
1.464	-1508.03	-15.03	-8.16	-11.21
1.536	-1127.65	-12.82	-6.11	-8.47
1.607	-767.63	-10.78	-4.36	-6.10
1.679	-467.21	-8.85	-2.90	-4.10
1.750	-271.09	-7.01	-1.74	-2.48
1.821	-181.64	-5.23	-0.87	-1.25
1.893	-133.30	-3.48	-0.29	-0.42
1.964	-50.36	-1.74	0.00	0.00

Table 43: Mast compression results from rig3C-14 analysis

n_{int}	r_i	α_i
1	0.00000 00000 00000	2.00000 00000 00000
2	±0.57735 02691 89626	1.00000 00000 00000
3	±0.77459 66692 41483	0.55555 55555 55556
	0.00000 00000 00000	0.88888 88888 88889
4	±0.86113 63115 94053	0.34785 48451 37454
	±0.33998 10435 84856	0.65214 51548 62546
5	±0.90617 98459 38664	0.23692 68850 56189
	0.53846 93101 05683	0.47862 86704 99366
	0.00000 00000 00000	0.56888 88888 88889

Table 44: Sampling points and weighting for Gaussian numerical integration

Order	r coordinates	s coordinates	Weighting
3	$r_1 = 0.16666\ 66666\ 667$	$s_1 = r_1$	$w_1 = 0.33333\ 33333\ 333$
	$r_2 = 0.66666\ 66666\ 667$	$s_2 = r_1$	$w_2 = w_1$
	$r_3 = r_1$	$s_3 = r_1$	$w_3 = w_1$
7	$r_1 = 0.10128\ 65073\ 235$	$s_1 = r_1$	$w_1 = 0.12593\ 91805\ 448$
	$r_2 = 0.79742\ 69853\ 531$	$s_2 = r_1$	$w_2 = w_1$
	$r_3 = r_1$	$s_3 = r_2$	$w_3 = w_1$
	$r_4 = 0.47013\ 20641\ 051$	$s_4 = r_6$	$w_4 = 0.13239\ 41527\ 885$
	$r_5 = r_4$	$s_5 = r_4$	$w_5 = w_4$
	$r_6 = 0.05971\ 58717\ 898$	$s_6 = r_4$	$w_6 = w_4$
	$r_7 = 0.33333\ 33333\ 333$	$s_7 = r_7$	$w_7 = 0.22500\ 00000\ 000$
13	$r_1 = 0.06513\ 01029\ 022$	$s_1 = r_1$	$w_1 = 0.05334\ 72356\ 088$
	$r_2 = 0.86973\ 97941\ 956$	$s_2 = r_1$	$w_2 = w_1$
	$r_3 = r_1$	$s_3 = r_2$	$w_3 = w_1$
	$r_4 = 0.31286\ 54960\ 049$	$s_4 = r_6$	$w_4 = 0.07711\ 37608\ 903$
	$r_5 = 0.63844\ 41885\ 698$	$s_5 = r_4$	$w_5 = w_4$
	$r_6 = 0.04869\ 03154\ 253$	$s_6 = r_5$	$w_6 = w_4$
	$r_7 = r_5$	$s_7 = r_6$	$w_7 = w_4$
	$r_8 = r_4$	$s_8 = r_5$	$w_8 = w_4$
	$r_9 = r_6$	$s_9 = r_4$	$w_9 = w_4$
	$r_{10} = 0.26034\ 59660\ 790$	$s_{10} = r_{10}$	$w_{10} = 0.17561\ 52574\ 332$
	$r_{11} = 0.47930\ 80678\ 419$	$s_{11} = r_{10}$	$w_{11} = w_{10}$
	$r_{12} = r_{10}$	$s_{12} = r_{11}$	$w_{12} = w_{10}$
	$r_{13} = 0.33333\ 33333\ 333$	$s_{13} = r_{13}$	$w_{13} = -0.14957\ 00444\ 677$

Table 45: Numerical integration points for integration in the triangular element natural coordinate system over the element areas

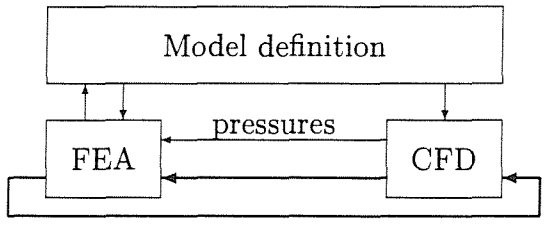

Figure 1: Aeroelastic solution structure

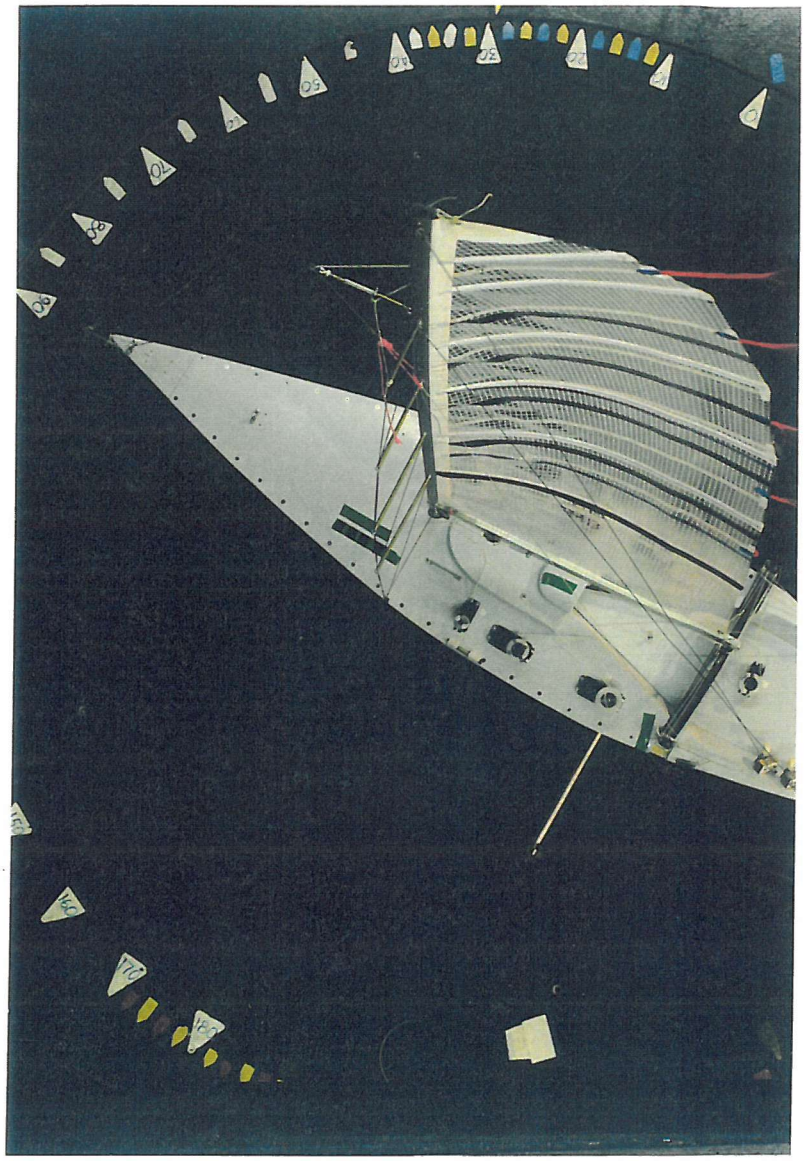

Figure 2: Mainsail under test with a tight leech

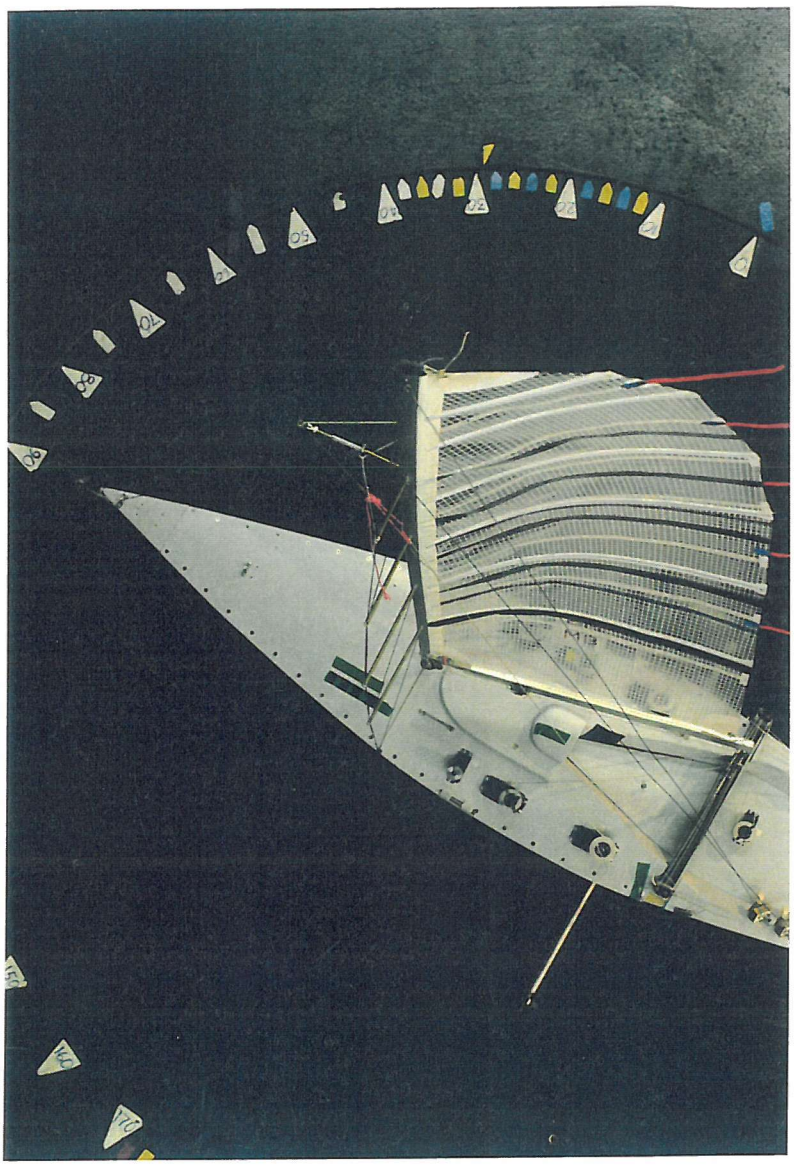

Figure 3: Mainsail under test with reduced leech tension

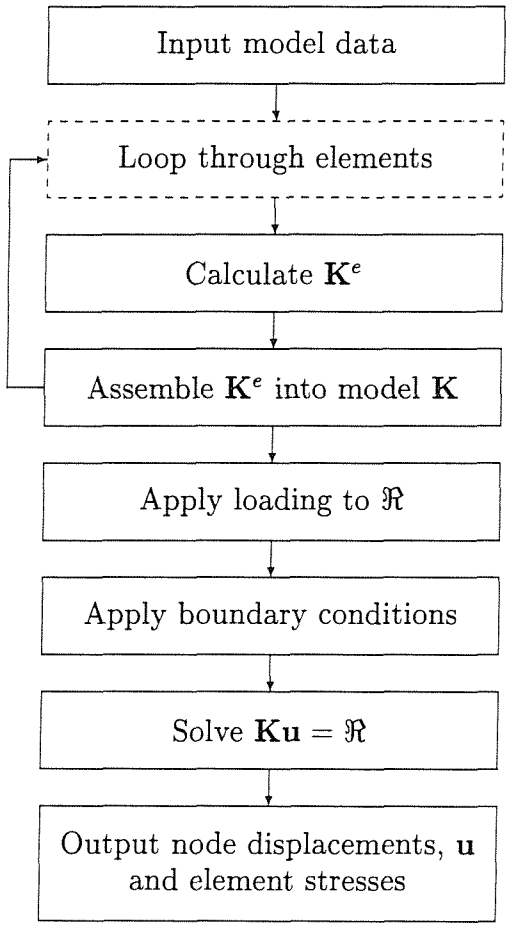

Figure 4: Program structure for linear finite element program

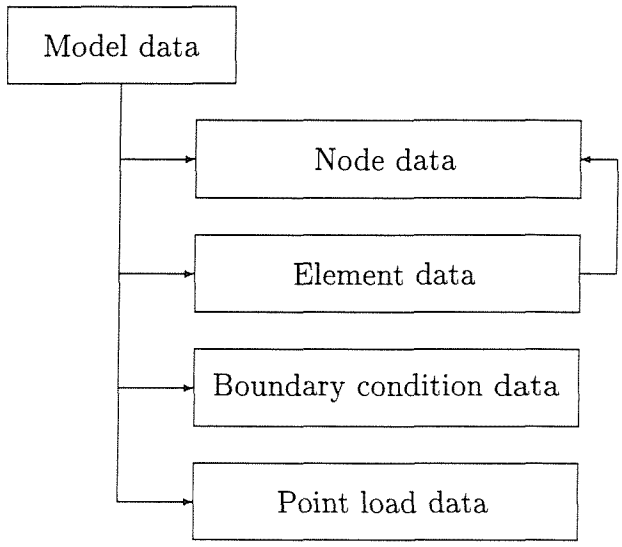

Figure 5: Arrangement of the data structure used in the linear finite element program

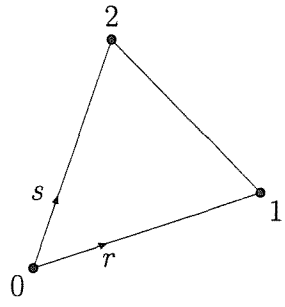

Figure 6: Linear triangular element natural coordinates

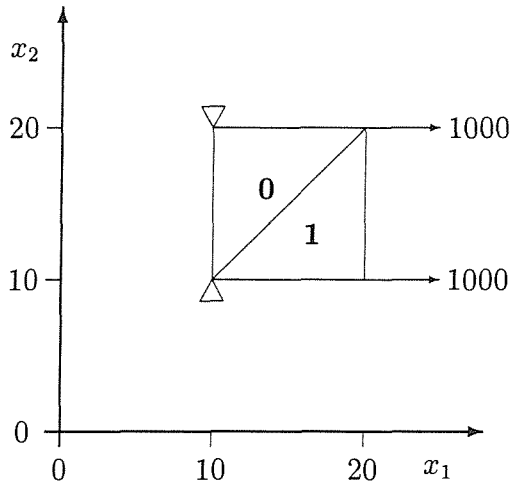

Figure 7: Two dimensional local coodinate validation model

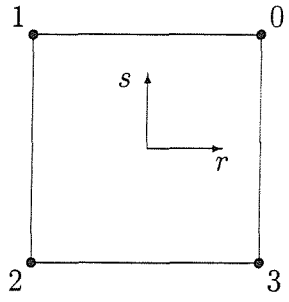

Figure 8: Four noded quadrilateral finite element

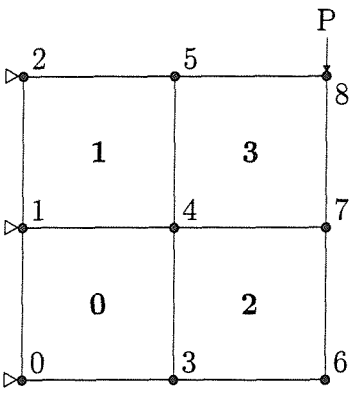

Figure 9: Four noded quadrilateral stress test model

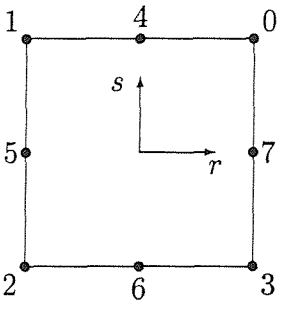

Figure 10: Eight noded quadrilateral finite element

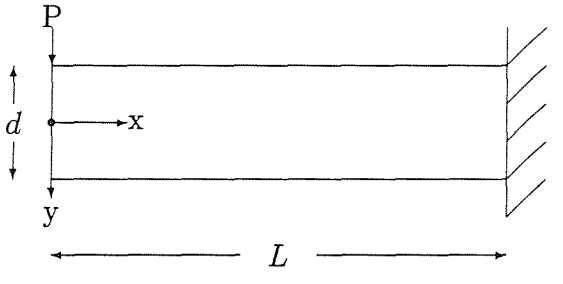

Figure 11: Timenshenko end loaded cantilever

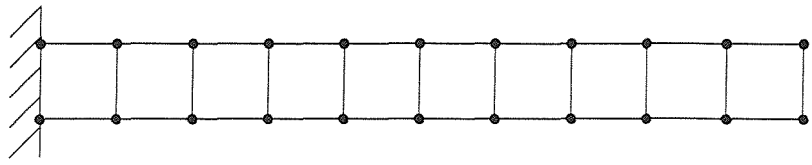

Figure 12: Four node quadrilateral cantilever analysis mesh

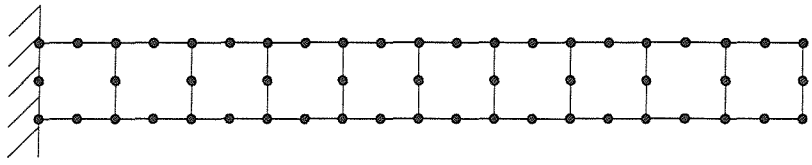

Figure 13: Eight node quadrilateral cantilever analysis mesh

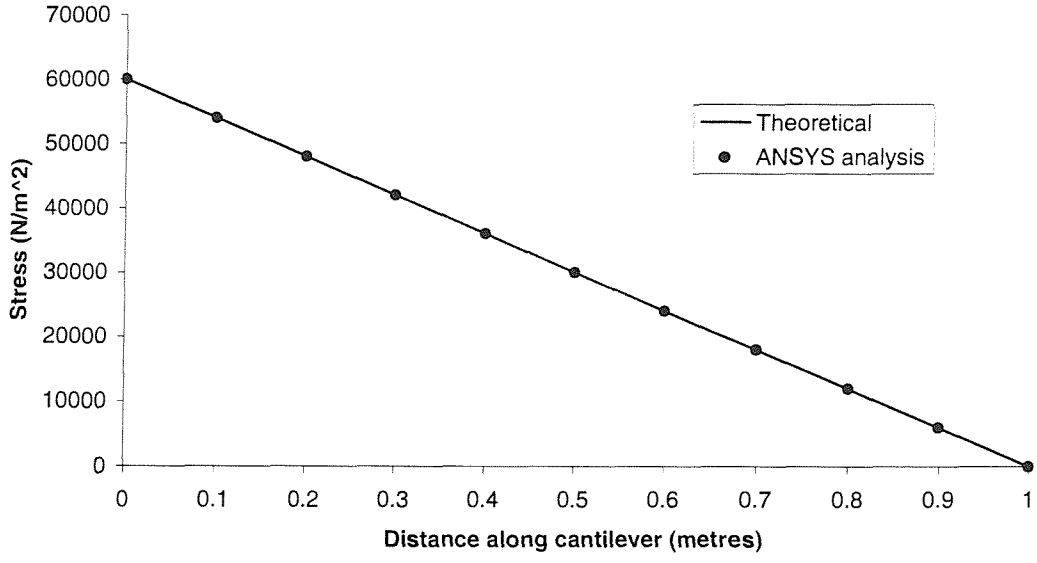

Figure 14: σ_{11} values for a tip loaded cantilever from Timenshenko theory and ANSYS analysis using 8 node quadrilateral elements

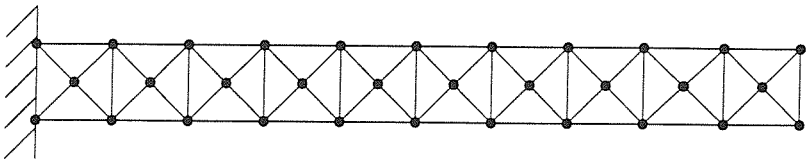

Figure 15: Three node triangle symmetrical mesh for cantilever analysis

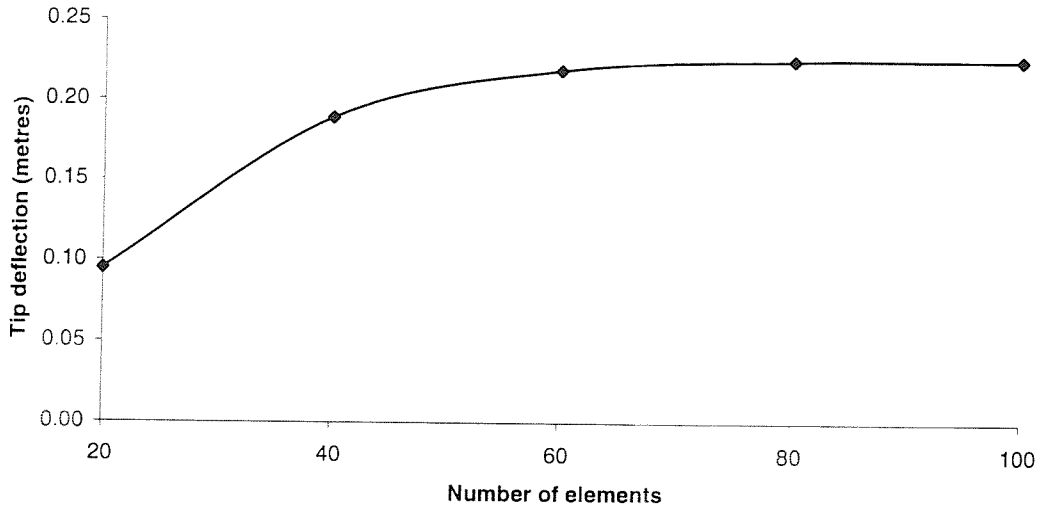

Figure 16: Tip deflection of point loaded cantilever modelled using symmetric mesh of three node triangular finite elements

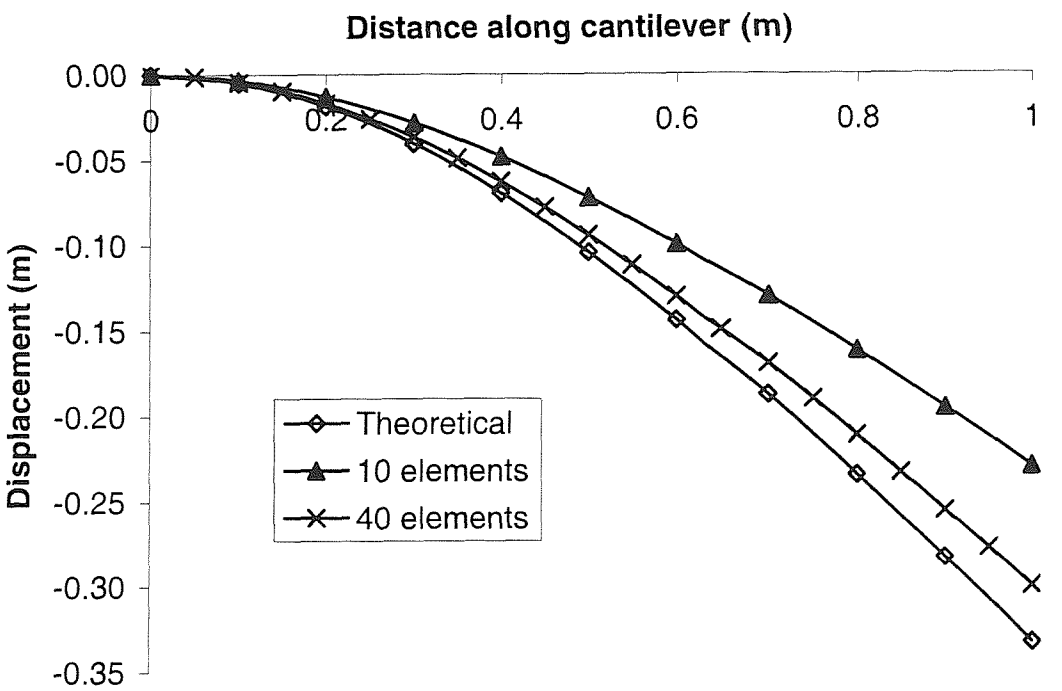

Figure 17: Deformed shape of tip loaded cantilever modelled using four node quadrilateral finite elements

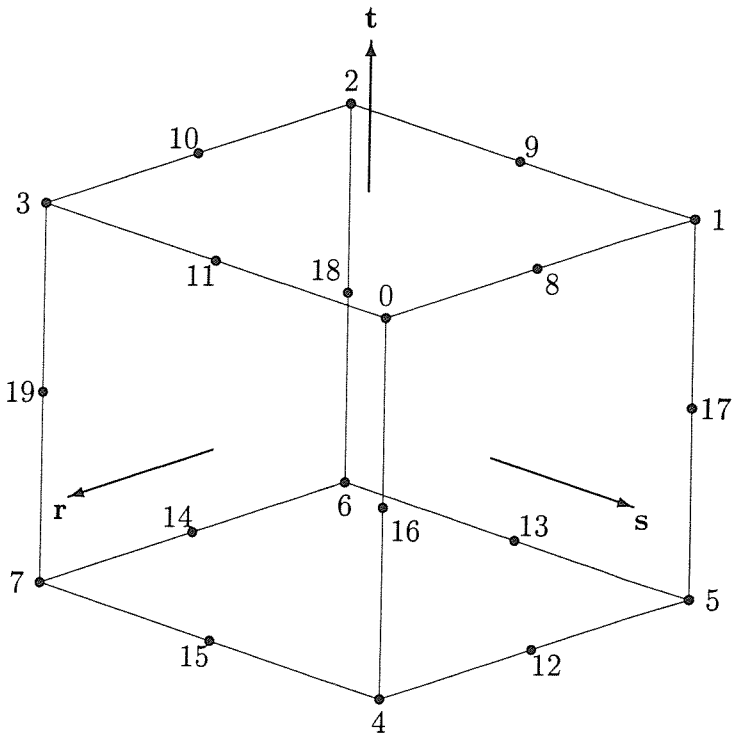

Figure 18: Twenty noded solid element

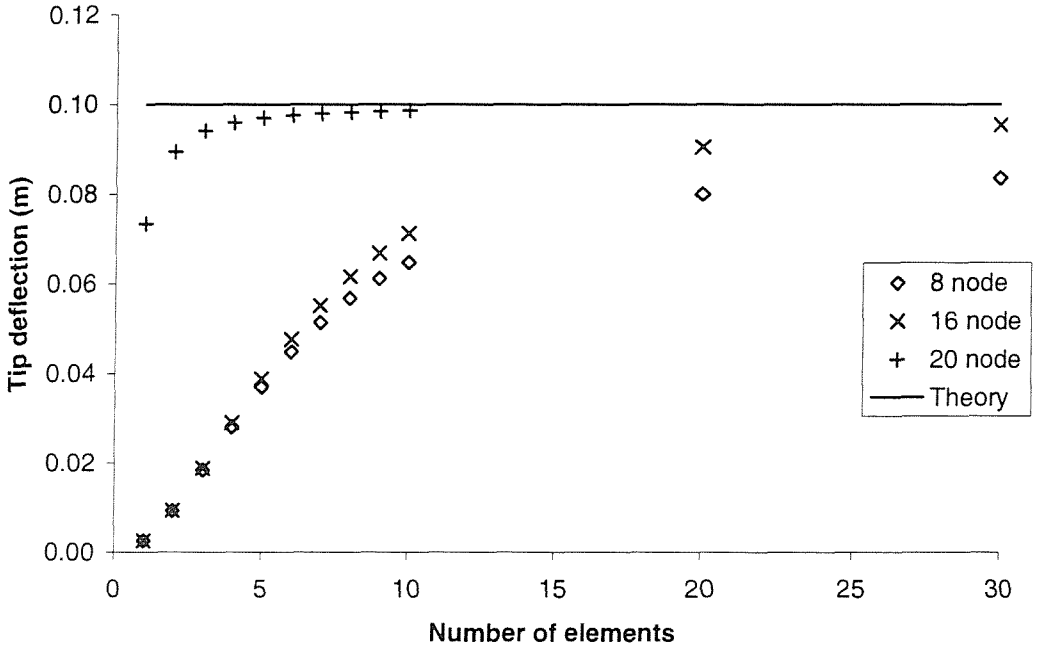

Figure 19: Tip deflections obtained from solid element analysis of a tip loaded cantilever

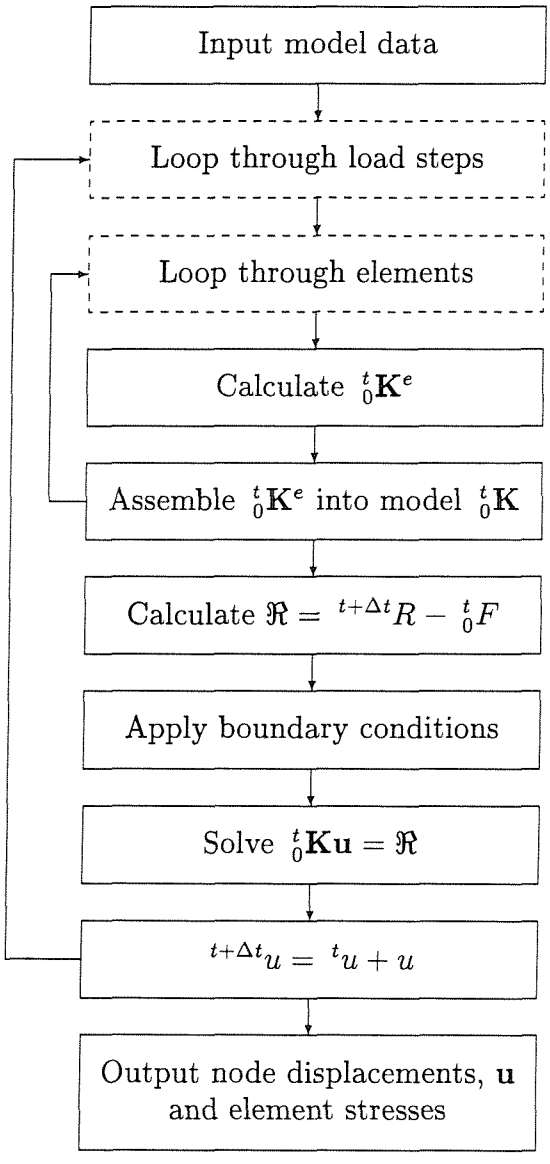

Figure 20: Program structure for non linear finite element program

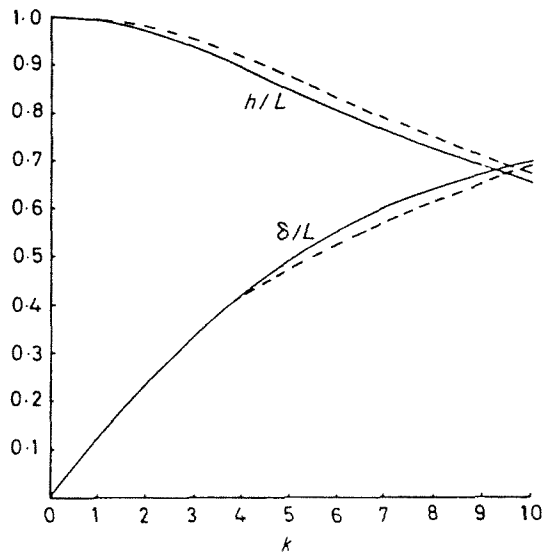

Figure 21: Theoretical deflections of uniformly loaded cantilever

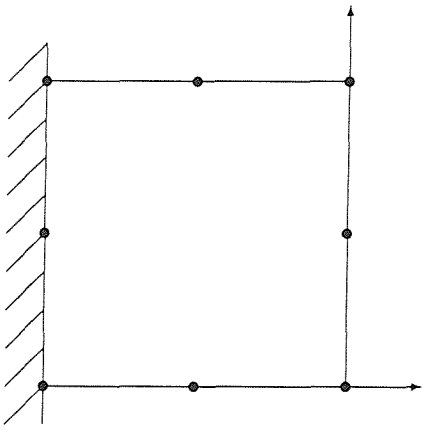

Figure 22: Single element model analysed by FENLA1

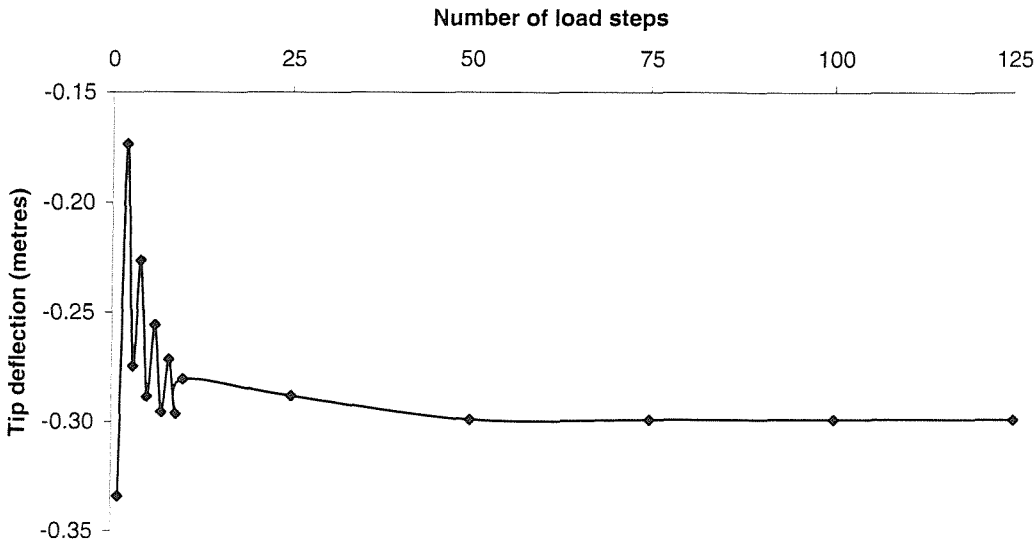

Figure 23: Tip deflection plotted against number of load steps for FENLA1 analysis of tip loaded cantilever

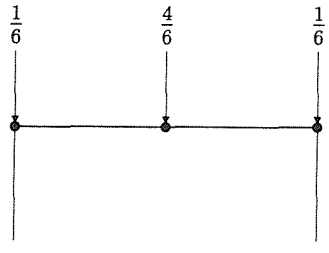

Figure 24: Lumped nodal loading for a uniformly distributed load of 1N on a side of an eight noded quadrilateral element

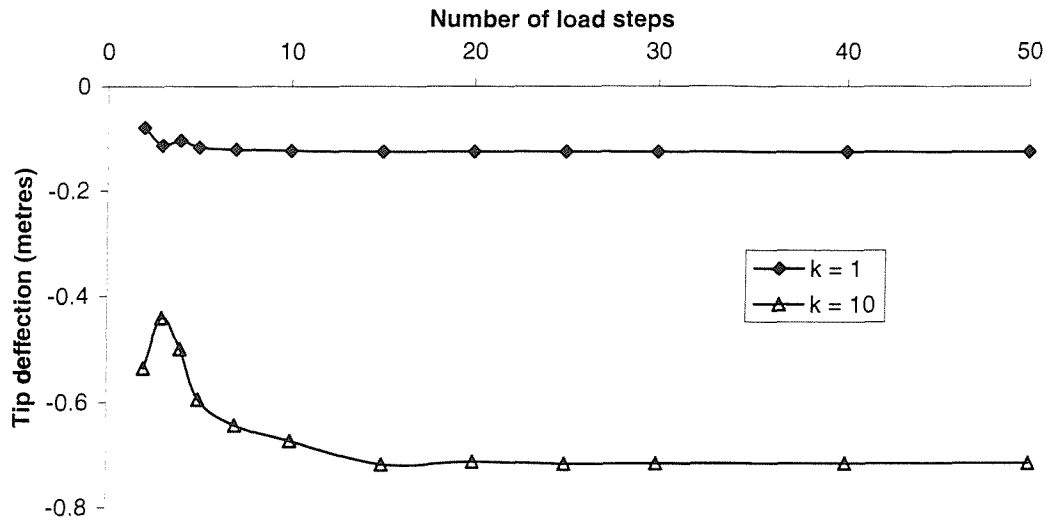

Figure 25: Tip deflection plotted against number of load steps for FENLA1 analysis of distributed loaded cantilever

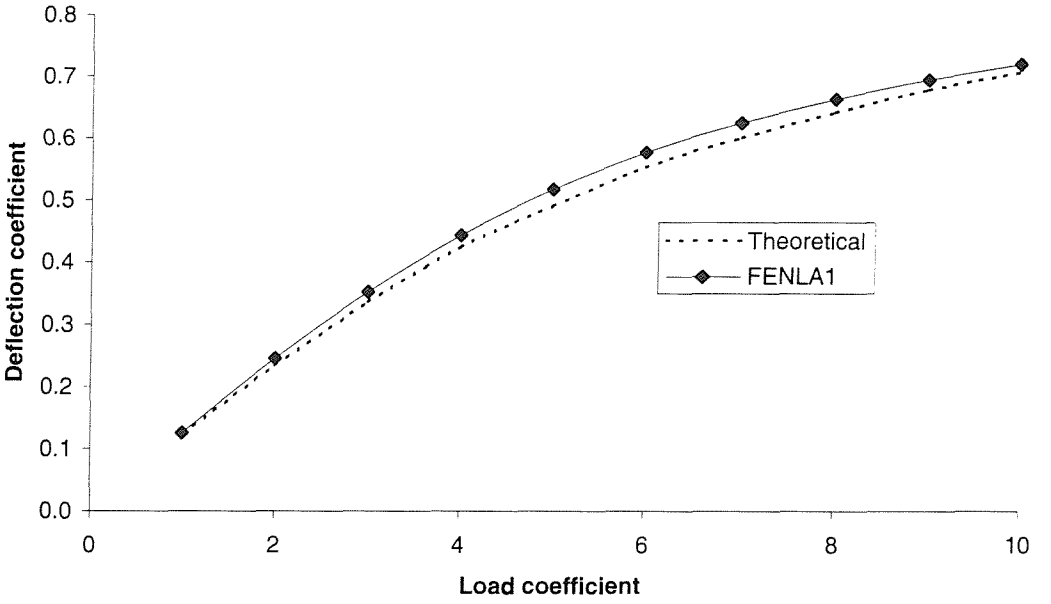

Figure 26: Deflection coefficient coefficient plotted against load factor for FENLA1 analysis of distributed loaded cantilever

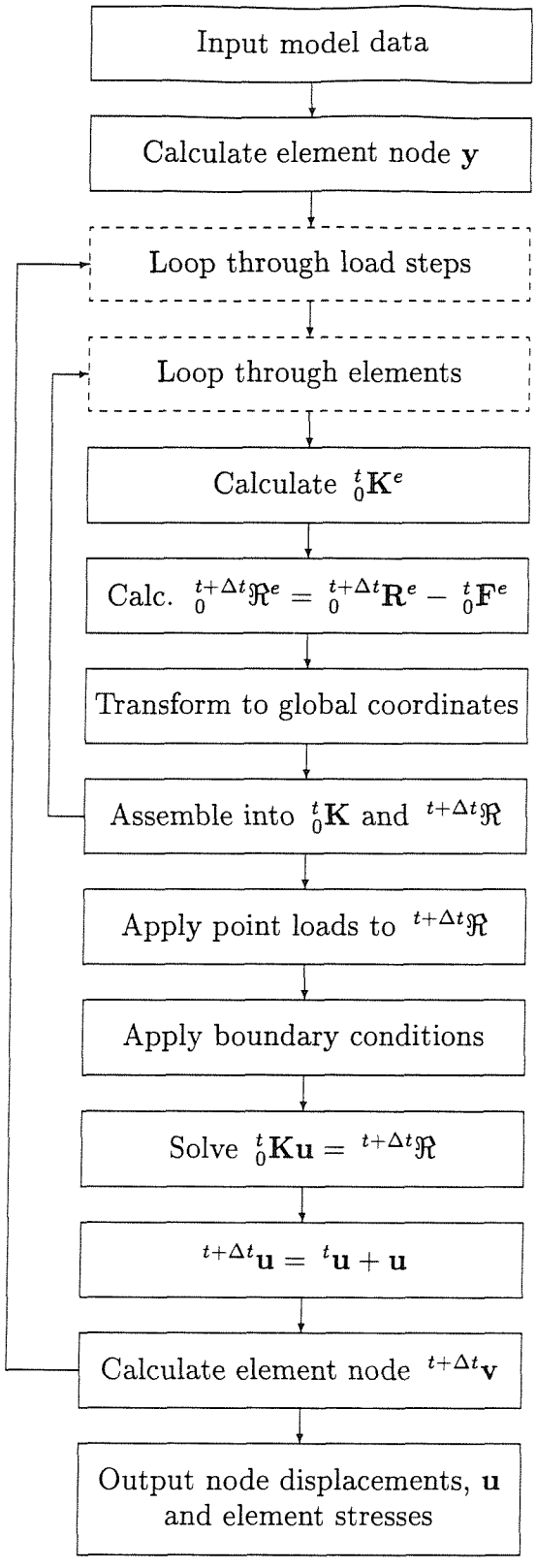

Figure 27: Program structure for non linear membrane finite element program

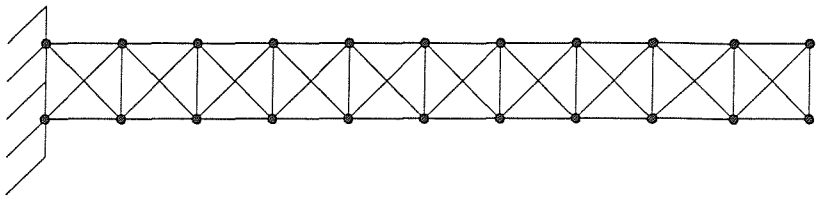

Figure 28: 40 element mesh used for analysis of cantilever using FENLA3-3

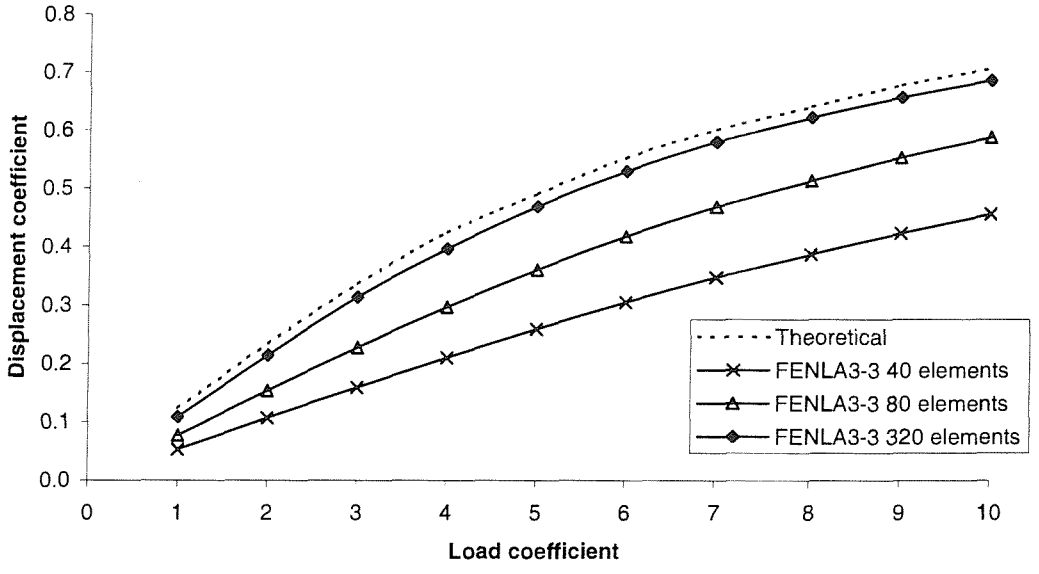

Figure 29: Tip deflection coefficient plotted against load coefficient for FENLA3-3 analysis of distributed loaded cantilever

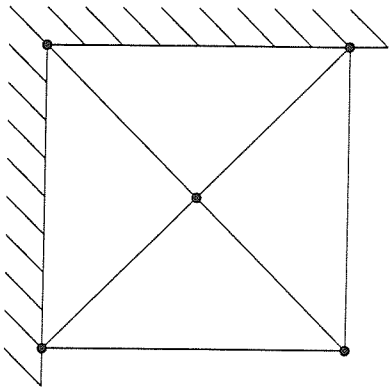

Figure 30: FENLA3-3 four element square membrane model

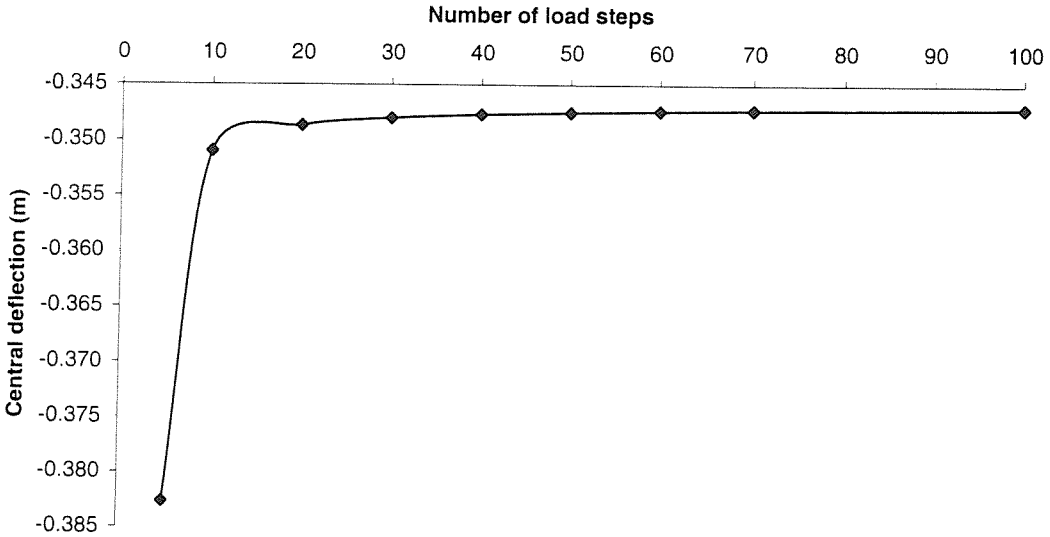

Figure 31: Central deflection of point loaded square membrane analysed by FENLA3-3 plotted against number of load steps

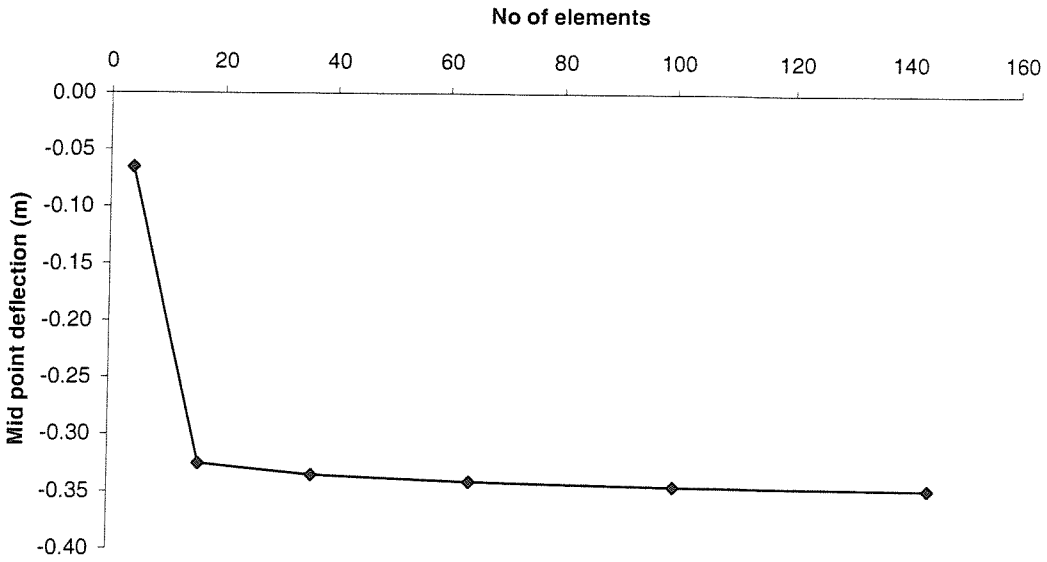

Figure 32: Central deflection of point loaded square membrane, analysed by FENLA3-3 using 100 load steps, plotted against number of elements

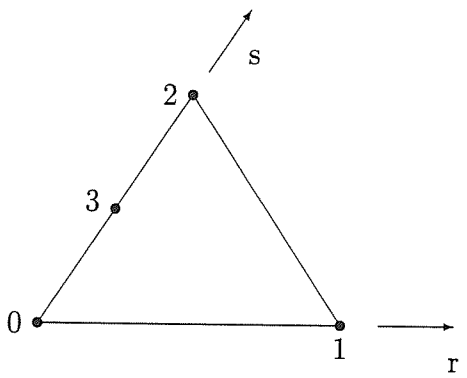

Figure 33: Four node triangular membrane element

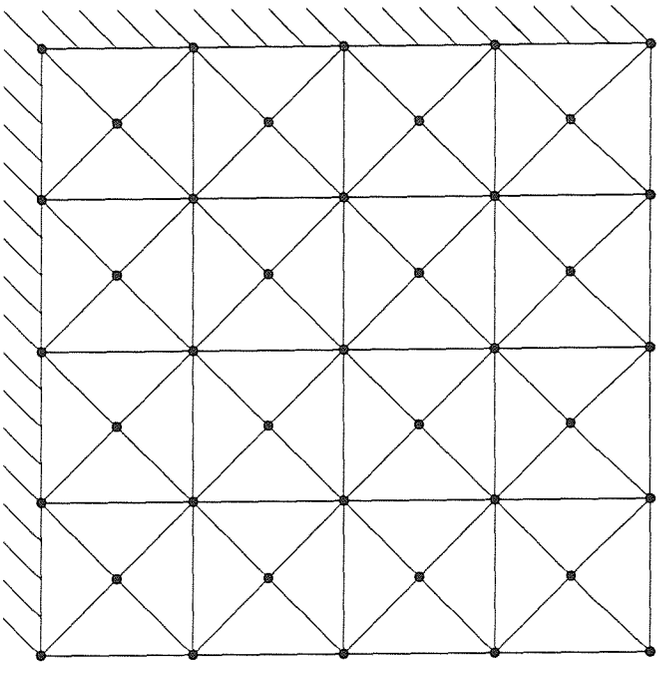

Figure 34: FENLA3-3 64 symmetric element model

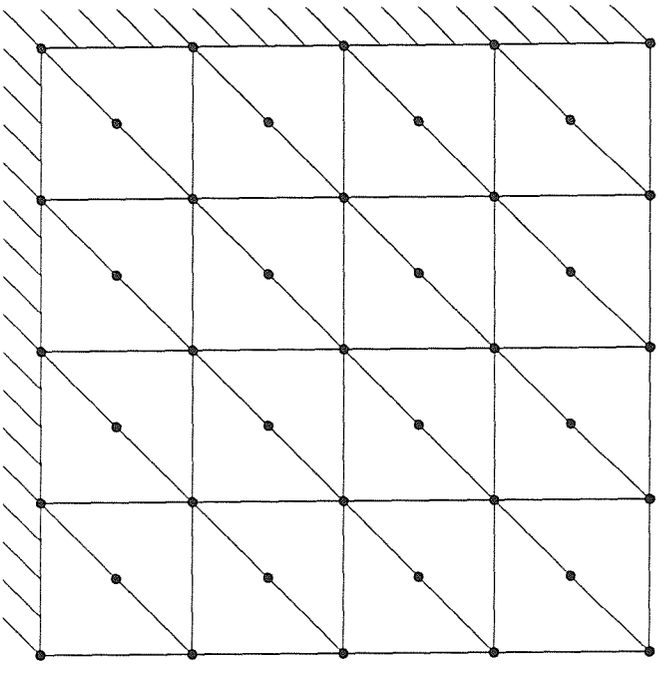

Figure 35: FENLA3-3 32 asymmetric element model

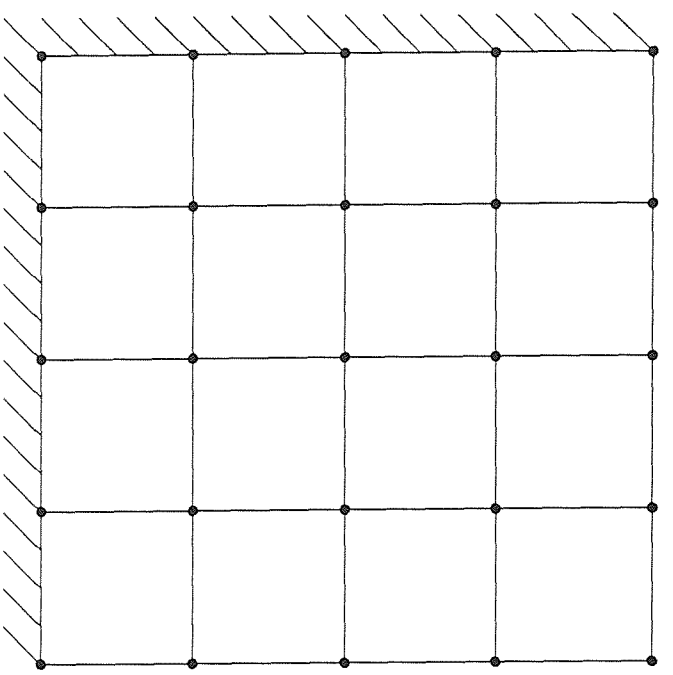

Figure 36: FENLA4 16 element model

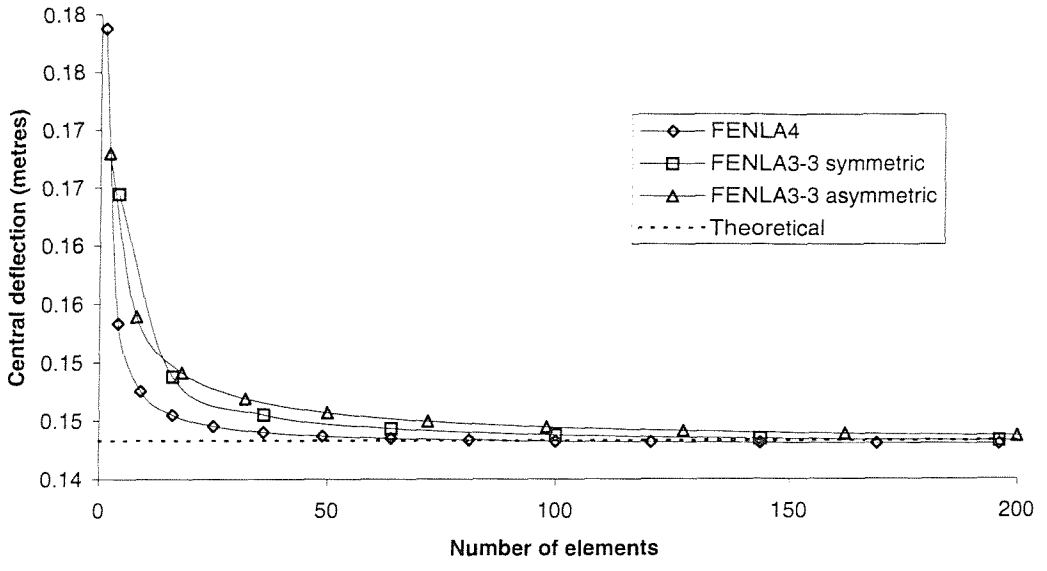

Figure 37: Central deflection of pressure loaded square membrane, analysed by FENLA3-3 and FENLA4, plotted against number of elements

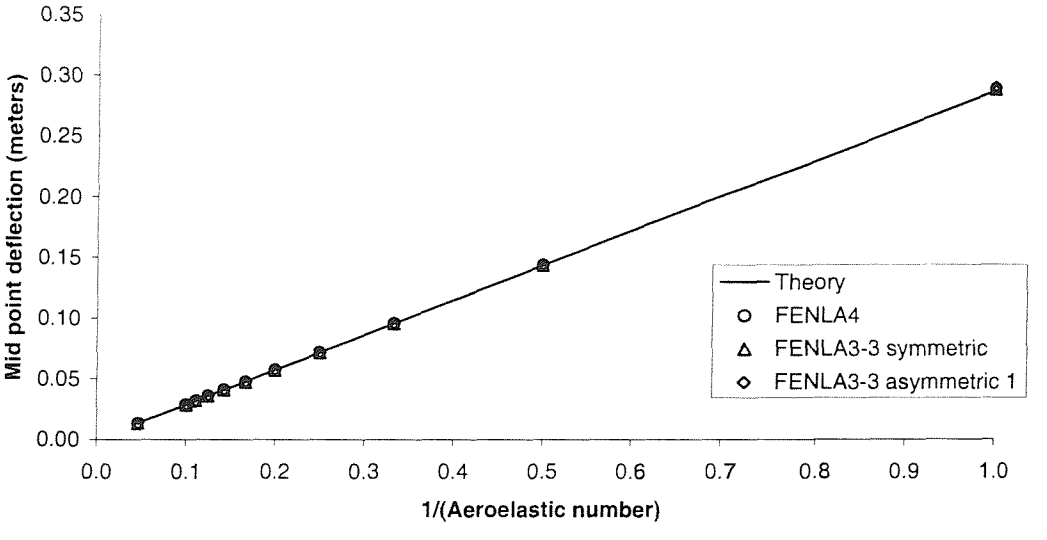

Figure 38: Central deflection of pressure loaded square membrane, analysed by FENLA3-3 and FENLA4, plotted against aeroelastic number

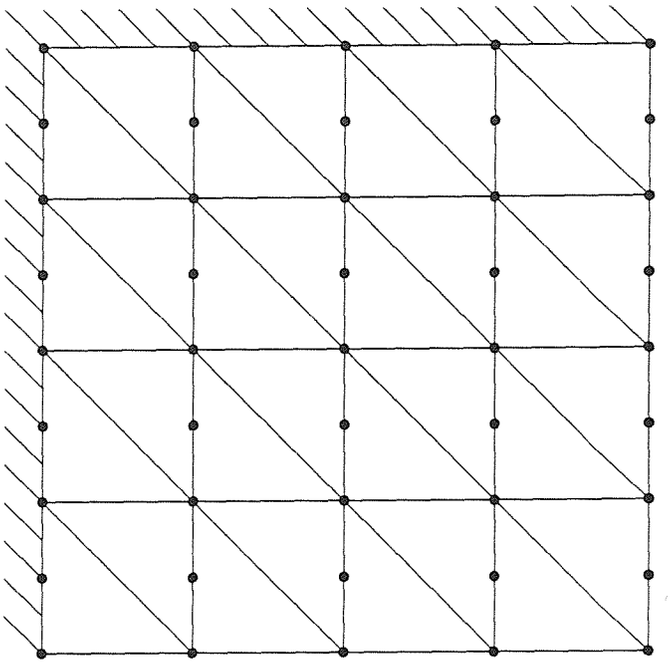

Figure 39: FENLA3-4 32 element square membrane model

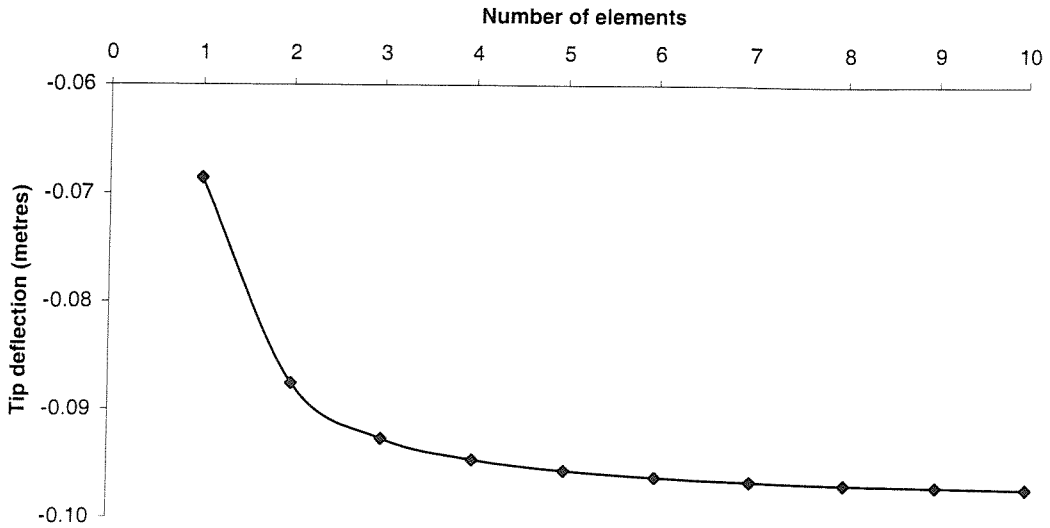

Figure 40: Tip deflection of tip loaded cantilever analysed by FENLA5 with 20 node elements plotted against number of elements

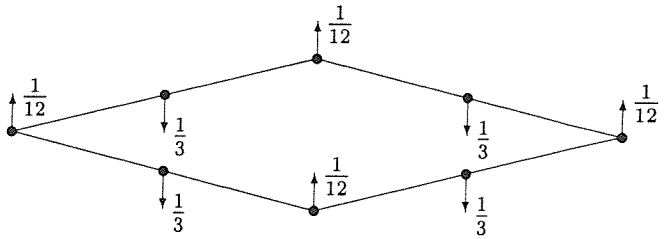

Figure 41: Equivalent nodal loads for pressure loaded face of a 20 node solid element

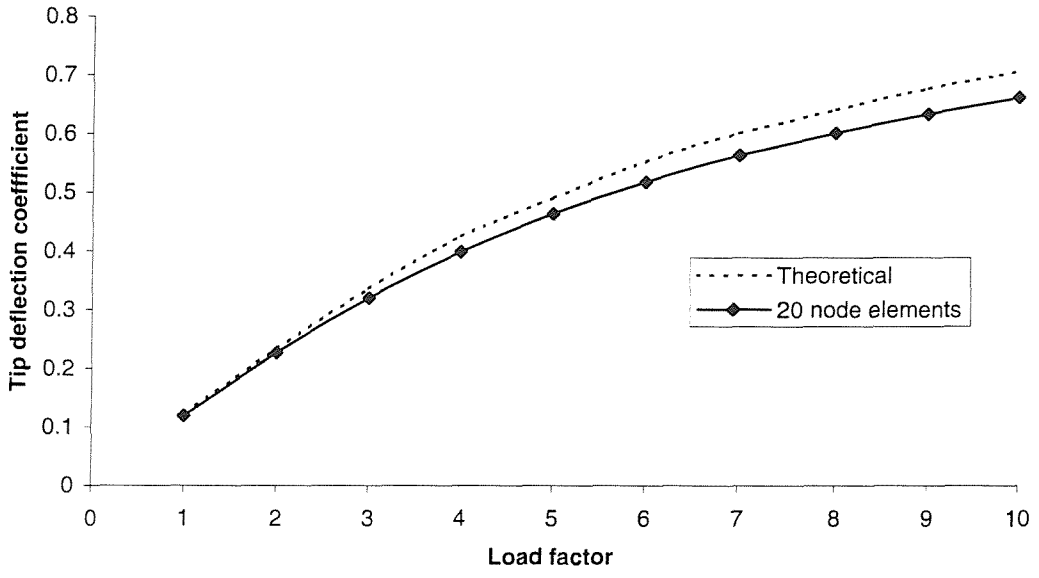

Figure 42: Tip deflection of distributed loaded cantilever, modelled using 20 node elements, analysed by FENLA5 using 20 load steps, plotted against load coefficient

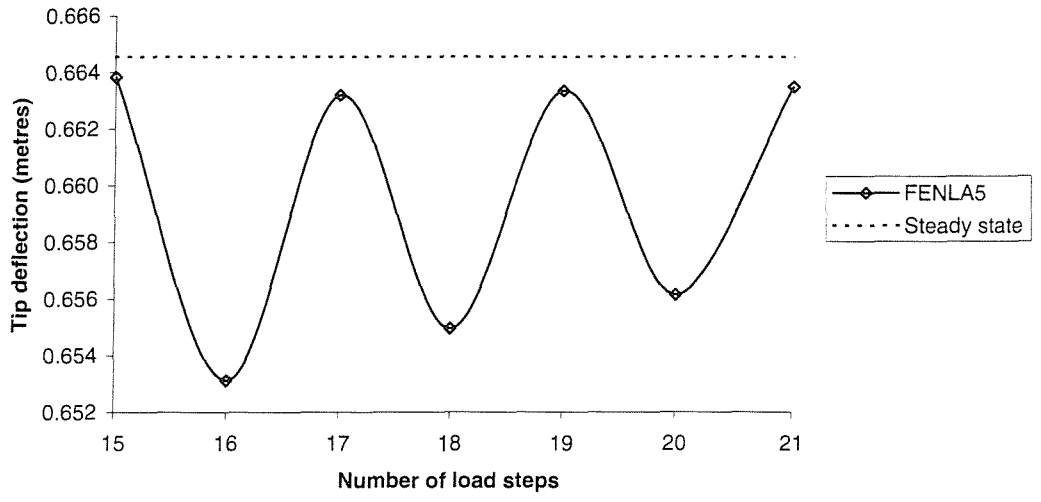

Figure 43: Tip deflection of distributed loaded cantilever with load coefficient 10, analysed by non iterative FENLA5-20, plotted against number of load steps

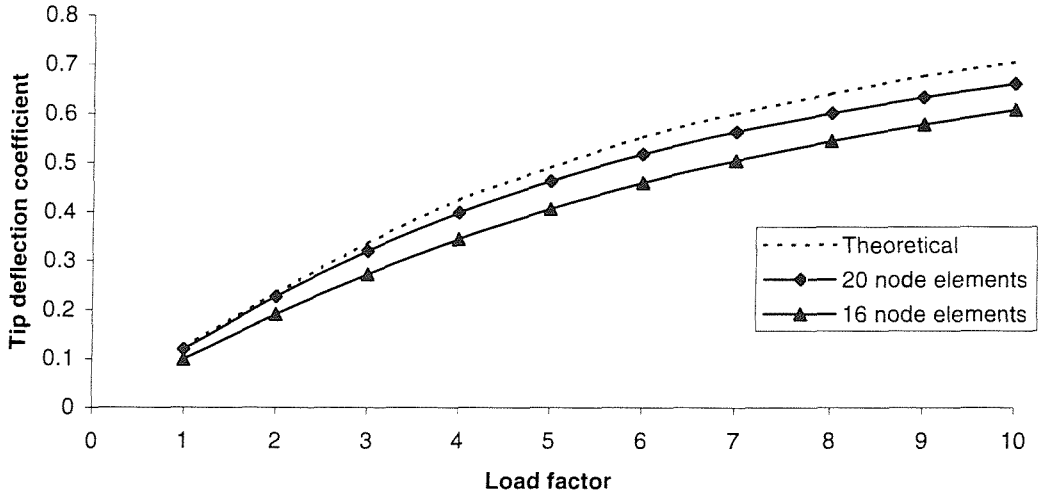

Figure 44: Tip deflection coefficient of distributed loaded cantilever, analysed by FENLA5-16 and FENLA5-20, plotted against load coefficient

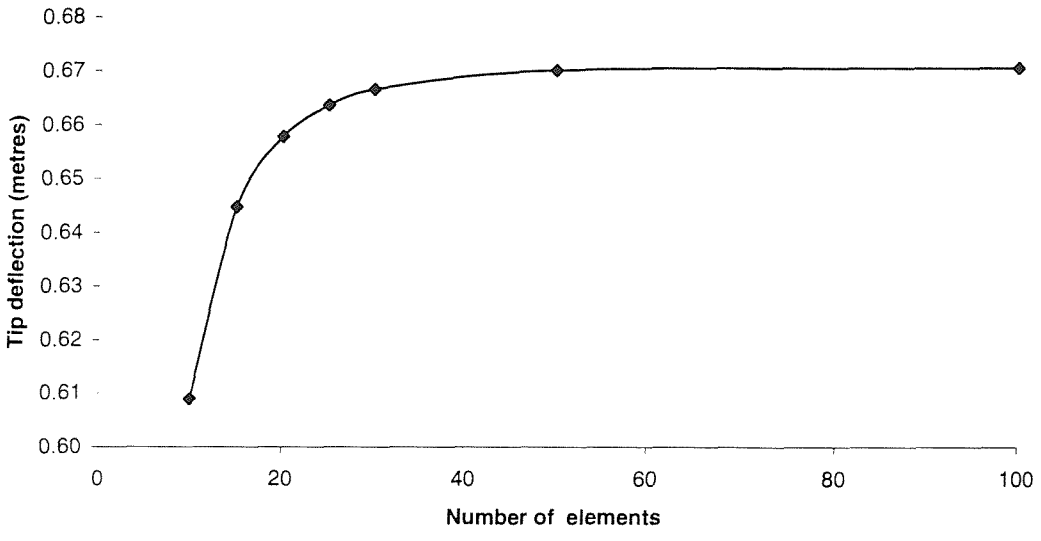

Figure 45: Tip deflection of distributed loaded cantilever with load factor 10, analysed by FENLA5-16 plotted against number of elements

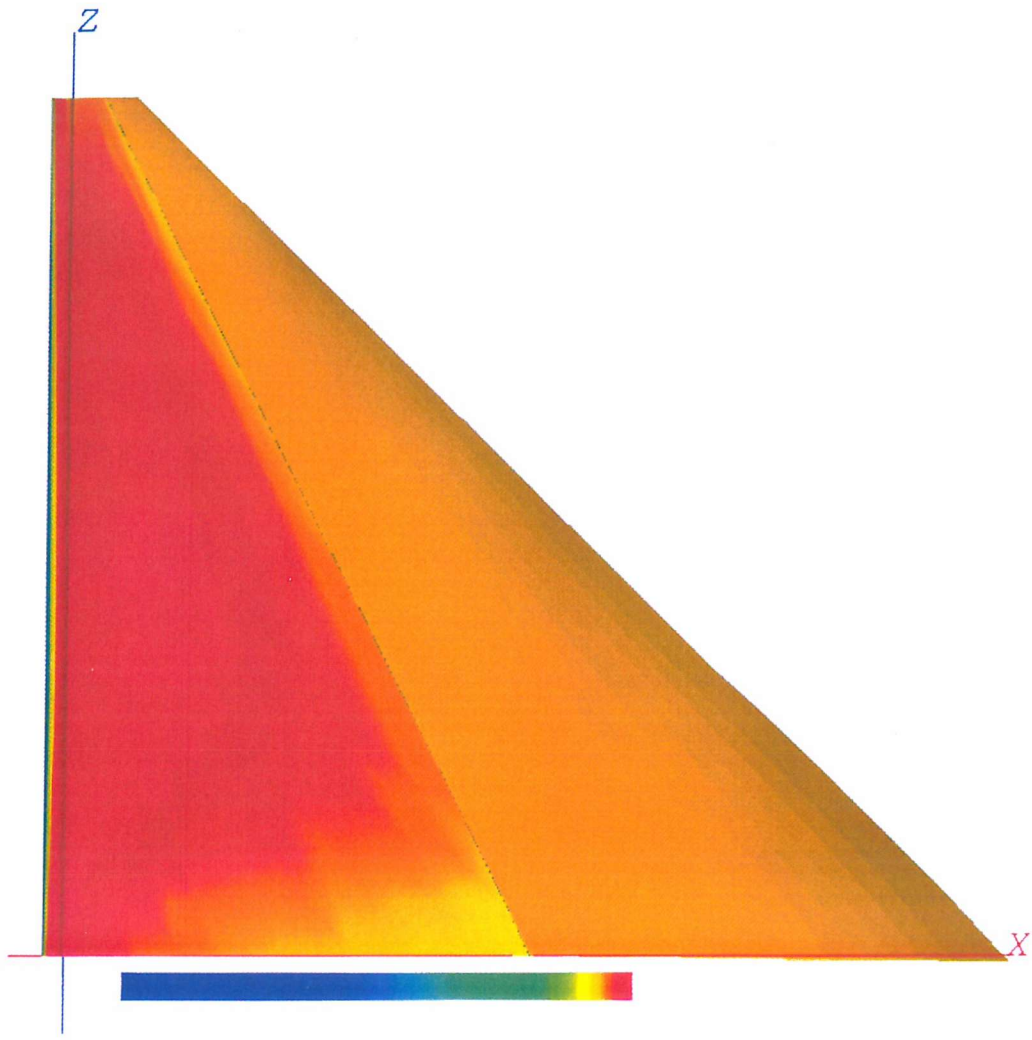

Figure 46: Pressure distribution on the windward side of a mast sail model calculated during aeroelastic analysis (including wake sheet). Pressure coefficient ranging from 1.0 to -2.0 in this figure

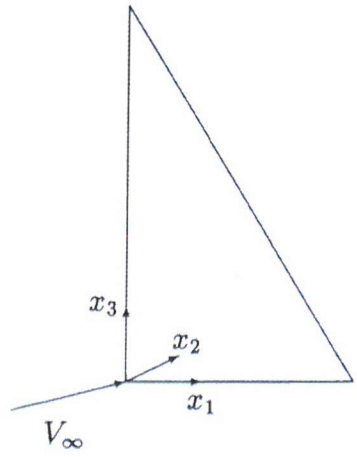

Figure 47: Model orientation for aeroelastic analysis

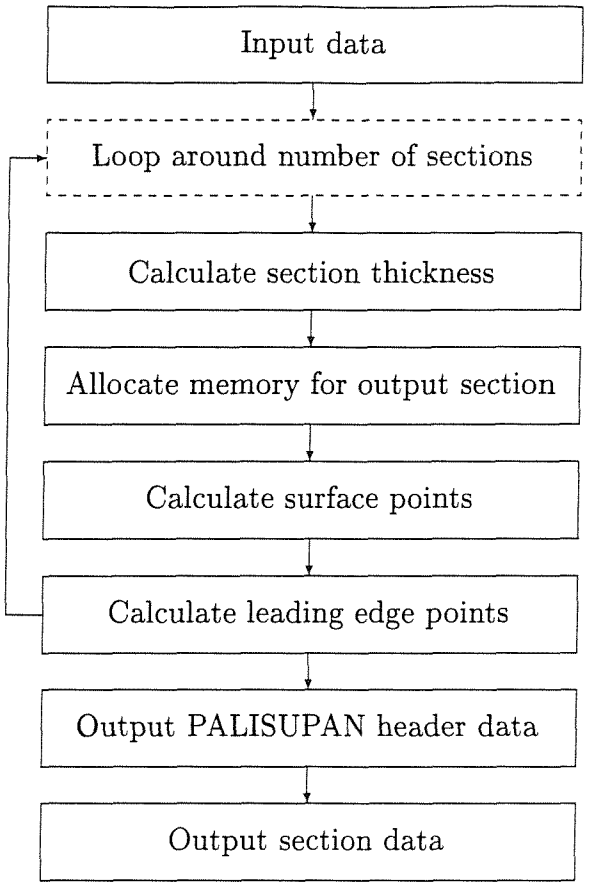

Figure 48: F-2-P program structure

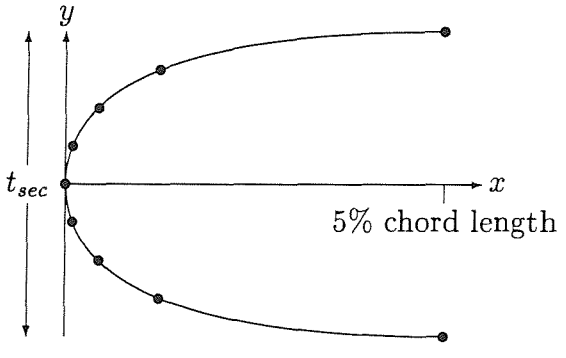

Figure 49: Leading edge ellipse definition for flat membrane

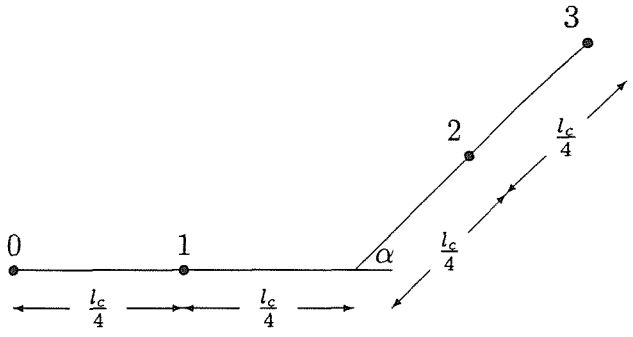

Figure 50: Bezier control points used for flat membrane wake generation

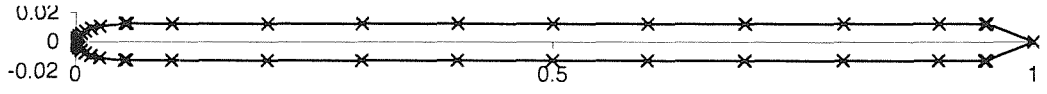

Figure 51: Cross section of flat membrane PALISUPAN geometry

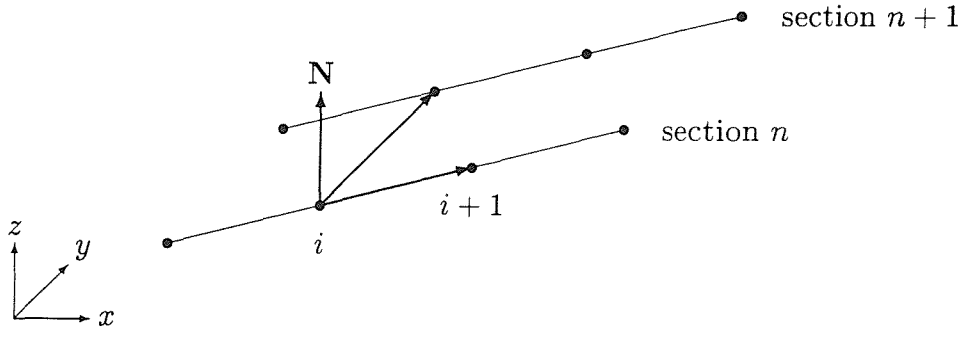

Figure 52: Normal calculations used for straight line sections in F-2-P-II

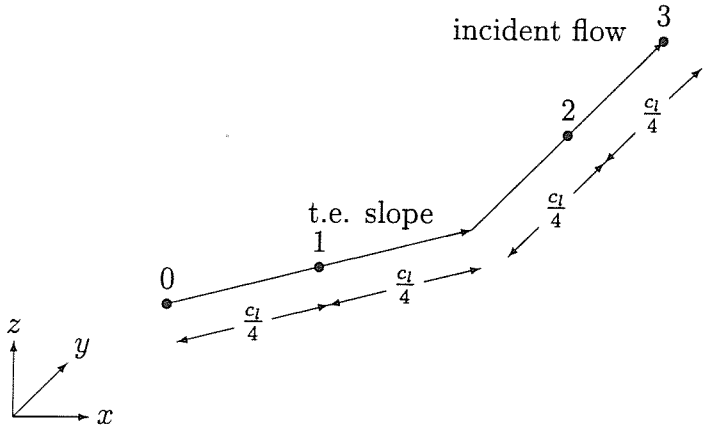

Figure 53: Bezier control points for three dimensional curves

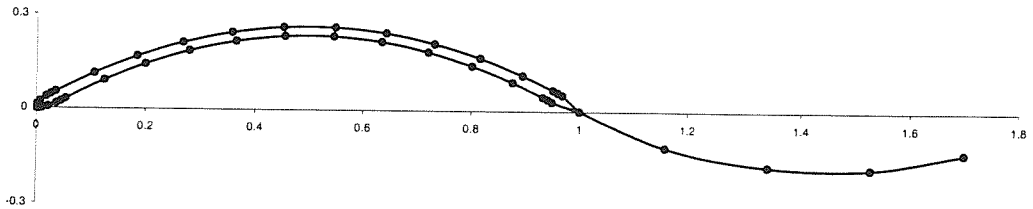

Figure 54: Cross section of curved membrane PALISUPAN section

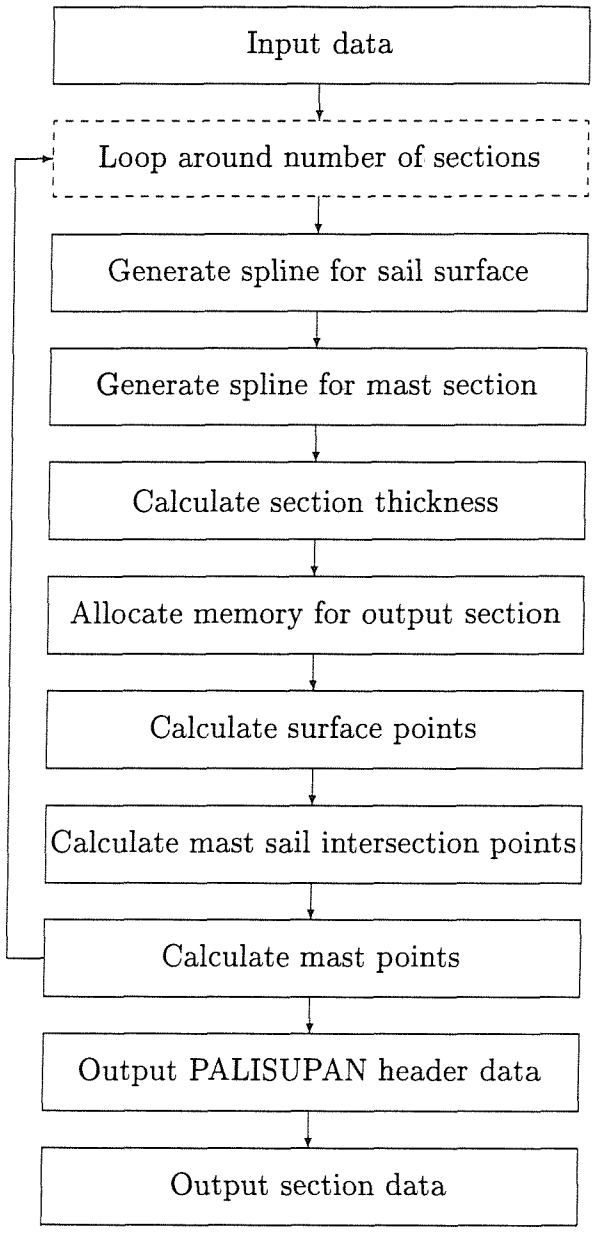

Figure 55: Rig model generation program structure

Figure 56: Direction of mast and sail splines. Mast and sail shown separated for clarity

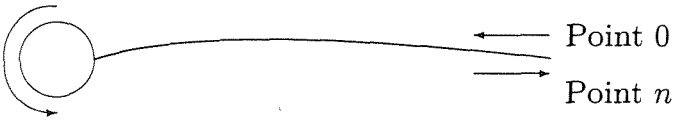

Figure 57: Order of points defining the PALISUPAN output section

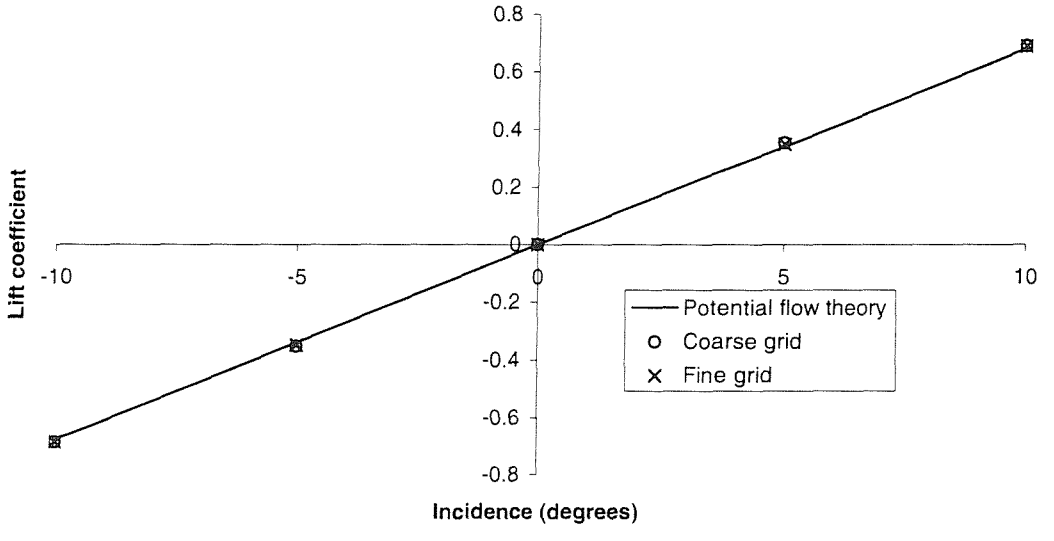

Figure 58: Lift coefficient against α, obtained by PALISUPAN analysis of flat membrane

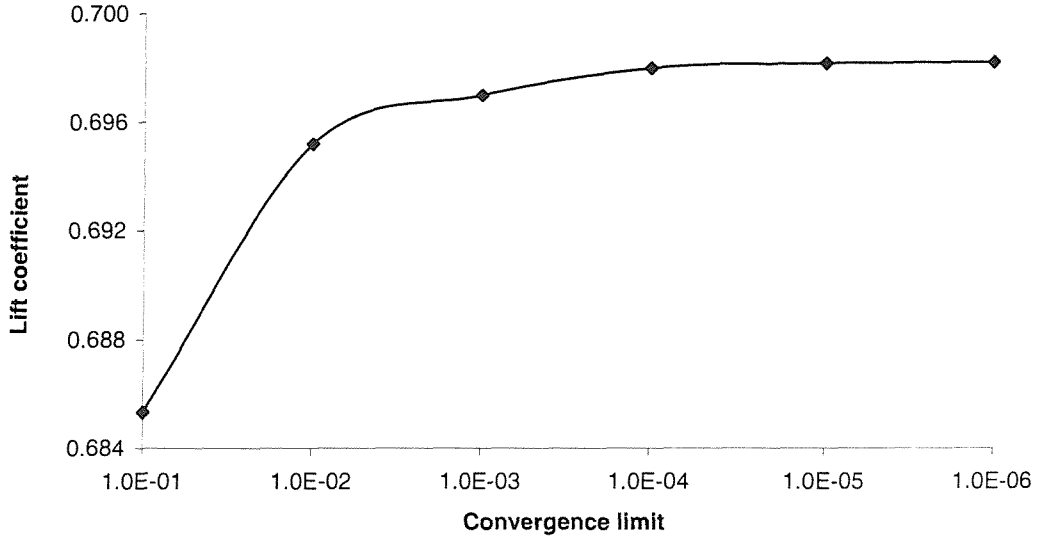

Figure 59: Effect of BMCC on lift coefficient calculated by PALISUPAN for a rectangular flat membrane

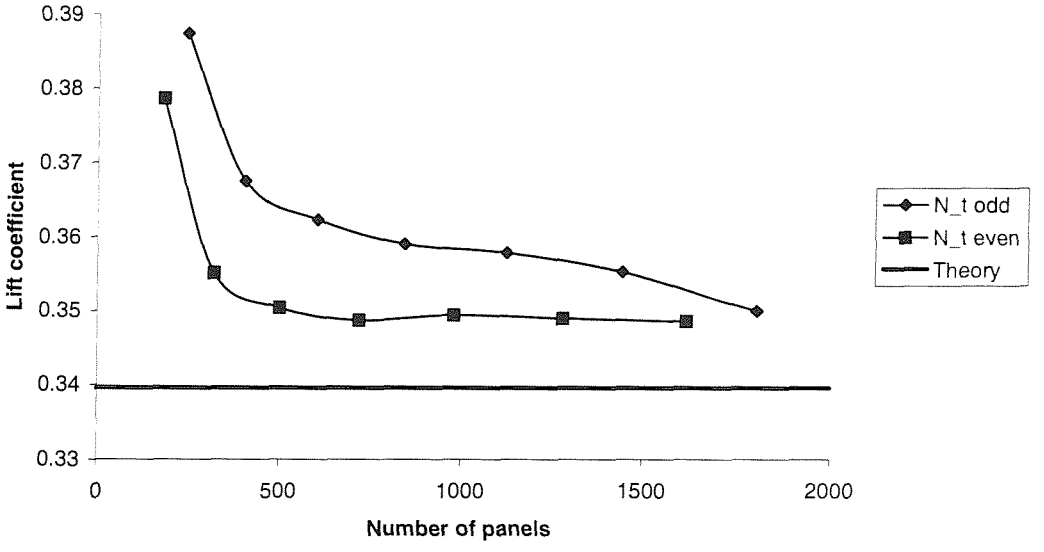

Figure 60: Effect of odd/even number of chordwise panels on lift coefficient for a rectangular flat membrane

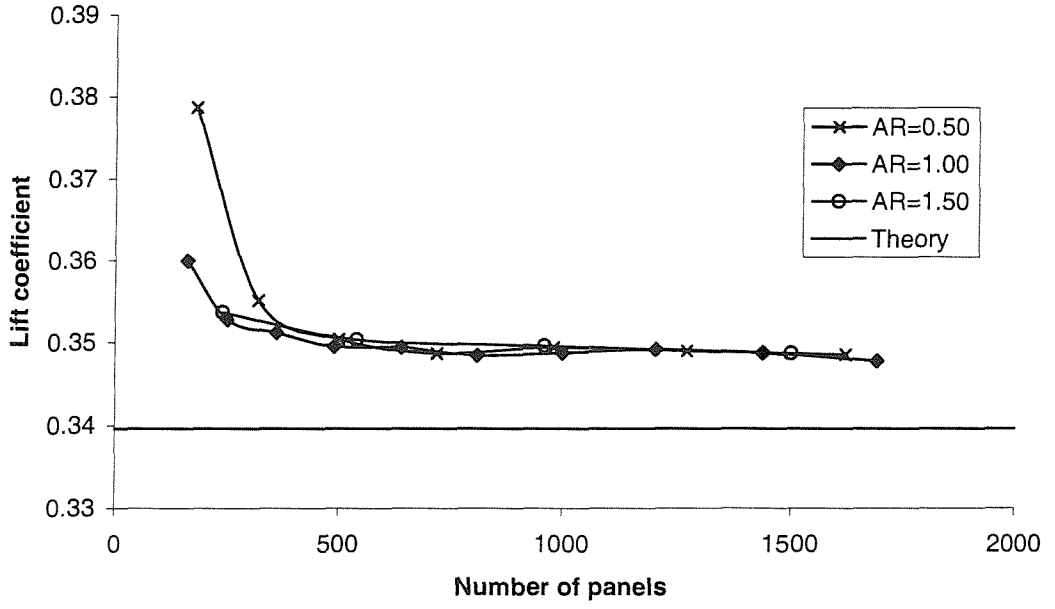

Figure 61: Effect of panel aspect ratio on lift coefficient for a rectangular flat membrane

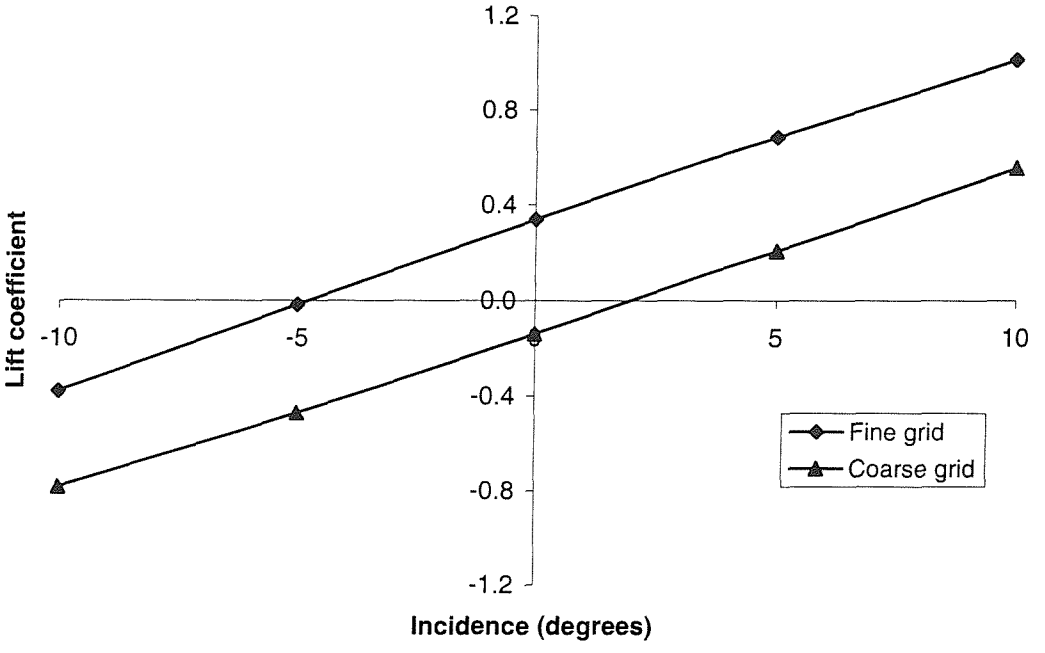

Figure 62: Plot of lift coefficient calculated by PALISUPAN for curved membrane against α

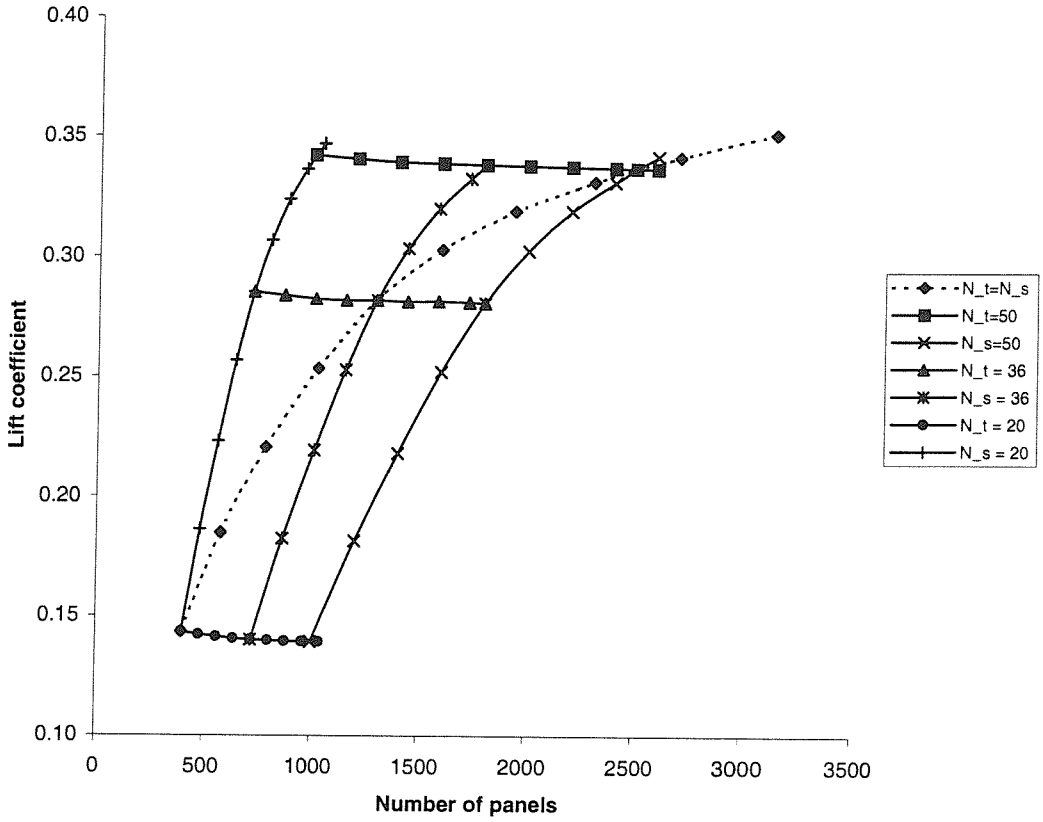

Figure 63: Lift coefficient for a curved membrane, aspect ratio 5, for various PALISUPAN panel densities

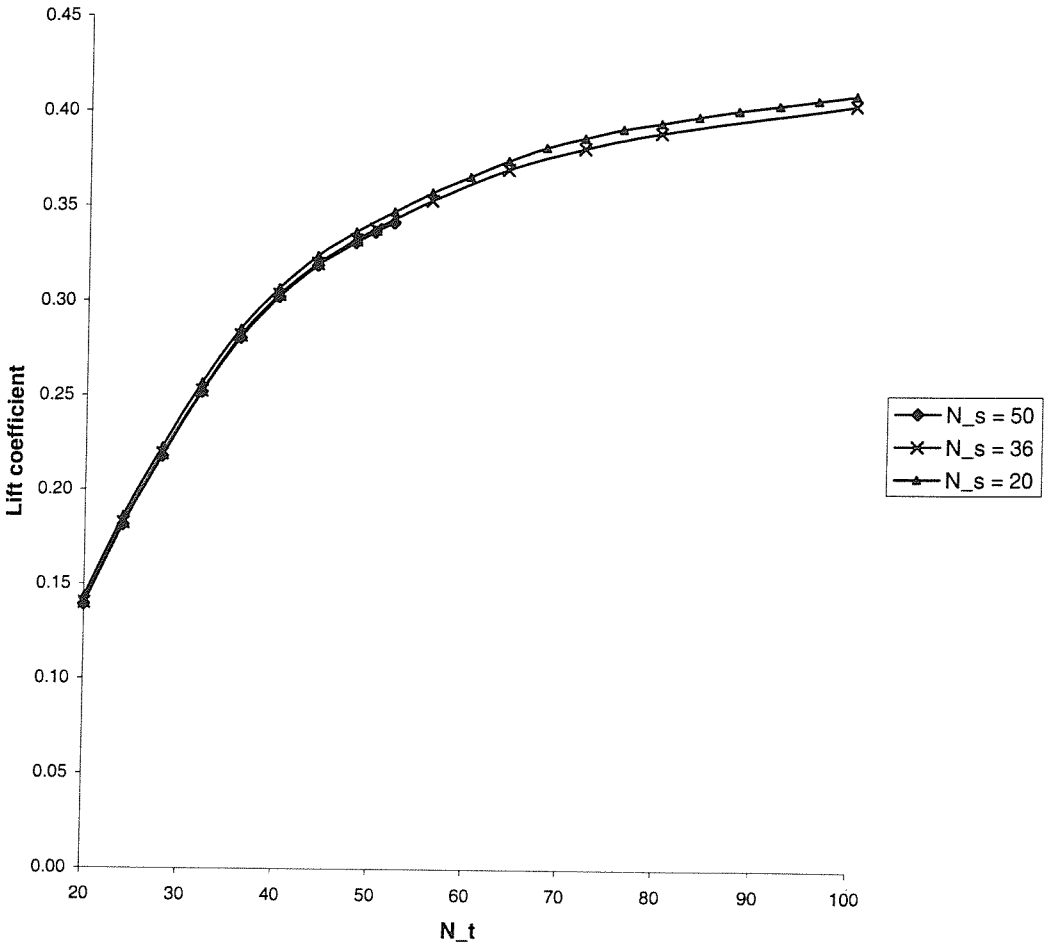

Figure 64: Lift coefficient for a curved membrane, aspect ratio 5, for various PALISUPAN panel densities with constant N_s

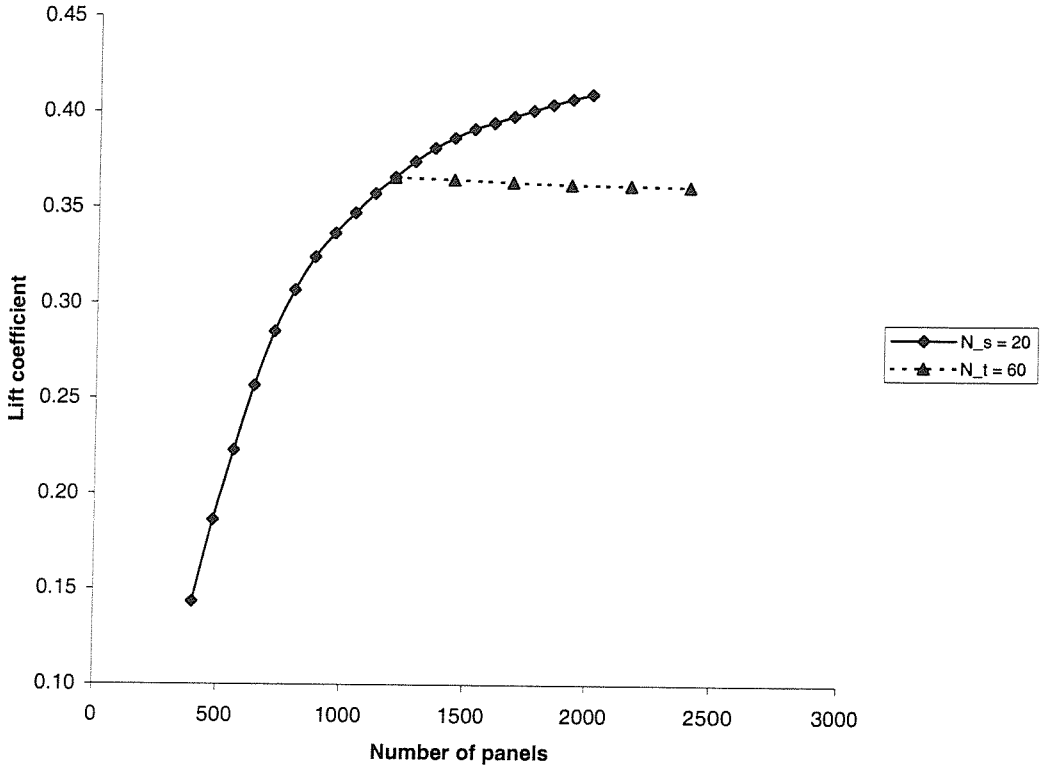

Figure 65: Lift coefficient for a curved membrane using $N_t = 60$ and for $N_s = 20$ with high N_t

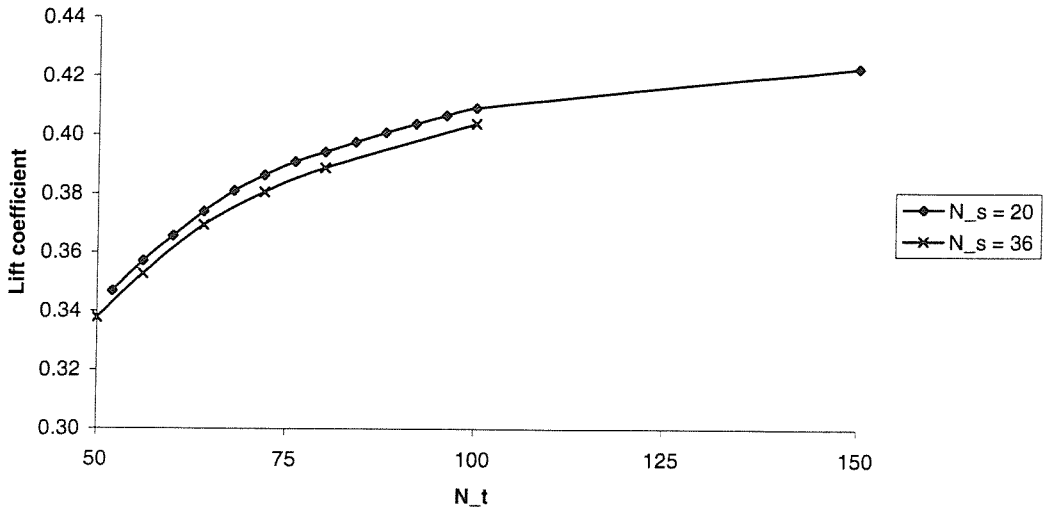

Figure 66: Lift coefficient for a curved membrane with large numbers of chordwise panels

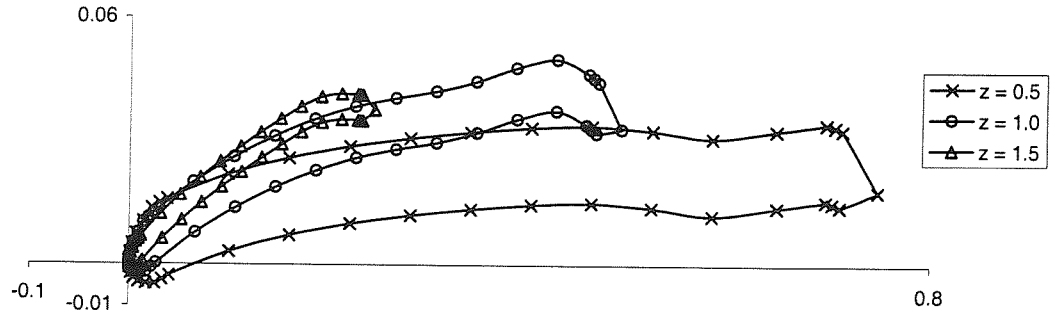

Figure 67: Deformed triangular membrane PALISUPAN input sections

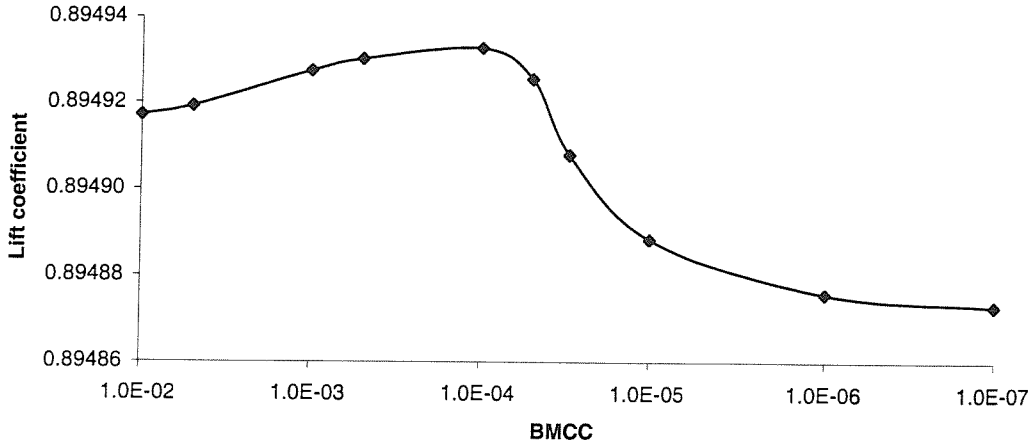

Figure 68: Effect of BMCC value on lift coefficient for deformed triangular membrane

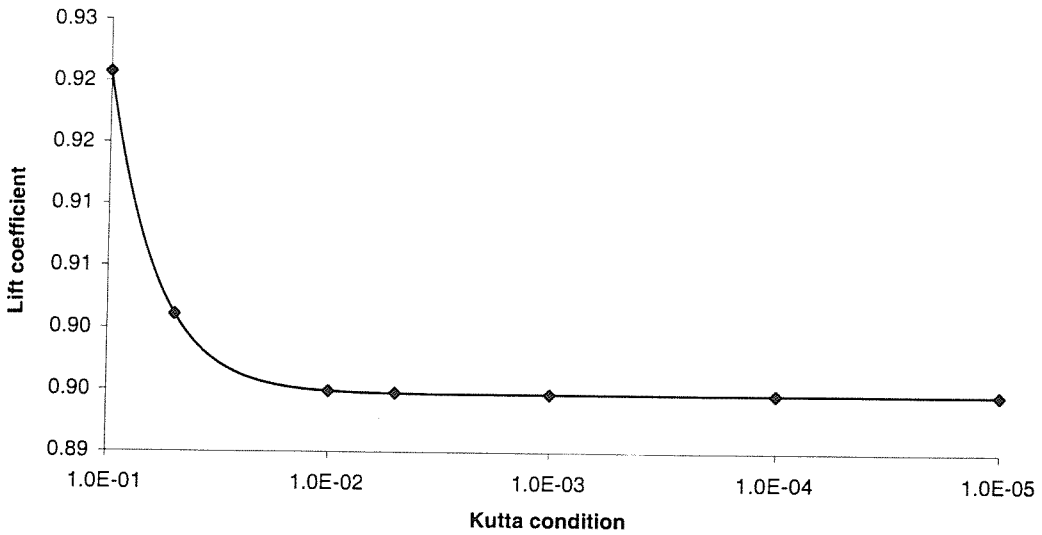

Figure 69: Effect of Kutta convergence limit on lift coefficient for deformed triangular membrane

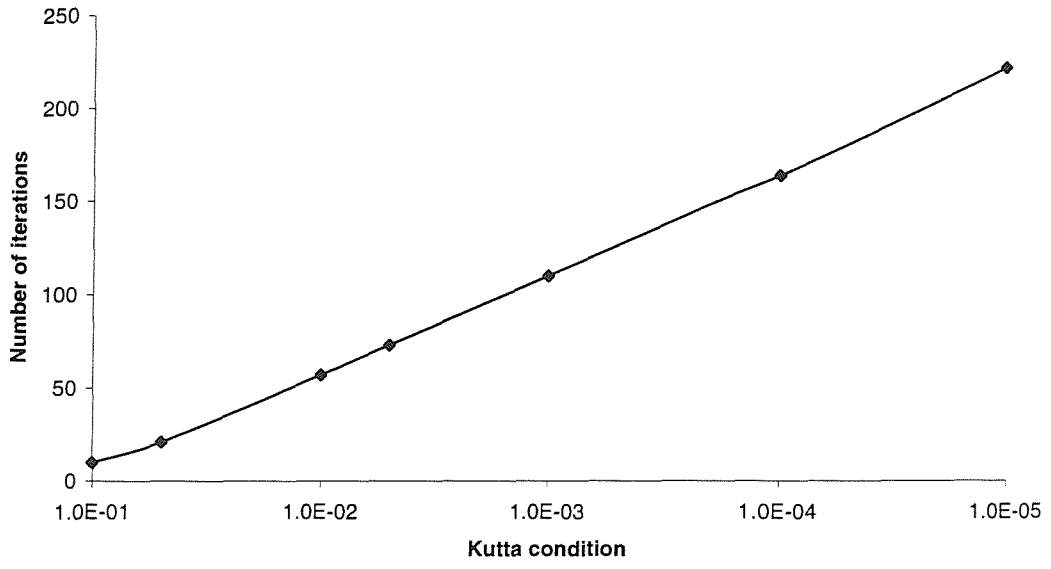

Figure 70: Number of iterations required to solve deformed membrane with varying Kutta condition limits

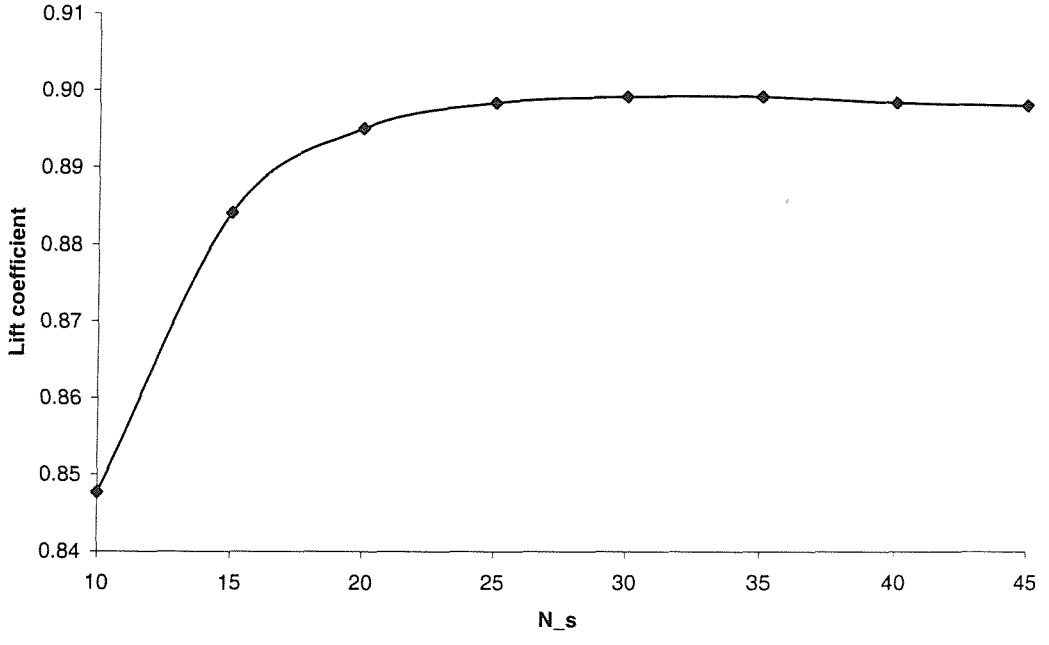

Figure 71: Effect of N_s on calculated lift coefficient of deformed triangular membrane for constant $N_t = 40$

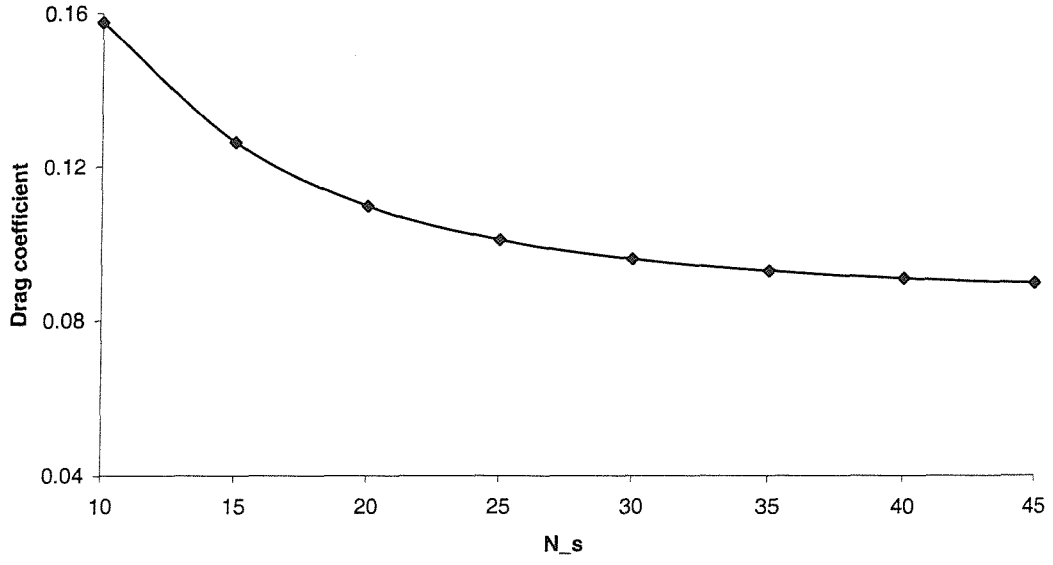

Figure 72: Effect of N_s on calculated drag coefficient of deformed triangular membrane for constant $N_t = 40$

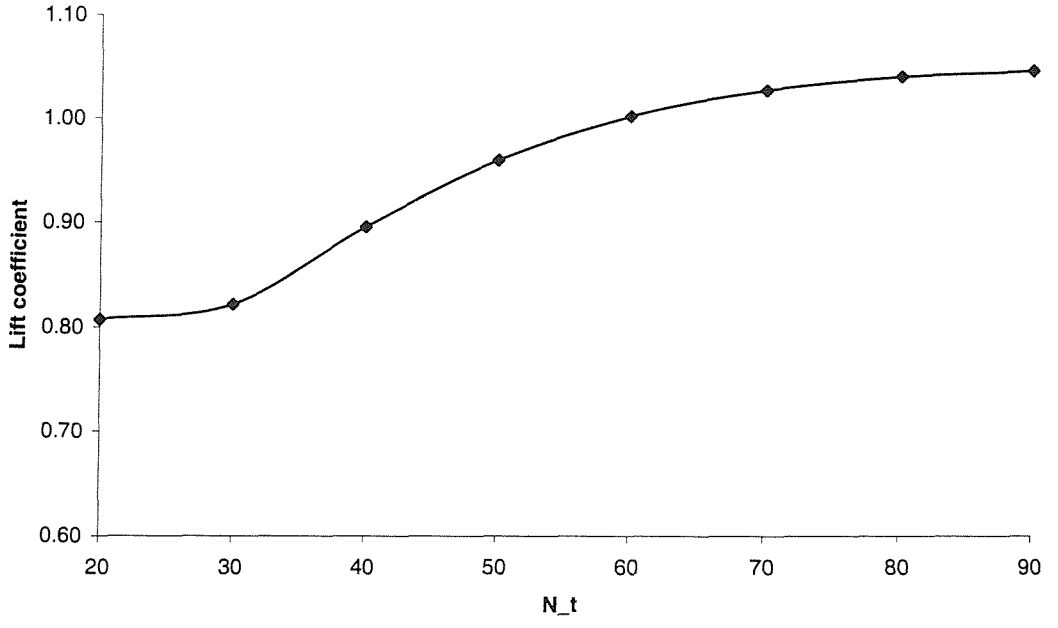

Figure 73: Effect of N_t on calculated lift coefficient of deformed triangular membrane for constant $N_s = 20$

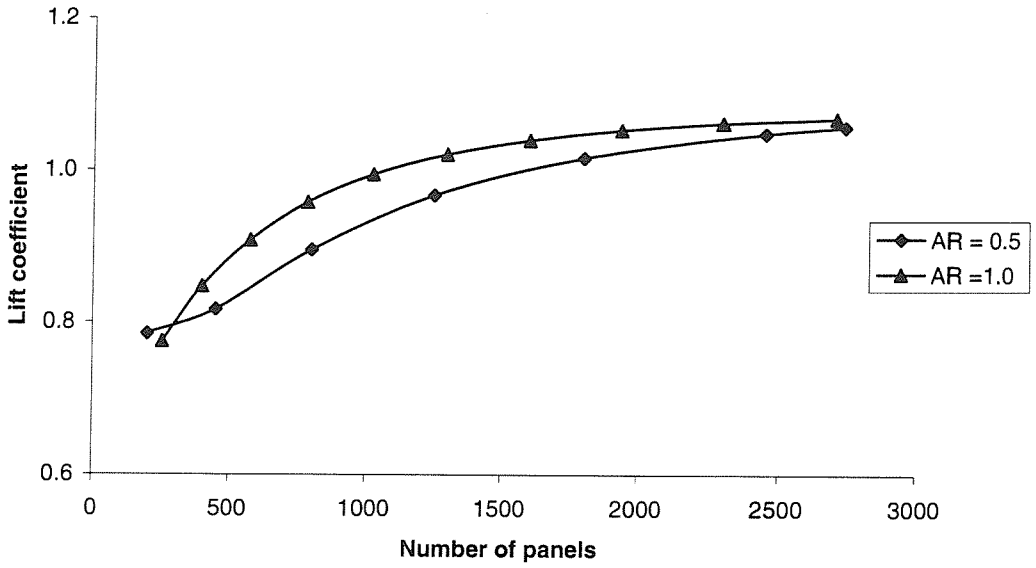

Figure 74: Lift coefficient for deformed triangular membrane for models with constant APAR

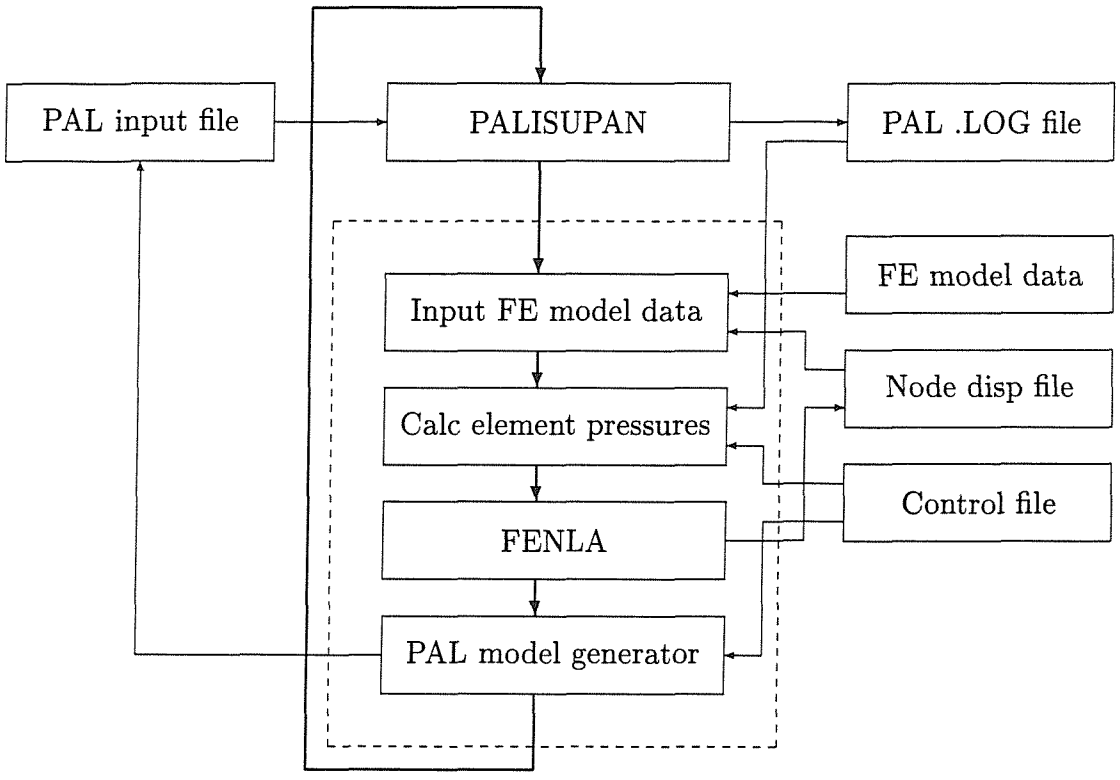

Figure 75: Aeroelastic program structure

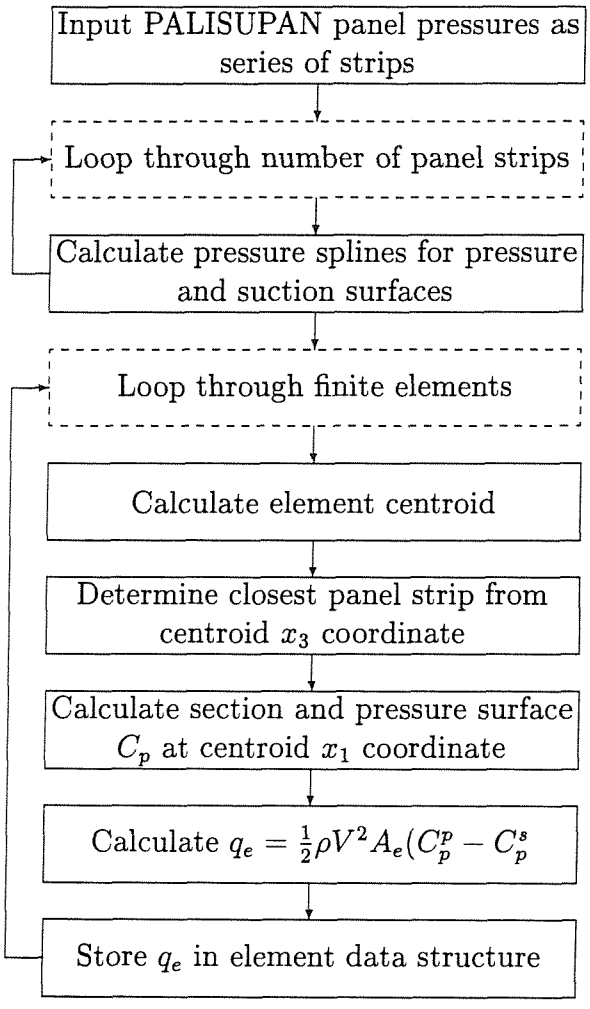

Figure 76: P-2-F program structure

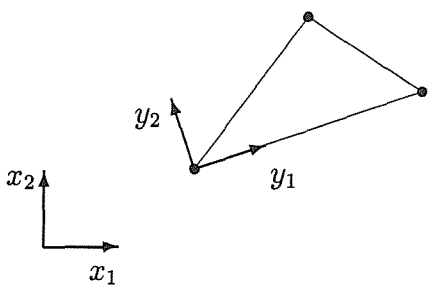

Figure 77: Triangular element local coordinates

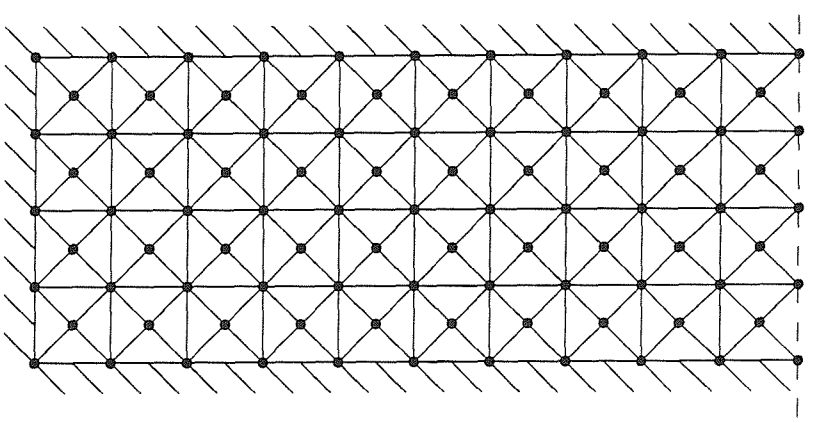

Figure 78: Symmetric triangular finite element mesh used for analysis of rectangular membranes

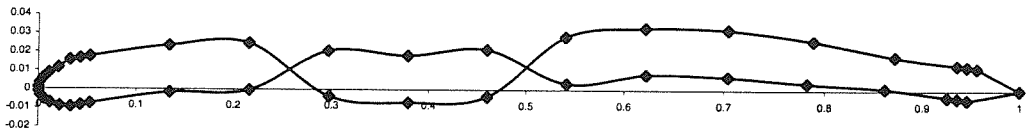

Figure 79: Failure of PALISUPAN model generation for membrane section with saddle point

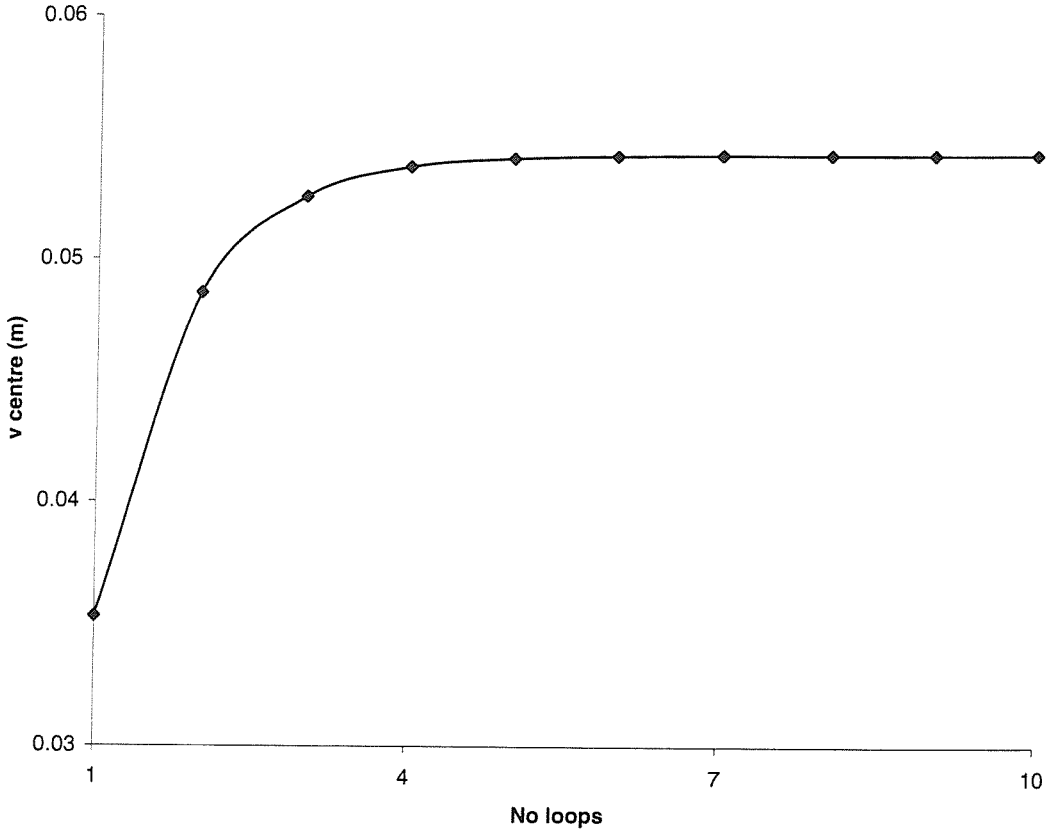

Figure 80: Convergence history of aeroelastic analysis of restrained membrane

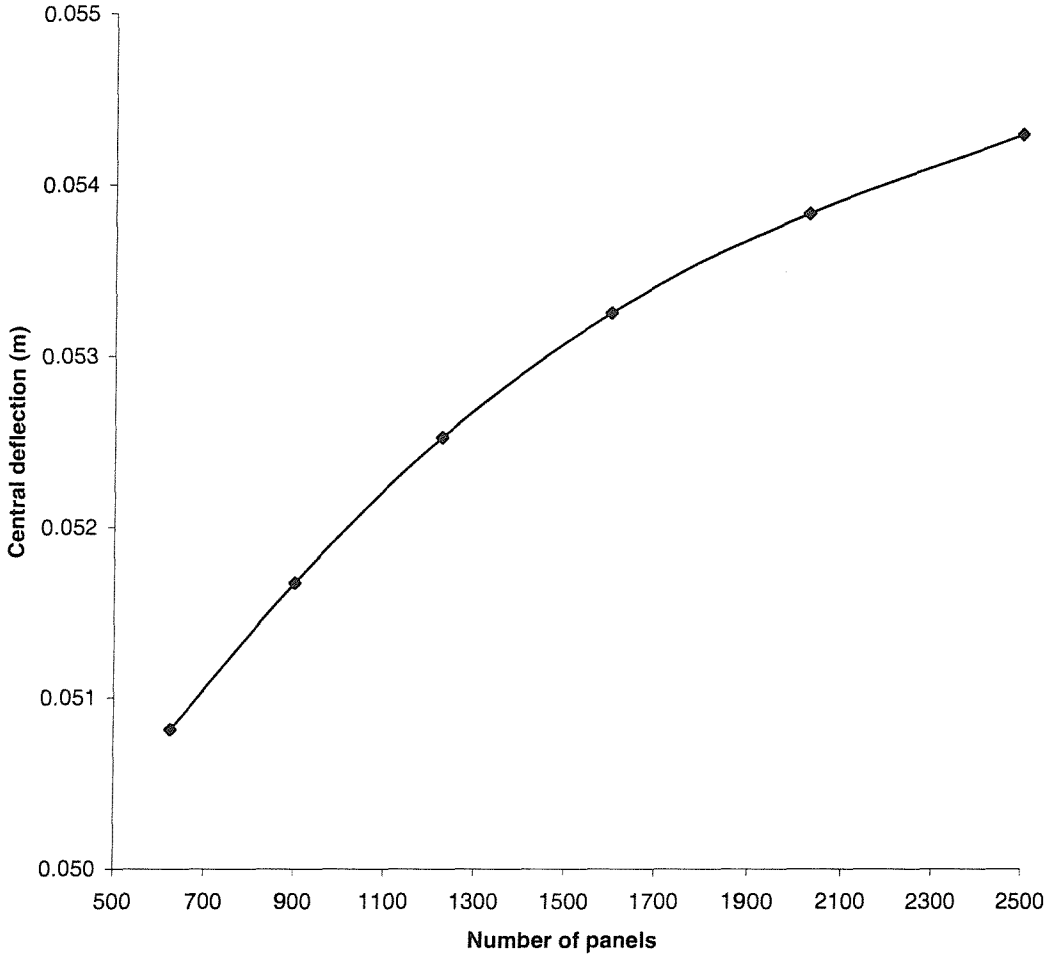

Figure 81: Effect of number of panels on central deflection of restrained rectangular membrane aeroelastic solution

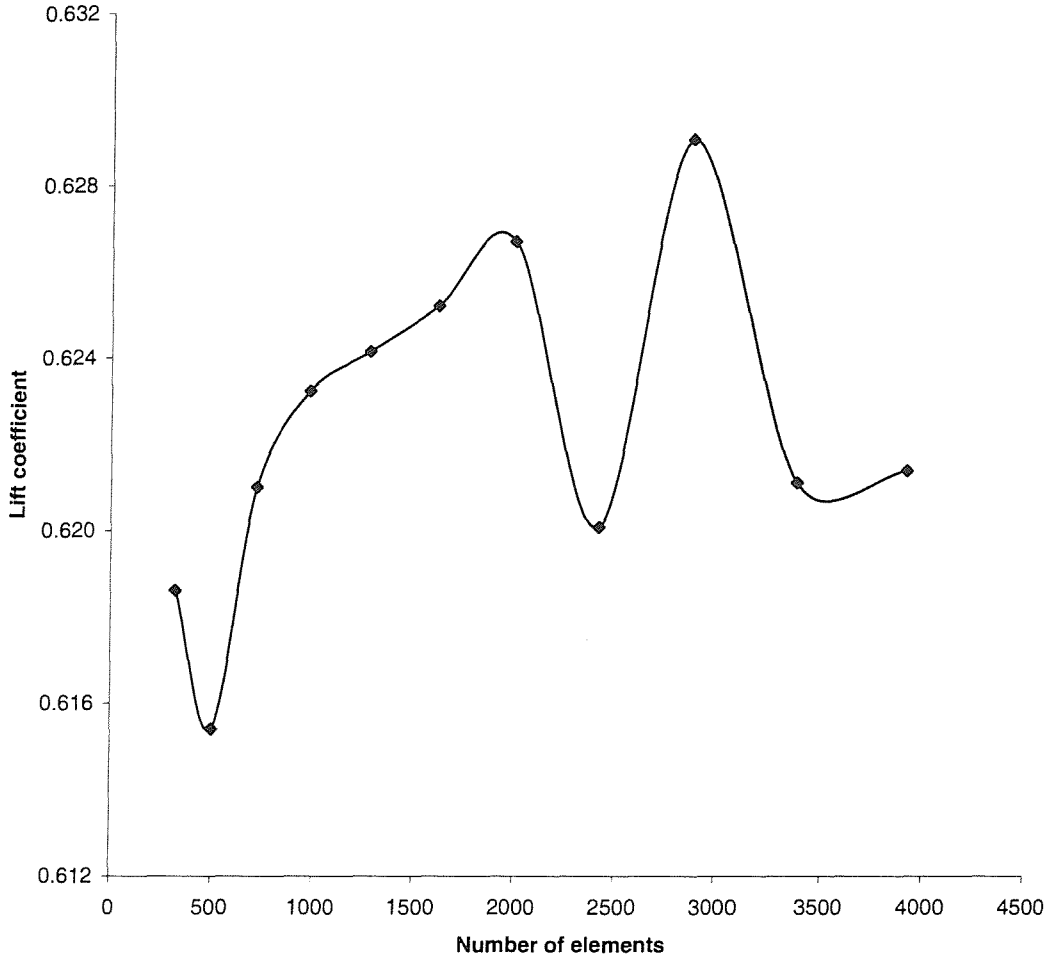

Figure 82: Effect of number of elements on lift coefficient of restrained rectangular membrane aeroelastic solution

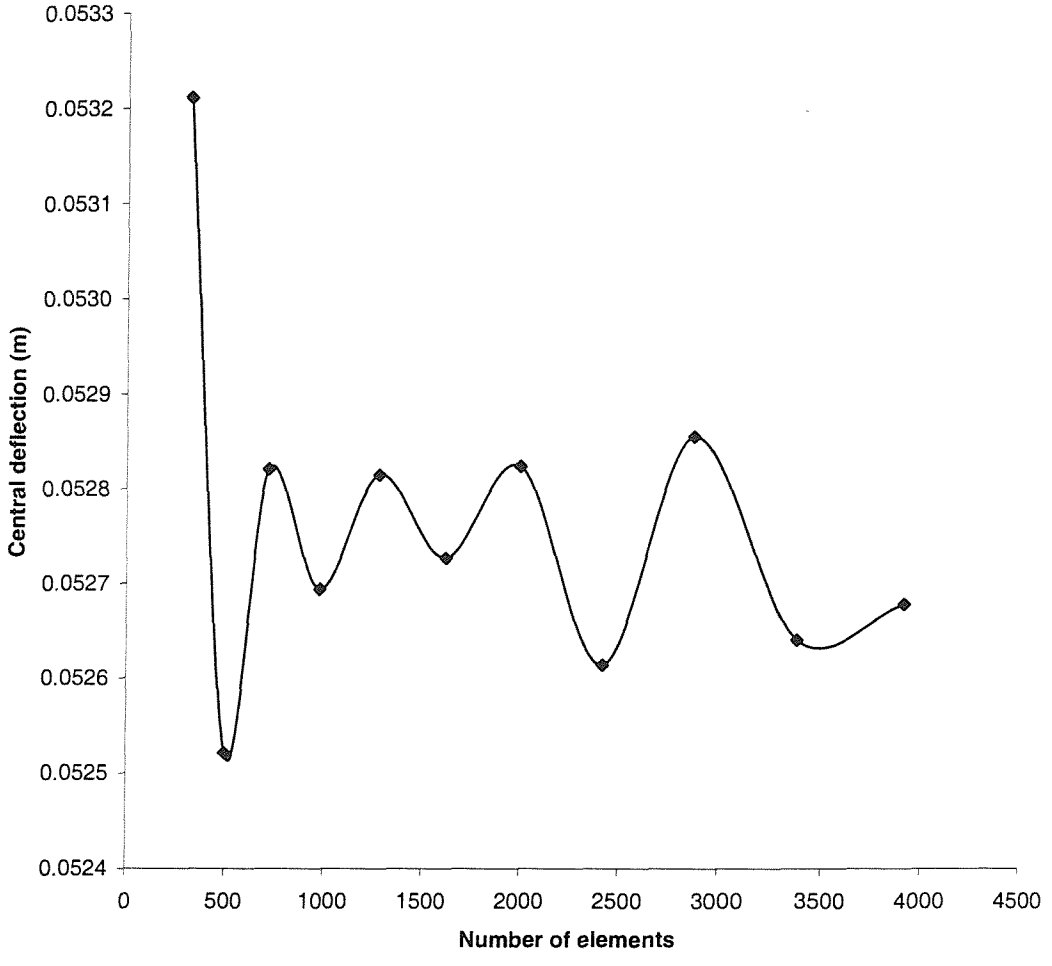

Figure 83: Effect of number of elements on central displacement of restrained rectangular membrane aeroelastic solution

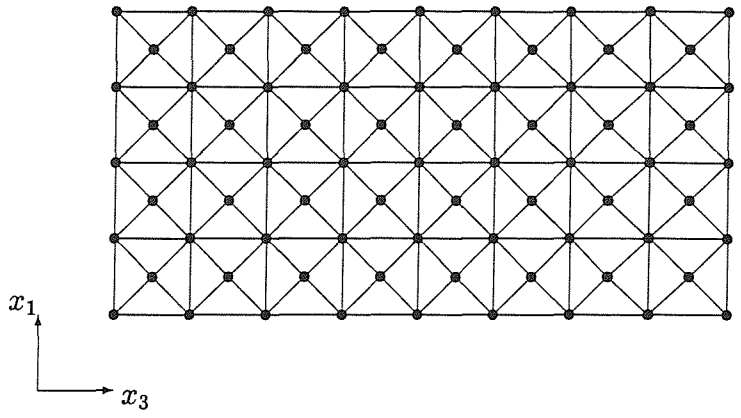

Figure 84: Symmetric triangular finite element mesh used for analysis of rectangular membranes with aspect ratio 2. Example shown consists of 128 elements

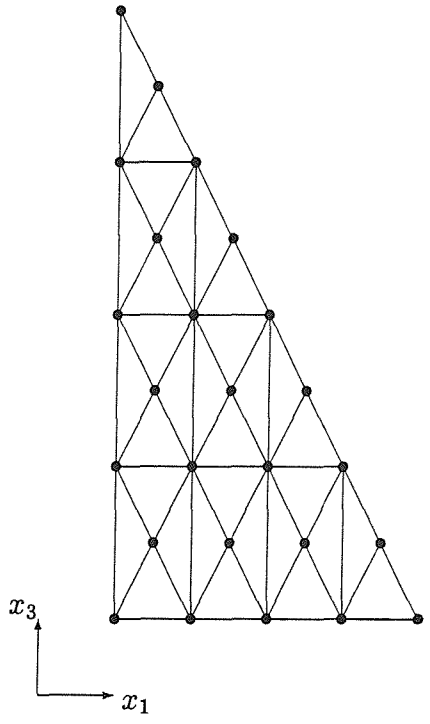

Figure 85: Triangular membrane mesh

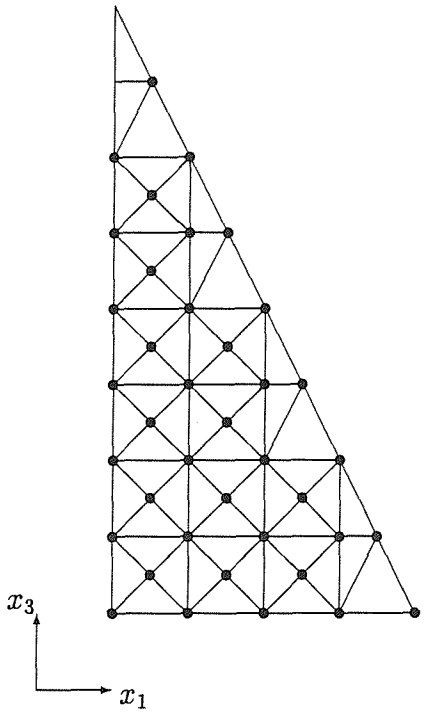

Figure 86: Revised triangular membrane mesh

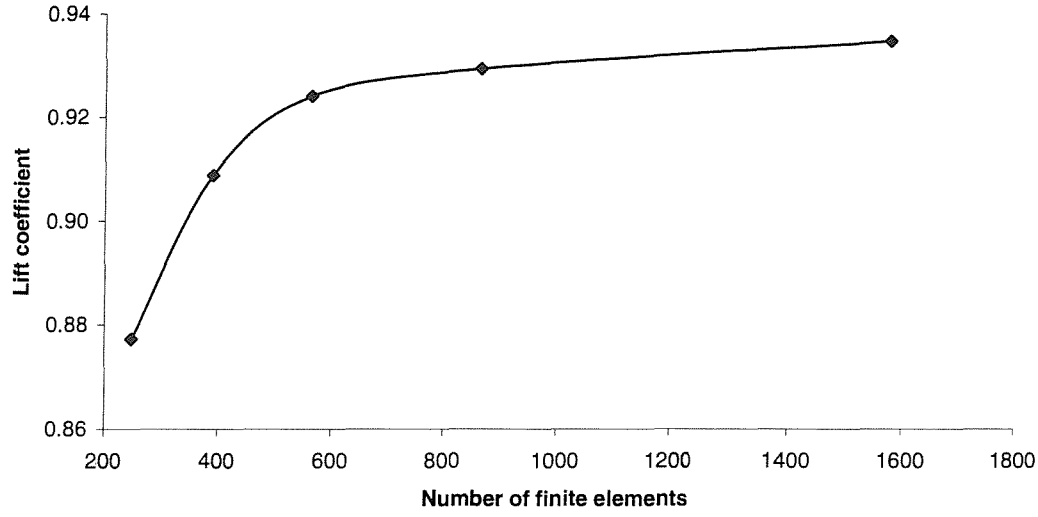

Figure 87: Lift coefficient against number of finite elements for MONSTA3 analysis of triangular membrane

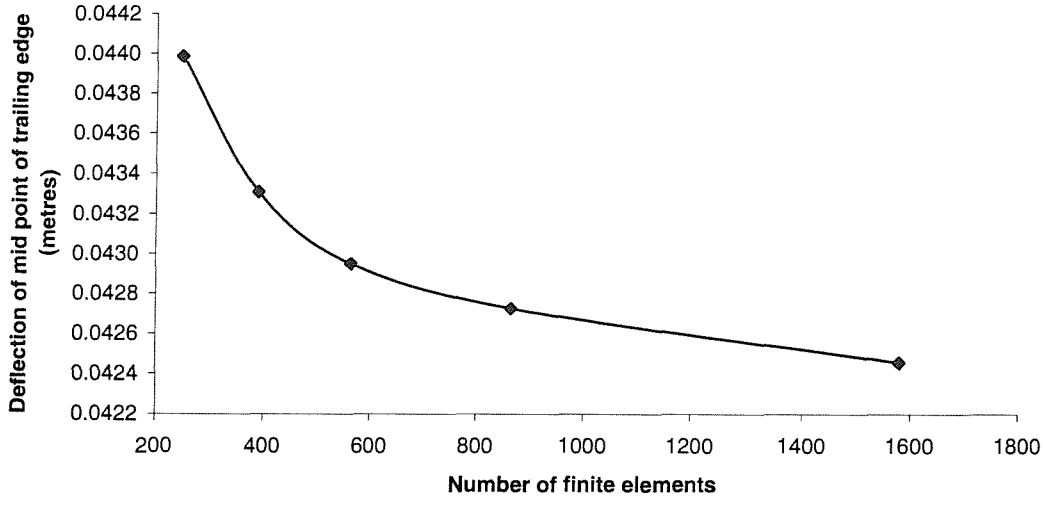

Figure 88: u_2 of mid point of trailing edge against number of finite elements for MONSTA3 analysis of triangular membrane

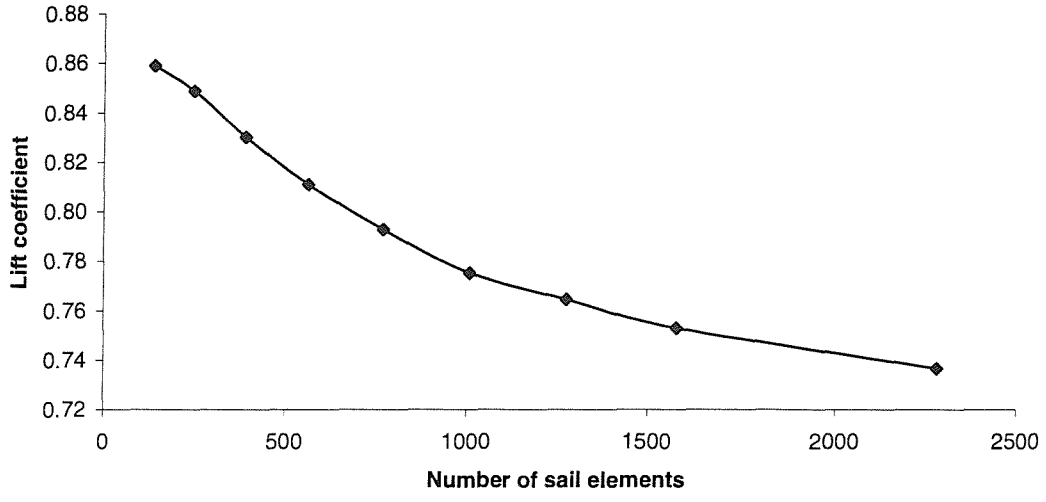

Figure 89: Lift coefficient against number of finite elements for aeroelastic analysis of rig1 model

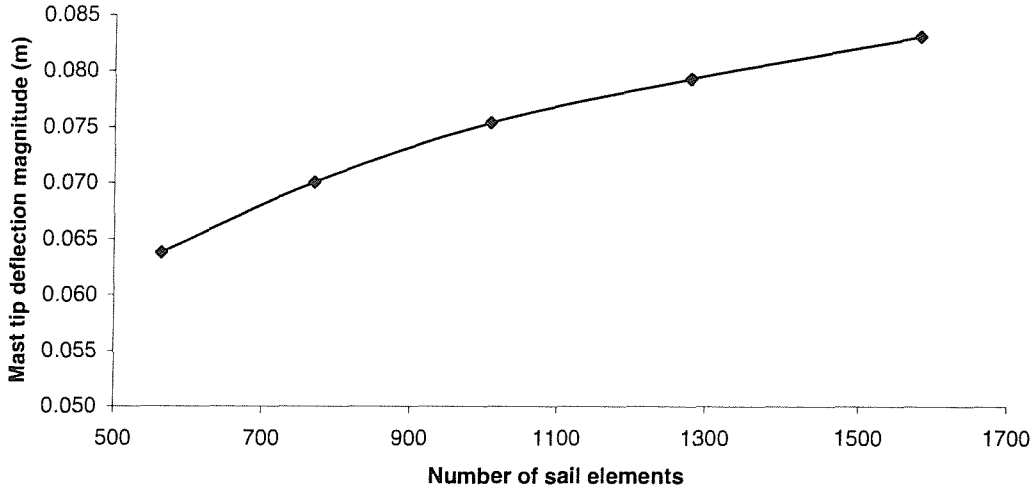

Figure 90: Magnitude of the mast tip deflection against number of finite elements for aeroelastic analysis of rig1 model

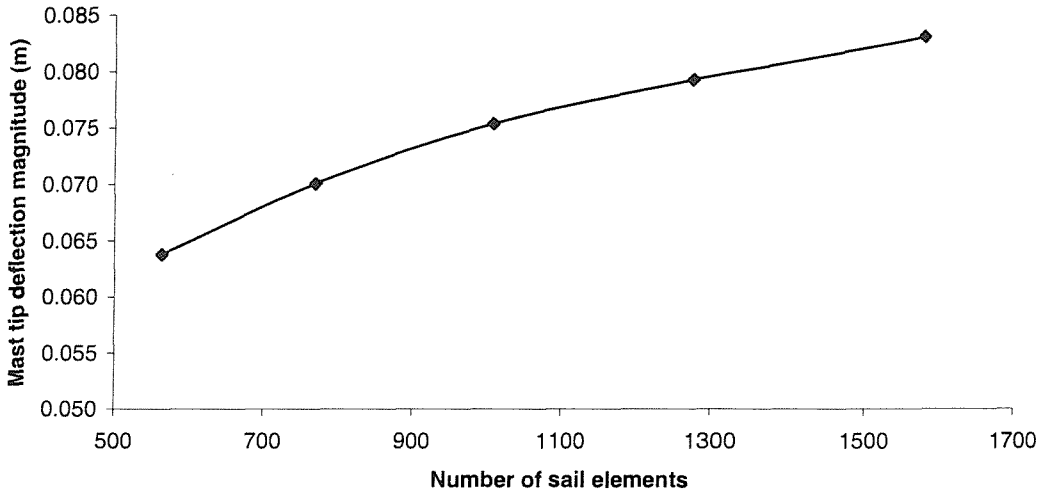

Figure 91: Magnitude of the mast tip deflection against number of finite elements for aeroelastic analysis of rig3 model

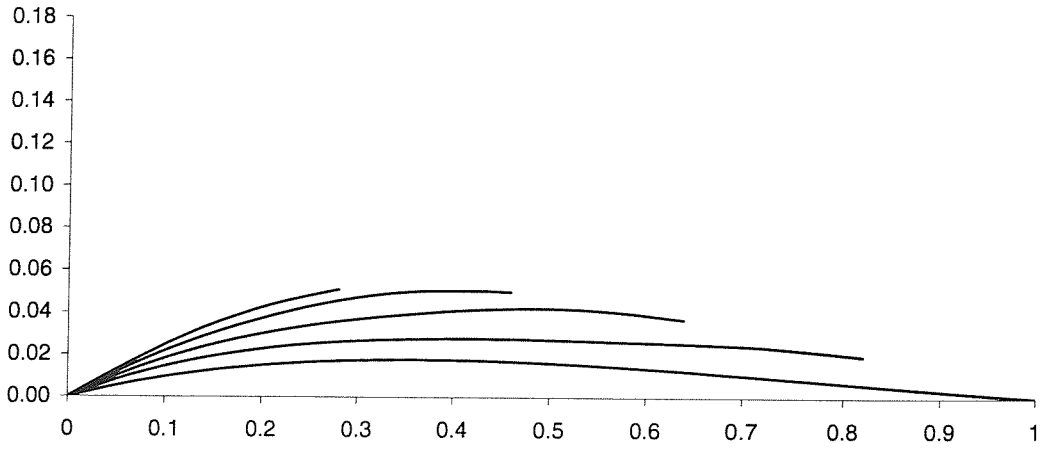

Figure 92: Deformed sail sections predicted by aeroelastic analysis of rig3R-14 model

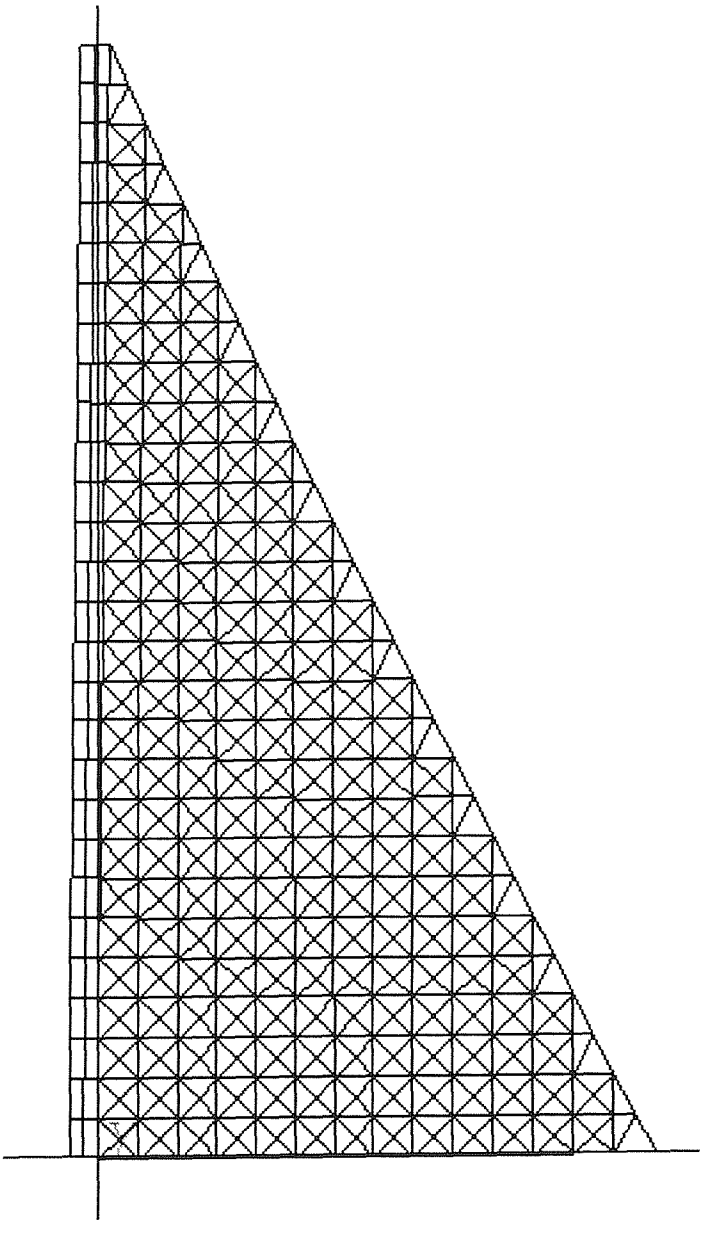

Figure 93: Deformed rig predicted by aeroelastic analysis of rig3C-14 model, view from side

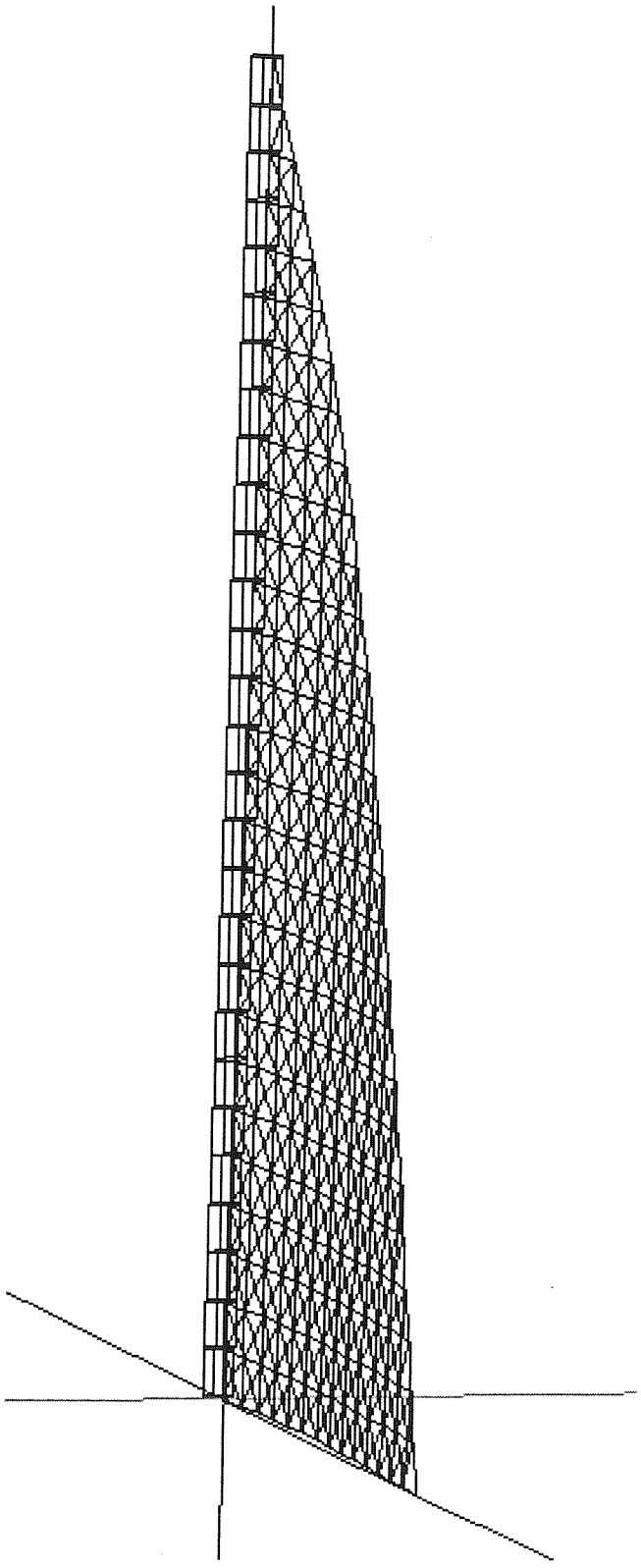

Figure 94: Deformed rig predicted by aeroelastic analysis of rig3R-14 model, view from downstream to windward

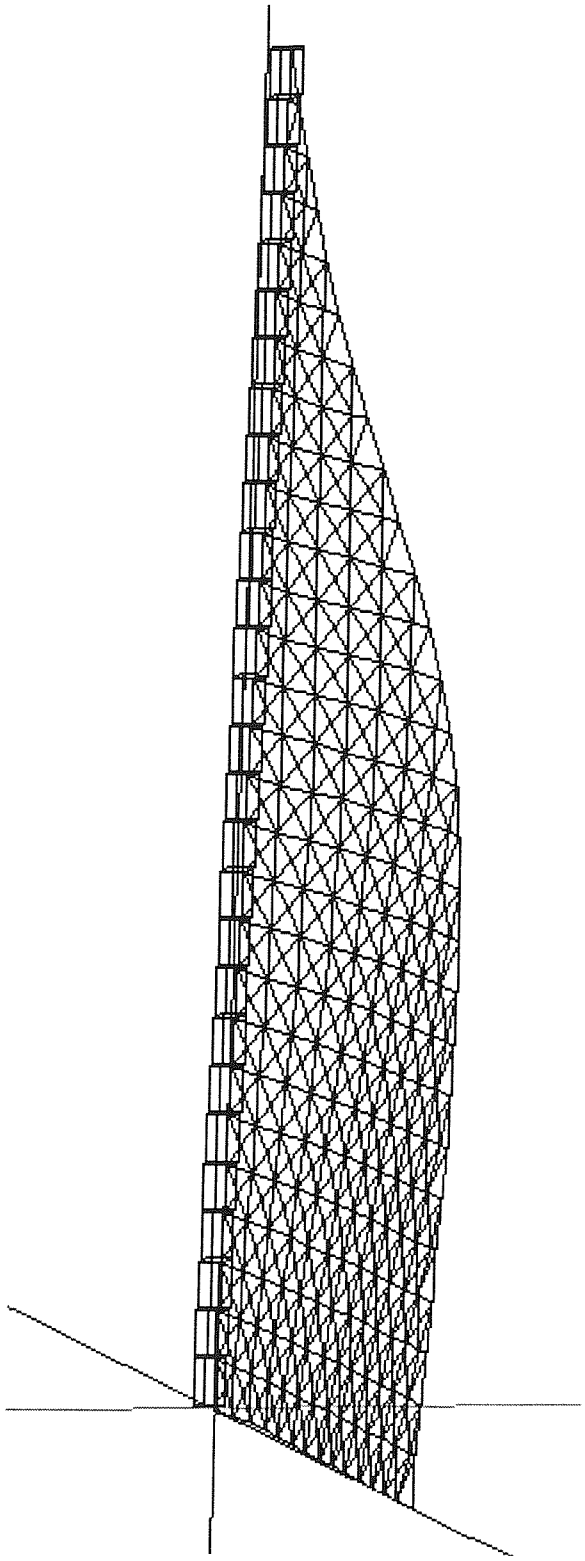

Figure 95: Deformed rig predicted by aeroelastic analysis of rig3-14 model, view from downstream to windward

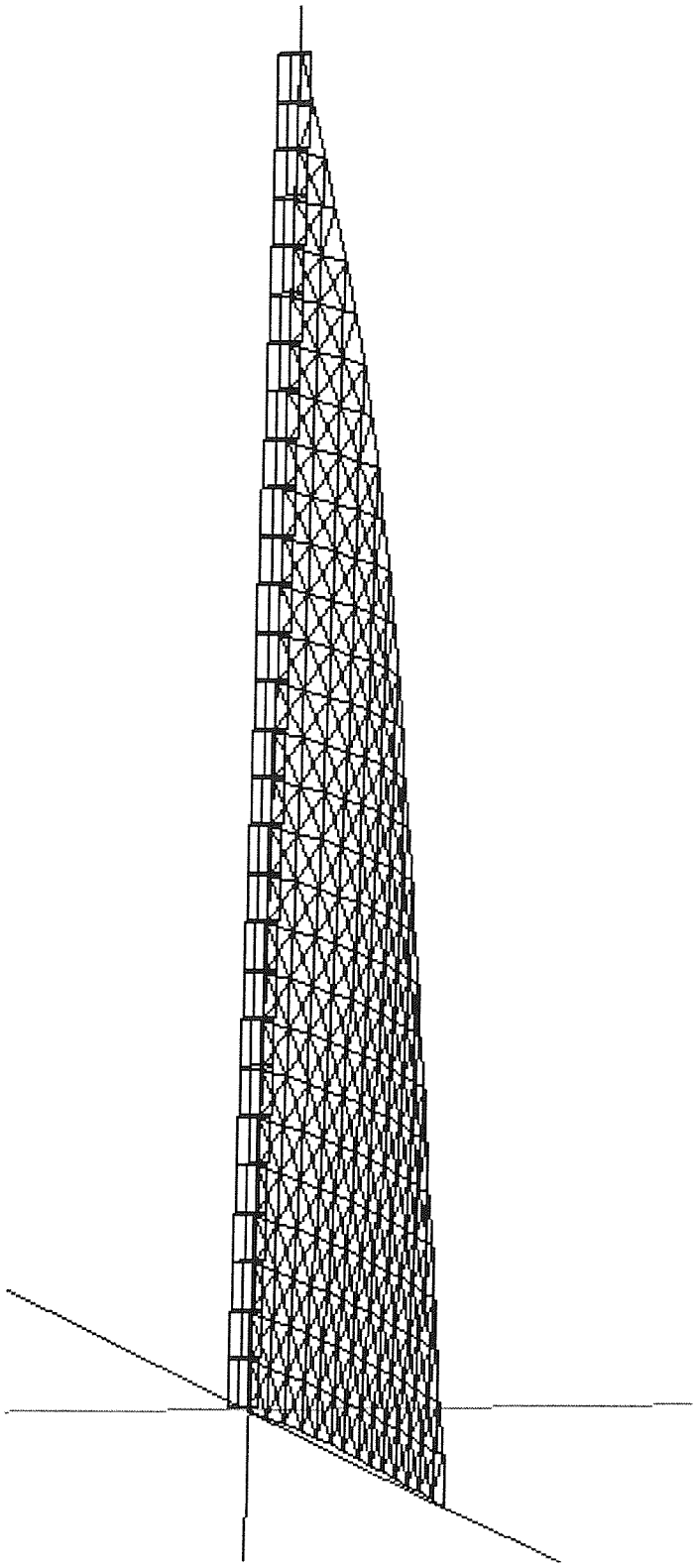

Figure 96: Deformed rig predicted by aeroelastic analysis of rig3CR-14 model, view from downstream to windward

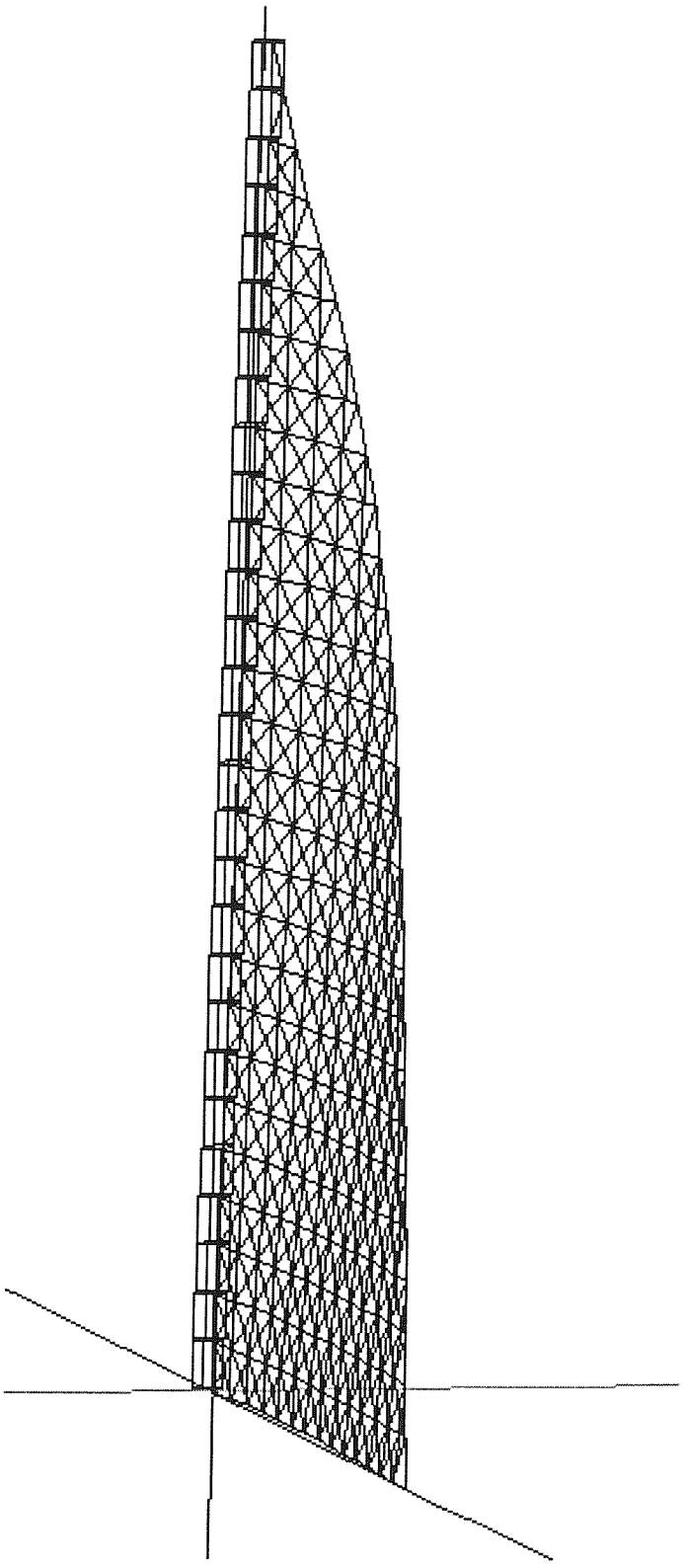

Figure 97: Deformed rig predicted by aeroelastic analysis of rig3C-14 model, view from downstream to windward

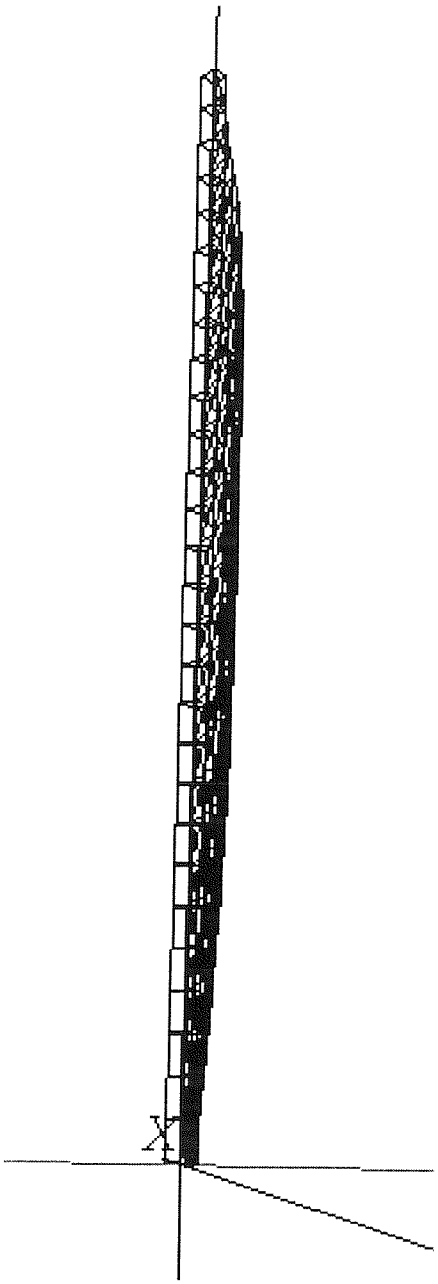

Figure 98: Deformed leech of the rig3CR-14 model, view from downstream to windward

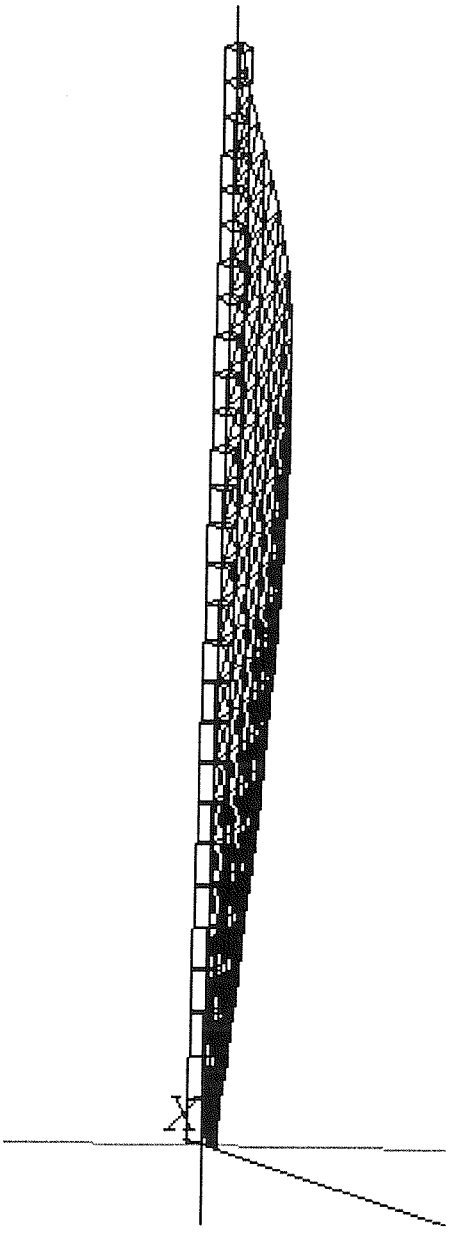

Figure 99: Deformed leech of the rig3C-14 model, view from downstream to windward

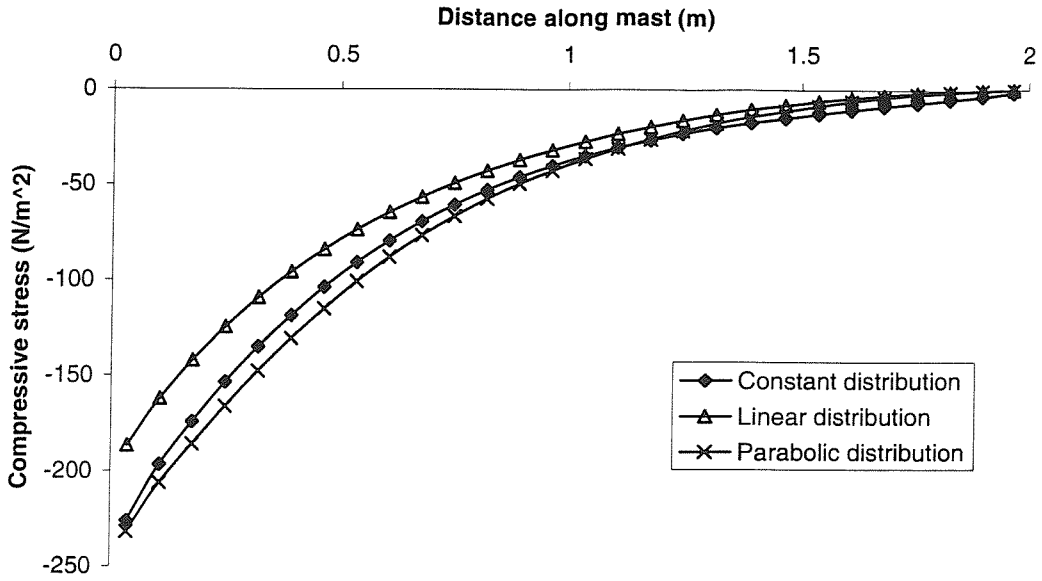

Figure 100: Mast compression predicted by distributed loading of rig3C-14 rig forces on a mast model

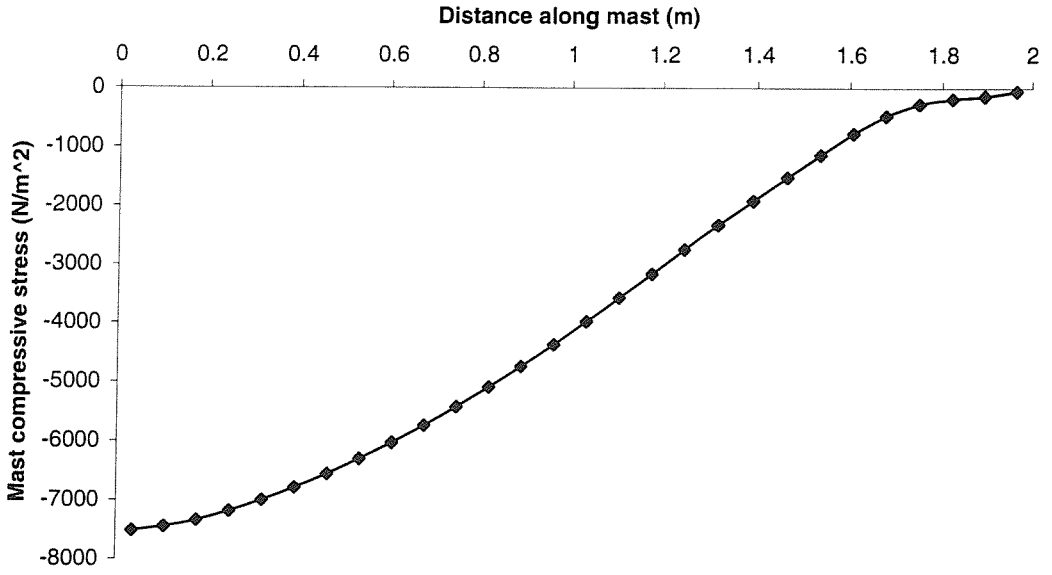

Figure 101: Mast compression predicted by aeroelastic analysis of rig3C-14 model

A Linear finite element theory

The finite element method represents a continuum with a series of discrete approximations. The particular area of interest examined here is the finite element method applied to structural mechanics, although the method can be used for any field problem.

A.1 The virtual work equation

The principle of virtual work equates the internal and external virtual work resulting from any compatible small virtual displacements imposed on the body in it's state of equilibrium. The virtual displacements are zero at prescribed displacements (boundary conditions) on the model, and are restricted to small displacements to validate the assumption of linear strain used in this formulation. Equating the internal and external work, where $\overline{\mathbf{U}}$ and $\overline{\epsilon}$ are the virtual displacements and strains, results in equation 149.

$$\int_V \overline{\epsilon}^T \tau dV = \int_V \overline{\mathbf{U}}^T \mathbf{f}^B dV + \int_{S_f} \overline{\mathbf{U}^{S_f}}^T \mathbf{f}^{S_f} dS + \sum_i \overline{\mathbf{U}^i}^T \mathbf{R}_C^i \qquad (149)$$

A.2 Discretization

Steps in the discretization of the continuum are as follows:

- The continuum is separated into finite elements.
- The elements are assumed to be interconnected at a discreet number of nodal points on the boundaries.
- A set of functions is chosen to uniquely determine the displacements within each element in terms of nodal displacements, which become the system unknowns.

- The state of strain in the elements is defined by the displacement functions in terms of the nodal displacements.
- A system of forces, concentrated at the nodes and balancing the boundary stresses and applied loads on the continuum is determined.

This results in a series of approximations:

- Displacement functions may not satisfy the requirements of displacement continuity between elements.
- Concentration of forces at nodes means that equilibrium is satisfied in an overall sense, not locally.

A.3 Displacement functions

The displacement field within an element, $\mathbf{u}$, is assumed to be a function of the displacements at the N element node points, as indicated in 150. This is the basis of the direct stiffness method, which allows an effective assembly of the finite element matrices into the model matrices.

$$u_i \approx \tilde{u_i} = \sum_{k=1}^{N} h_k u_i^k \tag{150}$$

$$\mathbf{u}^{(m)} = \mathbf{H}^{(m)}\mathbf{U}^{(m)} \tag{151}$$

Element shape functions, h_k are functions of the coordinate system used in the formulation of the strain displacement matrix, chosen such that $h_k = 1$ at node k and $h_k = 0$ at all other nodes in the element.

A.3.1 Element strain and stress calculation

With the assumption detailed in equation 150, the element strains can be evaluated from the node displacements using the strain displacement matrix, **B**, equation 152. This matrix is obtained by differentiation and combination of the interpolation functions.

$$\epsilon^{(m)} = \mathbf{B}^{(m)}\mathbf{U}^{(m)} \tag{152}$$

As an example of the derivation of **B** the strain displacement relationship for a two dimensional plane stress case is considered below. Equation 153 shows the relationship between the strain vector and displacements for this strain case. Introducing the displacement assumptions of equation 150 leads to the definition of the strain displacement matrix shown in equation 154.

$$\epsilon = \begin{bmatrix} \epsilon_x \\ \epsilon_y \\ \gamma_x y \end{bmatrix} = \begin{bmatrix} \delta u/\delta x \\ \delta v/\delta y \\ \delta u/\delta y + \delta v/\delta x \end{bmatrix} = \begin{bmatrix} \delta/\delta x & 0 \\ 0 & \delta/\delta y \\ \delta/\delta y & \delta/\delta x \end{bmatrix} \begin{pmatrix} u \\ v \end{pmatrix} \tag{153}$$

$$\epsilon^{(m)} = \mathbf{B}^{(m)}\mathbf{U}^{(m)} = \begin{bmatrix} h_{1,1} & 0 & & h_{N,1} & 0 \\ 0 & h_{1,2} & \cdots & 0 & h_{N,1} \\ h_{1,2} & h_{1,1} & & h_{N,2} & h_{N,1} \end{bmatrix} \mathbf{U}^m \tag{154}$$

The stresses in the finite element can be calculated from the element strains and initial stress, τ_I^m according to equation 155, where $\mathbf{C}^m$ is the element constitutive matrix.

$$\tau^{(m)} = \mathbf{C}^{(m)}\epsilon^{(m)} + \tau_I^{(m)} \tag{155}$$

A.4 Formulation of the finite element equations

The virtual work equation 149 can be re-written as a sum of integrations over the volume and areas of all finite elements, equation 156.

$$\sum_m \int_{V^{(m)}} \overline{\epsilon}^{(m)T} \tau^{(m)} dV = \tag{156}$$
$$\sum_m \int_{V^m} \overline{\mathbf{U}}^{(m)T} \mathbf{f}^{B(m)} dV + \int_{S_1^{(m)},\ldots,S_q^{(m)}} \overline{\mathbf{U}}^{S(m)^T} \mathbf{f}^{S(m)} dS^{(m)} + \sum_i \overline{\mathbf{U}}^{i^T} \mathbf{R}_C^i$$

Since the integrations in equation 156 are performed over element volumes and surfaces, different coordinate systems can be used for each element in the calculations. In order to sum the element contributions, they must be transformed into a common coordinate system before summation.

If the interpolations defined in the previous section are applied to the virtual displacements and strains, the virtual work equation 149 can be written in terms of the strain displacement matrix, interpolation functions and nodal displacements. Using the same interpolations for the virtual displacements results in symmetric stiffness matrices. Nodal point displacement vectors, $\mathbf{U}$ and $\overline{\mathbf{U}}$ are independent of the element, (m) and can be taken out of the summation signs, resulting in equation 157.

$$\overline{\mathbf{U}}^T \left[\sum_m \int_{V_{(m)}} \mathbf{B}^{(m)T} \mathbf{C}^{(m)} \mathbf{B}^{(m)} dV^{(m)} \right] \mathbf{U} =$$
$$\overline{\mathbf{U}}^T \left[\left\{ \sum_m \int_{V_{(m)}} \mathbf{H}^{(m)T} \mathbf{F}^{B(m)} dV^{(m)} \right\} \right.$$
$$+ \left\{ \sum_m \int_{S_1^{(m)},\ldots,S_q^{(m)}} \mathbf{H}^{S(m)^T} \mathbf{F}^{S(m)} dS^{(m)} \right\}$$
$$\left. - \left\{ \sum_m \int_{V_{(m)}} \mathbf{B}^{(m)T} \tau^{I(m)} dV^{(m)} \right\} + \mathbf{R}_C \right] \tag{157}$$

By applying virtual displacements of unit displacement on each degree of freedom in turn, with all other displacements set to zero, equation 157 reduces

to a set of linear equations, shown in equation 158. The stiffness matrix, $\mathbf{K}$ is defined in equation 159 and the load vector, $\mathbf{R}$ is defined in equation 160.

$$\mathbf{KU} = \mathbf{R} \tag{158}$$

$$\mathbf{K} = \sum_{m} \int_{V^{(m)}} \mathbf{B}^{(m)T} \mathbf{C}^{(m)} \mathbf{B}^{(m)} dV^{(m)} \tag{159}$$

$$\mathbf{R} = \mathbf{R}_B + \mathbf{R}_S - \mathbf{R}_f + \mathbf{R}_C \tag{160}$$

The load vector consists of components due to element body forces, surface forces, initial stresses and concentrated nodal loads which correspond to the right hand side terms in equation 157. The non zero rows and columns of the matrices and vectors, corresponding to the degrees of freedom of the element nodes, are calculated for each element. If a local coordinate system is used in calculation of the element characteristics, the element matrices and vectors are transformed into the model global coordinate system. Assembly of the model stiffness matrix and load vectors is carried out using the connectivity of the elements.

A.5 Application of boundary conditions

A.6 Boundary conditions

The method used for application of the boundary conditions allows any displacement to be specified on a degree of freedom. The transformation used is shown in equation 161, where displacement u_2 is given an applied displace-

ment, Z.

$$\begin{bmatrix} k_{11} & k_{12} & k_{13} & k_{14} \\ k_{21} & k_{22} & k_{23} & k_{24} \\ k_{31} & k_{32} & k_{33} & k_{34} \\ k_{41} & k_{42} & k_{43} & k_{44} \end{bmatrix} \begin{Bmatrix} u_1 \\ Z \\ u_3 \\ u_4 \end{Bmatrix} = \begin{Bmatrix} P_1 \\ P_2 \\ P_3 \\ P_4 \end{Bmatrix} \equiv \tag{161}$$

$$\begin{bmatrix} k_{11} & 0 & k_{13} & k_{14} \\ 0 & 1 & 0 & 0 \\ k_{31} & 0 & k_{33} & k_{34} \\ k_{41} & 0 & k_{43} & k_{44} \end{bmatrix} \begin{Bmatrix} u_1 \\ Z \\ u_3 \\ u_4 \end{Bmatrix} = \begin{Bmatrix} P_1 - k_{12}Z \\ Z \\ P_3 - k_{32}Z \\ P_4 - k_{42}Z \end{Bmatrix}$$

A.7 Stress calculation

Calculation of the element stresses in a linear finite element model in two dimensions is carried out according to equation 162.

$$\begin{Bmatrix} \sigma_{xx} \\ \sigma_{yy} \\ \tau_{xy} \end{Bmatrix} = \mathbf{C} \begin{Bmatrix} \epsilon_{xx} \\ \epsilon_{yy} \\ \gamma_{xy} \end{Bmatrix} \tag{162}$$

The strain in the element can be calculated according to equation 163, where $\mathbf{u^n}$ is a vector of the node displacements.

$$\begin{Bmatrix} \epsilon_{xx} \\ \epsilon_{yy} \\ \gamma_{xy} \end{Bmatrix} = \mathbf{B}\mathbf{u^n} \tag{163}$$

A.8 Isoparametric formulation

The iso-parametric element uses a element based natural coordinate system. The natural coordinate system employed in the two dimensional linear triangle element is shown in figure 6. Interpolation functions are defined in terms

of the element natural coordinates and the same functions are used interpolate both coordinates and displacements within the element, as shown in equations 164 and 165.

$$x_i = \sum_{j=1}^{N} h_j x_i^j \tag{164}$$

$$u_i = \sum_{j=1}^{N} h_j u_i^j \tag{165}$$

To calculate the stiffness matrix of the element, it is necessary to evaluate the strain displacement matrix, $\mathbf{B}$, which contains derivatives of the element displacements with respect to the element local coordinates. Element displacements are defined in terms of element natural coordinates, and the Jacobian operator, $\mathbf{J}$, defined in three dimensions in equation 166, is used to relate the derivatives in normal coordinates to the local coordinate derivatives, equation 168.

$$\begin{bmatrix} \frac{\partial}{\partial r} \\ \frac{\partial}{\partial s} \\ \frac{\partial}{\partial t} \end{bmatrix} = \begin{bmatrix} \frac{\partial x}{\partial r} & \frac{\partial y}{\partial r} & \frac{\partial z}{\partial r} \\ \frac{\partial x}{\partial s} & \frac{\partial y}{\partial s} & \frac{\partial z}{\partial s} \\ \frac{\partial x}{\partial t} & \frac{\partial y}{\partial t} & \frac{\partial z}{\partial t} \end{bmatrix} \begin{bmatrix} \frac{\partial}{\partial x} \\ \frac{\partial}{\partial y} \\ \frac{\partial}{\partial z} \end{bmatrix} \tag{166}$$

$$\frac{\partial}{\partial \mathbf{r}} = \mathbf{J} \frac{\partial}{\partial \mathbf{x}} \tag{167}$$

$$\frac{\partial}{\partial \mathbf{x}} = \mathbf{J}^{-1} \frac{\partial}{\partial \mathbf{r}} \tag{168}$$

The elements of the Jacobian matrix can be found from differentiation of the coordinate interpolations, equation 164. Derivatives of the interpolation functions with respect to the element local coordinate system can then be

found from the inverse of the Jacobian matrix and the derivatives of the interpolation functions with respect to the element natural coordinates. These can then be used to assemble the strain displacement matrix, $\mathbf{B}$. The element stiffness matrix, equation 159 will now contain strain displacement matrices which are functions of the element natural coordinates. The volume integral extends over the natural coordinate volume, and the volume differential needs to be written in terms of the natural coordinates, equation 169, where $\det \mathbf{J}$ id the determinant of the Jacobian operator.

$$dV = \det \mathbf{J} \; dr \; ds \; dt \tag{169}$$

Since the integration over the volume integral is generally not effective in the case of higher order elements, numerical integration is employed to calculate the stiffness matrix, equation 171. Here $\mathbf{F}_{ijk}$ is $\mathbf{F}$ evaluated at the numerical integration point, (r_i, s_j, t_k), and α_{ijk} is a constant dependent on the integration point.

$$\mathbf{F} = \mathbf{B}^T \mathbf{C} \mathbf{B} \det \mathbf{J} \tag{170}$$

$$\mathbf{K} = \sum_{i,j,k} \alpha_{ijk} \mathbf{F}_{ijk} \tag{171}$$

A similar process is used to calculate the force vectors defined in equation 160.

B Numerical integration schemes

Gaussian integration schemes are used for the two dimensional elements. The sampling point coordinates, r_i, and weighting, α_i for the numerical integration are given in table 44 for integration over the interval -1 to +1 using n_{int} points, and these are used to evaluate an integral according to equation 172. Gaussian integration of order n will exactly evaluate an expression of order (2n-1).

$$\int_{-1}^{+1} F(r)dr = \sum_{i=1}^{n} w_i F(r_i) \tag{172}$$

The one dimensional formulae can be used to integrate over two and three dimensions in quadrilateral and solid elements respectively by applying the one dimensional formulae in each direction, as shown in equation 173 for the three dimensional case.

$$\int_{-1}^{+1}\int_{-1}^{+1}\int_{-1}^{+1} F(r,s,t)dr\ ds\ dt = \sum_{i=1} n \sum_{j=1} n \sum_{k=1} n w_i w_j w_k F(r_i, s_j, t_k) \tag{173}$$

Integration over three dimensions can be carried out with the same order of accuracy as a twenty seven point (3x3x3) integration by using only 14 points, as described by Irons [25]. The sampling point coordinates and weighting are obtained from equation 174, using the following values:

- B=0.886426593, b=0.795822426;
- C=0.335180055, c=0.758786911.

The accuracy of this scheme was demonstrated by Hellen [19] for cantilever analysis.

$$\int_{-1}^{+1}\int_{-1}^{+1}\int_{-1}^{+1} F(r,s,t) = \tag{174}$$
$$B\{F(-b,0,0)+F(b,0,0)+F(0,-b,0)+\cdots \text{ 6 terms}\}$$
$$C\{F(-c,-c,-c)+F(c,-c,-c)+\cdots \text{ 8 terms}\}$$

B.1 Triangular elements

The integration over the area of triangular elements is carried out using the coordinates and weighting of figure 45 (obtained from Bathe [4]) as shown in equation 175.

$$\int_0^1\int_0^1 F(r,s)dr\ ds = \frac{1}{2}\sum_{i=1}^{n} w_i F(r_i,s_i) \tag{175}$$

C Aeroelastic program data and control files

C.1 Control file

The format of the control file for the aeroelastic program is as listed below:

- N_t - Number of chordwise panels for PALISUPAN model
- N_s - NUmber of spanwise panels for PALISUPAN model
- N_{ss} - Number of sail panels for PALISUPAN model
- V_{infty} - Freestream velocity
- N_free - Number of free wake panels (as the wake is fixed this has no effect on the solution)
- α - Angle of flow incidence
- N_{eb} - Number of elements along the boom in the finite element model
- N_{sec} - Number of sections used to generate the PALISPAN model
- N_{le} - Number of points used to define the leading edge/mast in the PALISUPAN input model
- N_{sur} - Number of points used to define the sail surface in the PALISUPAN input model
- t_m - Thickness multiplier to calculate sail thickness for PALISUPAN input model

C.2 Finite element data file

The finite element data file uses the following format:

- Number of nodes
- Number of sail elements
- Number of mast elements
- Number of boundary conditions
- Number of point loads
- Number of material properties
- Number of load steps
- Element thickness
- Initial stress
- Convergence criteria
- Realxation factor β_1
- Relaxation factor β_2
- List of material properties:
  - Reference number
  - Youngs modulus
  - Poissons ratio
- List of node data
  - Reference number

  - Global coordintes

- List of sail element data
  - Reference number
  - Material property
  - List of nodes defining element
- List of mast elements (format as for sail elements)
- List of boundary conditions
  - Node number
  - Flag to indicate degree of freedom restrained
- List of point load data
  - Node number
  - Flag to indicate direction of load
  - Load magnitude